Research into the Design and Validation of an Innovative Intraoperative Load Sensor for Total Knee Replacements through Experimental and Cadaveric Investigations

By: Samira Al-Nasser

A thesis submitted in partial fulfilment of the requirements of Bournemouth University for the degree of Doctor of Philosophy (Ph.D.)

Collaborating Establishment: Zimmer Biomet

Bournemouth University

Faculty of Science and Technology

2024

Abstract

Balancing the force between compartments in the knee joint during a Total Knee Replacement (TKR) is a vital parameter for surgeons to achieve successful outcomes for patients due to the complexity of the joint, articulating surfaces, tendons, and ligaments. These structures are all impacted by the forces created in the joint following a TKR. A lack in equilibrium can cause an asymmetric gait, pain, a decrease in range of motion (ROM), loosening of the implant, and premature wear resulting in early revision surgeries. Load balancing involves the use of implants and tools to ensure the forces on the joint are evenly distributed across the articulating surfaces of the medial and lateral compartments. Surgeons typically rely on haptic feedback and experience to determine if the joint is balanced; however, the use of an objective device would help to quantify this objectively and ensure positive postoperative outcomes as opposed to traditional subjective methods.

Current literature implies that such systems, which measure the load in the knee intraoperatively, require improvements to the accuracy and design before the impact can be further investigated. The design and validation of an objective tool to be used intraoperatively to balance the load in the knee was the subject of this research. The novelty of this system is in the gap in accuracy and sensitivity amongst existing systems on the market combined with design features which integrate well with the surgical workflow. Additionally, the compatibility of prior sensors with a variety of implant systems is a limitation of their use.

Through this research the design of two sensors were fabricated and investigated. The design of these sensors included features to increase the sensitivity and accuracy for determining the magnitude of the load and its location. Finite Element Analysis (FEA) aided in design optimisation including strain gauge placement and material selection. Additionally, the development and use of Artificial Intelligence (AI) in this system was paramount. This was due to the complex geometry of the sensors meaning there was no closed form solution to determine the load and location of the femur's articulation with the sensor in each compartment. Based on this nature of this problem an Artificial Neural Network (ANN) was used and was optimised based on physically collected training data. This research also aided in increasing the overall confidence of AI in the medical field which will aid regulatory bodies in their decision to allow for the clinical use of such devices to improve patient outcomes.

A mixed method approach was used that included both quantitative and qualitative assessments of the design and the in-service use of the sensors. This included laboratory testing to investigate the performance of the AI in predicting the load and location of the contact force. Accuracy testing uncovered an average accuracy of about 90% for the Zimmer Specific sensor and about 88% for the Ring sensor when predicting the load. When predicting the centre of pressure, the average distance of the predictions from the actual location was 5.30 mm and 4.39 mm for the Zimmer Specific and Ring sensors respectively. Moreover, cadaveric testing improved the design of the sensor from the perspective of an experienced orthopaedic surgeon as well as confirmed the usability and proper function by comparing results to expected kinematic and kinetic behaviours of the knee.

Abbreviations

ACL	Anterior Cruciate Ligament
AI	Artificial Intelligence
AM	Additive Manufacturing
ANN	Artificial Neural Network
BFGS	Broyden–Fletcher–Goldfarb–Shanno
BR	Baysian regularization
BW	Body Weight
CAD	Computer-Aided Design
CNC	Computer Numerical Control
CNN	Convolution Neural Network
CNT	Carbon Nanotube
CT	Computer Tomography
dB	Decibel
FDA	Food and Drug Administration
FEA	Finite Element Analysis
GBP	Pound sterling
JCF	Joint Contact Force
kg	Kilogram
kgf	Kilogram Force
lbf	Pounds of force
LCL	Lateral Cruciate Ligament
LM	Levenberg-Marquardt
ML	Machine Learning
MCL	Medial Cruciate Ligament
MHRA	Medicines and Healthcare products Regulatory Agency
mm	Millimeter
mse	Mean squared error
msw	Mean squaed weights
NHS	National Health Service
NJR	National Joint Registry
N	Newton
OA	Osteoarthritis
PCB	Printed Circuit Board
PCL	Posterior Cruciate Ligament
PDMS	Polydimethylsiloxane
PET	Polyethylene terephthalate
PI	Polyimide
PLA	Polylactic acid
PKS	Persona Knee System
PP	Polypropylene
PU	Polyurethane
RA	Rheumatoid Arthritis
RNN	Recurrent Neural Network
ROM	Range of Motion
TKR	Total Knee Replacement
UTM	Universal Testing Machine

List Figures

List of Tables

Publications List

1.1   Journal Papers

1. **Al-Nasser, Samira**, Siamak Noroozi, Adrian Harvey, Navid Aslani, and Roya Haratian. 2024. "Exploring the Performance of an Artificial Intelligence-Based Load Sensor for Total Knee Replacements" Sensors 24, no. 2: 585. https://doi.org/10.3390/s24020585
2. **Al-Nasser, Samira**, Siamak Noroozi, and Adrian Harvey. 2024. **"**Cadaveric Testing of a Novel Intraoperative Load Sensor for Soft-tissue balancing during Total Knee Replacements" Clinics in Surgery Clin Surg. 2024;9(1):3700. DOI: 10.25107/2474-1647.3700
3. **Al-Nasser S**, Noroozi S; Harvey A. Design of a Novel Intraoperative Sensor for Load Balancing and Tracking during Total Knee Replacements (TKR). Ann Materials Sci Eng. 2024; 8(1): 1050.

1.2   Conference Papers

1. **Al-Nasser, S**.; Noroozi, S.; Haratian, R.; Harvey, A review of balancing methods for Total Knee Replacements. ICBEAAE 2022: 16th International Conference on Biomedical Engineering Applications and Advanced Technologies
2. **Al-Nasser, S**.; Noroozi, S.; Haratian, R.; Harvey, Review of Kinematics and Joint Load Forces in Total Knee Replacements Influencing Surgical Outcomes**.** 18th International Conference on Condition Monitoring and Asset Management, CM 2022
3. **Al-Nasser, S**.; Noroozi, S.; Haratian, R.; Aslani, N.; Harvey, A. Load Prediction using an Intraoperative Joint Sensor and Artificial Neural Network. In Proceedings of the 19th International Conference on Condition Monitoring and Asset Management, CM 2023, Northampton, UK, 12–14 September 2023; p. 2024.
4. **Al-Nasser, S**.; Noroozi, S.; Harvey, A. Cadaveric Testing of a Novel Sensor for Non-Destructive Load Balancing in Total Knee Replacements (TKRs). In Proceedings of the 20th International Conference on Condition Monitoring and Asset Management, CM 2024, Oxford, UK, 19–20 September 2024
5. **Al-Nasser, S**.; Noroozi, S.; Harvey, A "Designing an Intraoperative Smart Sensor for Compartmental Balancing in Total Knee Replacements with a Foundation in Literature"- submitted to the 22nd International Conference on Research and Education in Mechatronics (REM) and will be held Tuesday through Thursday, September 24 – 26, 2024 in Dead Sea, Jordan.

Acknowledgements

Table of Contents

Chapter 1: Introduction

.

1.1 Introduction

The knee joint is one of the largest, most complex joints in the human body, the most susceptible to injury, and the most affected by arthritis (Felson et al. 1987). Replacement of the joint, either totally or partially, is the best treatment for end-stage arthritis by relieving pain and restoring function for the patient. When the surgery is unsuccessful, the patient can have a limited range of motion (ROM), instability, improper gait kinematics, and/or severe pain resulting in a premature revision surgery. Providing patients with a functional and pain free knee is challenging as it depends on numerous factors including gap balancing, load balancing, surgical methods/materials used, patient specific anatomy, and surgeon experience to name a few. This research focuses on quantifying the load balancing in the knee by validating the design of a novel and robust intraoperative sensor.

The development of the Total Knee Replacement (TKR) procedure over the years includes the development of technology and improved surgical techniques. A comprehensive literature review of balancing techniques, typical knee kinetics and kinematics both in the normal knee and intraoperatively, and other sensors on the market will aid in the development and validation of a new sensor.

The aim of this research is to optimise the design of a new intraoperative joint transducer, test it in a laboratory setting, observe the useability of this device in cadavers, and begin to understand more about the kinematics and kinetics in the knee. The development of this novel device will aid surgeons during the TKR to optimally balance the knee in accordance with the ideal joint kinematics. The success of sensors in aiding surgeons with joint balancing and tensioning would be quantified by a reduction in the number of early revision surgeries needed. This chapter explains the general background information that will highlight the importance of this research and give context to the later sections.

1.2 Biomechanics Terms

Understanding the anatomical terms is important to provide clarity. Proper anatomical terminology is in reference to a human body that is oriented with the person standing upright, arms by the side, palms forward and thumbs pointing away from the body. The legs are shoulder width apart with the toes facing forward.

There are three main anatomical planes that split the body: sagittal, coronal, and transverse planes (Figure 1.1). The sagittal plane creates a vertical line that splits the body into a left and right side, this plane is relevant when discussing TKRs.

Anatomical Body Planes and Directional Terms
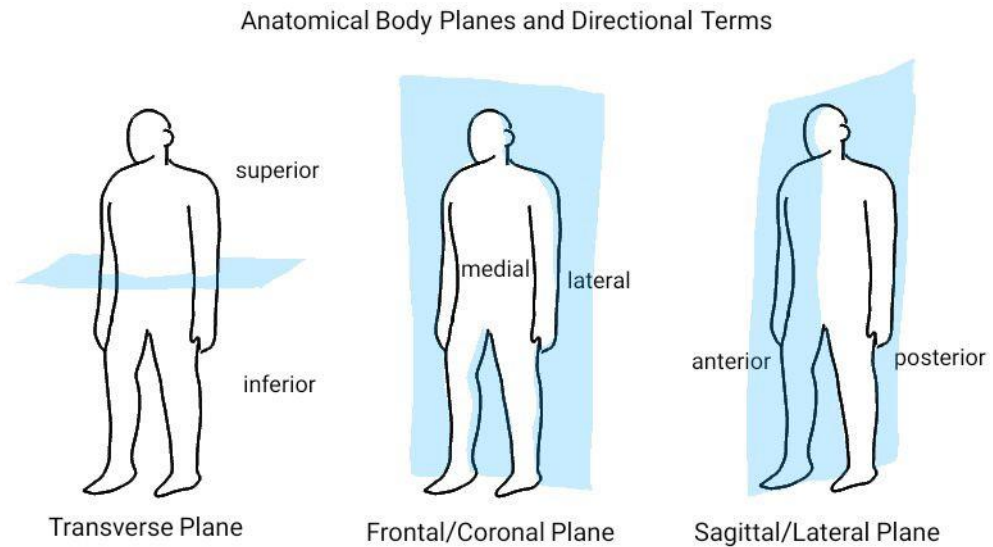
Figure 1.1: Body Planes and Directional Terms

There are several directional terms that help describe the position of certain structures in relation to one another. Along the sagittal plane, anterior refers to the front while posterior refers to the backwards direction. Along the coronal plane, the term lateral refers to the side or the direction away from the midline and medial refers to the orientation closer to the midline. Distal refers to the positioning farther away from the origin and proximal is nearer or closer to the origin. These terms are important when discussing the knee (Figure 1.1).

There are different movements of body parts around a certain axis which are described by different terms. Flexion refers to the decreasing of the angle between two structures, where extension is the opposite, increasing the angle between two structures (Figure 1.2). For the knee specifically the main movement is flexion and extension. In reference to the lower limb and the knee it is important to understand the varus and valgus orientations. Varus deformity of the knee is when the distal part of the leg is deviated inward in relation to the femur giving a bow-legged appearance to the limb. A valgus deformity occurs when the distal part of the leg below the knee deviates outward giving a knock-kneed appearance (Figure 1.3).

3
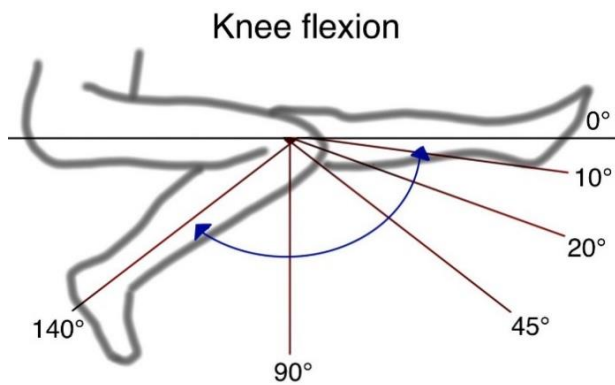
Figure 1.2: Knee Flexion Angles
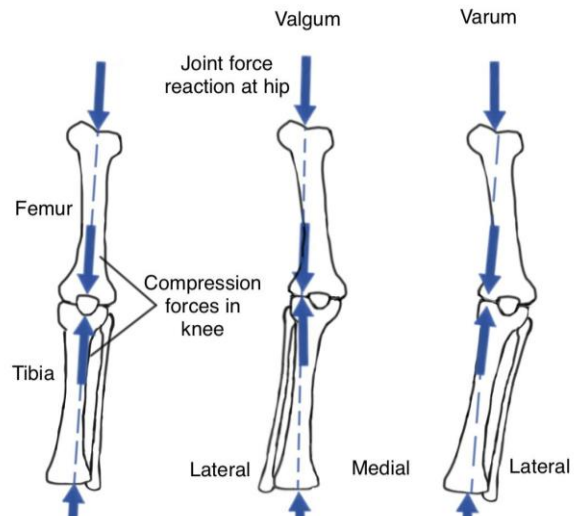
Figure 1.3: Varus and Valgus Movements

1.3   Knee Joint

The knee joint complex consists of two joints: the patellofemoral joint, where the patella and femur articulate, and the tibiofemoral joint, where the tibia and femur articulate. The main biomechanical roles of the knee joint complex are to allow motion of the legs with minimal energy from the muscles and to provide maximum stability to the body over various terrains. Additionally, the knee joint complex should transmit, absorb, and redistribute forces to the knee during daily activities. The knee joint is a synovial, hinge joint. A synovial joint, or diarthrosis joint, contains synovial fluid enabling the joint to move smoothly. A hinge joint operates like the hinge of a door, moving in one direction along one plane.

The knee joint complex consists of several structures that provide stability to the joint through different motions and loading conditions. There are three bones that make up the knee joint, the femur, patella, and tibia. The femur and the tibia are long bones, and the patella is a sesamoid bone. The femur meets, articulates, with the top of the tibia and the patella moves along a groove at the anterior distal end of the femur. The soft tissue in the knee joint provides stability to the joint by resisting excessive displacements between bony segments and controlling the joint's path of motion. Articular cartilage covers the surfaces of the distal femur, proximal tibia, and posterior patella allowing the bones to glide over one another during flexion and extension of the knee as well as absorb the forces sustained to the knee during locomotion. The soft tissue stretches and develops tensile force to resist excessive elongation when external

4

loads are applied to the joint. The knee meniscus is a thick pad of cartilage between the femur and tibia, where there are two menisci per knee: the medial and lateral meniscus. The menisci help to distribute weight bearing forces, absorb shock, stabilise the knee, and allow the surfaces of the knee to move smoothly when the knee is moving and bearing weight. Another component of the knee are the ligaments, which help prevent excess knee motion, varus and valgus stresses on the knee, anterior and posterior movement of the tibia under the femur, medial and lateral rotation of the tibia under the femur and stabilise the rotations of the tibia. The muscles around the knee load the joint according to the required movement and provide stability.

These structures within the knee joint complex work to provide smooth movement of the knee while providing stability and efficiency in movement (Abulhasan and Grey 2017).

1.3.1 Common Knee Problems

The complex and intense load bearing of the knee can create several problems. The knee accounts for more pain and disability than any other joint and is one of the most common sites for Osteoarthritis (OA) (Felson et al. 1987). When there is a loss of healthy articular cartilage knee arthritis can arise. A factor that can contribute to the wear of the articular cartilage is injury which can lead to instability causing knee arthritis. There are more than 100 distinct types of arthritis. However, the most common affecting the knee is OA or degenerative arthritis, which occurs when the cartilage in the knee deteriorates with use and age, and rheumatoid arthritis (RA), a chronic, autoimmune condition.

When the muscles of the quadriceps, hamstring and calf, gastrocnemius, are weak they cannot provide adequate support and stability to the knee which can accelerate OA or cause some common knee injuries including:

- ACL injuries: the Anterior Cruciate Ligament (ACL) tears. Common in athletes of sports that require sudden changes in direction.
- Fractures: Fractures of the bone, including the patella.
- Torn meniscus: The meniscus can be torn with a sudden twist of the knee while bearing weight.

- Knee Bursitis: The bursa of the knee, a small sac of fluid that cushions the outside of the knee joint, becomes inflamed known as bursitis. Bursitis of the knee happens often when there is an injury to the patella.

1.3.2 Knee Replacement Surgeries

A TKR is necessary for patient's experiencing debilitating pain and/or loss in function and is executed by removing the weight bearing surfaces from the knee (Rönn et al. 2011). A TKR is the best option for pain relief and restoring function to the knee joint in patients with arthritis. There are several factors that contribute to the increase in knee replacement surgeries in the United Kingdom (UK) including the ageing population, longer life expectancy, and an increase in BMI. The only treatment for end-stage OA is a knee replacement. Knee replacement surgery is needed when the knee joint is so worn or damaged that there is reduced mobility and increased pain. Over three years in the UK (2020-2023), 232,550 primary TKRs were performed mostly for end-stage OA where OA was listed as the reason for surgery in 98% of all primary knee procedures in 2022 (Achakri et al. 2023)

There are two main types of knee replacement surgeries: a TKR where both sides of the knee joint are replaced and a partial knee replacement (PKR) where only one side of the knee joint is replaced. The latter is a smaller operation with a shorter recovery period. For a TKR, the surgeon will bend the knee to expose the surfaces of the joint to remove the damaged femur and tibia and replace it with an implant. There are usually three components that make up the traditional TKR implants: the femoral component, tibial component, and sometimes a patellar implant. The femoral component is usually made from metal alloys most commonly a cobalt-chromium alloy and is made up of two symmetric arc-shaped condylar surfaces (Pande and Dhatrak 2021). The tibial component consists of two parts: the tibial insert which is mostly made of ultra-high molecular weight polyethylene (PE), and typically a titanium alloy for the tibial tray, used to reduce the friction in the joint (Pande and Dhatrak 2021). If a patellar implant is needed during a replacement surgery, usually a dome-shaped implant made of PE is attached to the remaining original patella bone (Roussot and Haddad 2019). After the implants are fitted, the surgeon will bend and rotate the knee to test for proper tension and alignment using haptic feedback.

Knee replacement surgeries have been performed in the UK since the 1970s and knee revision surgeries introduce a difficult challenge due to the soft tissue (Achakri et al. 2023). According to Sharkey et al. (2014) a review on 212 revision knee replacements uncovered that the top three reasons for revisions were PE wear (25%), aseptic loosening (24.1%), and instability (21.2%). All three of these reasons can be attributed to improper tension in the joint, where a balanced knee would theoretically be defined as the forces between compartments being equal. Revision TKRs are complicated procedures and carry greater risks to the patients with higher costs for the NHS than primary TKRs. The costs of knee revision surgeries can vary depending on complexity and geographical region; however, on average the cost to the hospital is about 20,000 pound sterling (GBP) per patient (Kallala et al. 2015; Alexiadis et al. 2024). Moreover, the number of total revision knee operations and their average costs can be calculated from this amount (Table 1.1) where it can be observed that over 18 years, revision knee surgeries have cost the NHS over 1.9 billion GBP.

Table 1.1: Cost of revision surgeries for the NHS over 18 years

Year of Revision	Total Revision Knee Operations	Average Cost (GBP)
2004	1,248	24,960,000
2005	2,002	40,040,000
2006	2,585	51,700,000
2007	3,518	70,360,000
2008	4,394	87,880,000
2009	4,872	97,440,000
2010	5,425	108,500,000
2011	5,608	112,160,000
2012	6,380	127,600,000
2013	5,999	119,980,000
2014	6,514	130,280,000
2015	6,771	135,420,000
2016	6,903	138,060,000
2017	7,033	140,660,000
2018	6,817	136,340,000
2019	7,005	140,100,000
2020	3,851	77,020,000
2021	5,411	108,220,000
2022	5,464	109,280,000
Total	85,677	1,956,000,000

Moreover, early revision surgeries can unnecessarily add to these costs. A retrospective study of 548 patients found that 179 (32.7%) needed early revisions and

369 (67.3%) had late revisions where the most common reasons for the early revisions were infection (31.3%), loosening (27.4%), and instability (10.1%) while the most common causes for late revisions were loosening (29.5%), infection (22.2%), and PE wear (20.3%) (Holbert et al. 2023). With an objective tool, this procedure can be done properly the first time, which would significantly reduce costs to hospitals and the NHS while reducing the risks associated with surgery to patients.

Chapter 2: Background

2.1   Introduction

The need to produce a more stable knee reflects directly on the patient's postoperative outcomes. To produce a more balanced joint intraoperative sensors can be used to aid surgeons during a TKR which is the focus of this research. To be able to understand the research questions, the background information must be understood to establish an in depth understanding of the subject. This includes understanding the anatomy of the knee and the structures that impact the stability of the knee both in normal knees and TKR knees. Additionally, gaining an understanding of the forces in the knee, the load path and intensity, and how they are commonly found helps to understand the design of intraoperative sensors since the function of such sensors are to set the initial tension of the knee during surgery.

2.2   Knee Joint Geometry

The tibiofemoral joint's primary motion is flexion and extension in the sagittal plane. However, the knee also rotates, pivots, and glides. These movements are controlled by three structures in the knee: the articular geometry, ligamentous balance, and muscular tension.

The ROM for translations is restricted by the fibrous capsule, ligaments, and muscles. The femur and tibia slide over one another with 6 degrees of freedom characterised by three rotations and three translations in all three planes. The greatest ROM is around the sagittal plane through flexion and extension. Moreover, abduction/adduction and the intra/extra rotation occur around the frontal and transverse planes where the motion is more restricted.

The articular geometry of the knee joint consists of the femur and tibia. The femur consists of the medial femoral condyle (MFC) and the lateral femoral condyle (LFC) that create the proximal articular surface with the two concave medial and lateral plateaus of the tibia (Figure 2.1). The MFC is larger with a more uniform radius of curvature, while the LFC is smaller and consists of two condyles with nonuniform radii (Abulhasan and Grey 2017).

Frontal View

Lateral
condyle

Medial
condyle

Anterior

Medial —
condyle

Lateral
condyle
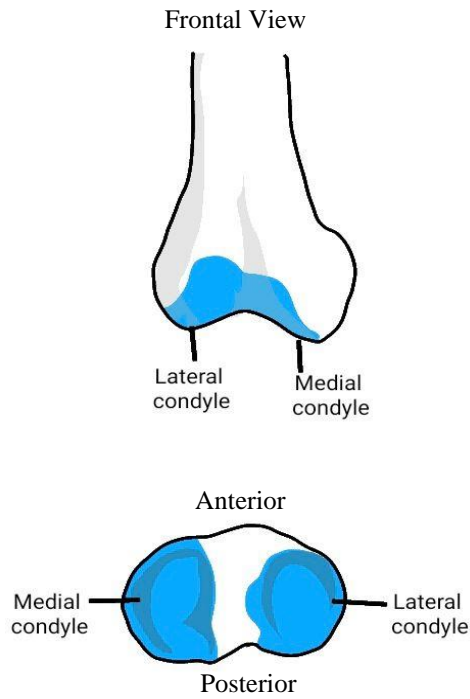
Posterior

Figure 2.1: Medial and lateral femoral condyles (Right knee)

The MFC remains mostly stationary during knee flexion, while the LFC travels posteriorly on the tibia, known as posterior rollback. During posterior rollback (Figure 2.2), the geometry of the MFC and LFC forces the distal femur to rotate externally. Posterior rollback of the LFC is important because it determines the point of terminal flexion, which is relevant for TKRs as it determines the terminal flexion point that allows for full deep flexion to occur. Without posterior rollback, the back of the femur would hit the tibia at 90º, but because the distal femur moves posteriorly to the tibia its clearance is increased to allows for deeper flexion. Eventually terminal flexion does occur where the lateral tibia and the posterior femur impinge.

ACL: Anterior Cruciate Ligament
PCL: Posterior Cruciate Ligament

Posterior roll back
of femur

PCL

ACL

Knee straight

Knee bent 45 degrees

Knee bent 90 degrees
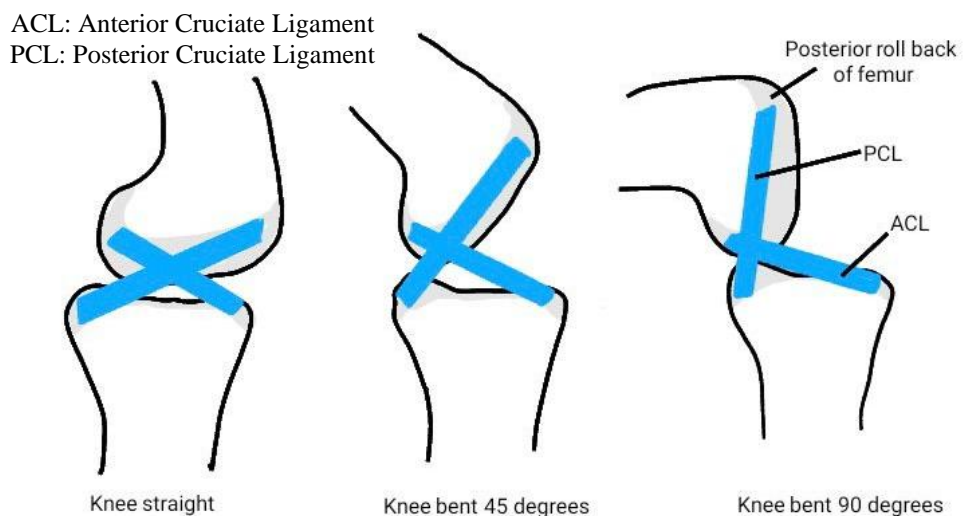
Figure 2.2: Posterior femoral rollback

11

The medial and lateral tibial plateau have different geometries so posterior rollback can occur during knee flexion. The lateral tibial plateau is flatter than the medial which prevents MFC rollback allowing for a pivot motion where the LFC rotates around the stable MFC.

As implied from the above descriptions, changes in the natural geometry of the articular surfaces will change the kinematics in the knee, thus creating different forces that wear on the knee differently (Bull et al. 2008).

2.3   Stabilisers for the Knee

The stability of the tibiofemoral joint comes from static and dynamic structures working together to balance the joint from excessive movement and instability which both can lead to knee injuries.

The knee is not an inherently stable joint and receives its stability from primary and secondary stabilisers. The ligaments in the knee are what provide the knee with primary stabilisation and the secondary stabilisation is provided by the muscles surrounding the knee.

2.3.1 Ligaments and Tendons

A ligament is a short band of fibrous connective tissue connecting bone to bone. In the knee, ligaments connect the femur and tibia together to hold the joint in place. The ligaments of the knee are tough and flexible. A tendon is a cord of strong fibrous collagen tissue that is flexible but inelastic, connecting muscle to bone.

The static stabilisers of the tibiofemoral joint are the anterior cruciate ligament (ACL) and posterior cruciate ligament (PCL), known in combination as the cruciate ligaments and the medial collateral ligament (MCL) and lateral collateral ligament (LCL) known together as the collateral ligaments. These four ligaments in the knee connect the femur to the tibia.

The cruciate ligaments, the ACL and PCL, are two ligaments that provide stability to the joint in the sagittal plane. The ACL is made of the three strands and provides the knee with 85% of its stability allowing for smooth and stable flexion and rotation of the knee (Ellison and Berg 1985). However, it is one of the most injured structures in the knee joint (Gianotti et al. 2009; Zlotnicki et al. 2016). When the ACL is

removed from the knee, full extension makes the femur shift posteriorly since the anterior pull of the tibia is unresisted. The presence of the ACL also impacts the wear patterns on the knee. When the ACL is intact the wear is on the anterior-medial aspect of the tibia, however, with no ACL the tibia moves forward, and the wear then occurs of the posterior medial aspect of the tibia. The PCL has two bundles: the anteromedial which is tight in flexion and the posterolateral which is tight in extension. The PCL is larger and stronger than the ACL and its orientation prevents posterior tibial translation to allow for the proper posterior rollback of the femur. Together with the ACL, the PCL works to control the anterior-posterior rolling and sliding kinematics of the tibiofemoral joint during flexion and extension. During TKR surgeries today, the ACL and/or the PCL are discarded, and the anterior/posterior constraint is dependent on the stability of the prosthetic.

The collateral ligaments, MCL and LCL, provide stability in the coronal plane. The MCL is a flat and broad ligament that sits inside of the knee and is partially attached to the medial meniscus. The MCL provides greater stability in flexion, 60% of the knee's stability in 5º of flexion and 80% of the stability in 25º of flexion (Parcells 2017). The LCL is a cordlike ligament located on the outside of the knee providing the knee with lateral stability. The LCL is loose when the knee is flexed reducing its restraining capability.

The Human Knee

ACL: Anterior Cruciate Ligament
PCL: Posterior Cruciate Ligament
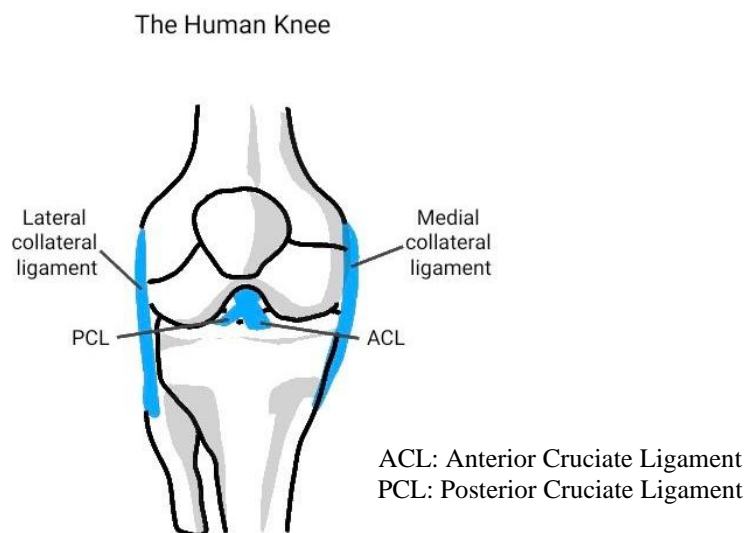
Figure 2.3: Ligaments of the tibiofemoral joint

The patella acts as a shield and due to its position, prevents excessive friction between the quadriceps tendon and the femoral condyles (Hungerford and Barry 1979; Steinkamp et al. 1993). The patella also aids in knee extension and allows for a wider

distribution of compressive stress on the femur by increasing the area of contact between the patellar tendon and the femur. The patellar tendon begins at the quadricep muscle and attaches the patella to the front of the tibia.

2.3.2 Muscles

Most of the muscles around the knee are monoarticular, crossing one joint, and work to primarily provide mobilisation and secondly to stabilise the knee. The quadriceps sits anteriorly on the thigh and consists of four different muscles: the rectus femoris, vastus lateralis, vastus medialis, and vastus intermedius. In general, the quadriceps provides the main muscle force for knee extension, and its weakness affects the patella tracking. The largest extensional moment occurs between 15° and 30° of knee flexion due to the posterior movement of the tibiofemoral contact point (Andriacchi et al. 1986). The extensional moment of the knee is defined as the torque produced by the knee extensors, the quadriceps, in response to the flexion of the knee (Andriacchi and Mikosz 1991). The quadriceps are also dynamic stabilisers for the patella, where the patella acts as a biomechanical lever. Near full extension, the quadriceps transfer the maximum amount of force to the patella and is reduced to 60% at 90° of flexion (Ellis et al. 1980; Huberti et al. 1984). The hamstring, a group of three muscles: biceps femoris, semimembranosus, and semitendinosus muscle, works antagonistically to quadriceps providing the main muscle force in the flexion of the knee.
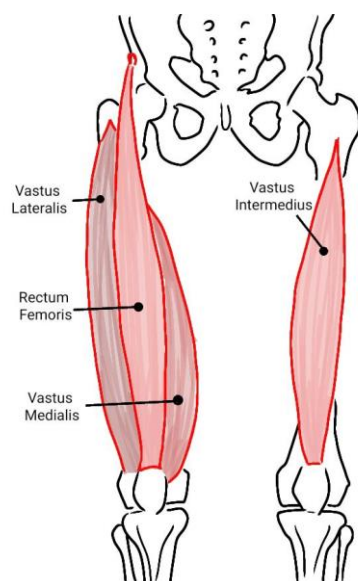
Figure 2.4: Muscles of the quadriceps

2.4   Normal Alignment

When considering the alignment of the normal knee there are two main axes to consider: the mechanical axis and the anatomic axis (Figure 2.5). The mechanical axis is created from a line drawn from the centre of the hip to the centre of the ankle. When this line passes through the centre of the knee the leg is in neutral mechanical alignment. The anatomic axis is created from lines drawn through the centre of the bones making up the leg. The anatomic axis of the femur is 6º from the mechanical axis while the anatomic axis of the tibia is in line with mechanical. This means that the knee angle, or femoral-tibial angle (FTA), is 6º valgus, inward, relative to the mechanical axis (Parcells 2017).
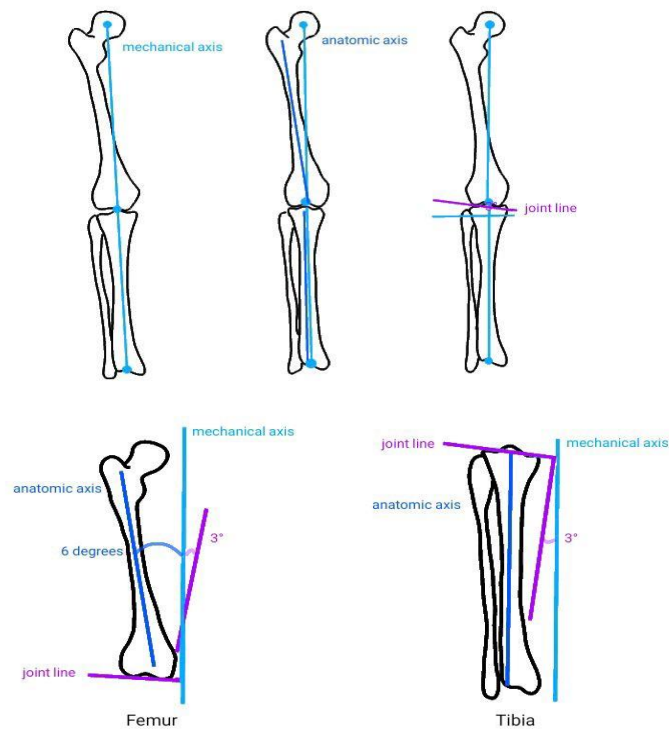
Figure 2.5: Axes of the lower limb and joint line

In a TKR these angles are simpler than the native knee since the tibia is cut perpendicular to the mechanical/anatomical alignment, making the angle 0º. Then, the femoral cuts are adjusted to be in line with the tibial cut.

2.5   Range of Motion (ROM)

The ROM helps determine the function of the knee and is often a functional patient outcome measure for TKRs. In a TKR, the passive motion of the knee joint is

especially important since during the surgery the patients are anaesthetised and to determine if the joint is balanced the surgeons will carry the leg through a ROM to "feel" if the joint is balanced.

The highest ROM in the knee joint comes from the flexion and extension movement. However, other movements contribute to the function of the knee including the anterior/posterior displacement, rotation, and varus/valgus motions.

The normal active ROM from full extension to full flexion ranges from 0º to 140º and changes with activity (Nordin et al. 1989; Traina et al. 2013). After a TKR, a normal ROM for knee flexion is accepted at 120º since this is sufficient for most daily activities with minimal risk to the patellofemoral joint (Rowe et al. 2000; Lee 2014).

The endpoint in normal knee flexion is about 140º, which is caused by the posterior tibia impinging on the femur (Parcells 2017). The ROM is a factor of the surgical procedure that greatly impacts postoperative patient satisfaction. Figure 2.6 depicts how the ROM in the knee changes preoperatively, intraoperatively, and postoperatively in flexion and extension (Mutsuzaki et al. 2017).
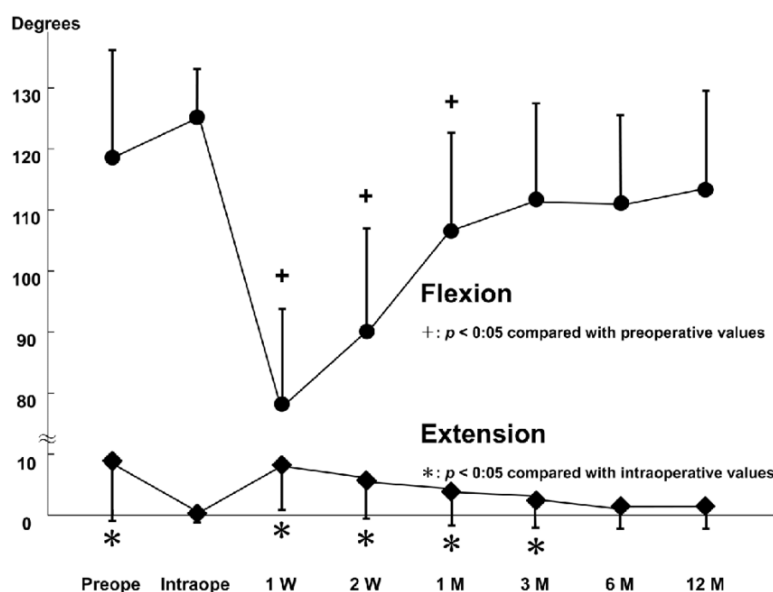
Figure 2.6: ROM throughout TKRs (Preoperatively, Intraoperatively, and Postoperatively) (Mutsuzaki et al. 2017)

2.6   Forces in the Knee

The largest force on the knee is the tibiofemoral force that is spread across the medial and lateral compartments. The passive tibiofemoral joint contact forces that act on the tibia consist of the joint reaction force, and lateral/medial forces that come from

the ligaments. However, as previously mentioned the centre of rotation is not fixed during the flexion/extension movement. During flexion, the femur pivots on the tibia causing a small degree of internal rotation, towards the midline, while during full knee extension there is a slight external rotation, away from the midline (Traina et al. 2013).

2.6.1 External vs. Internal Forces

The forces acting on the knee can be divided into external and internal forces. External forces are caused by body weight (BW), ground reaction forces on the foot, and acceleration and deceleration of the limb segments (Andriacchi et al. 1986). On the other hand, internal forces work to balance the external forces and are generated by muscle contractions, ligament forces, and joint contact forces. While the external forces can be generated in laboratory simulations the internal forces require more complex measuring techniques (Draganich et al. 1984; D'Lima et al. 2012).

2.6.2 Joint Contact Forces

Joint contact forces are one of the internal forces affecting the knee joint. The tibiofemoral joint contact force is the force on the articulating surface between the tibia and femur. The forces include the net joint reaction force and forces exerted by the muscles surrounding the knee. Contact stresses in the knee have the potential to exceed the acceptable load intensity and yield strength of the PE component in TKRs, which would lead to failure of the component (Hood et al. 1983; Bartel et al. 1986; Szivek et al. 1996; Kuster et al. 1997). Increasing the thickness of the PE insert during a TKR can also increase the forces in the knee throughout a ROM. In a study of cruciate retaining (CR) TKRs, the MCL and LCL forces increased by 38 N and 74 N, respectively, as PE insert thickness changed from 9 mm to 11 mm using a previously validated musculoskeletal model of a TKR patient (Figure 2.7) (Tzanetis et al. 2021).
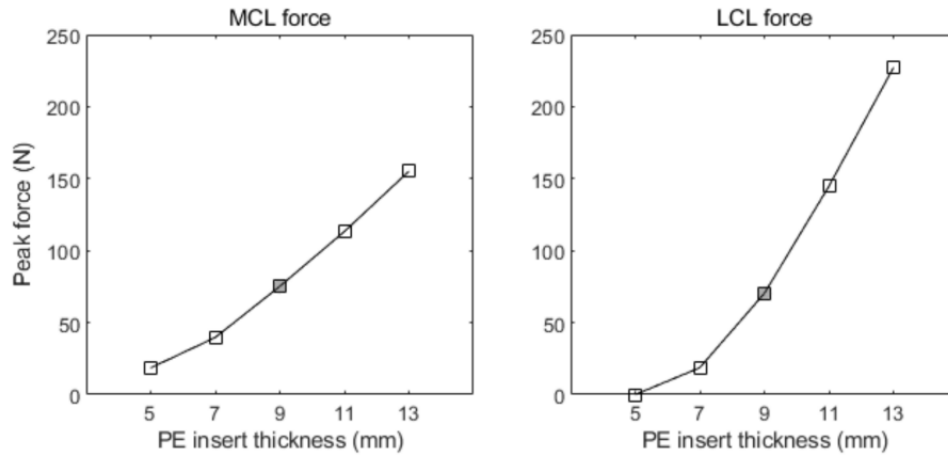
Figure 2.7: Change in Force on Ligaments with Increasing PE Thickness (Tzanetis et al. 2021)

Contact forces during TKRs are important for soft tissue balancing and implant alignment. In a model of the lower extremity during a TKR, validated from cadaveric studies, the tibial contact forces have been observed based on the flexion angle. In this model the forces are measured perpendicularly to the surface of the tibia (Figure 2.8), where the red arrow represents the shear force (Hashemi et al. 2011).
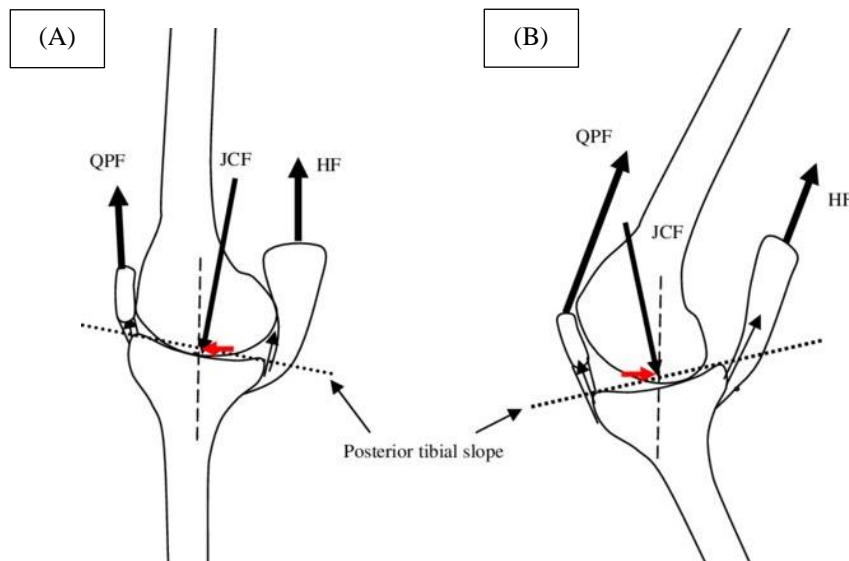
Figure 2.8: Location of Joint Contact Force (JCF) Based on Knee Angle a)
Full Extension b) Moderate Flexion. QPF: Quadriceps patellar tendon
force; HF: Hamstring force (Hashemi et al. 2011)

Figure 2.9 demonstrates that contact forces decrease as the flexion angle increases for a CR TKR (blue) and PCL resection TKR (red) with a slight increase past 45° for the CR TKR (Kebbach et al. 2019).
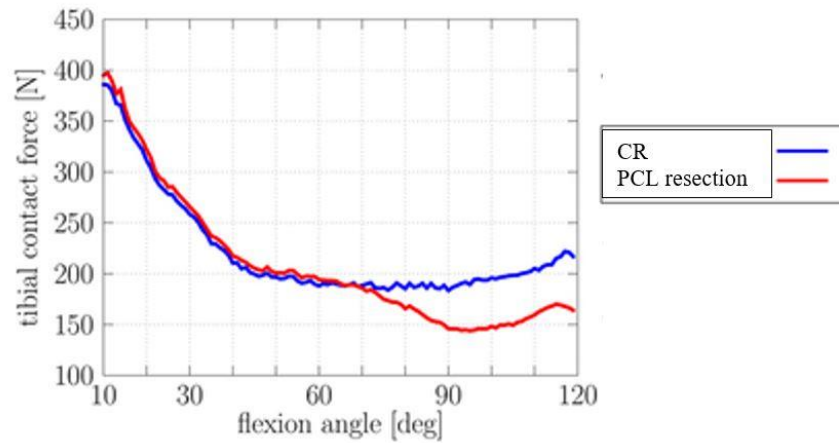
Figure 2.9: Tibial contact forces versus flexion angle in Cruciate Retaining and PCL Resection TKRs (Kebbach et al. 2019)

Moreover, similar observations were made in Figure 2.10, where BG represented a TKR with a balanced gap. Forces, in this study using cadaver knees, decreased until around 45° and then increased through the rest of the flexion arc (Jeffcote et al. 2007).
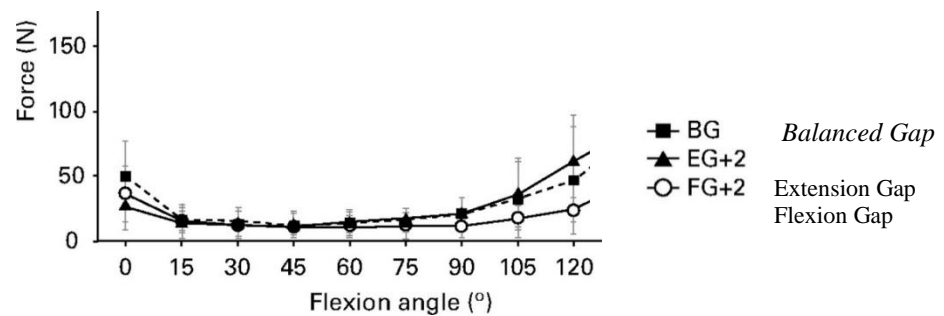
Figure 2.10: Tibiofemoral Forces through the Flexion Arc (Jeffcote et al. 2007)

Additionally, during cadaveric testing of different methods to flex the knee (Figure 2.11), a heel push (HP) test and thigh pull (TP) test, compartmental forces in the knee were recorded (Figure 2.12). It can be noted that the load behaves similarly through the flexion arc as the previous research and that medial loads were higher through the flexion arc for both tests (Verstraete et al. 2017).

19
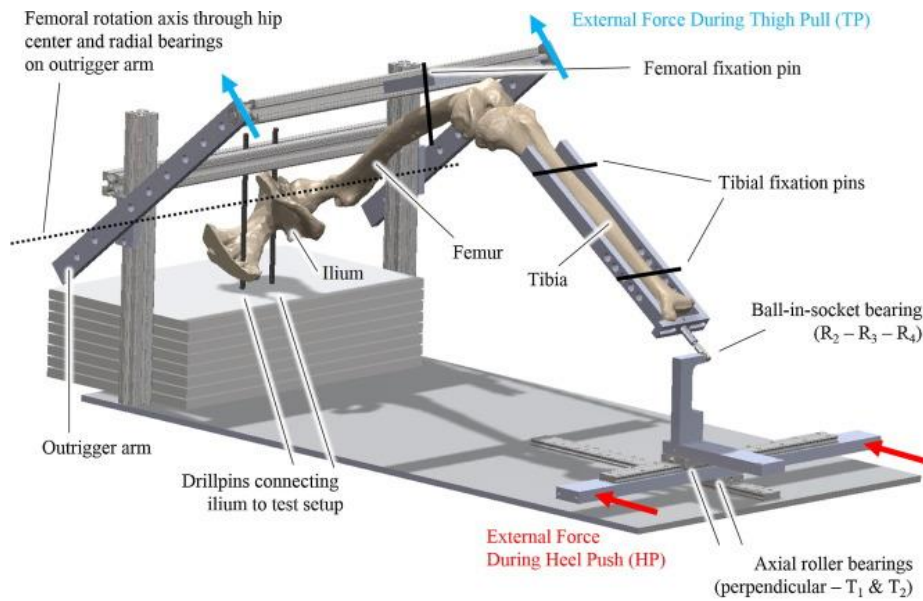
Figure 2.11: Forces Applied During HP and TP (Verstraete et al. 2017)
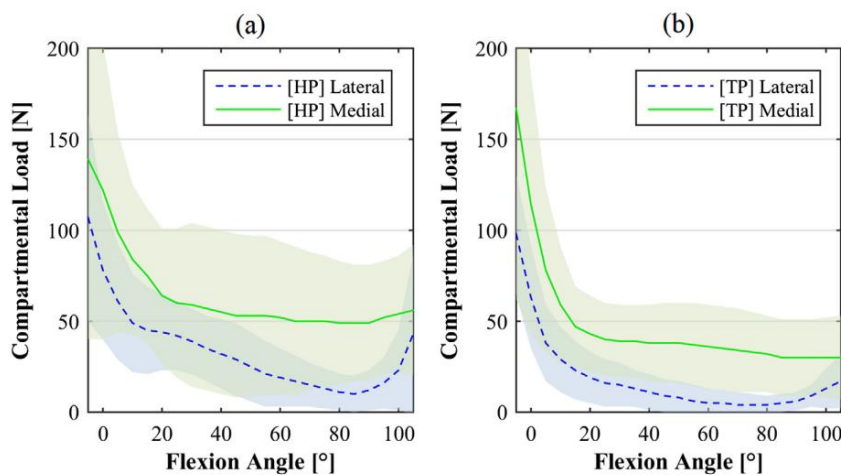
Figure 2.12: Compartmental Loads during Heel Push and Thigh Pull (Verstraete et al. 2017)

Furthermore, the distribution of the force on the bone in the knee can be discussed more thoroughly. From the results of deformation, stress, and contact pressure testing, it is evident that the medial compartment is more loaded than the lateral through the flexion arc. This conclusion was also confirmed in clinical practice observing the gait cycle (Dungl 2005), where it was found that the contact load was mainly distributed medially. Simulated models of the knee based on computer tomography (CT) data, and FEA revealed that again during the gait cycle the load is more medially distributed (Kubíček and Florian 2009). However, theoretically having the medial compartment loaded more heavily than the lateral can be detrimental as there would be increased wear on the medial compartment of the joint. This questions whether balancing the load,

which kinematically would be beneficial, is preferred over having a higher load medially which is what is observed in the natural knee.

2.7   Joint Contact Points

As mentioned previously, the femur articulates with the tibia and through the flexion arc the contact points change to allow for deep flexion by femoral rollback. Figure 2.13 depicts the contact points in the normal knee where through flexion angles 10º-90º the contact points in the lateral compartment move posteriorly compared to the medial compartment (Pinskerova and Vavrik 2020).
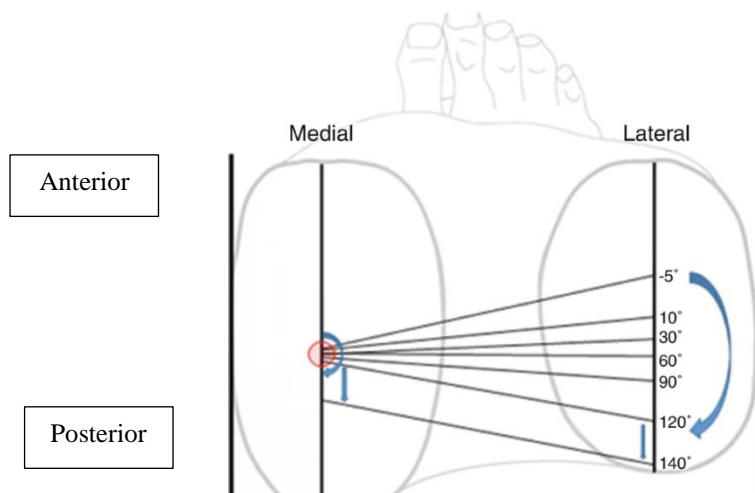
Figure 2.13: Contact Points in the Normal Knee through the Flexion Arc (Right Knee)
(Pinskerova and Vavrik 2020)

A study using fluoroscopic surveillance on the gait cycle post TKR also noted the contact point shifting posteriorly through the flexion arc of the left knee (flip to compare to the right knee) for both the normal knee and a TKR knee (Figure 2.14) (Dennis et al. 2003).
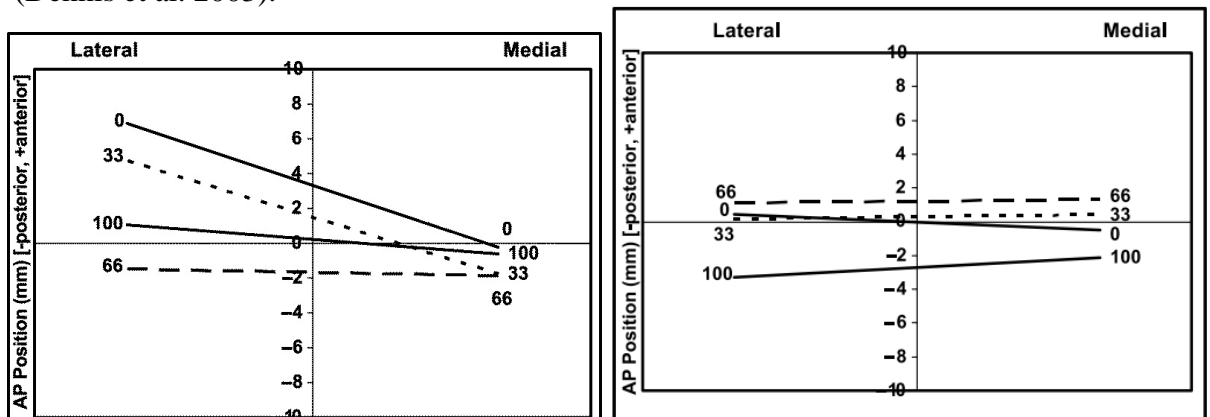
Figure 2.14: Contact Points after a TKR through the Flexion Arc a) Normal Knee b) TKR Knee (Dennis et al. 2003)

21

A similar behaviour was observed through a retrospective study of TKRs (Deckard et al. 2022). The image below, Figure 2.15, is of the left knee and backwards facing posteriorly instead of anteriorly, so the image can be rotated and flipped to be compared to Figure 2.13. It can be observed that the contact points during and after a TKR through the flexion arc are similar to what has been observed in other research.
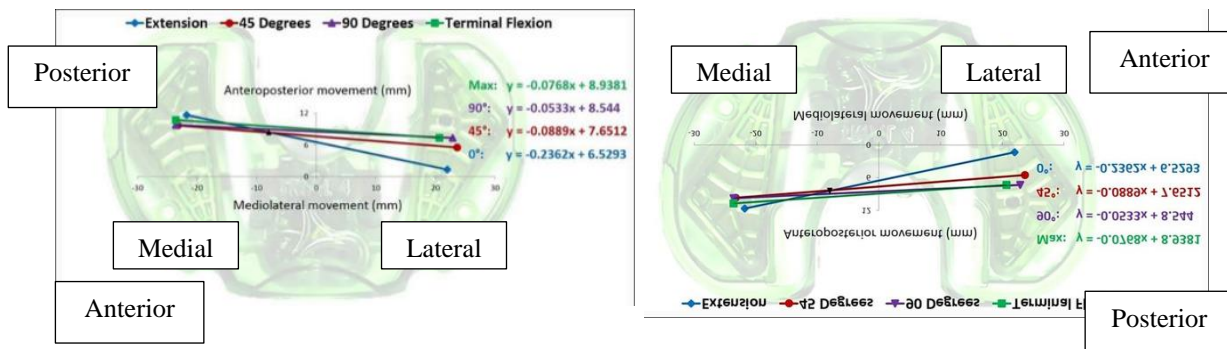
Figure 2.15: Contact Points during TKR through the Flexion Arc (Deckard et al. 2022)

The current literature surrounding the contact points in the tibiofemoral joint show a shift posteriorly through the flexion arc (Iwaki et al. 2000; Dennis et al. 2003; Moonot et al. 2009; Meneghini et al. 2017; Pinskerova and Vavrik 2020; Deckard et al. 2022; Hashimoto et al. 2022) which provides context to intraoperative contact point readings seen later in this research.

2.8   Conclusion

In conclusion, accurate measurement and tracking of the joint contact forces in the knee can be directly linked to the joint in-service performance and durability. However, computational predications are inherently inaccurate. Experimental in vivo research using tibial force sensors have been used to shed light on intraoperative forces. However, the technology and research in general could be expanded upon to improve accuracy and validity of the results.

Moreover, combining a joint force sensor with the use of other systems like fluoroscopy and robotics can validate the hypothetical assumptions of the load and contact point results. Additionally, comparing kinematic results from the patient's good knee can ensure symmetry between the legs using validated methods.

Chapter 3: Balancing a TKR Knee

3.1   Introduction

The goal of a TKR is to restore the original function of the knee as closely as possible. The success of this surgery can be defined clinically by symmetric and balanced gaps in flexion and extension, symmetric gait, implant positing, and soft tissue balancing. When these are not achieved, it can lead to premature implant failure and the need for an early revision surgery (Parratte and Pagnano 2008; Bozic et al. 2010; Rodriguez-Merchan 2011; Lombardi Jr et al. 2014).

After a TKR, the contact stresses at the surface contribute to wear and loosening of the implant and when there is a high congruency at the contact surface, the contact stress is low. To increase the longevity of the implanted knee it is important to understand what is involved in balancing the knee during a TKR, how to redistribute or reduce the load intensity at the contact points, and how this impacts postoperative success.

3.2   Soft Tissue Tension

The soft tissue, namely ligaments, surrounding the knee are responsible for the passive stability of the joint (Blankevoort et al. 1991; Halewood and Amis 2015) and is a principal factor for success after a TKR. When the ligaments surrounding the knee have improper tension, stability can be compromised leading to problems performing daily functions. Ligament tension can be indirectly measured by the contact loads in the tibiofemoral joint during a TKR. Postoperatively, active forces from muscles, and dynamic loads from movements like walking, running, and stair climbing are added to the knee which means the materials of the implant can fatigue rapidly under these high loads if not properly balanced during the operation.

Functional improvements of the knee have been observed when soft tissue is balanced. Ample research supports this idea where postoperative instability was reported as a major cause for early TKR revisions (Ghirardelli et al. 2019). Additionally, research observed that 50% of early revision TKRs were related to instability, malalignment, or fixation problems, confirming imbalance as a significant cause for revision (Sharkey et al. 2014); another study found that unbalanced ligaments accounted for 35% of early TKR revisions (Gustke (c) et al. 2014). Several more studies have reported that proper balancing can improve outcomes of a TKR by decreasing

postoperative instability, improving flexion and functional results, and increasing the survival of the implants (Winemaker 2002; Matsuda et al. 2005; Unitt et al. 2008; Babazadeh et al. 2009; Anastasiadis et al. 2010; Del Gaizo and Della Valle 2011; Watanabe et al. 2013; Gustke (c) et al. 2014; Elmallah et al. 2016; Meneghini et al. 2016; Nodzo et al. 2017; Golladay et al. 2019; Shalhoub et al. 2019). A study comparing the revision rates from TKRs, observed 1,634 TKRs from 2007 - 2012 and found the average revision surgery was performed about 4 years postoperatively where the shortest revision was 8 days. Moreover, it was found that the most common mechanical failures included loosening of the femoral, tibial, or both components, and instability. The conclusion of this research was that a theoretical advantage of a well-balanced knee would be an improvement to the implant's longevity (Moussa et al. 2017). Early revisions in these cases can be easily avoided with proper joint balancing intraoperatively, which is of benefit to the surgeons, hospitals, NHS, patients, biomedical companies, and for global sustainability by reducing the unnecessary overconsumption of the materials used for implants and the surgical procedure.

As well as functional improvements, patient reported outcomes were also studied to confirm their improvement when the knee was balanced. Notably, patients with balanced knees were more likely to have decreased pain (Babazadeh et al. 2009). Gustke (a) et al. (2014) reported that balanced knees have better pain, functional and activity scores than unbalanced knees after a one year follow up. Patient satisfaction from a balanced knee was also confirmed with later research, where 96.7% of patients were satisfied when the was knee balanced and 82.1% when the knee was unbalanced (Gustke (a) et al. 2014; Gustke (b) et al. 2014). In addition, clinical scores were found to be significantly higher after TKRs balanced with a sensor compared to manually balanced TKRs (Chow and Breslauer 2017).

However, some disagreement is present surrouding the correlation between balanced knees and postoperative improvements. Livermore et al. (2020) reported no improvement to short-term patient-reported outcome measures (PROMs), radiological outcomes, or ROM when compared to conventional TKR techniques. Similar research noted no significant difference in 6-month or 1-year postoperative flexion or patient satisfaction rates (Wood et al. 2021). Additionally, Song et al. (2019) found that the outcomes of the sensor assisted TKR were not better than those manually balanced

when the patients were matched for both demographics and preoperative knee condition.

Despite this, there is still an argument for the accuracy of the sensors used in those studies. Additionally, the state of unbalanced, slightly or severally unbalanced, can dramatically change these results and therefore, the use of a sensor for load balancing by inexperienced surgeons is a must to avoid associated complications. Although still debated in literature, the ability to measure the load and track it would still improve surgical outcome by determining optimal loads intraoperatively to improve mechanical outcomes especially for inexperienced surgeons who are less likely to achieve a balanced or close to a balanced knee.

3.3   Creating a Balanced Knee

Setting the correct tension in the knee remains a challenging task for surgeons. Over-tensioning and insufficient tensioning both lead to improper load distribution which causes the need for an early revision knee surgery. Excessive ligament tension can result in painful and stiff knees and deficient tension can result in instability (Delanois et al. 2016; Gustke et al. 2017; Kwon et al. 2017; Verstraete et al. 2017; Kappel et al. 2018; Walker et al. 2018; Watanabe et al. 2020). Having a tool to aid in proper soft tissue tensioning could eliminate these postoperative complications by providing proper tension and stability to the knee. Research found the proportion of balanced knees after TKRs were higher in sensor-guided TKRs done by inexperienced surgeons than surgeon-guided TKRs performed by experienced surgeons (72% vs. 60%) (Golladay et al. 2019). Research by MacDessi et al. (2021) demonstrated that surgeons struggled to identify a balanced knee where in an analysis of 322 TKRs expert surgeons were only able to accurately determine a balanced knee 63% of the time at 10° of flexion, 57.5% at 45°, and 63.7% at 90°. Additionally, Golladay et al. (2019) confirmed the success of intraoperative sensors by reporting that more balanced knees were achieved when TKRs were performed with a sensor versus without (84.0% vs. 50.6%), where patients were more satisfied with the balanced knees. Moreover, researchers found that when identifying and correcting overstuffing in TKRs, tibial forces were more useful than varus-valgus laxities (Roth et al. 2021).

This literature demonstrates that surgeon experience alone can be inadequate when balancing the joint, compared to intraoperative sensors. Therefore, through the

introduction of an intraoperative sensor, a surgeons' ability to balance the knee can improve.

3.4   Defining a Balanced Knee

There have been various debates on what defines a balanced knee. According to the developers of VERASENSE, a commercial intraoperative load sensor, a balanced knee is achieved when the following two points are satisfied.

1.   The joint is stable in the sagittal plane
2.   The compressive loads are below 244.7 N for the medial compartment and 200.2 N for the lateral compartments, and the intercompartmental load difference is below or equal to 66.7 N (LaPrade et al. 2008; Gustke (a) et al. 2014; Gustke (b) et al. 2014; Gustke (c) et al. 2014)

The first definition of a balanced knee was confirmed after a study in which surgeons performed a TKR according to his or her standard balancing procedure. Then the VERASENSE sensor was used, and the mediolateral loading values were recorded at 10º, 45º and 90º of flexion. Patients' reports were taken before and after the operation (6 weeks, 6 months and annually for 3 years). The 6-month and 1-year outcomes found that the patients within the 66.7 N difference exhibited higher function, less pain, increased satisfaction, and greater activity levels within an acceptable ROM compared to those outside of that range of force (Gustke (a) et al. 2014; Gustke (b) et al. 2014; Gustke (c) et al. 2014; Gustke (d) 2014). Elmallah et al. (2016) later used previous research to form their definition of a balanced knee according to the following points on intraoperative load:

1.   Mediolateral load differential of 66.7 N through a ROM (10º, 45º, and 90º of flexion)
2.   An absolute load between 44.5 N and 177.9 N

These definitions of the load desired to create a balanced knee are widely used and informed by biomechanical research and previous literature (Gustke (c) et al. 2014; Walker et al. 2014; Elmallah et al. 2016; Amundsen et al. 2017; Risitano et al. 2017). This includes evidence from biomechanical research clarifying contact loads from the joint in a passive state (Walker et al. 2014), intraoperative observations made by surgeons quantifying varus/valgus stresses and load changes with orientation (Walker et al. 2014), and a decrease in postoperative outcome scores in patients with an

intercompartmental load difference greater than 89.0 N (Gustke (a) et al. 2014; Gustke (b) et al. 2014; Gustke (c) et al. 2014)

The definitions of a balanced knee still need support from more research to confirm their validity, but they do provide a frame of reference for comparing research done in this field.

3.5 Load Distribution

The optimal load distribution for TKRs is debated as there are different theories when balancing the knee: should the load be evenly distributed to avoid early wear of the components, or should the load distribution more closely mimic the natural knee? These questions mean that it is difficult to provide a validated target load through literature to define a balanced knee. However, the working definition mentioned previously, and the ideal loads discussed below are what most literature use to classify a balanced knee.

When balancing the knee during TKRs, the maximum acceptable load has been studied and argued. While using VERASENSE, Gustke (c) et al. (2014) concluded that the maximum load should be 177.9 N, Risitano et al. (2017) found that 311.4 N should not be exceeded, and Song et al. (2019) determined 244.7 N to be the maximum acceptable load on either compartment. However, studies all agreed that the VERASENSE developer's recommendation of a maximum mediolateral difference of 66.7 N and a maximum medial or lateral load of 311.4 N should not be exceeded because of an increased risk of postoperative stiffness and early PE wear (Gustke (c) et al. 2014; Meere et al. 2016; Risitano et al. 2017; Song et al. 2019). Maintaining compartmental load values between 89.0 N and 177.9 N with a constant magnitude through flexion and extension has also been recommended (Asano et al. 2004). Risitano et al. (2017) classified kinematically stable knees as those with a mean force of 222.4 N ± 89.0 N on the medial compartment, with a mediolateral intercompartmental difference within 44.5 to 89.0 N.

Some research has indicated that the intercompartmental load differential should ideally not be exactly equal because of the load distribution in the normal knee. In a study using eLibra, a lower differential of mediolateral forces in extension were associated with a greater risk of patient dissatisfaction (Jacobs et al. 2016). This research was not the first to suggest that imbalances in the load might be beneficial

compared to a truly balanced load. Research supports that some patients prefer mild to moderate mediolateral laxity (Edwards, Miller and Chan, 1988). This was confirmed by more research observing higher average loads in the medial compartments during sensor assisted TKRs (Song et al. 2019).

These unequal compartmental forces are not always associated with poor patient reported and functional outcomes. Having greater compressive forces on the medial compartment through the ROM can reproduce the medial pivot and lateral femoral rollback seen in the natural knee (Iwaki et al. 2000; Okazaki et al. 2006; Gustke (c) et al. 2014). More research also confirmed that slightly greater pressures on the medial compartment are more consistent with natural knee kinematics and as a result, may be more optimal in TKRs (Matsumoto et al. 2011).

According to the literature it can be understood that although perfectly balancing the load may be optimal theoretically, in practice mimicking the original kinematics of the knee may lead to greater success. This was demonstrated by understanding that the load between the medial and lateral compartments does not necessarily need to be exactly equal, but some success has been seen when the difference in loads between the medial and lateral compartment is about 66.7 N and the loads on each side are below 311.4 N.

Table 3.1: Ideal target loads for TKRs according to literature

Force	(Gustke 2012)	(Risitano et al. 2017)	(Song et al. 2019)	VERASENSE
Maximum	177.9 N	311.4 N	244.7 N	311.4 N
Medial	≤ 177.9 N	222.4± 89.0 N	≤ 244.7 N	≤ 244.7 N
Lateral	≤ 177.9 N	155.7 ± 89.0 N	≤177.9 N	≤ 200.2 N
Difference	≤ 66.7 N	66.7±22.2 N	≤ 66.7 N	≤ 66.7 N

Table 3.1 describes what various studies have determine was the optimal load values in the compartments. The maximum load in either compartment varied amongst different researchers along with the compartmental loads and the intercompartmental load difference. These varying optimal load distributions can be more accurately investigated with a more robust sensor which can more accurately record the load intraoperatively and correlate this with patient reported and functional outcomes both short and long term.

3.6   History of Load Sensors

Since the 1960s, strain gauges have been the standard electrical component used in smart implants (Ledet et al. 2018). The first measurement of a TKR knee was documented in 1975 where Perry et al. (1975) used a tibial plate to measure forces in the knee. Four strain gauges were later used in the tibial tray to measure forces in the knee (Kaufman et al. 1996). Improvements to the technology used radiofrequency transmission of tibiofemoral compressive forces and locations (D'Lima et al. 2005). The first computerised tibial sensor was reported by Wasielewski et al. (2004) to detect unequal compartment loads intraoperatively. This device was developed by modifying a pressure-sensing matrix array and incorporating it into a PE insert of the same size as the tibial tray. This sensor was not proposed for soft tissue balancing particularly, rather for understanding the forces in the knee intraoperatively. Later, the tibial tray was improved to use postoperatively to determine that peak axial contact forces during walking increased substantially over the first three weeks postoperatively, peaking at 2.8BW (Heinlein et al. 2009).

A 9-channel telemetry system was created for in-vivo load measurements in the knee by Graichen et al. (2007) and used in research by Kutzner et al. (2010) to measure intraoperative load measurements in the knee following a TKR. It was deduced that the resultant contact forces during dynamic activities were much lower than what was predicted by mathematical models like the one created by Wismans et al. (1980) and suggested that axial compression represents the primary loading direction on the tibia with a 60-40 medial-lateral load distribution respectively (Kutzner et al. 2010).

More recent advancements have allowed microelectronic sensors to be embedded in a tibial insert which can be connected wirelessly to a monitor (Roche et al. 2014). This type of pressure sensor allows the surgeon to receive visual feedback specific to the patient which provides a quantitative assessment for balancing the soft tissue for each surgery. Modern intraoperative sensors have been reported to significantly improve patient reported outcome scores and functional postoperative outcomes (Roche et al. 2014; Delanois et al. 2016). A common criticism for the use of a sensor guided tibial trial is that it provides passive forces rather than active because the knee is not loaded by contracted muscles and weight bearing intraoperatively. However, still (Wasielewski et al. 2004) reported that TKRs with uneven compartment pressures correlated with abnormal femoral condylar lift-off during postoperative fluoroscopic

kinematic studies demonstrating that compartment pressure balance significantly impacted kinematic performance postoperatively.

3.7 Modern Sensors

Measuring the forces in the knee can provide surgeons with an accurate, quantifiable, and reproducible method for soft tissue balancing. Research has found that there is a significant correlation between the soft tissue tension and the intercompartmental contact forces where a linear relationship has been demonstrated using a validated mechanical knee model throughout the flexion arc (0°, 30°, 45°, 60°, 90°, and 110°) (Figure 3.1) (Sanz-Pena et al. 2019). Intraoperative sensors aim to accurately measure tibiofemoral contact forces in real time throughout a ROM (Crottet et al. 2005). The need for such device is apparent where at least 60% of TKRs needed additional balancing procedures in a study by Batailler et al. (2021), where having a quantitively balanced knee provided higher patient satisfaction scores.
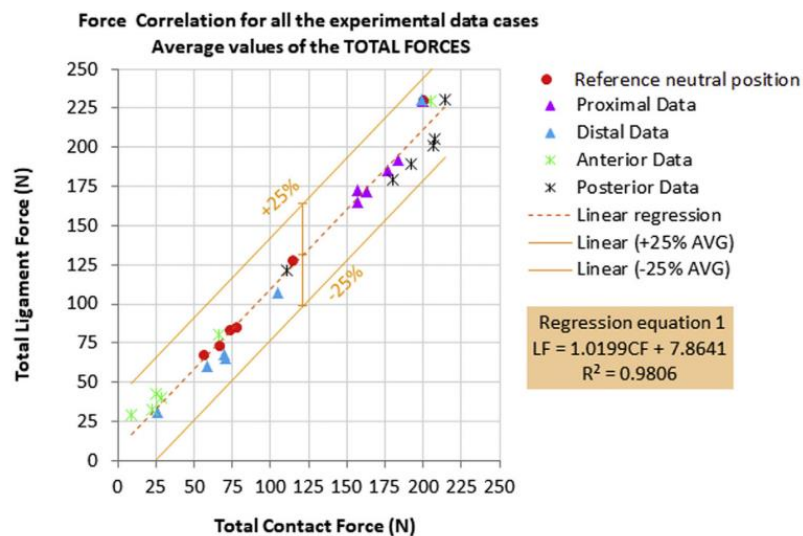
Figure 3.1: Correlation Between Total (medial + lateral) Ligament Force and Total Contact Force (Sanz-Pena et al. 2019)

For intraoperative sensors to achieve proper results, according to Roth et al. (2017) the design of the device must meet the following criteria:

- The sensor must be interchangeable with the tibial base tray
- It must be able to identify the location and force of femorotibial peak contact points over the whole surface of the implant because of the contact points located at the edge of the tibial insert during flexion of the knee

31

- Must be able to identify the location and load in both the medial and lateral compartments.
- Have a low error margin for the force at contact points (< 5 mm).
- Have low error boundaries of locating femorotibial kinematics.
- Must be able to withstand up to 450 N force at contact points to identify any imbalances after the TKR.

In addition, the introduction of a sensor to the TKR procedure should not significantly increase the surgical time. Cochetti et al. (2020) confirmed that intraoperative sensors could satisfy this point by finding that the average surgical times increased by only 8 minutes for TKRs performed with sensors.

Today, there are two intraoperative sensors which have been commercialised: VERASENSE and the eLibra system. These sensors quantify load data through laxity testing and flex-extension cycles to give orthopaedic surgeons data that supports a decision regarding balancing the soft tissue and positioning the implant. Moreover, independent load sensors have also been used to understand the kinematics and forces in the knee as well.

3.8   Conclusion

In conclusion, a TKR is necessary for patients experiencing debilitating pain from injuries such as end-stage arthritis, most commonly osteoarthritis. The progression of the surgery over time has introduced more advanced equipment including intraoperative load sensors. This addition has shown to improve the surgeon's ability to balance the knee. It is thought that insufficient soft tissue balancing can limit the ROM, cause malalignment, knee instability, improper tracking of the patella, premature mechanical failure, and pain (Fehring 2000; Matsuda et al. 2005). However, validation of what a balanced knee is and correlating the balanced knee to improved outcomes are topics that should be explored more deeply as well as the accuracy of such devices.

The development of the TKR procedure, in general, aims to increase the success of the surgery by providing restored function and decreased pain in the joint. This can be measured through a patient satisfaction scoring system or a more quantitative approach, like a reduction in early revision surgeries.

Chapter 4: Current Intraoperative Load Sensors

4.1 Introduction

Various companies and researchers have attempted to create intraoperative load sensors for TKRs. There were two commercial sensors on the market, VERASENSE by OrthoSensor and later bought by Stryker and eLibra by Zimmer Biomet. As of 2023, eLibra was no longer in use and there are plans for the removal of VERASENSE from the market. This leaves a gap in the market for a more robust tool to aid in TKRs.

Moreover, independent knee joint sensors for measuring tibiofemoral joint forces have been created since 1996 with new sensors being created as of 2023. Understanding the previous sensors provides a foundation for creating a more robust intraoperative load sensor.

4.2 VERASENSE

VERASENSE, a single use tibial trial sensor, provides load data through a ROM about the tibiofemoral contact points in flexion and extension (Siddiqi et al. 2020). To balance the ligaments, VERASENSE has three load transducers in each compartment that predict the centre of pressure and location in each compartment. The location and magnitude of compartmental loads is displayed by triangulating the feedback from 3 piezoresistive sensor (Park and Song 2021). Therefore, the sensing area only occupies 22% of the area of each compartment (Gustke 2012; Park and Song 2021). It has been reported that the precision of both the force and location were greatly reduced when the load was outside the sensing area (Nicolet-Petersen et al. 2018), meaning increasing the sensing area of the sensor would increase the accuracy of the device.

The exact values for defining a balanced knee and its impact on the outcome of a TKR has been debated through the literature. Clinical research on VERASENSE suggests that balancing is achieved when the intercompartmental load, the difference in load between the medial and lateral compartment, is less than or equal to 66.7 N (15 lbf) while the load in each compartment is within the range of 22.2 N to 177.9 N (5 lbf - 40 lbf) through the passive ROM (10º, 45º, and 90º).

The graphical user interface (GUI) of VERASENSE includes four calibration indicators represented by assorted colours to indicate which range the load sits in. Green indicates the load is between 22.2 N and 177.9 N (5 lbf and 40 lbf) which, according

VERASENSE, is the advised measurements range. When the load is above 311.4 N (70 lbf) the device is considered overloaded, and the results are not accurate.

The developers of VERASENSE reported that the force measurements are accurate within ±8.9-13.3 N (±2-3 lbf) for each measurement; however, an independent study found that for a range of forces between 66.7 N – 133.3 N (15 lbf-30 lbf) the average bias was -23.6 N (-5.32 lbf) which is almost double what VERASENSE suggests (Nicolet-Petersen et al. 2018). This research demonstrates the need for a more robust and accurate sensor which is not only accurate within this range but can also track the load over the whole surface of the sensor.

Figure 4.1: VERASENSE Display and Sensor (Anon. 2024a)

4.2.1 Literature using VERASENSE

To investigate and validate the design of a next generation of intraoperative load sensors, it was important to critically appraise the sensors on the market and the research which informed the determination of proper load balancing. This also aided in identifying gaps in knowledge surrounding ideal values for load balancing in the knee and the load sensor itself.

Balancing with VERASENSE:

The first use of the VERASENSE system found a balanced knee showed greater improvements compared to the unbalanced knee. Specifically finding that well-balanced TKRs were 2.5 times more likely to have significant improvements in patient-reported outcomes 6-months postoperatively and continued to have superior patient satisfaction

scores ($p < 0.085$) and Knee Society Scores ($p < 0.001$) after 1-year compared to TKRs which were not well balanced (Gustke (b) et al. 2014).

Additionally, VERASENSE or other load sensors can aid surgeons of all levels in balancing the knee. Research investigated 84 TKRs and determined that only 35.7% of knees were balanced initially while using standard balancing procedures then those unbalanced knees were redone with VERASENSE 94% were able to be balanced with an intercompartmental load difference of less than 66.7 N (15 lbf) (Cho et al. 2018). Another study observed that patients with TKRs balanced by VERASENSE had significantly lower compartmental loads at 10°, 45° and 90° of flexion, compared to TKRs with traditional manual balancing techniques, concluding that sensors provide objective feedback for soft tissue balancing and can potentially improve knee balancing and rotational alignment (Elmallah et al. 2016). A study by Geller et al. (2017) compared sensor assisted TKRs to manually balanced TKRs and found that the sensor assisted group had improved ligament balancing with a significant reduction in manipulation under anaesthesia required after the TKR. Another study compared 75 intraoperative sensor-guided TKRs with a control group where classic instruments were used for balancing. This research found that the sensor group had a substantially lower unexpected usage of constrained inserts (5.3%) when compared to the control group (13.8%) (Amundsen et al. 2017). Constrained inserts limit movement of the knee (Konopka et al. 2018) and lead to increased PE wear which leads to component loosening (Green et al. 2000; DeHeer et al. 2001; Fisher et al. 2004; Naudie et al. 2007). A cadaveric study found that in 5 out of 6 knees, additional soft tissue balancing was required when balanced without VERASENSE (Riis et al. 2019). This literature proves that surgeons alone are not always the best at balancing the joint properly, leading to reduced patient outcomes and increased revision surgeries, this also proves the advantage of using such devices even for experienced surgeons.

According to research surrounding VERASENSE it seems there was more emphasis on the balancing the loads within a certain range versus achieving a singular value. However, validation of the clinical outcomes from balancing the intercompartmental forces within the 66.7 N (15 lbf) cut-off was challenged. It was reported that having major differences in intercompartmental forces did not impact clinical outcomes, concluding that the 66.7 N (15 lbf) cut-off was arbitrary (Meneghini et al. 2016; Risitano et al. 2017). This finding contradicts the VERASENSE developer's

implication that 66.7 N (15 lbf) was crucial in TKR satisfaction; however, it does highlight the need for additional research on quantifying the loads in the knee and/or the need for a more accurate sensor.

Several studies have aimed to provide insight on these passive loads by using VERASENSE to observe the medial and lateral loads throughout the ROM. During a TKR, the highest loads were observed in full extension with most of the load transmitted through the medial compartment. This was confirmed by research stating that VERASENSE balanced TKRs had greater forces medially compared to traditional TKRs where the forces were higher laterally (Meere et al. 2015; Manning et al. 2019; Sabatini et al. 2021). This was the load distribution more commonly seen in the natural knee (Becker et al. 2013), which could explain why patients tend to prefer it. Similarly, a review of 189 TKRs balanced with VERASENSE found that mean medial forces (314.5 N (70.7 lbf)) were higher than the lateral forces (195.7 N (44.0 lbf)) at 0º, 45º, and 90º of flexion; they also noted that PROM outcomes were not related to the medial and lateral compartment loads being balanced (Meneghini et al. 2016). Additionally separate studies found that with increased flexion the pressure decreased in both compartments (Schnaser et al. 2015; Manning et al. 2019; Sabatini et al. 2021; Shah et al. 2021). From this research it can be understood that a more accurate load sensor could provide researchers with a deeper understanding of the optimal load distributions in the knee and what values are ideal for implant longevity and patient satisfaction. Specifically, having a sensor which is able to track posterior femoral rollback which is not visible using VERASENSE due to its limited sensing area.

4.3   eLibra

The eLibra system was another sensor developed to balance the knee during a TKR. The sensor, unlike VERASENSE, is placed beneath the tibial spacer and has force transducers on the medial and lateral sides that display its values on a screen, from a scale of 0 to 20 units, where each unit represents about 15 N (3.4 lbf).

Using eLibra, a study balanced the knee's flexion gap for 50 patients where they all showed significant improvements in terms of reliance on assistive devices for movement and significant decreases in pain (Nevins and Leffers 2009). A study by Jacobs et al. (2016) observed 50 TKRs intraoperatively with eLibra and determined that having greater forces medially may result in improved patient reported outcomes,

increased patient satisfaction, and may have the greatest effect on more demanding activities like using stairs. Additionally, a study reviewing eLibra found the device simple to use, highly accurate, and reproducible (Camarata 2014).
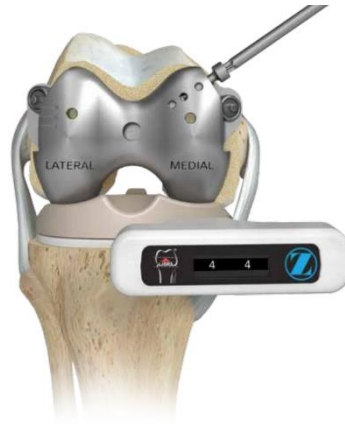
Figure 4.2: eLibra Sensor (Anon. 2024b)

4.4   Limitations of VERASENSE and eLibra

Despite the advances in the technology surrounding intraoperative sensors, there were still limitations to such devices. These limitations can impact the accuracy and reliability of the research surrounding the forces, kinematics, and balancing of the knee that use these sensors.

First, for both VERASENSE and eLibra the sensors are arranged triangularly in the medial and lateral compartments, creating a relatively limited sensing area. As a result, when contact points were outside of this area the accuracy of the device was greatly compromised. A study on VERASENSE's accuracy confirmed this by finding that the biases for the loads outside of the sensing area were more than two (outer anterior) and three (outer posterior) times greater than that of the loads within the sensing area (Nicolet- Petersen et al. 2018). This does not fulfil the design criteria determined by Roth et al. (2017), namely by its inability to determine the location and force over the full articular surface. This point is especially necessary in deep flexion where contact points are near the posterior edge because of femoral rollback.

Additionally, VERASENSE was only calibrated to withstand passive forces, up to 310 N (69.7 lbf) and eLibra 300 N (67.4 lbf) in each compartment and therefore with higher loads, the devices were no longer reliable (Shah et al. 2021). Moreover, the criteria mentioned by Roth et al. (2017) was not satisfied in this case since 450 N was determined as the upper limit required for a tibiofemoral sensor.

Additionally, the physical design of the sensors was of concern for different reasons. eLibra's tibial sensor was flat and as a result this system does not mimic the in-service environment for which the tibial spacer exists. Furthermore, eLibra is not able to determine the location of the applied load over its surface, Although VERASENSE uses a curved tibial sensor and is able to determine the location of the load, the compatibility was of concern since the new generation of VERASENSE was compatible with only three prosthetics none of which included the Persona Knee System (PKS) which was provided by the sponsors of this research.

Moreover, the cost of these sensor may outweigh the benefits. The cost of the VERASENSE sensor was about 400 GBP (Park and Song 2021). The benefit of this system may be questioned where some studies have found no improvements in clinical outcomes or patient satisfaction (Song et al. 2019; Wood et al. 2021). Whether this is because the ideal tension has not been found, or the system is inaccurate in defining the load is unknown. This observation makes the benefit of the system debatable as these sensors were single-use, costly additions to the surgical procedures. Research agrees that the cost-benefit ratio of the sensor needs to be studied further (Song et al. 2019; Wood et al. 2021).

Lastly, there were debates over ideal loads for balancing the compartments which was a limitation of these sensors. Although the developers recommend the values mentioned previously there has also been success with more medially loaded knees suggesting that the developers' recommendations were arbitrary. Therefore, more research on the ideal loads using these sensors could improve physiological outcomes and reduce revision rates.

After discussions with an eLibra representative it was uncovered that eLibra has been discontinued. The reasons stated were the cost of the disposable device, not knowing what the target was for the load, the units not being specific, and insensitivity especially with posterior stabilized (PS) implants where it did not work at all or a thicker insert than intended was needed to register any load.

Although research has shown some success in using both systems there were still significant limitations that may be improved upon. This research aims to address some of these limitations by validating the design of a new intraoperative sensor and adding to the existing literature surrounding the forces in the knee.

4.5   Independent Load Sensors

Moreover, independent researchers have dedicated time and effort developing their own joint force sensors various methodologies. This section aims to review those sensors to inform the development of the sensor used in this research. Table 4.1 displays the different load sensors used in joint force measuring applications and their working principles for analysis.
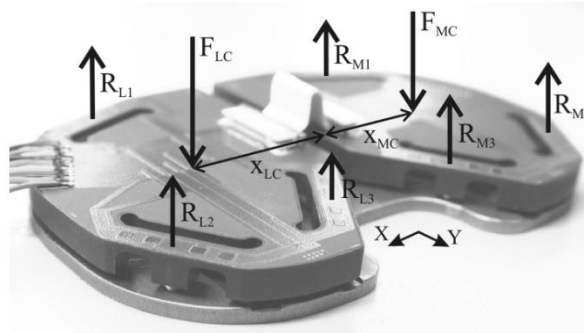
Figure 4.3: Independent Knee Sensor by Crottet et al. (2005)

Table 4.1: Independent Joint Load Sensors

Reference	Sensor Type	Num of Sensors	Housing Unit		Load Range	Error	Testing
			Shape	Material			
(Kaufman et al. 1996)	240 Ω strain gauges	4	-Flat -6 mm thicker than standard insert	Stainless Steel	Up to 667N -Assumes linear behaviour	-0.3-3.2% -0.58-0.79 mm	Lab testing
(Skrinskas et al. 2003)	Strain gauge	4	Flat rectangular	Modified tensioning device	Maximum: 200N	-2.7 N -Does not measure location	Cadaveric testing
(Wasielewski et al. 2004)	Pressure sensor	2 matrix arrays	Curved to fit over femur	PE	Max: 130N/cm^2	-	Clinical trials
(Crottet et al. 2005) Figure 4.3	Thick-film piezoresistive	6	- Flat -Slits for load concentration -Separate medial and lateral compartments -No adjustable height	-	0N-500N	2.6 N 0.8 mm	Knee simulator and cadaveric testing
(Nicholls et al. 2007)	Strain gauges	6	-Flat	Brass	10N-285N	-10% within triangular sensing area -Neglected shear component - No mention of location measurement	Cadaveric testing
(Nolten et al. 2009)	Piezoresistive	6	Curved and cut in half	PE (tibial trial from Columbus implant from Aesculap AG)	Up to 100N	-No temperature compensation -No location measurement	Lab testing
(Wu et al. 2009)	Piezoresistive	6	-Flat -27.3-38.3 mm thick	Unspecified rigid material	0-15 N	- 0.098 N - Does not measure location	Cadaveric testing (5 knees)
(Anastasiadis et al. 2010)	Load cell	4	Flat	Surgical grade stainless steel 316L	- Each load cell: 0-200 N	-Small rectangular sensing area	Lab and cadaveric testing

					- Testing range: 100 N-400 N		
(Hasenkamp et al. 2013)	3.2kΩ strain gauge	2	Flat surface	Polyimide (PI)	200 N-3100 N Non-linear	-38% error after 10 seconds - 85% after 100 seconds	FEA and Lab testing
(Forchelet et al. 2014)	3.2kΩ strain gauge	2	-Flat -Sits under tibial spacer - Long term implantation	PE	0 N-900 N	--No mention of location measurements	Mechanical knee simulator
(Verstraete et al. 2017)	Tekscan type 4011 pressure sensor	2	- Flat - Small sensing area (12.7 mm x 25.4 mm)	3D printed Polylactic acid (PLA) filament	50 N-300 N	- ±13.1% -No mention of location measurements	Cadaveric testing
(Jiang et al. 2019)	Piezoresistive	6	Curved surface	Medical-level polycarbonate	0 N-45 N	±5 N	Mechanical knee simulator
(Safaei et al. 2019)	Piezoelectric	6	-Flat -Rectangular (75 mm x 45 mm x 8 mm)	3D printed PLA	50 N – 1500 N	-6% for force (6 sensors) -1 mm for contact points	Lab testing
(Jain et al. 2021)	Triboelectric harvesters	-	-	PE	450-650 N -Aimed to detect unsafe loads	Max error: 3.48% -No mention of location measurements	Rig for cyclic loading
(Ives et al. 2022)	Electrode capacitive microfluidic force sensor	6	- Hip sensor -Ball and socket	3D printed Resin	Up to 400 N	-	FEA and mechanical hip simulator
(Wang et al. 2022)	Piezoelectric	6	Curved	Flexible polyethylene terephthalate (PET) substrate	Range: 0-50 N	0.08-0.14N (<2%)	Knee joint simulation
(Kuriyama et al. 2023)	-	6	-Curved -Small sensing area	-	Minimum- 22 N	-Does not measure location - Resolution -4.45 N	Cadaveric

(Ge et al. 2023)	Pressure sensitive electrode	197 measuring points	-Flat -Unicompartmental - 45 x 35 mm^2	Pressure sensitive material with insulating layer	Maximum 500 N/cm^2	< 1 % (unclear how they measured this) -Does not measure location	-Cadaveric testing 60 knees -Clinical trials 122 knees
(Yin et al. 2023)	Piezoresistive	12	-Curved -Thick -Small sensing area	-Carbon nanotube (CNT) layer -Polydimethylsiloxane (PDMS) composite	0 -200 N	-Axial: good sensitivity from 50 – 100 N - Shear: Max is 80 N	-Lab testing

The sensors in Table 4.1 include a wide variety of materials, electronics, design shapes, and testing methodologies. Overall, there were 19 joint sensors included from 1996-2023 where 18 were knee joint sensors and 1 was a hip sensor. Of the 18 knee sensors, 6 used strain gauges, 5 used piezoresistive sensors, 4 used pressure sensors, and 2 used piezoelectric sensors. Moreover, most of the sensors used 6 sensors within the device; others used either 12, 4, 2, or matrix arrays which were unspecified.

The main criticisms of most devices were that the sensing range was not inclusive of the loads required for intraoperative balancing during a TKR and that the geometry of the housing unit was flat/not curved to match the femoral implant. This meant that sensor was prone to sliding on the tibia during use and that the sensor did not replace the tibial spacer used in final implantation which creates inconsistencies in its use. Some of the flat tibial sensors specify having a curved PE insert placed on top of the sensor to maintain congruency between the femoral implant, the tibial spacer, and sensor. However, this will decrease the sensitivity, not register a load, or require a thicker PE insert to register a load as what was observed when using eLibra (Yapp et al. 2021). Moreover, for many of the sensors, the load is shared through the supports, without passing through the sensors first. This means that there is no way to know how much of the total load is recorded by the tibial sensor.

The sensor area was also limited based on the placements of the electronics. For example, a sensor made by using a pressure sensor only had an area of 322.58 mm^2 which compared to the size of the sensor is small, especially considering the sensor was flat (Verstraete et al. 2017). Figure 4.4 depicts the sensing area in comparison to the size of the sensor.
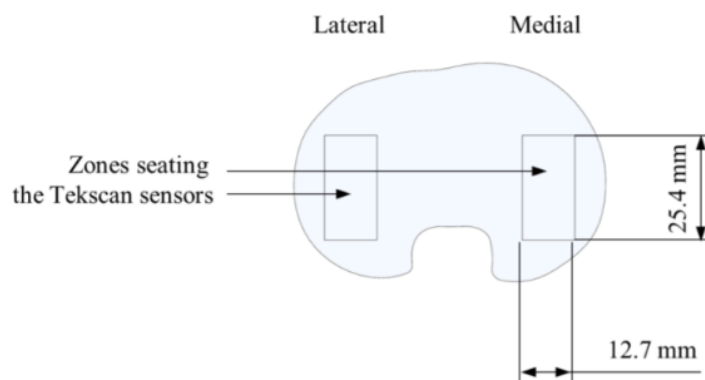
Figure 4.4: Sensing Area from an Independent Knee Sensor by Verstraete et al. (2017)

Another sensor made by Anastasiadis et al. (2010) claimed to have good accuracy for measuring the load and location intraoperatively however, only tested points within their sensing region which had an area of 800 mm^2 compared to the sensor's area of 3,500 mm^2 (Figure 4.5). This neglected the outer contours and included space between the two compartments which do not have contact points with the femur intraoperatively.
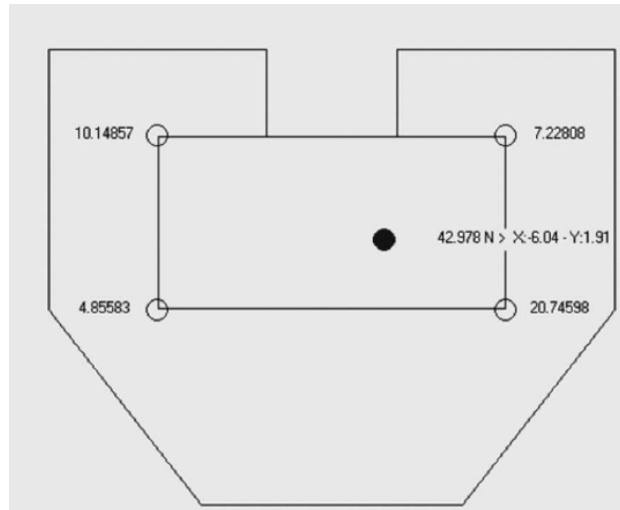
Figure 4.5: Anastasiadis et al. (2010) Sensor and Sensing Area

Furthermore, the sensors which claim to have good accuracy and or sensitivity fail to include an acceptable sensing range. For example, research by Wu et al. (2009) which claims to have an accuracy of 0.098 N, but only measures within the range of 0 N – 15 N. Moreover, most the curved sensors fail to mention accounting for the shear forces in their calculations where during full extension there is a larger shear component from the joint contact forces (JCF) (Hashemi et al. 2011). Many of the sensors also failed to mention having a method of identifying the centre of pressure which is a disadvantage to such systems.

Additionally, most sensors either did not include or failed to mention if there was a method for increasing the thickness of the sensor. This would mean that if a thicker PE insert was required, the sensor would have to be entirely changed. Without the use of a method of increasing the height, which is underneath the sensors, the thicker sensors would suffer from a reduction in sensitivity requiring more deflection to receive readings which would also compromise the integrity of the sensor. Of the sensors mentioned only 2 separated the medial and lateral compartments to avoid mechanical crosstalk (Crottet et al. 2005; Nolten et al. 2009) and only one of those used

slits in the sensors surface to concentrate the load to the sensors (Crottet et al. 2005). This sensor had a good sensing range and was tested using a knee simulator and in cadavers. However, the drawback was that the surface of the sensor was flat, the sensing area was limited by triangulation, and there was no mention of ability to adjust the thickness of the sensor.

Moreover, the structural integrity of the sensor is not to be overlooked, where the sensitivity and the flexibility have a good trade-off with the strength. Polymers were most used where 11 sensors were made using a variety of polymers using various fabrication methods (Wasielewski et al. 2004; Nolten et al. 2009; Hasenkamp et al. 2013; Forchelet et al. 2014; Yin et al. 2015; Verstraete et al. 2017; Jiang et al. 2019; Safaei et al. 2019; Ives et al. 2022; Wang et al. 2022; Ge et al. 2023) , while 4 mentioned using metals (Kaufman et al. 1996; Skrinskas et al. 2003; Nicholls et al. 2007; Anastasiadis et al. 2010). 3D printed plastics may suffer from decreased strength as demonstrated by one sensor which used a 3D printed PLA filament and broke during testing (Verstraete et al. 2017).

4.6   Conclusion

In conclusion, the two main sensors which are/were on the market are eLibra and VERASENSE. eLibra is no longer on the market and there are plans to remove VERASENSE. They both operate using triangulation to calculate the load and track the location and have decreased accuracy outside the sensing area. However, research has shown success in using both systems as well as some limitations that may be improved upon. Moreover, independent researchers have attempted to create intraoperative joint force measurement tools which have been reviewed in this section also with their own advantages and disadvantages. This research aims to address some of the limitations of joint force measurement devices by validating the design of a new intraoperative sensor.

4.7   Aims, Objectives, and Outline

This research aims to develop and validate the design of a new intraoperative load sensor to improve the outcomes of TKRs by using cadaveric and laboratory accuracy testing to investigate the effectiveness, accuracy, and repeatability of the sensor in measuring the load intraoperatively. Currently the VERASENSE system by

OrthoSensor and the eLibra system by Zimmer Biomet were the two sensors which made it to market. However, the literature identifies some key limitations, as well as the limitations of independently made knee joint sensors.

The sensor in this research aims to find accurate and instantaneous measurements of JCF throughout a ROM in the knee over the entire surface of the tibial insert. This will in turn increase the understanding of the forces in the knee intraoperatively that are relevant for balancing the load and increasing the success of a TKR surgery while allowing the orthopaedic surgeons to adjust the soft tissue in real time. With the increased accuracy and expanded sensing surfaces, the orthopaedic surgeon can accurately track and measure the JCF, and the centre of pressure can be identified in various positions and orientations across the whole contact surface of the sensor.

The use of the sensor in TKR surgeries can provide a more balanced knee resulting in an easier and shorter recovery time as well as a better quality of life in terms of decreased pain, increased mobility, and longer durability of the joint. Additionally, the sensor could reduce the need for early revision surgeries which would decrease the economic burden endured by the NHS.

For this research a parallel mixed method approach was employed which uses a combination of quantitative and qualitative research methods to develop, investigate, and validate this sensor (Figure 4.6). To design and validate an accurate intraoperative load sensor for use in TKRs, the following objectives have been set to accomplish this.

1. Integration of design features to increase the accuracy and sensitivity of the sensor.
2. Fabrication of a new and novel load sensor that can be adopted to different joints in the body.
3. Use of AI to link electronics and the applied load and location on the surface of the sensor.
4. Evaluation of the accuracy and performance of the sensor in real time.
5. Understanding of the useability of the device in the clinical setting along with determining the success of the sensor based on expected kinetic and kinematic patterns intraoperatively.
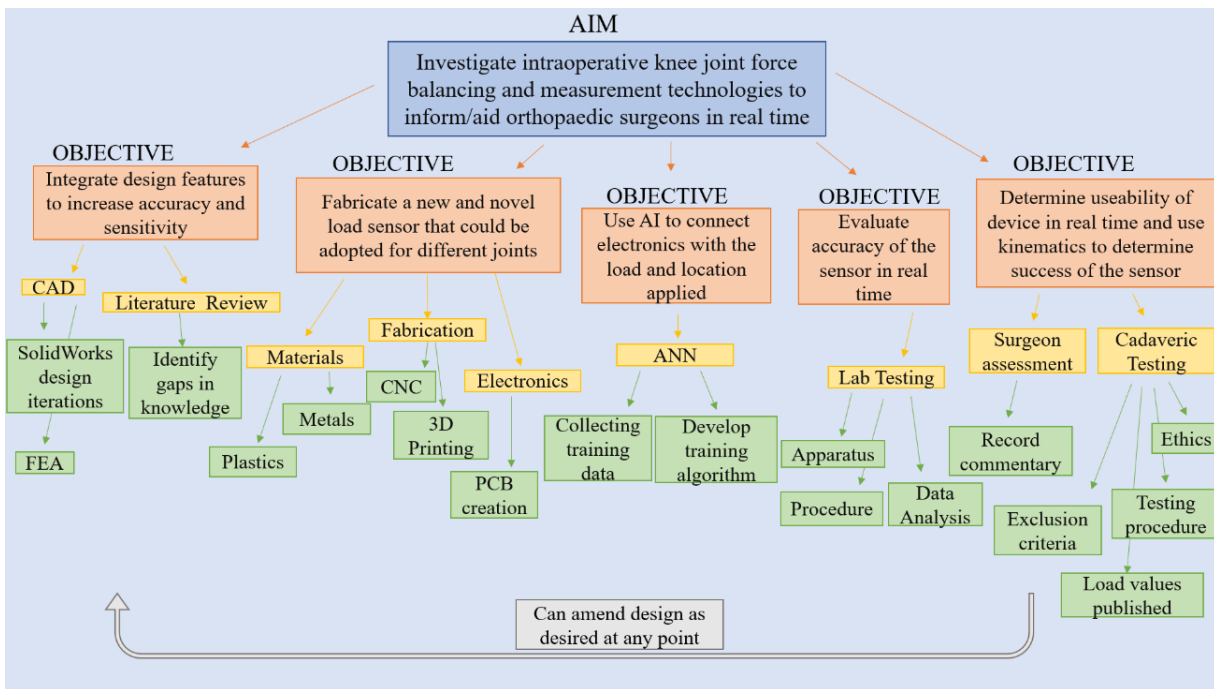
Figure 4.6: Aims and Objective

The following chapters describe the research that occurred and are as follows:

Chapter 5: details the design and fabrication of the sensor.

Chapter 6: describes the design and use of the artificial intelligence (AI) used

Chapter 7: details the laboratory accuracy testing of the sensors.

Chapter 8: describes the cadaveric testing of the Zimmer specific sensor.

Chapter 9: discusses and critically appraises the thesis by chapter and concludes this research.

Chapter 5: Sensor Design and Fabrication

5.1   Physical Sensor Design

When designing and fabricating the physical sensor there were several elements to consider. This included having the design be compatible with the Persona Knee System (PKS) and maintaining the adjustable thicknesses of the system called shims. Moreover, the design should be made while including the following: increasing sensitivity, reducing mechanical crosstalk, avoiding load sharing between the compartments, and having enough strength to withstand the load during training of the AI and intraoperative use. Therefore, when designing the sensor several stages ensued including the Computer Aided Design (CAD) drawing of the physical sensor using the PKS, design optimisation, stress raises for sensor placement, material selection, and fabrication which are described in the subsequent sections.

5.1.1 Sensor Designs

The design of the physical sensor was an iterative process with the aim of maximising the space for the electronics while maintaining the structural integrity of the sensor. Moreover, the design features aimed to increase to the quality of the readings at the sensor locations for the AI to be able to make accurate predictions. To start, CAD drawings, in SolidWorks, of the PKS provided by Zimmer Biomet were used to create a tibial insert that would be compatible with the femoral insert and replace the tibial spacer (Figure 5.1). The goals of these designs were to be compatible with the PKS, including a method for adjusting the thickness, not to overcomplicate the design by increasing the number of parts necessary, to raise the stress at the locations of the sensors, have enough strength to withstand the loads, and to isolate the loads between the compartments.
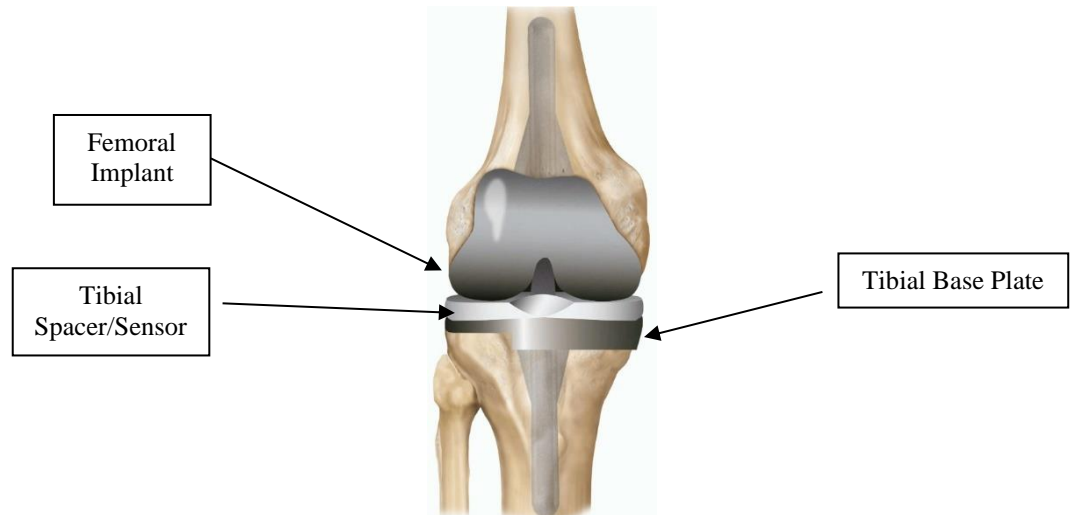
Figure 5.1: Location of Sensor Relative to the Implant System

From these goals the three designs were created. One was a general design which could fit any implant system titled 'Ring Design' and used spacers/rings of different thicknesses to replace the shim system of the PKS. The second was a design that used the Persona's shim system to adjust the height and was called 'Zimmer Specific Design'. The last design was the first prototype used to develop various design features. The three designs used the tibial spacer from the PKS to maintain consistency between the curvature of the femoral implant and the sensor and were modelled for the right knee in the medium size (size E/F in PKS sizing).
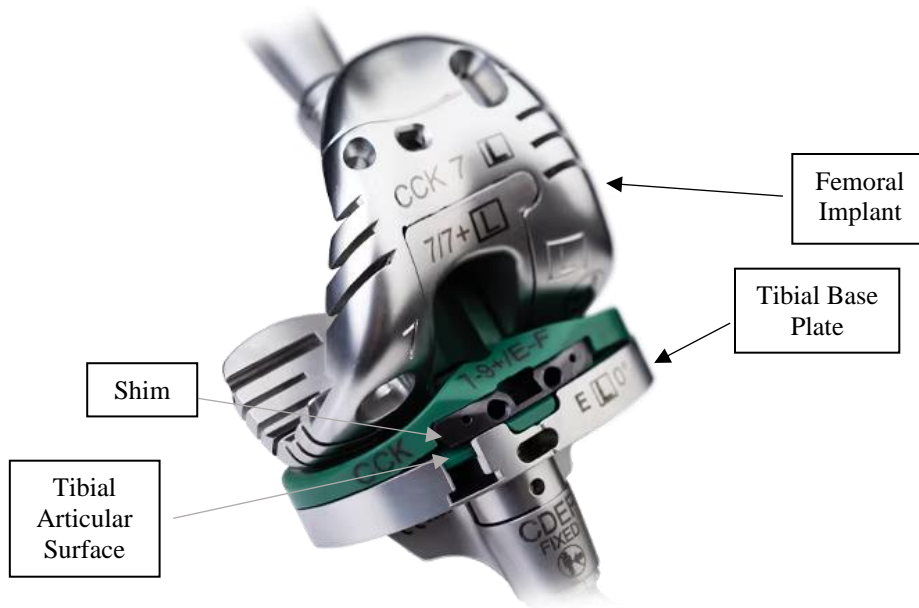
Figure 5.2: Persona Knee System (PKS) (Anon. 2024a)
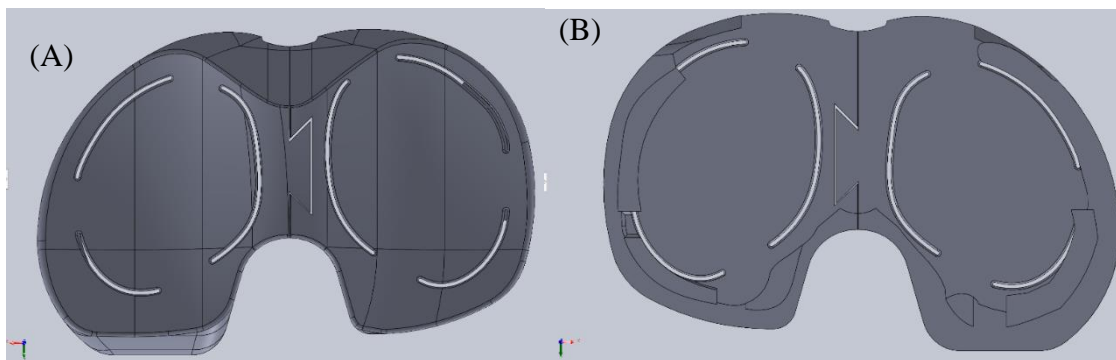
Figure 5.3: CAD drawing for Ring design a) Top View b) Bottom View (according to X, Y, and Z Coordinates in Figure)

The Ring design can be seen in Figure 5.3, the third angle projection drawings can be seen in the Appendix (A.II). The dovetail kept the medial and lateral compartments together in the X and Y-axis while avoiding load sharing by allowing movement in the Z-axis. The slits through the surface of the sensor transferred the load to the tabs formed by the space between slits where the sensors were attached beneath. The aim of this feature was to reduce mechanical crosstalk and increase the sensitivity in these areas. The rings clipped into the bottom perimeter of the sensor to allow for varying thicknesses, to adjust the tension in the joint (Figure 5.4). The calibrated rings ranged from 1mm-6 mm in 1 mm increments which was standard for knee implant systems including Persona's Shim System.
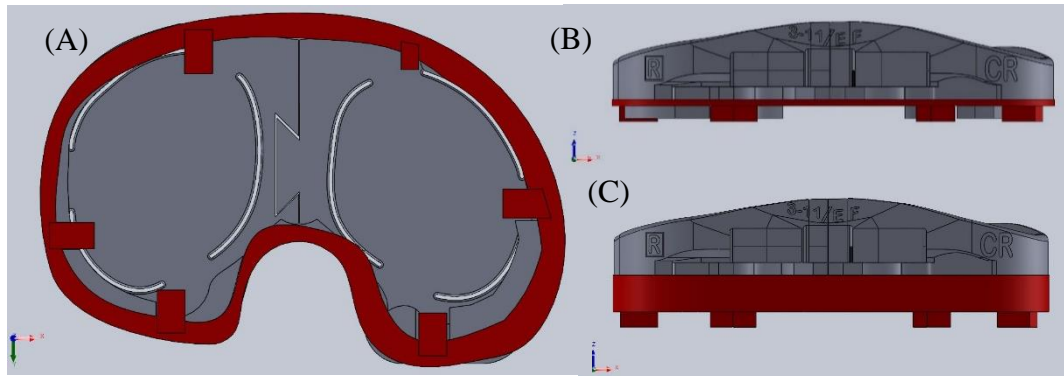
Figure 5.4: Ring Design a) 1 mm Ring Attached (Bottom View) b) 1 mm Ring Attached (Front View) c) 6mm Ring Attached (Front View)

The Zimmer Specific design, Figure 5.5 and Appendix A.II, maintained the use of the shims which allowed for the variable thickness and smooth integration of the existing elements of the PKS. The slits were carried forward from the Ring design with the same aim.
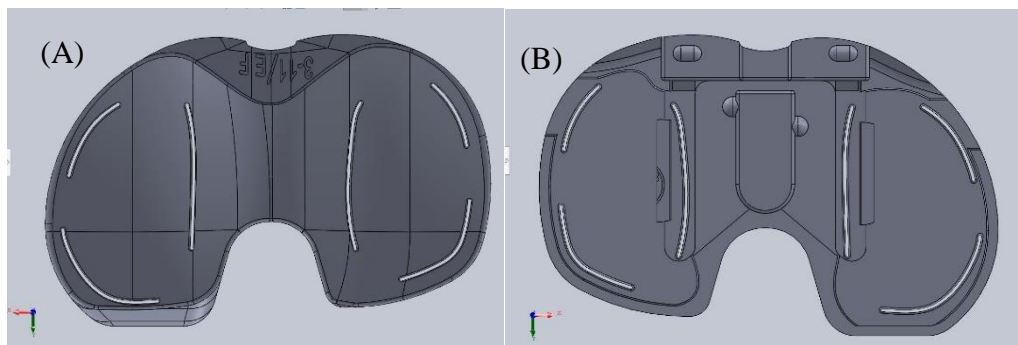
Figure 5.5: Zimmer Specific Design a) Top View b) Bottom View

The Zimmer Specific sensor in configuration with the rest of the PKS can be seen in Figure 5.6.
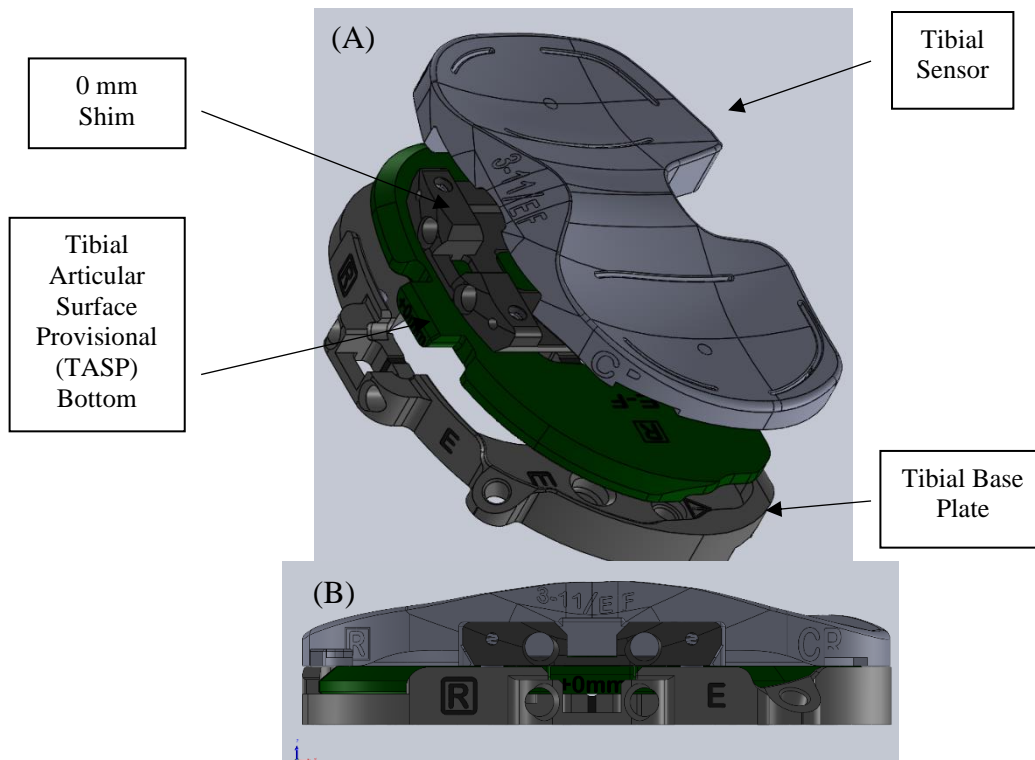
Figure 5.6: Zimmer Specific Sensor Configuration with PKS a) Exploded View b) Front View

The third design (Figure 5.7) was a design used for the first iteration of prototyping. This design included the division of the medial and lateral compartments by splitting the compartments, but without the dovetail to limit movement in the X-axis and Y-axis. The use of the variable thickness trays instead of Persona's shim system or rings can be seen, however there was no system to clip in the trays.
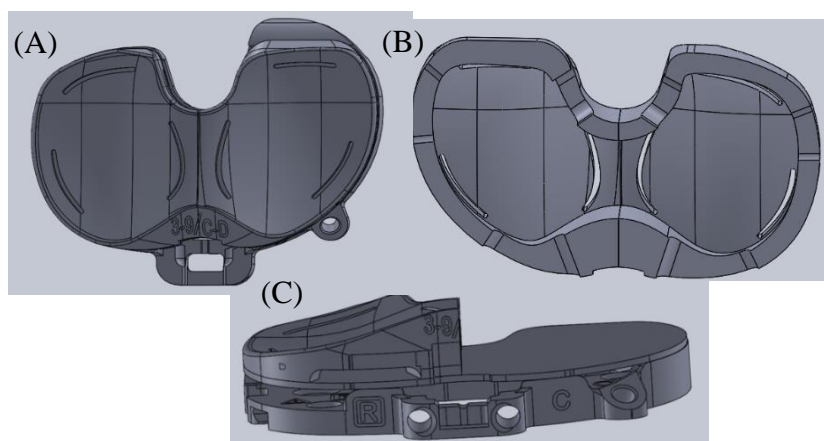
Figure 5.7: Third Design a) Top View b) Bottom View c) Front View

5.1.2 Materials

The materials for the sensor required some investigation. Metals and plastics were both explored since stress is not defined by the material used. Metal was used to provide strength while plastic and was lighter and cheaper to fabricate for initial proof of concept. The metals considered in this research were steel, aluminium, and titanium. Steel and titanium have high strength and hardness making it a good choice; however, they are more expensive. An added benefit to titanium is its biocompatibility. Aluminium, on the other hand, is not as strong, but it is lighter and cheaper to manufacture. Aluminium alloys would also increase the yield strength enough for the temporary implantation and use of this sensor. Aluminium, steel, and titanium are heavier than plastics; however, this is not a problem since the relatively high point loads needed for training the device with AI meant the adequate material strength is necessary.

In this research the two plastics investigated were polyurethane resin (PU) and polypropylene (PP). PP was durable with high toughness and resistance to impact, relatively inexpensive, and was also used in certain biomedical applications which was ideal for prototyping and mass production. PU resin had a smooth finish and high impact strength. However, plastics, especially 3D printed, have the potential for cracking because of the high residual stress concentrations caused by the printing and cooling process, which can be problematic with high stresses. Despite this, it was hypothesized at this stage that the AI could be trained with lower point loads as stress is material independent and AI is used to generate a transfer function between input and output. The table below, Table 5.1, shows the materials in order from lowest yield strength to highest.

Table 5.1: Advantages and Disadvantages of Different Materials

Material	Advantages	Disadvantages
Polyurethane (PU) resin	Smooth finish High impact strength	Lowest yield strength Thermoset
Polypropylene (PP)	High tensile strength Lightweight (low density) Low water absorption Biocompatible Can be recycled (relatively low environmental impact) Thermoplastic	Granular finish
Aluminium	Cheapest of the metals Lowest density of the metals Stronger than plastics Easy to machine Alloys can make stronger	Lowest yield strength of the metals
Steel	Good strength	Most dense of the metals used
Titanium	Great strength to weight ratio Biocompatible	Difficult to machine Expensive

In summation, when choosing the proper material there were a few considerations. Firstly, the first design iteration of the sensor required a good trade-off between the cost, strength, machinability, durability. While titanium was a good choice in terms of strength and biocompatibility, it was expensive and difficult to machine making it ideal for the final design, but not for prototyping.

5.2   Sensor Design Validation

Finite Element Analysis (FEA) was a useful tool to investigate the maximum allowable load, sensor placement by confirming stress raises at tabs, the minimisation of load sharing, and the ability to collect training data for the AI.

The two designs created in the previous section, the Ring design and the Zimmer Specific design, were analysed using FEA in SolidWorks. Homogeneity and linear elasticity were assumed. The metals and plastics discussed in the previous section were investigated as well including PU resin, PP, steel, titanium, and an aluminium alloy, Table 5.2.

Table 5.2: Material Specifications from SolidWorks

Material	Elastic Modulus	Poisson's Ratio	Yield Strength
Polyurethane (PU) Resin	0.920 GPa	0.320	0.370 MPa
Polypropylene (PP) Copolymer	0.896 GPa	0.410	13.400 MPa
Aluminium 6063 Alloy	69.000 GPa	0.330	240.000 MPa
316L Stainless Steel	200.000 GPa	0.265	170.000 MPa
Titanium CP-Ti	105.000 GPa	0.370	500.000 MPa

Additionally, the parts were constrained in the way they fit together with the rest of the implant parts (rings/shims and tibial tray) seen in Figure 5.8 and based on the PKS. For the Ring design, the dovetail was set as contact between the compartments. Moreover, the sensor locations were added to both designs with a size of 1.8 mm x 1.0 mm where the average strain can be used as a means of validation. Overall, the boundary conditions were selected due to trial and error.
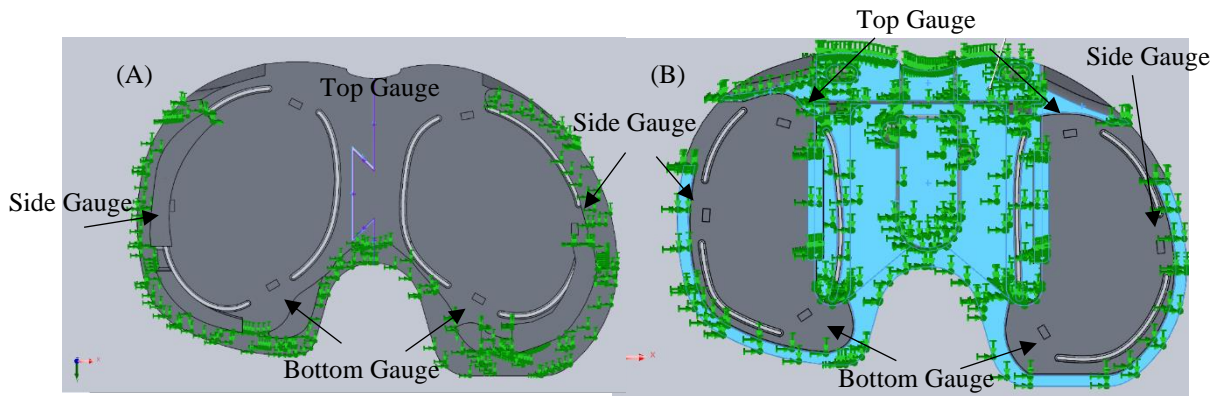
Figure 5.8: Fixtures and Connections and Strain Gauge Locations a) Ring b) Zimmer

5.2.1 Mesh Convergence

To ensure best result, a detailed mesh converge study was performed. A converged mesh model offers a good trade-off between accuracy and computational load/time to execute. This allows the results to be easily validated with the actual system, so the results simulated are mimicked in the real use of the system. Without this, the simulated results are useless. On the other hand, due to the iterative nature of this process, the time and computational load to execute should be limited.

Ring Design:

Each compartment was meshed independently where they both used a blended-curvature mesh with tetrahedral elements (Table 5.3). For each compartment, a total of 7 different mesh sizes were used.

Table 5.3: Mesh Number with Total Number of Elements for Each Compartment (Ring Sensor)

Mesh Number	Medial Compartment Total Number of Elements	Lateral Compartment Total Number of Elements
1	4677	3721
2	16573	23445
3	69098	59211
4	98067	70736
5	111388	91865
6	143888	126407
7	182771	144160

A point force of 200 N was applied in the centre of the compartment (Figure 5.9) and the average von Mises stress taken from the area of the top sensor was recorded. The von Mises stress was used since is provides a single value to represent the combined effect of the stresses at one location, which simplifies analysis especially with complicated geometry and converges quicker with mesh refinement.
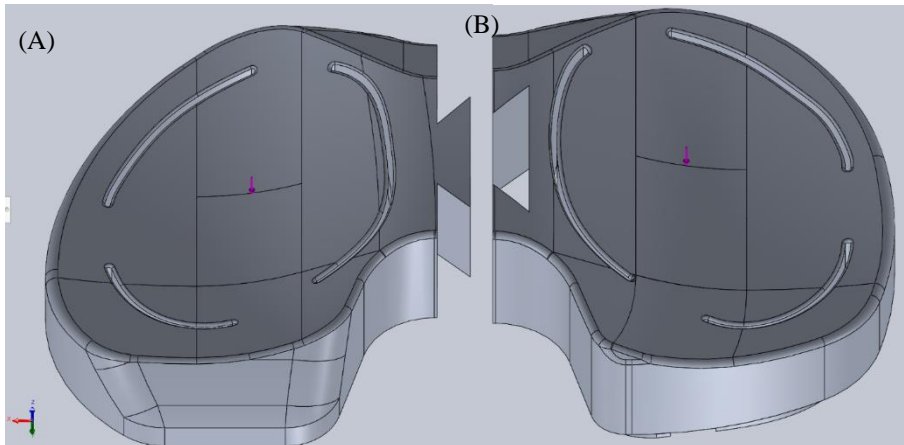
Figure 5.9: Location of Applied Load (200 N) a) Medial Load b) Lateral Load

The results of the medial compartment indicated that the Mesh 3 (69,098 total elements) provided sufficient mesh density for repeatable stresses (Figure 5.10 (a)) since the percent difference of stress results from Mesh 3 and 4 was only 0.65%, while the percent difference between Mesh 1 and 3 was 12.12%.

For the lateral compartment the Mesh 3 was also a sufficient density (Figure 5.10 (b)) where the percent difference between Mesh 3 and 4,5,6, and 7 were all less than 1.00% while the percent difference between Mesh 1 and 3 was 4.09%. The differences in the results between the compartments can be due to the size difference, sensor location, and slit location between the compartments.
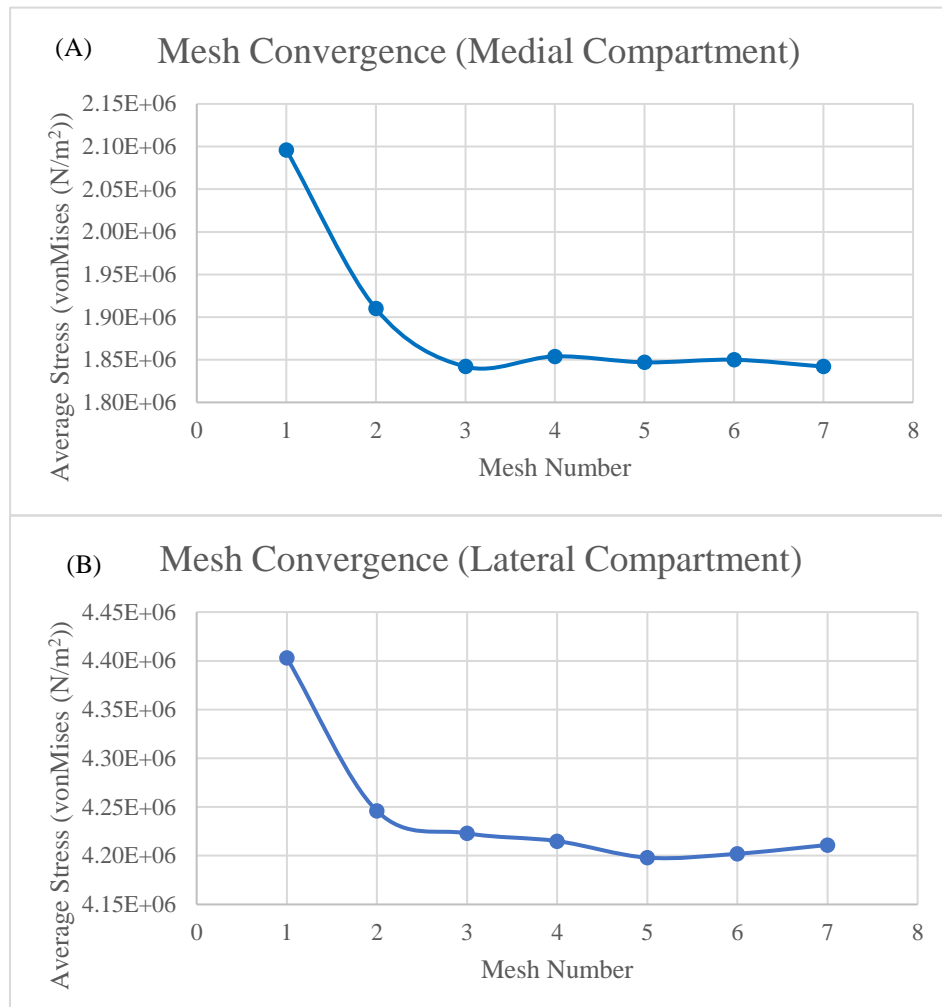
Figure 5.10: Ring Design Mesh Convergence a) Medial Compartment b) Lateral Compartment

The final mesh for the Ring design was used for subsequent FEA (Figure 5.13 (a)), where the total number of elements was 128,309.

Zimmer Specific Design:

For the Zimmer Specific design, a similar process was followed for determining the proper mesh density; however, since this design was one part it was meshed together using 7 different meshes with a varying number of elements (Table 5.4).

Mesh Number	Both Compartments
	Total Number of Elements
1	9639
2	20754
3	28382
4	41471
5	75033
6	119280
7	173052

A point force (200 N) was applied to each compartment concurrently and the average von Mises stress over the area of the top sensor was recorded for each compartment (Figure 5.11).
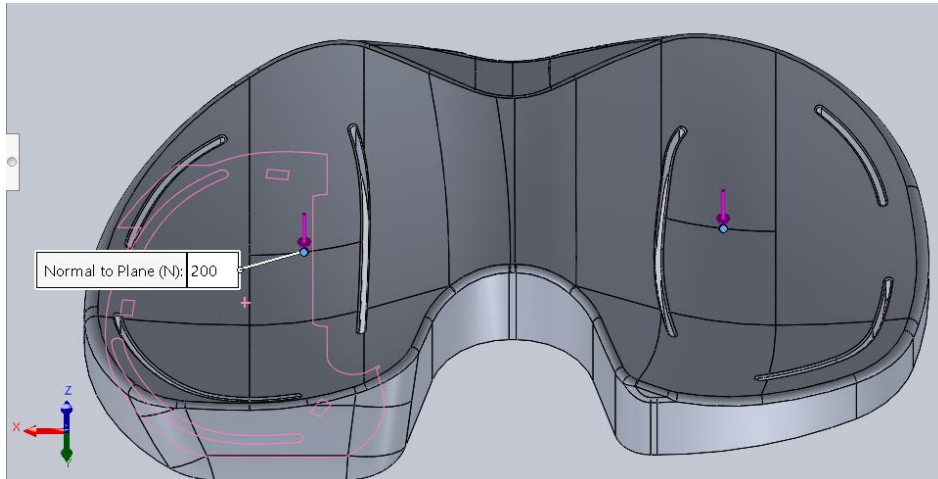
Figure 5.11: Location of Applied Load (200 N) on both Medial and Lateral Compartments

The results of the mesh convergence investigations indicated that the Mesh 5 had converged with 75,033 elements, providing enough mesh density for both compartments. For the medial compartment, the percent difference between Mesh 1 and 5 was 88.12% while Mesh 5 and 7 had the same stress results (Figure 5.12(a)). For the lateral compartment, the percent difference of the stress results between Mesh 1 and 5 was 20.57% where the difference between Mesh 5 and 7 was 0.60% (Figure 5.12(b)).
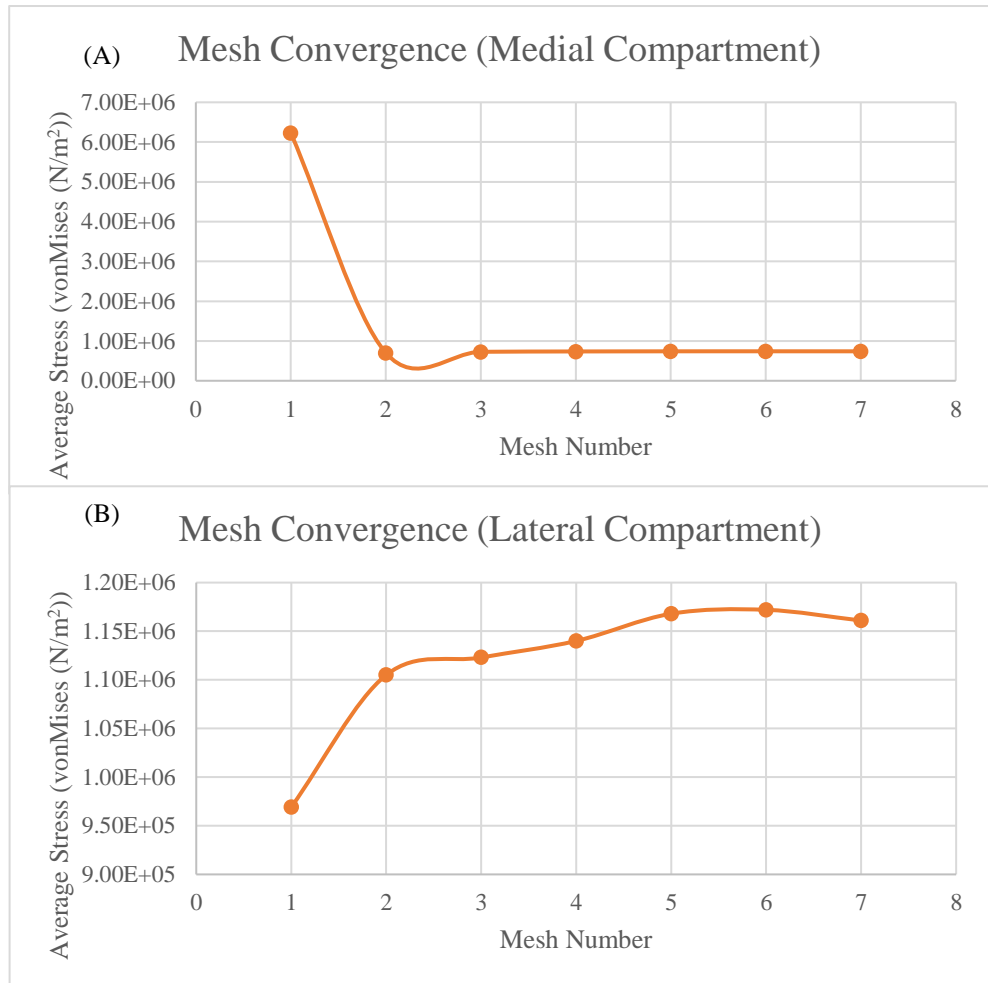
Figure 5.12: Zimmer Specific Mesh Convergence a) Medial Compartment b) Lateral Compartment

Both compartments were investigated because although the medial compartment had stabilised at Mesh 3, the lateral compartment required a finer mesh to converge (Figure 5.12). As a result, a finer mesh size (Mesh 5) was required for the whole part. The final converged meshes can be seen in Figure 5.13.
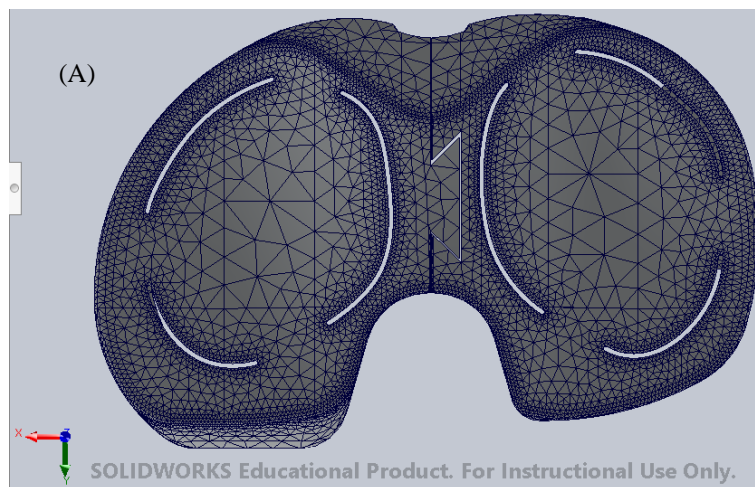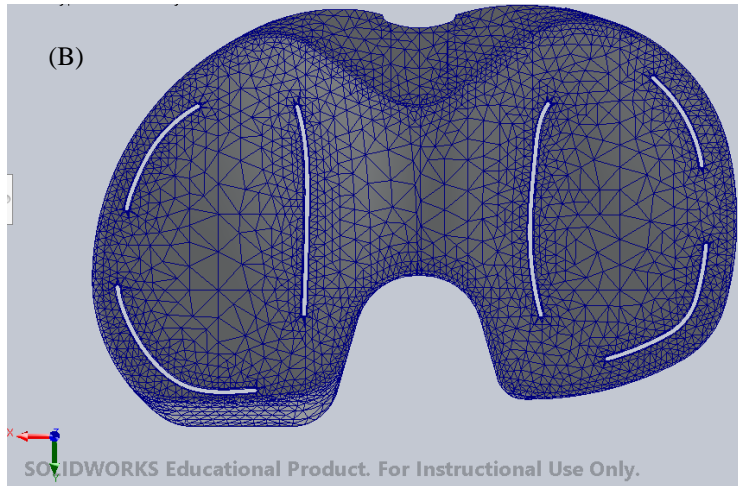
Figure 5.13: Final Mesh a) Ring Design b) Zimmer Specific Design

5.2.2 Defining External Load

In theory, the slits transfer the force to the tabs and therefore, the method of applying the load will be independent of the readings at the tabs. To confirm this, the effect of different definitions of a point load were investigated by applying five different external loads to the same location on the surface of the sensors.

The same mesh densities and constraints were used for each design. To mimic the use of a ball bearing, two spherical areas (radius 1 mm and 2 mm) were created on the surface of the tibial sensor's FEA models (Figure 5.14).
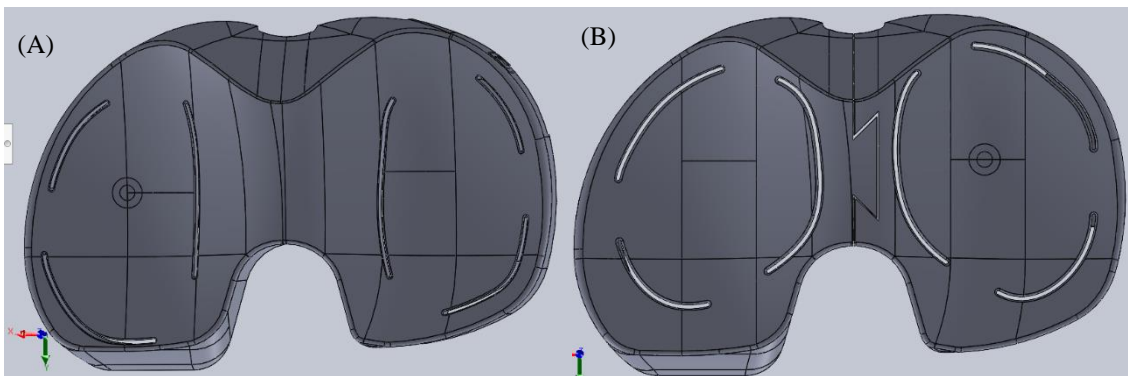
Figure 5.14: Location of Applied Load a) Zimmer Specific (Medial) b) Ring (Lateral)

To apply 200 N as pressure, the surface areas were measured and divided by the 200 N force. For the Zimmer Specific and Ring sensors, the pressures applied were 15.88 and 15.91 MPa for the 4 mm diameter circle and 63.55 and 63.69 MPa for the 2

62

mm diameter circle respectively. For comparison, force was applied to the same areas and to a point in the centre. A list of the 5 forces applied are in Figure 5.15.
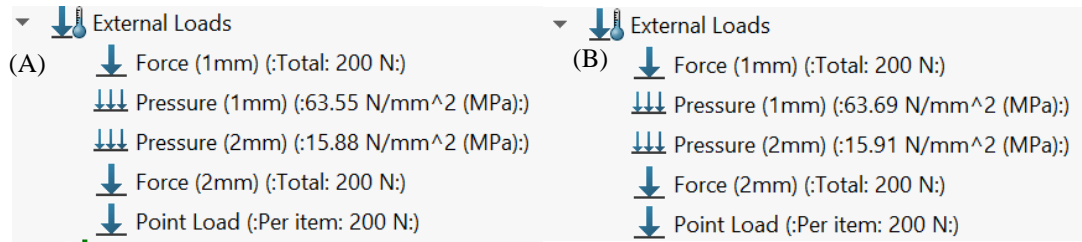
Figure 5.15: Types of Loads Applied a) Ring Specific Values b) Zimmer Values

The medial compartment of the Zimmer Specific design was used, and the average stress was taken from the location of the three sensors: Top, Side, and Bottom for each compartment. The local and contact stresses are not relevant to this investigation since the strain gauge measurements are what will be recorded by the sensor and by the time the stress reaches the gauges it has averaged to the nominal stress/strain. The results for all loading methods yielded very similar results in terms of the von Mises stress at the sensors (Figure 5.16) where the maximum percent difference between for each gauge was less than 3.50%.
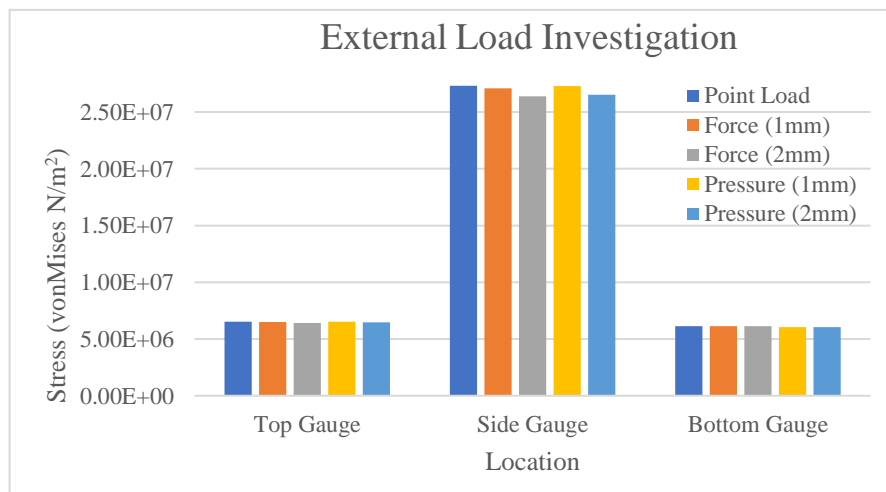
Figure 5.16: Effects of Different Types of Loads on the Stress at the Sensors (Zimmer Specific)

The same procedure was repeated for the Ring design, where the same loads were applied to the lateral compartment and the maximum percent difference of the measured stress between the gauges was less than 2.00% (Figure 5.17).
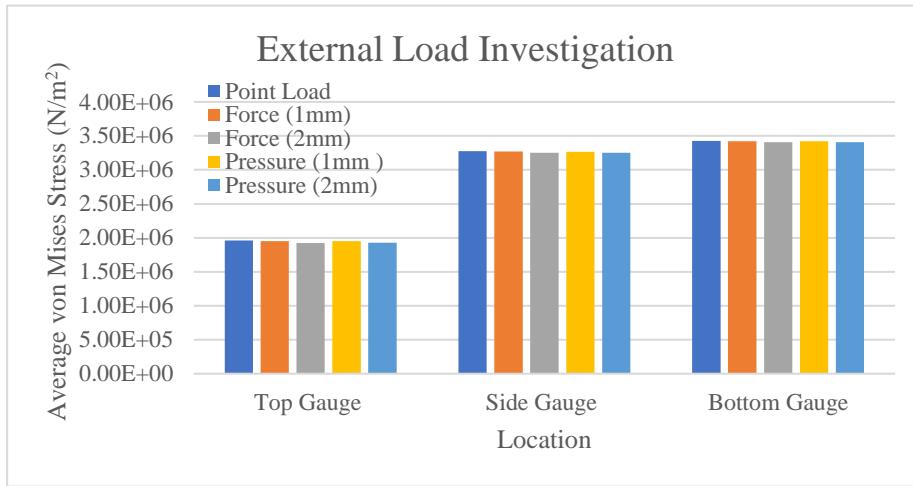
Figure 5.17: Effects of Different Types of Loads on the Stress at the Gauges (Ring)

This exercise proved that the method of applying the load for FEA was immaterial to the investigation into the Factor of Safety (FOS) and stress investigations at the tabs for both designs due to the distance between the load applied and gauge area. As a result, the point load was chosen for the subsequent analyses since the applied load could be closer together without overlapping and was less time consuming to simulate.

Moreover, the validation of these sensors was done by comparing the strain values to the FEA principal strain values to confirm its accuracy (Al-Nasser et al. 2024).

5.2.3 Maximum Load

According to the literature, a robust sensor should be able to withstand 450 N. To determine the appropriate material and any design flaws impacting the structural integrity of the sensors, it was necessary to establish a FOS. To collect training data for the Artificial Intelligence (AI), point loads must be applied over the surface of the sensor so two points were investigated for each compartment, one in the centre and the other near the edge (4 mm from the slit) (Figure 5.18). The method of applying the load, point load, and the boundary conditions, mesh size and constraint, were used as determined in the previous sections.
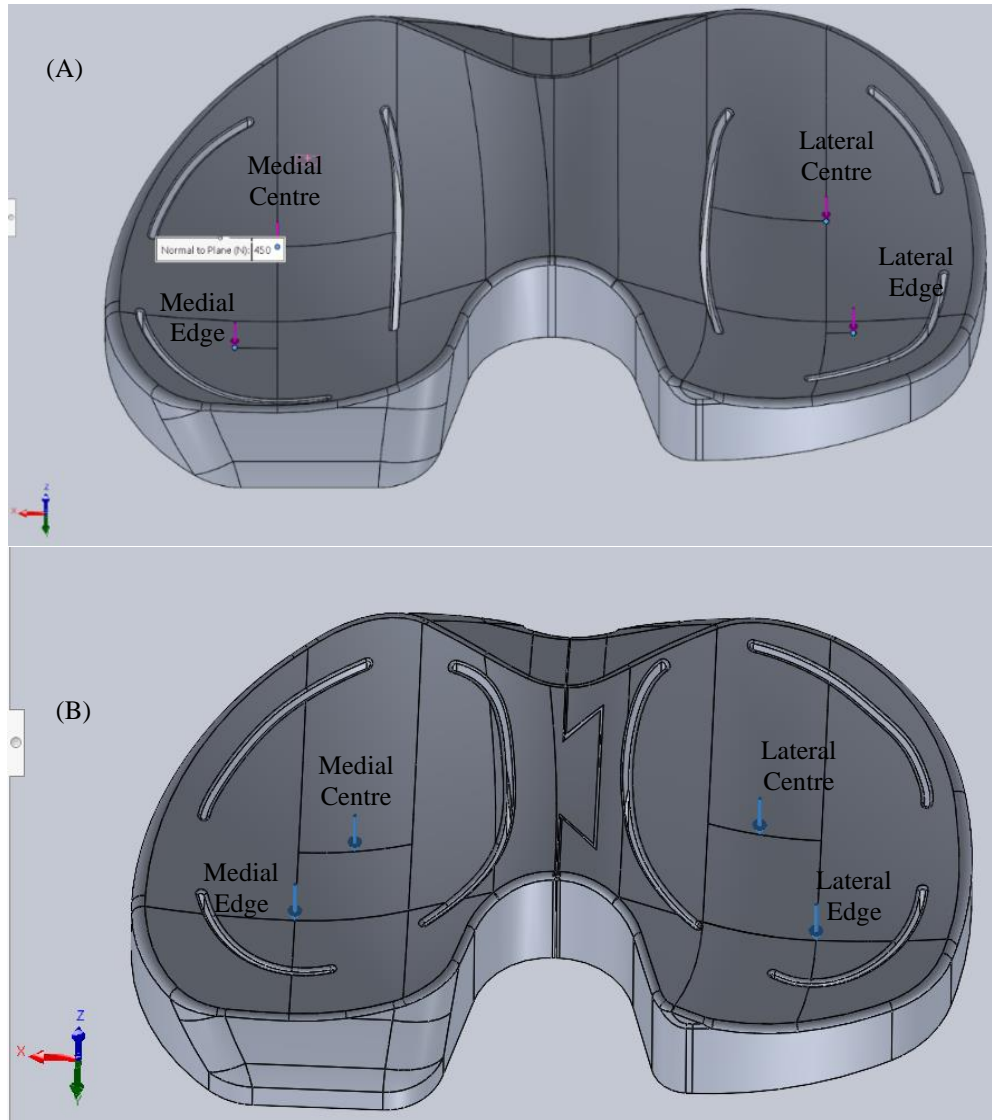
Figure 5.18: Locations of Applied Loads for Maximum Load Investigation a) Zimmer Specific b) Ring

The minimum acceptable FOS was set to 1.5 for this application since these loads would only be applied momentarily and during intraoperative use of the sensor the load would be distributed across the surface. Table 5.5 summarised the FOS for each material with 450 N applied to each compartment at both the centre and the edge.

Table 5.5: FOS for Different Materials when 450N Applied to Centre and Edge

Material	Minimum FOS							
	Ring Medial		Ring Lateral		Zimmer Medial		Zimmer Lateral	
	Centre	Edge	Centre	Edge	Centre	Edge	Centre	Edge
Polyurethane (PU) Resin	0.005	0.002	0.003	0.001	0.003	0.002	0.003	0.001
Polypropylene (PP) Copolymer	0.200	0.090	0.090	0.050	0.100	0.060	0.100	0.050
Aluminium 6063 Alloy	3.000	1.600	1.700	0.800	1.800	1.000	1.900	0.800
316L Stainless Steel	2.200	1.100	1.200	0.500	1.200	0.700	1.300	0.600
Titanium CP-Ti	6.100	3.400	3.500	1.700	3.800	2.200	4.100	1.700

In conclusion, the FOS was acceptable for all cases in both sensors while using Titanium which would be the optimal material for the final version of this sensor to ensure the sensor can withstand higher loads for training and repeated use. For the aluminium alloy, the edges resulted in a lower FOS due to the overhang created by the slits. Since this was the first prototype the aluminium alloy was chosen where training loads could be lowered.

It is also important to note that if this system is single use or reusable will have an impact on the FOS. With the repeated use of the sensor, the maximum allowable stress and cyclic loads use will have to be investigated.

5.2.4 Load Transfer

The next exercise was to create stress raises to improve signal to noise ratios. For that purpose, the slits were created through the surface of the sensor to increase the sensitivity and reduce the occurrence of mechanical crosstalk. To prove this was occurring, a 450 N force was applied to the centre of both compartments, like the previous section, and the von Mises stress was recorded for 6 equidistant points leading up to the centre of the strain gauge for both designs. For the Zimmer Specific design, the side gauge was used and for the Ring design the top gauge was used to provide a variation in investigated location (Figure 5.19 (a and b)).
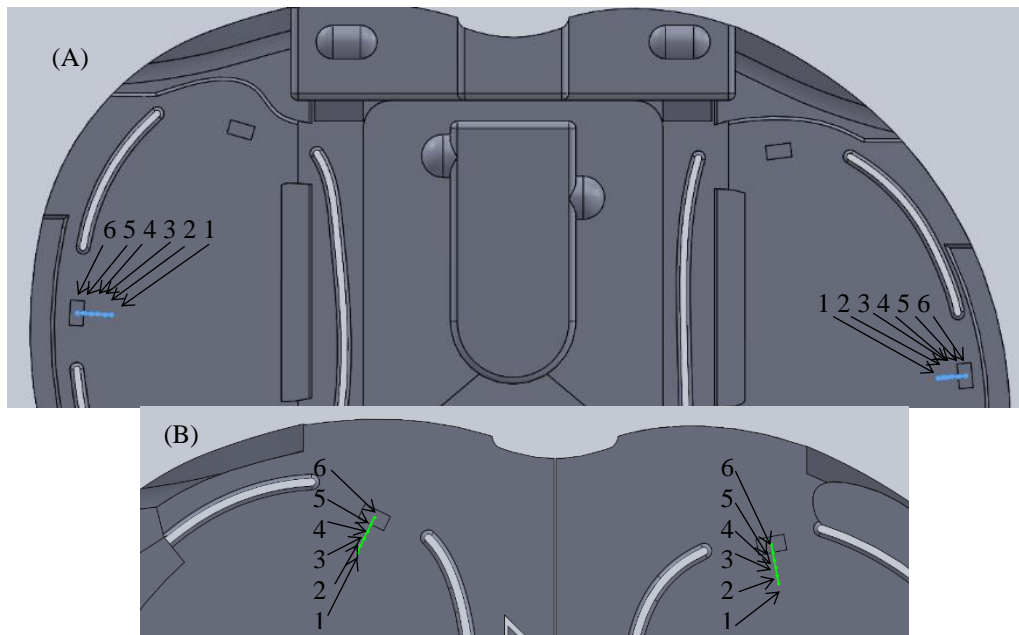
Figure 5.19: Points on Sensor Leading to Centre of the Gauge to Observe Load Transfer a) Zimmer Specific b) Ring

The results in Figure 5.20 depicted how the stress increased on the path towards the centre of the strain gauges. This proved the impact of adding the slits, where the stress distributions can be seen in Figure 5.21.
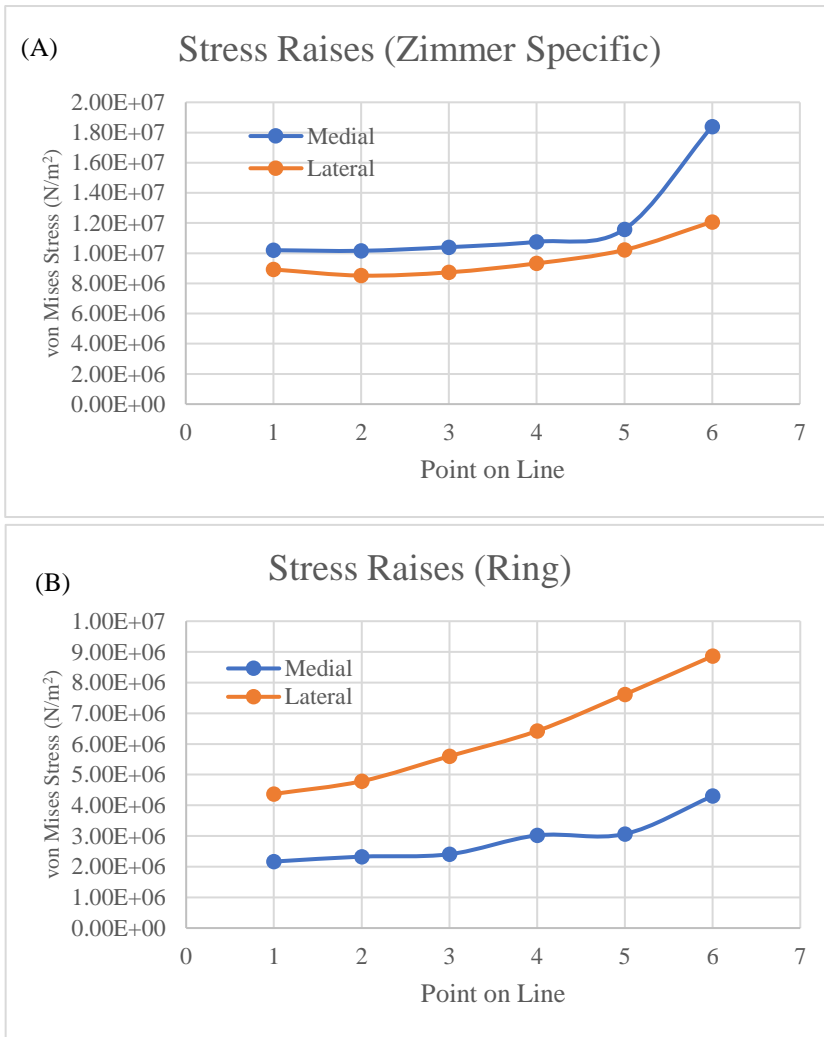
Figure 5.20: Load Transferring to Tabs a) Zimmer Specific b) Ring
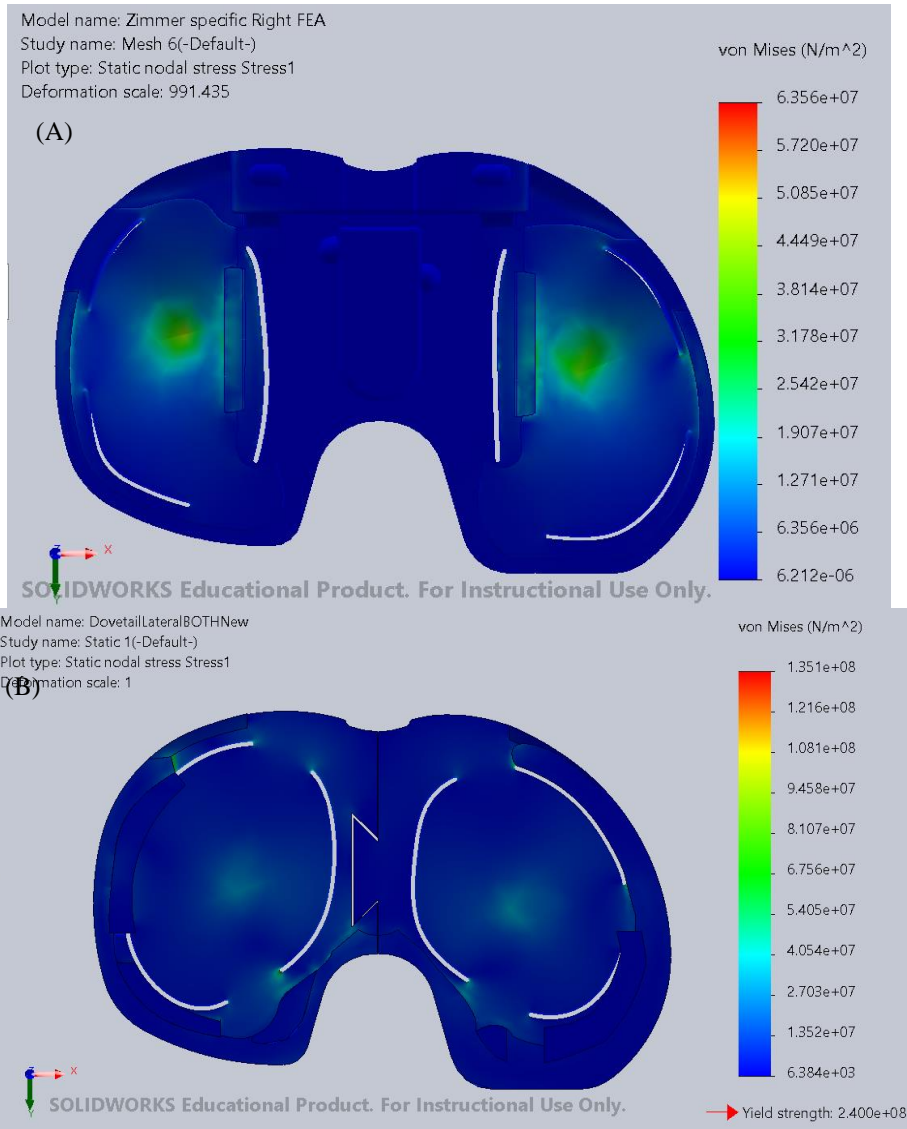
Figure 5.21: Stress Distributions (Stress Raises at Tabs) a) Zimmer Specific b) Ring

5.2.5 Load Sharing

The goal of the sensor is to provide the surgeon with the visuals of the compartmental load and its centre of pressure to ensure balanced loads between compartments. For accurate representation of intercompartmental results there should be no load sharing between the compartments as this would impact the perceive state of balance in the knee. To investigate this, a 700 N point load was applied to the centre of one compartment and the average stress at the strain gauges in the opposite compartment was recorded. Then, the same was repeated on the other compartment. The same boundary conditions from the previous sections were used, including the interaction between the dovetail on the Ring design being in contact.

69

Table 5.6: Average Von Mises Stress at Strain Gauges from Unloaded Compartment

Von Mises Stress (N/m²)	Medial Compartment			Lateral Compartment		
	Top Gauge	Side Gauge	Bottom Gauge	Top Gauge	Side Gauge	Bottom Gauge
Ring	2.65E-03	1.72E-03	1.87E-03	1.53E-03	1.24E-02	1.66E-02
Zimmer Specific	69.21	16.71	2.14	45.69	12.66	35.47

The stress at the gauges (the opposite compartment to the applied load) was relatively low, Table 5.6. Since the dovetail physically separated the compartments in the Ring design, the stress was much lower in the opposite compartment compared to the Zimmer Specific design. But when comparing the stresses measured in the same compartment as the applied loads it was still insignificant which proved there was minimal load sharing between compartments even under high loads.

5.2.6 Conclusion

In conclusion, FEA was a useful tool to ensure that the material selected would be able to withstand a high enough load for training, the design features were causing the stresses to be transferred to the strain gauges, and there was minimal load sharing between compartments. The aluminium alloy was chosen as the ideal material for both designs since there was a good trade-off between weight, strength, and cost. While using the aluminium alloy, the edges of both designs were not able to withstand a 450 N point load, which was the maximum load determined by Roth et al. (2017). As a result, when training the AI, a lower maximum load was to be used.

5.3   Fabrication

The aluminium alloy was predicted to be the best option during the design iteration and sensor development for prototyping through FEA. A wide variety of materials were fabricated to investigate different fabrication techniques for the materials. The two types of fabrication methods considered were 3D printing and Computer Numerical Control (CNC) machining. 3D printing provided greater design freedom and complexity with faster prototyping. However, there was lower precision and accuracy compared to CNC machining with limited material property options. For one off printing 3D printing is typically cheaper, however, for mass producing the per

unit cost is typically higher than with CNC machining. However, CNC machining provides less design freedom compared to 3D printing. Therefore, both CNC machining and 3D printing were used to investigate the product and the viability of using such methods. Table 5.7 included the different materials, fabrication methods, and tolerances given by the manufacturers used for each.

Table 5.7: Fabrication of Sensor using Different Methods and Materials

Material	Fabrication Method	Tolerance
Stainless Steel (SUS316L)	Selective Laser Melting (SLM) 3D Printing	± 200μm
Polypropylene (PP) Glass-filled (PPGB)	Selective Laser Sintering (SLS) 3D Printing	± 300μm
Polyurethane (PU) Rigid 1000 Resin	Stereolithography (SLA)	±100 μm
Aluminium 6082	Computer numerical control machining (CNC)	±100 μm

5.3.1 3D Printing

The first design was 3D printed stainless steel to investigate the quality of 3D printed metals and the use of 3D printing in general. However, the surface finish was rough and required smoothing to attach the strain gauges (Figure 5.22) and the data from the strain gauges was unstable which could be from the non-uniform, inhomogeneous, anisotropic properties caused by 3D printing fabrication techniques resulting in the formation of residual stresses in the finished parts (Malekjafarian et al. 2017; Somireddy and Czekanski 2020).

Smoothed surface

Rough surface
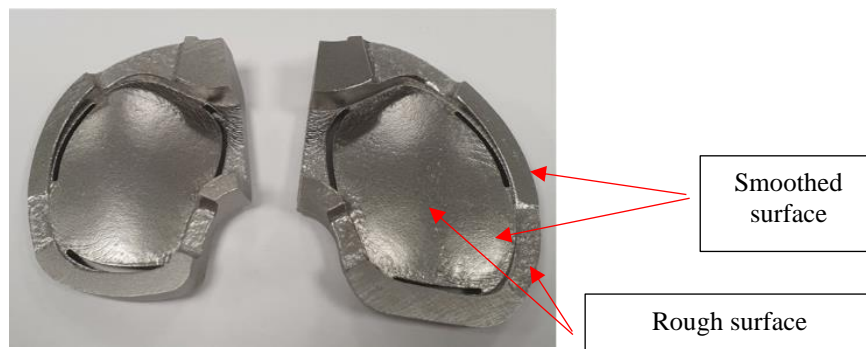
Figure 5.22: 3D Printed Stainless Steel (First Design)

Plastics were also explored including 3D printed polypropylene (PP) which was manufactured using SLS 3D printing. These parts were rough and some moderate design flaws were identified. However, the fabrication of these parts provided insight into how the parts function and fit together after fabrication.
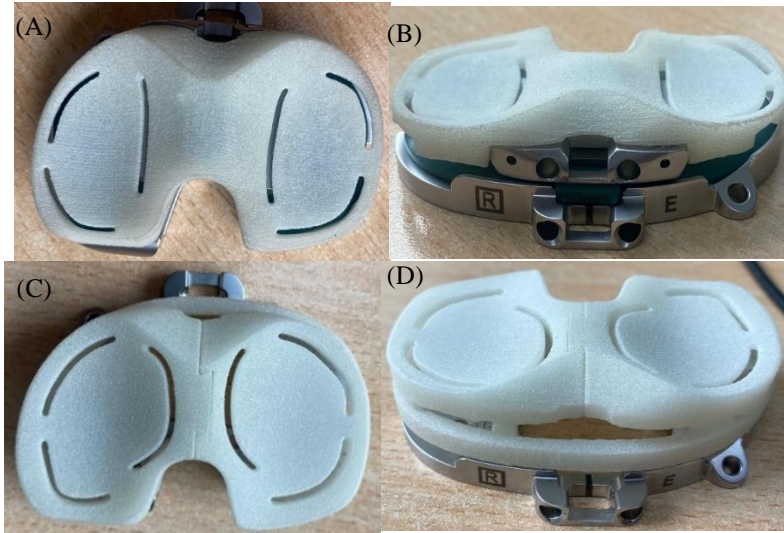
Figure 5.23: 3D Printed PP a) Zimmer Specific (top view) b) Zimmer Specific (front view) c) Ring (top view) d) Ring (front view)

Moreover, for the rings, the 1mm ring was distorted while manufacturing, which can be seen when comparing the 1 mm and 4 mm PP rings and the 1 mm PP and Polyurethane (PU) ring in Figure 5.24 (a&b). Geometrical accuracy is a significant problem for both PU and PP during additive manufacturing (AM) leading to the shrinking and warping of parts (Spoerk et al. 2020; Perera et al. 2023). From these findings it was thought that the use of a combination of metals and plastics may offer some benefits.
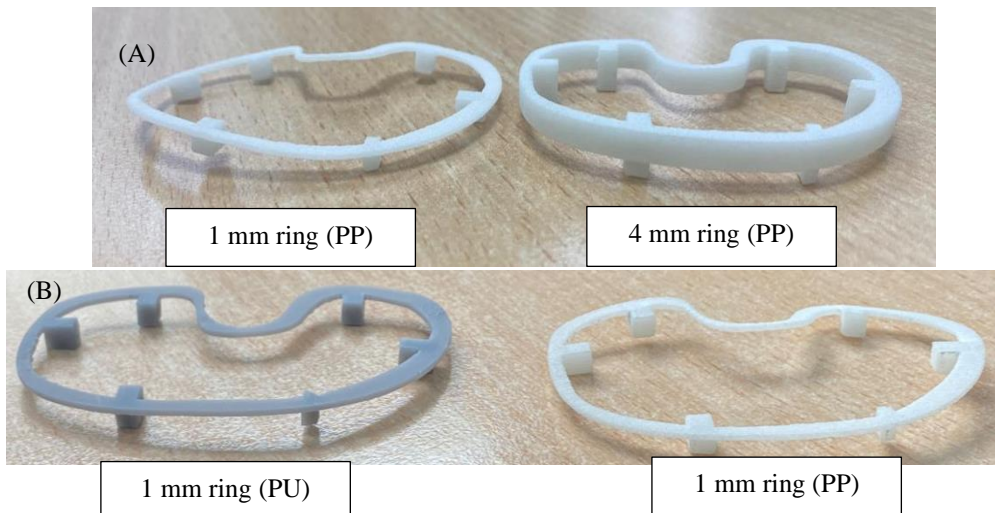
Figure 5.24: Rings (PP and PU) a) 1mm ring (PP) compared to 4mm ring (PP) b) 1mm ring (PU) compared to 1mm ring (PP)

Next, the PU resin was used, and the surface was much smoother than 3D printed PP or stainless steel (Figure 5.25). However, FEA determined that this material

would not be able to withstand a 50 N (5.10 kg) point load near the edges/slits; but did confirm the proper design of the sensor to include the shims (Figure 5.26).

Figure 5.25: PU Sensor a) Zimmer Specific b) Ring (top view) c) Ring (front view)
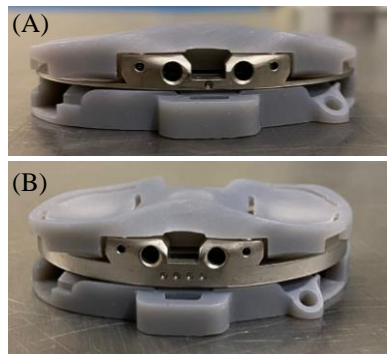
Figure 5.26: Zimmer Specific (PU) (front view) a) 1 mm Shim b) 4mm Shim

Additionally, the base the first design of the Ring sensor did not include attachments needed to secure the ring to the sensor. This was noticed when the PP design was fabricated and amended for the PU.
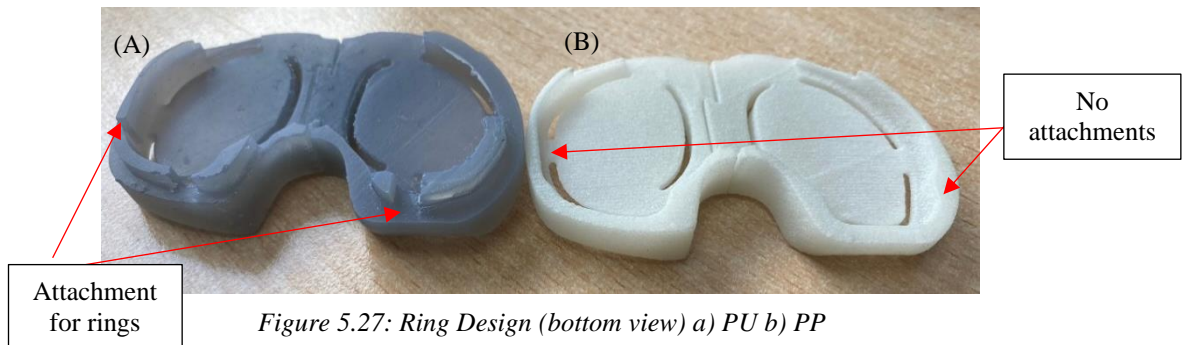
Figure 5.27: Ring Design (bottom view) a) PU b) PP

5.3.2 Computer Numerical Control (CNC)

To investigate the merit of a metal-based transducer, aluminium alloy parts were manufactured using CNC and investigated. Initially, it was found that while using CNC, some of the design details were harder to manufacture, namely the dovetail in the Ring design and the guide bars for the shims on the Zimmer Specific design. Therefore, it was decided that due to a limitation in tooling, the dovetail was omitted; however, it

was added in future designs. The guides for the shim were hand filed in the first prototype and later manufactured separately and attached (Figure 5.29). Additionally, the slits were larger and will be narrower in the final prototype (Figure 5.28).

Figure 5.28: Aluminium CNC Sensor (top view) a) Zimmer Specific b) Ring c) Ring with Dovetail
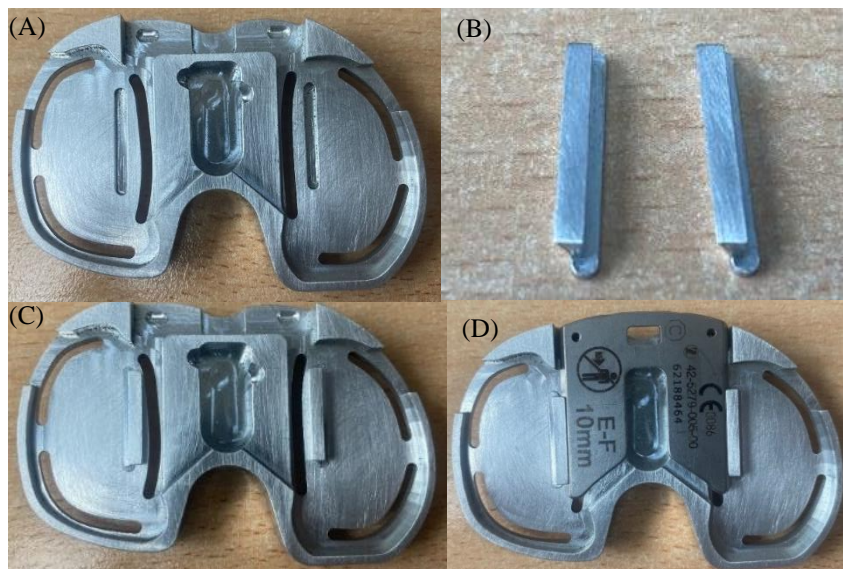
Figure 5.29: Re-design of Shim Inserts for Zimmer Specific design a) Bottom view without guides b) Guides c) Bottom view with guides attached d) Bottom view with guides and shim inserted

5.4   Electronics Design

The design and configuration of the electronics were investigated including the type of sensors used, the circuit, and the PCB design.

5.4.1 Circuit

Transducer Type

Choosing which transducer to use was based on previous literature surrounding knee force sensors, the sensor principles, and compatibility with the physical design of

the sensor. Based on previous literature surrounding knee force sensors a few transducers were considered for this application: metal-bonded strain gauges, piezoresistive strain gauges, and piezoelectric. Nolten et al. (2009) used piezoresistive pressure sensors for their intraoperative load sensor for knee replacements and another research used piezoelectric sensors (Wang et al. 2022), however, piezoelectric sensors were typically used for measuring dynamic pressure. Consequently, to have a good trade-off between sensitivity, robustness, size, and cost, metal-bonded strain gauges were used for this application.

Since these gauges were small and flexible, they can be attached to the surfaces of the sensor where deformation on the surface of the device causes the strain gauges to change resistance. Other researchers measuring intraoperative load in the knee also utilised strain gauges (Kaufman et al. 1996; Skrinskas et al. 2003; Hasenkamp et al. 2013; Forchelet et al. 2014).

For this sensor three 350 Ohm (SGT-1/350-TY11) precision strain gauge transducers were used in each compartment plus the same amount for temperature compensation. This totalled 12 gauges for each sensor. The use of three was necessary in providing the AI with enough data to develop a relationship between the location and magnitude of the load and the electronics based on the size and shape of the tibial insert surface.
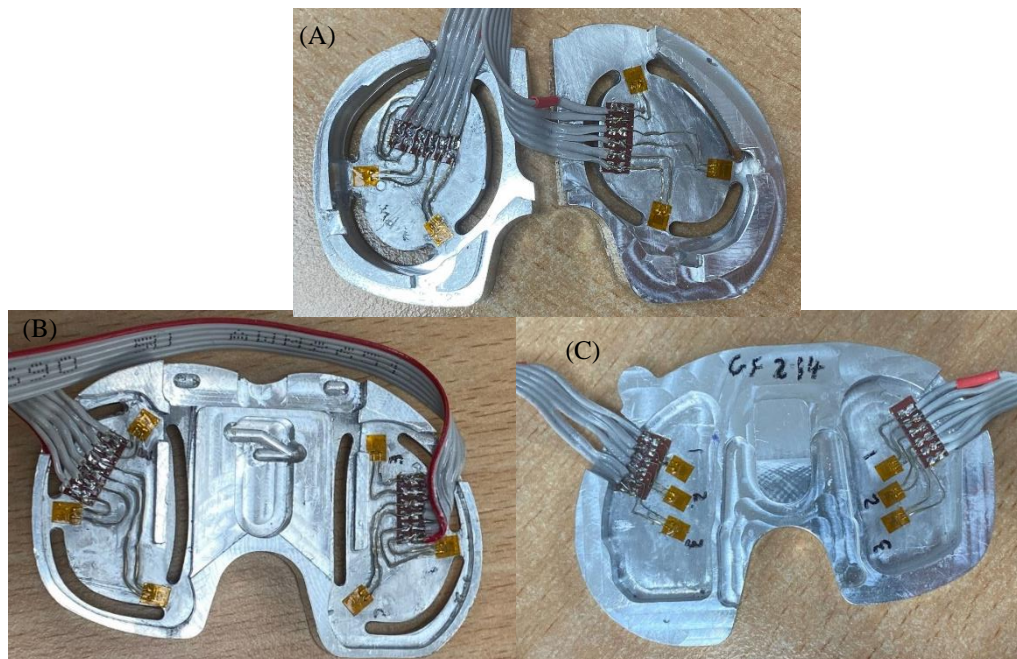
Figure 5.30: Metal-Bonded Strain Gauges a) Ring Design b) Zimmer Specific Design c) Temperature Compensation

Wheatstone bridge:

A Wheatstone bridge was used for this application as it can measure small changes in resistance in electrical circuits from the load applied to the surface. When the load was applied to the device there was a change in resistance of the gauges which caused a change in voltage where the Wheatstone bridge became unbalanced. The half bridge configuration of the Wheatstone bridge was utilised since there was a need to compensate for change in temperature experienced by the strain gauges during training and use of the sensor.

One bridge consists of four resistors arranged in a bridge configuration with a voltage source (5 V) applied. In this application two resistors were replaced with two strain gauges (350 Ω), one that was active and the other that was passive for temperature compensation. The other two resistors were 470 Ω and since they were equal, balanced each other. When referring to Figure 5.31 the unloaded sensor is balanced and the relationship between the resistances is:

$$\frac{R1}{R3} = \frac{R2}{R4}$$
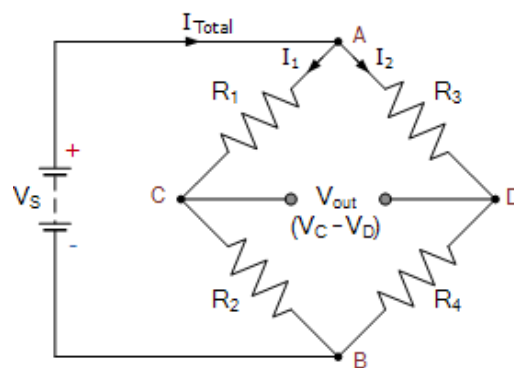
Figure 5.31: Wheatstone Bridge

The Wheatstone bridge configuration was repeated three times for each side. To increase the amount of input data from the sensor there was an option to increase the amount of Wheatstone bridges to 4; however, this also would increase the cost and complexity of the sensor and without any indication that a fourth would be needed.

The output of the Wheatstone bridge was amplified and converted from analogue to digital signal (Load Cell Amplifier (HX711 by SparkFun) and connected to a microcontroller (Teensy 4.1 Microcontroller) expressed by Figure 5.32.
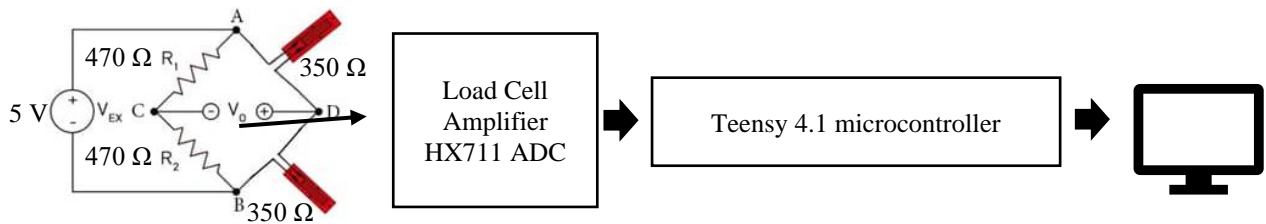
Figure 5.32: Electronics Configuration

5.4.2 Breadboard Prototype

The first prototype was created on a prototyping breadboard with 8 Wheatstone bridge configuration, 2 added as a backup, or for the possible use of an Inertial Measurement Unit (IMU). This board had a lot of wires crossing over in the back which caused noise in the output readings. However, it was an easy and quick way to have a working prototype. The amplifiers chosen were SparkFun's HX711 Load Cell amplifiers which were relatively cheap and had programmable gain options of 32, 64, or 128, where the default gain of 128 remained. These amplifiers were connected to a Teensy 4.1 microcontroller, an opensource microcontroller, which had enough channels for all bridges. In total, these elements, including the strain gauges attached to the sensor, makeup this prototyping breadboard seen in Figure 5.33.
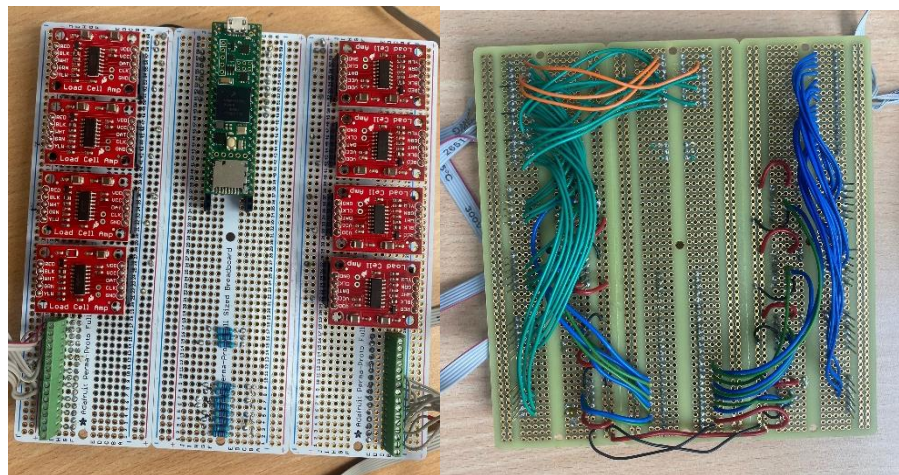
Figure 5.33: Breadboard Prototype

5.4.3 Printed Circuit Board (PCB)

The noise from the wires on the prototyping breadboard were eliminated by using a Printed Circuit Board (PCB). The first design iteration of the PCB used one

77

Wheatstone bridge, (Figure 5.34) which simplified the circuit board and allowed for the investigation of different features. For example, the attachment of the strain gauges to the boards.
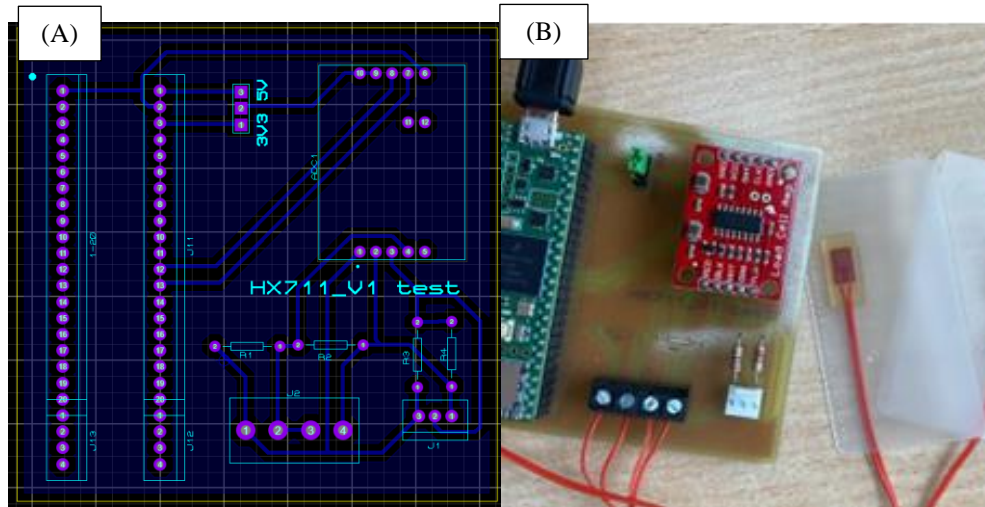
Figure 5.34: PCB 1 a) Simulation b) Assembled PCB

The next version of the PCB was the complete 8 Wheatstone bridge configuration which was assembled and programmed (Figure 5.35). This PCB was created to reduce the noise from the wires and increase the compactness of the electronics.
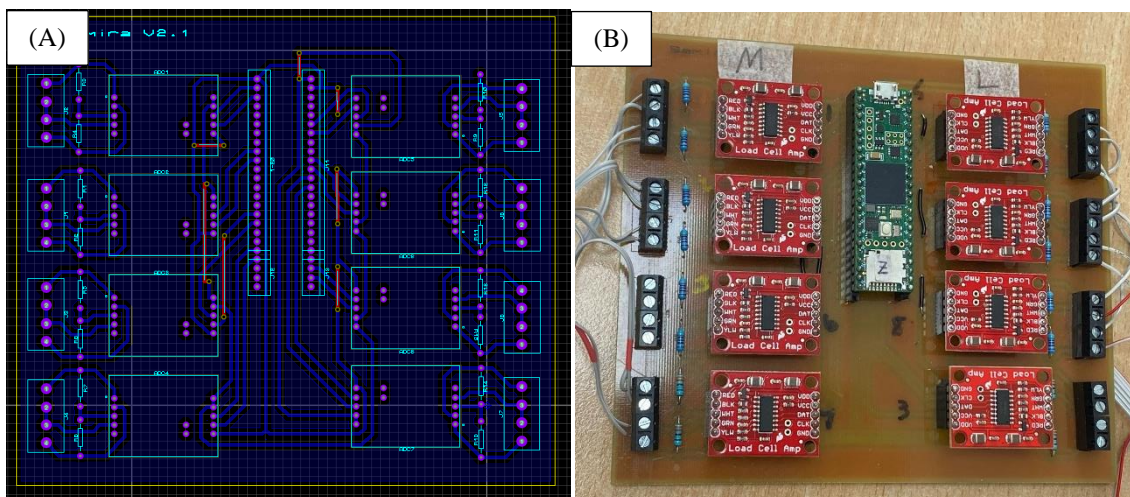
Figure 5.35: PCB 2 a) Simulation b) Assembled PCB

5.5   Full Prototypes

In summation, through CAD iterations, FEA, qualitative observations of fabrication methods, and electronics design, two working prototypes were finally made and trained in the following chapter. This consisted of 2 configurations of the tibial insert (the Ring and the Zimmer Specific) and 6 temperature compensations gauges attached to the same material (aluminium alloy) which could be connected and disconnected from the PCB based on the desired design. The configuration of the devices can be seen in Figure 5.36.
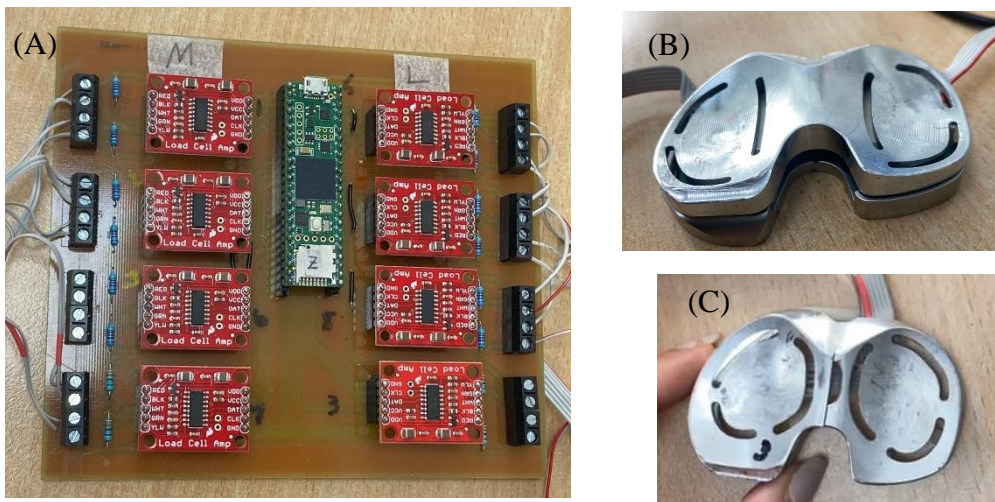
Figure 5.36: Full Prototype a) PCB b) Zimmer Specific Design Tibial Sensor c) Ring Design Tibial Sensor

Chapter 6: Artificial Intelligence (AI)

6.1   Introduction

Machine learning and its subset, deep learning, are types of artificial intelligence (AI) that use computer science and data to enable problem solving in machines. Machine learning typically requires human correction; however, deep learning algorithms improve results through repetition. Deciding which type of AI to use for this application was based on the algorithm's advantages and disadvantages outlined in Table 6.1.

Table 6.1: Artificial Intelligence Algorithms

Type	Use	Advantage	Disadvantage
Machine Learning (ML)	Classification Problems	Can identify trends or patterns	Requires manual feature extraction
Artificial Neural Network (ANN)	Pattern classification, prediction, and control optimisation	Good generalisation and success with nonlinear data	Proper structure requires trial and error
Convolution Neural Network (CNN)	Image processing and object detection	Efficient image processing	High computational requirements
Recurrent Neural Networks (RNN)	Image captioning, time-series analysis, and handwriting recognition	Can process any length of input	Training can be difficult

6.1.1 Reason for AI

This research employed a deep learning algorithm called an Artificial Neural Network (ANN) for its good prediction and generalisation ability with nonlinear data. This feature sets this sensor apart from VERASENSE, eLibra, and other independent load sensors since using AI circumvents the use of triangulation or other mathematical modelling techniques to determine the magnitude of the force and the centre of pressure on a highly non-linear, curved surface. Additionally, a closed form solution does not exist due to the complex geometry of the surface of the tibial sensor. This is an inverse problem with potentially infinite solutions, so to create a unique solution an ANN was adopted based on different introduced load intensities recorded at the tabs. Therefore, the ANN was able to provide a link between the sensor outputs and the applied load and its location which also increases the total sensing area of the surface depicted in Figure 6.1.
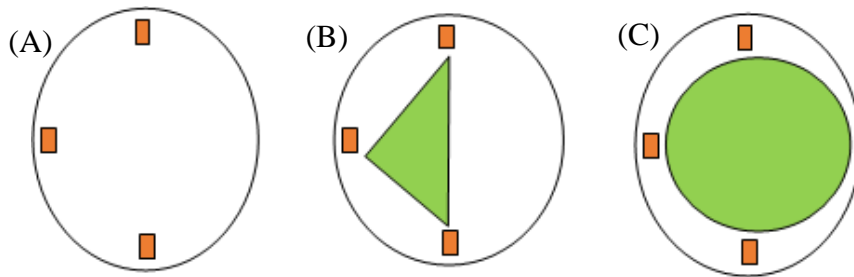
Figure 6.1: a) Strain Gauge Placement b) Sensing Area (Triangulation) c) Sensing Area (AI)

Specifically, for the two designs, Zimmer Specific and Ring, the projected sensing area with and without AI were determined based on the placement of the strain gauges (Figure 6.2). The results indicated at least a 245% increase in sensing area in each compartment for both designs (Table 6.2) when using AI compared to triangulation.
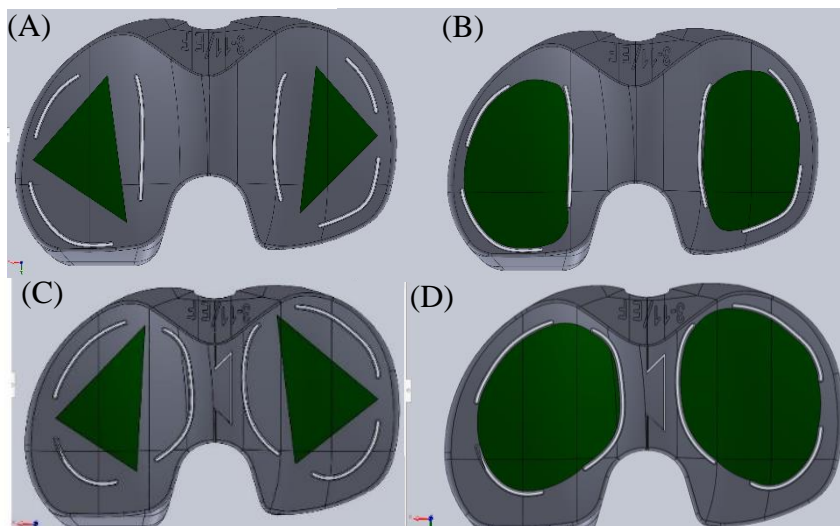
Figure 6.2: Sensing Area a) Zimmer Specific Sensing Area without AI b) Zimmer Specific Sensing Area with AI c) Ring Sensing Area without AI d) Ring Sensing Area with AI

Table 6.2: Sensing Area Increase with AI

	Zimmer Specific		Ring Design	
	Medial	Lateral	Medial	Lateral
Sensing area without AI	218.18 mm^2	175.85 mm^2	222.89 mm^2	245.68 mm^2
Training area with AI	541.25 mm^2	475.05 mm^2	593.76 mm^2	625.99 mm^2
Percent Increase	248%	270%	266%	255%

6.1.2 ANN Background

An ANN operates in a similar manner to the neurons in the brain where ANNs contain nodes consisting of an input layer, hidden layer, and output layer.
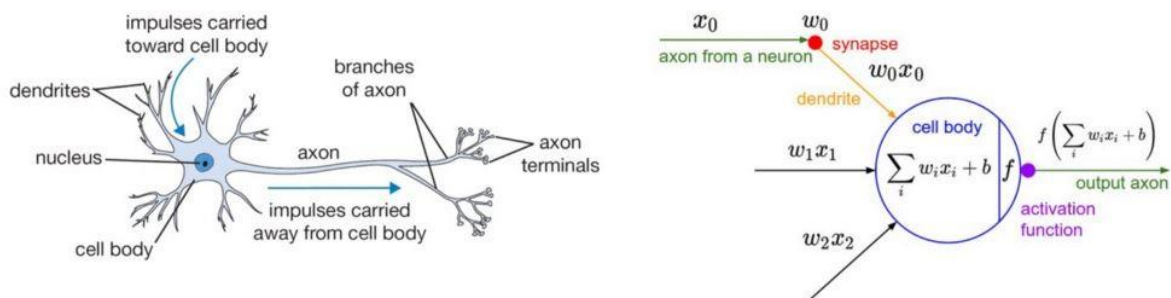
Figure 6.3: ANN Compared to Neuron in Brain

In general, the inputs are weighted and summed and then a bias is added to this sum and passed to the activation function to produce an output. In the absence of any closed form solution between the inputs and outputs, ANNs can be employed due to their ability to recognise and predict patterns from nonlinear data. In this application the ANN would be able to identify new loads and locations from weights and biases found during training. The ANN's ability to predict using nonlinear data, from the strain gauges, meant that the sensor could predict the load and location outside of the sensing area which exhibits highly nonlinear behaviour. ANNs can also generalise well which allows the sensor to respond well to real time data. This means that while introducing new strain readings, the network can use patterns of strain to create a prediction based on what was learned from the training data (Han et al. 2018).

Training the sensor for his application involved using the output from the circuitry of an unbalanced Wheatstone bridge to determine the magnitude of the load being applied and its location. Since this was a prediction problem, the best way to solve this was by using an ANN to predict the load and location based on inputs directly from the change in voltage caused by the load changing the resistance of the strain gauges.

For the first stage, the feedforward stage, of the ANN, weights and biases are chosen randomly initially (Han et al. 2018). The inputs are passed to the hidden layers where a weighted sum, z_j, is computed as follows:

$z_j = \sum_{i=1}^{m} w_{ij}x_i + b_j$; where w_{ij} is the weight between the input node and the hidden node, x_i is the input from the previous layer, and b_j is the bias of the hidden

node; i and j are the node number of the input and hidden layer respectively, m is the number of input features.

This weighted sum has an activation function, f, applied to each hidden layer node represented as:

$a_j = f(z_j)$; which becomes the input to the next layer.

This process is repeated for all hidden layers until reaching the output layer, where the same process is repeated:

$$z_k = \sum_{j=1}^{p} w_{jk} a_j + b_k \text{ and } y_k = f(z_k);$$ where p is the number of nodes in the last hidden layer, w_{jk} is the weight between the previous hidden node and the output node, a_j is the output from the previous hidden node, and b_k is the bias of the output node; j and k is the node number of the hidden and output layer respectively, f is the transfer function, and y_k is the predicted output of the network.

To calculate the error or loss in the system, the predicted output value is compared to the actual value. To increase the accuracy, backpropagation of the ANN was used which computes the error for each output and then backpropagates the error values through the network to adjust network weights according to the error (Munro 2010).
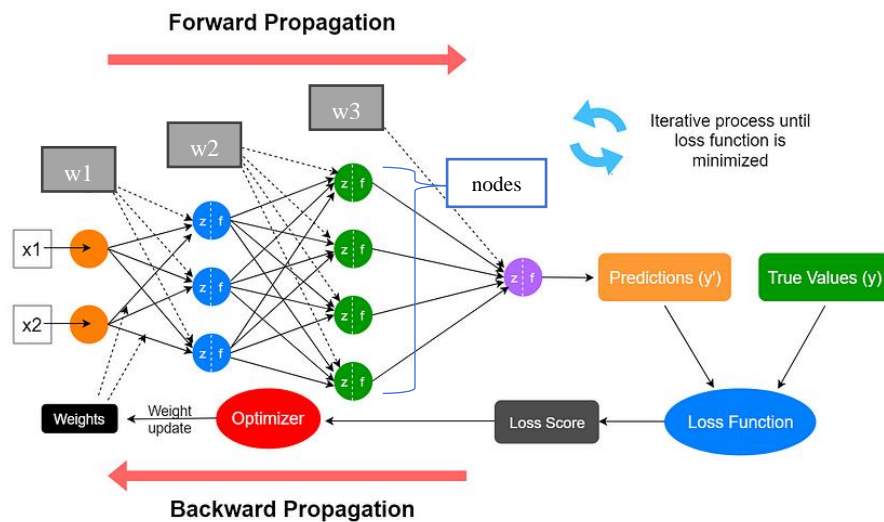
Figure 6.4: Forward Propagation and Backpropagation

Implementing the ANN required many steps including collecting the training data, preprocessing the data, optimising the ANN to identify the optimal weights and biases, and implementing the ANN in real time.

84

6.1.3 Inputs and Outputs

For this application the medial and lateral compartments of each sensor were trained separately. The inputs to each ANN were the 3 voltage readings from the unbalanced Wheatstone bridges. The outputs of each compartment were divided to two ANNs: the loads in kilograms of force (kgf) and the location described by (X,Y) coordinates. This process was repeated for both the medial and lateral compartments of the sensor and for both the Zimmer Specific and Ring designs. Figure 6.5 depicts the inputs and outputs of 2 ANNs for one compartment of one design.
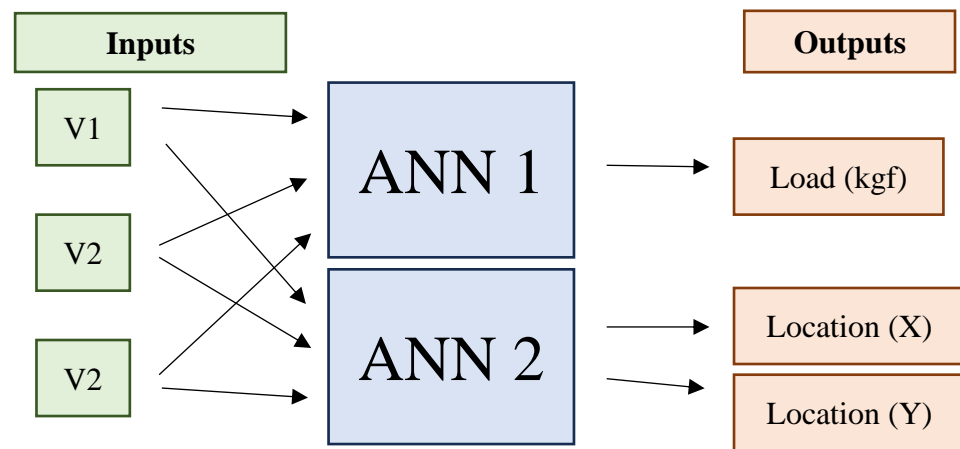
Figure 6.5: Inputs and Outputs of the ANNs for One Compartment

6.2 Collecting Training Data

To train the ANN, known loads in increments were applied at known locations, causing strain at the tabs thus unbalancing the Wheatstone bridge. This change in voltage was recorded for locations which covered the surface of the sensor using a wide range of loads. This was done to train the ANN by uncovering the optimal weights and biases. To collect this data, the type of contact point, the method of applying the load, and how to create the training dataset were discussed.

6.2.1 Contact Point

The type of contact point used to apply the loads was debated. All variations of the flat tip point load were quickly eliminated because of the limited contact surface with the curvature of the sensor and the damage it would cause to the surface at higher

loads. A small ball bearing with a 7.17 mm diameter was ultimately chosen to align with the grid size on the surface of the sensor.
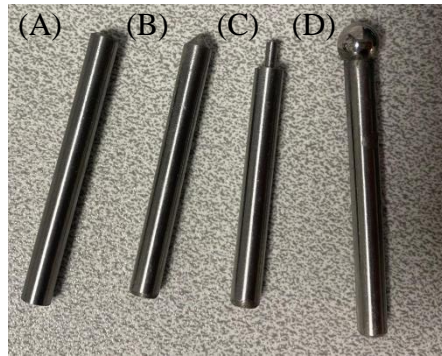
Figure 6.6: Types of Contacts Points to Apply Load a) Rounded Tip b) Flat Point c) Elongated Flat Point d) Ball Bearing (7.17mm)

A ball bearing ensures a normal force was applied to each point in order to create the most realistic and practical loading condition possible which more closely mimics the joint contact forces. Using the ball bearing of this size for training allowed the force to be concentrated on each specific point of the cartesian coordinate grid while also eliminating the effect of contact force mechanics by increasing the distance of the applied load from the gauges so the local deformation remains away from the strain gauges (Figure 6.7).
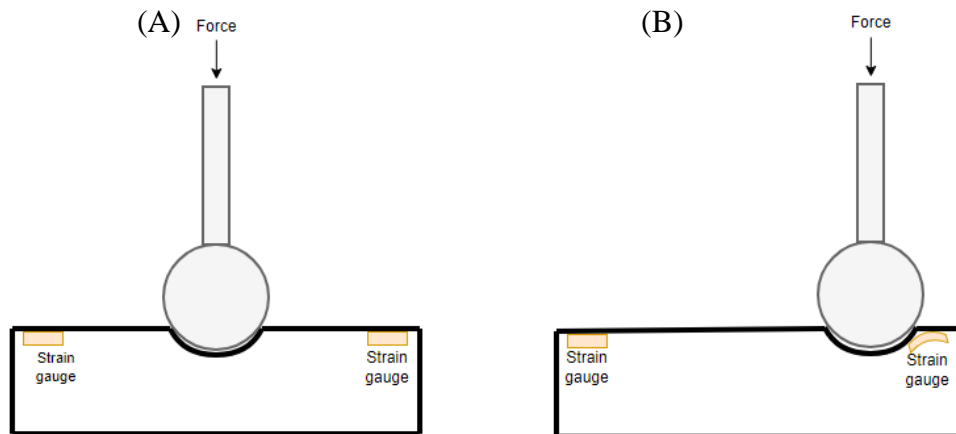
Figure 6.7: Impact of Contact Point on Contact Mechanics

To validate this theory, the same load (5 kgf) was applied to the centre of the Zimmer Specific sensor (Medial compartment (1,2) (Figure 6.12 (b))). This was done with small (5 mm diameter) and a large (10 mm diameter) ball bearing 10 times and then averaged. There was no significant difference ($p>0.05$) between the voltage

readings while changing the contact point (Figure 6.9). The colours represent the gauge locations based on Figure 6.8.
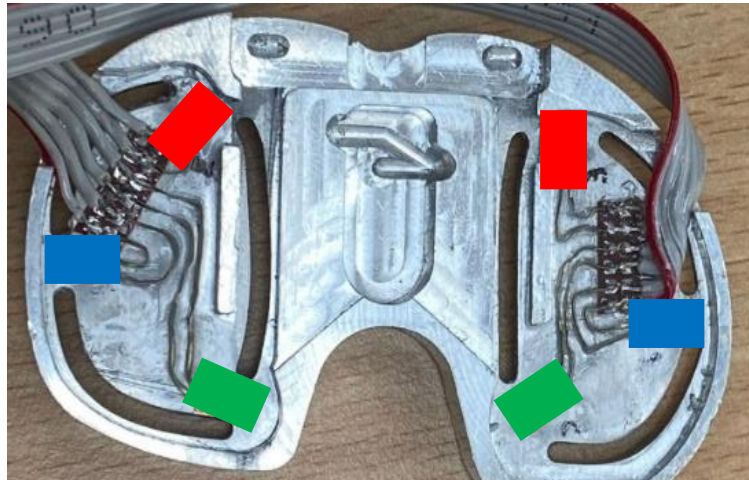
Figure 6.8: Gauge Colour Representations
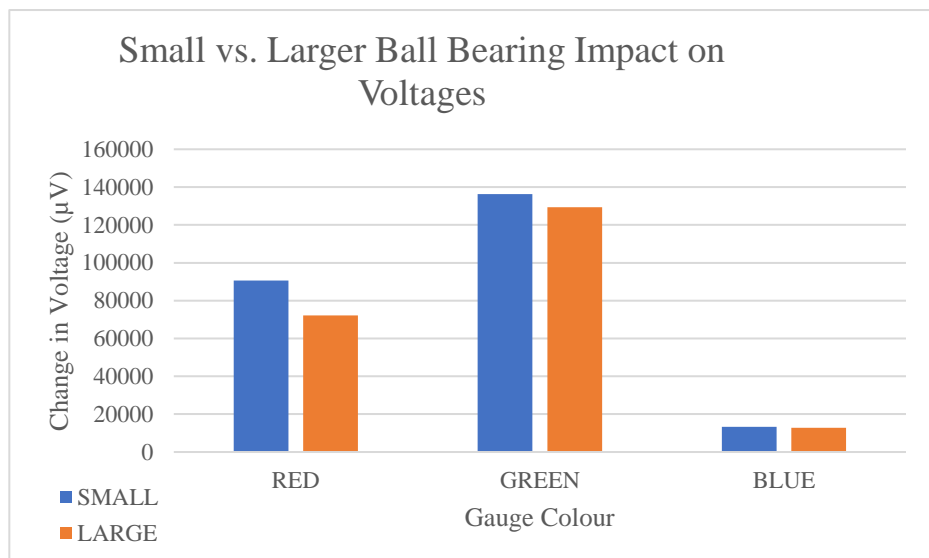
Figure 6.9: Impact of Ball Bearing Size on Output of Wheatstone Bridge

6.2.2 Applying the Loads

The method for applying the loads to the sensor was investigated. A training rig (Figure 6.10) to add known weights to the sensor was used initially. However, this meant only adding smaller loads between a range of 9.8 – 49.0 N (1 – 5 kgf) since higher loads, would cause the rig to slip on the surface of the sensor. However, the larger loads were determined to be necessary to accurately determine the behaviour of the system and improve the resolution.
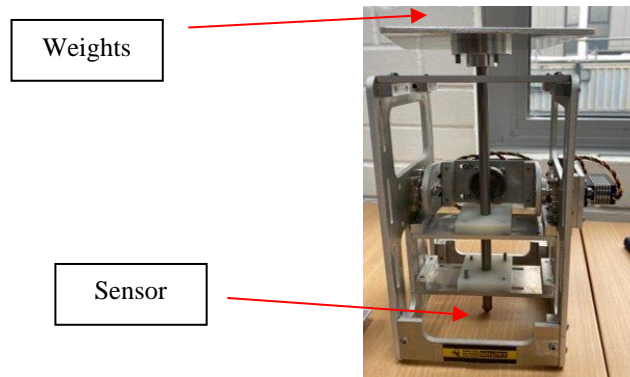
Figure 6.10: Training Rig

Figure 6.11 was the result of increasing loads (0 – 196 N or 0 – 20 kgf) applied to the training point (1,3) on the lateral compartment of the Zimmer Specific sensor. It can be noted that one of the bridges (the blue line from the blue gauge) increased until about halfway, then decreases sharply. If the applied load range was 1 – 5 kgf (0 – 49 N) this behaviour would not be included.
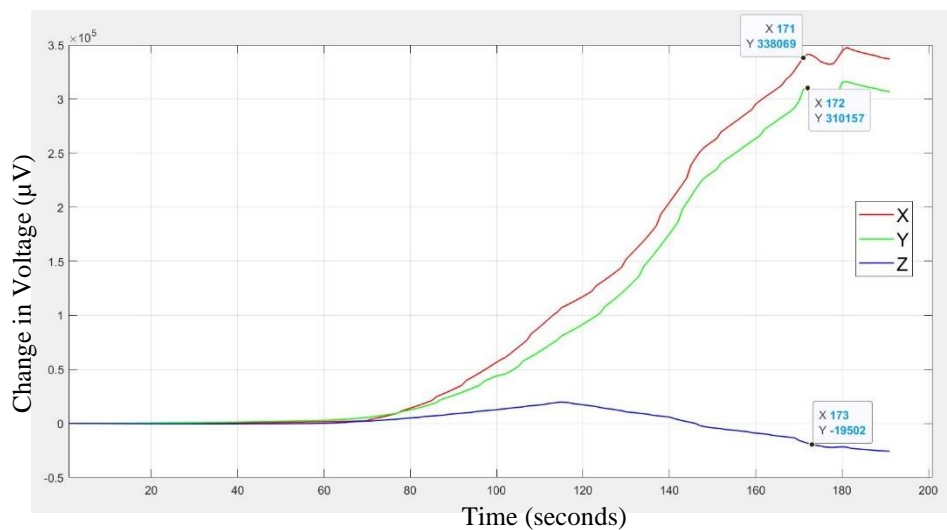
Figure 6.11: Nonlinear behaviour with larger training ranges

A Universal Testing Machine (UTM) by Testometric Micro 350/719 was used instead of the testing rig to apply higher loads at different locations across the whole surface of the sensor. The loads applied were 49 N, 147 N, 244 N (5 kgf, 15 kgf, and 25 kgf).

To increase repeatability, a standardised Cartesian coordinate system was created on the surface of the sensor using a 5 mm grid. These points were used for training and included some points which were out of the triangular sensing area made by the strain

gauges (Figure 6.12). To form to the curvature of the sensors and increase durability and to secure the grid to the sensor, clear tape was added to both sides. In total 27 points were loaded on the Ring design (14-Medial and 13-Lateral) and 29 on the Zimmer Specific design (14-Medial and 15-Lateral) for a total of 43 points on across both sensors.
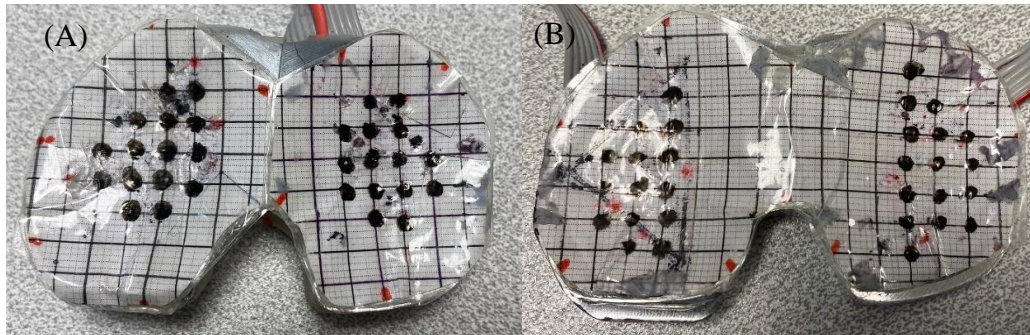
Figure 6.12: Grids Attached to Surface a) Ring b) Zimmer Specific

The UTM was set to compression mode to maintain the load for each desired force at each point while collecting data. The outputs from the applied loads were 3 voltage readings (from each side) from the now unbalanced Wheatstone bridges.
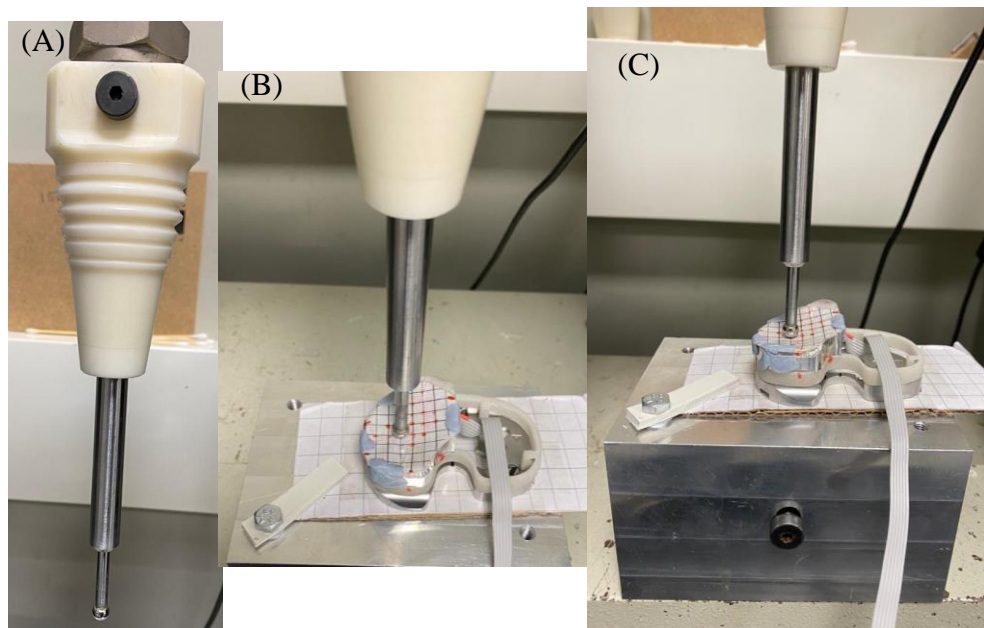
Figure 6.13: Attachment for UTM a) Contact Point b) Ring Design with Load Applied (Top View) c) Ring Design with Load Applied (Font View)

An app was created using MATLAB's App Designer pictured in Figure 6.14 to collect training data. The (X,Y) coordinates were added by the user to the table along with the load applied. First, the device was connected by pressing the "Connect" button,

upon the successful completion of this task a green LED appeared (Figure 6.15), if there was an error connecting the system, a red LED would appear.
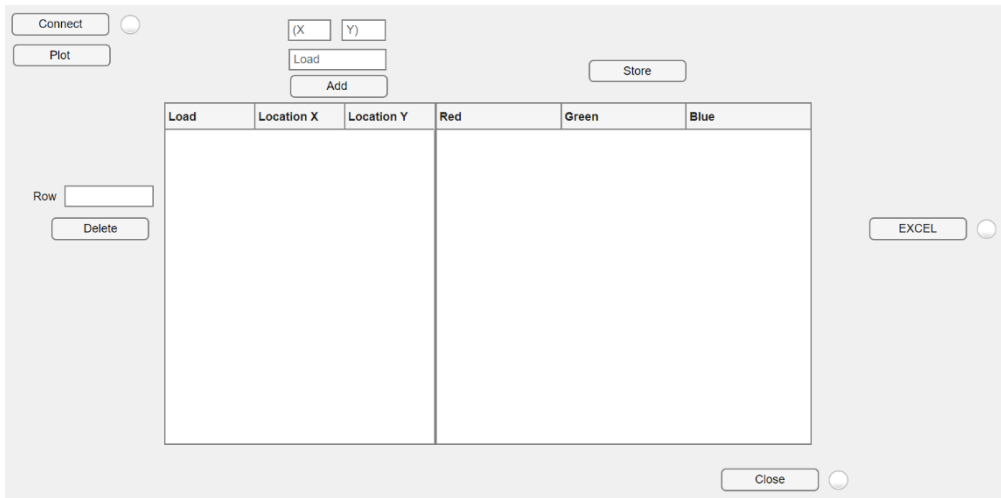
Figure 6.14: App Designed for Training

Then the values from the circuitry were plotted by pressing the "Plot" button where a figure would appear (Figure 6.16). Then the loads were incremented and applied to each point with the UTM. Once the load was applied, the user would wait 5 seconds for the results to stabilise, and the "Store" button was pressed to collect the values from the plot (Figure 6.17) where the values were stored in the table in the app (Figure 6.18).
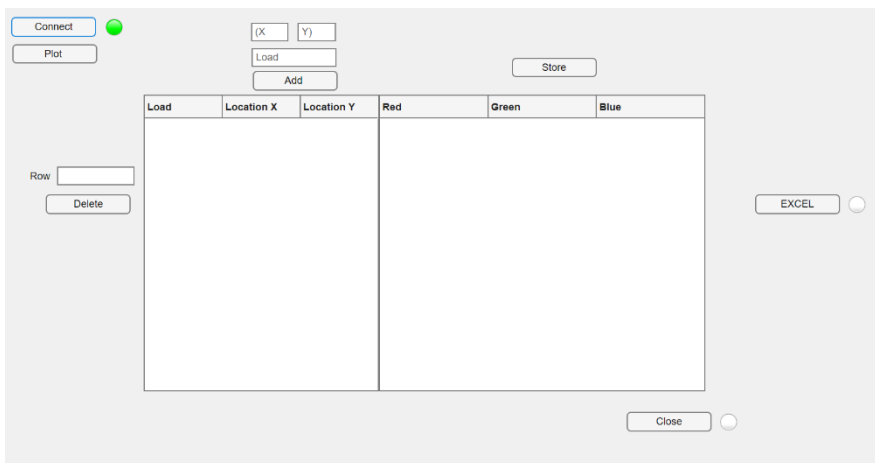
Figure 6.15: SerialPort Connected
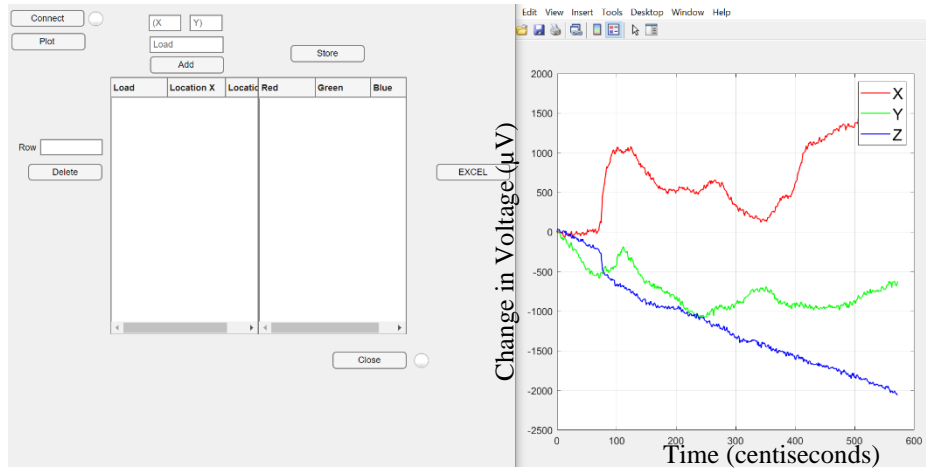
Figure 6.16: App After Plot Button Pressed and Corresponding Plot
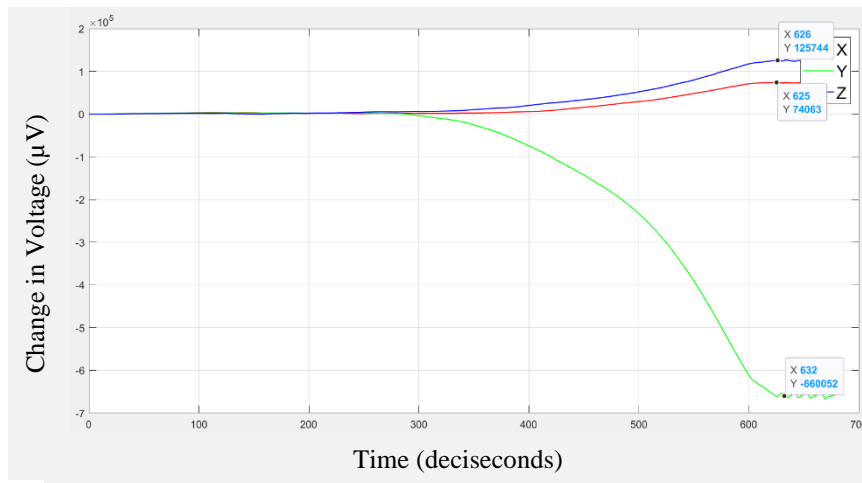
Figure 6.17: Output of Wheatstone Bridge on Point (2,0) on the Medial Compartment of the Ring Design when 20 kgf was Applied

Figure 6.18: Data Stored in Table in App

Following the collection of all the data at each point the table was exported to Excel by pressing the "EXCEL" button and the serial port was closed by pressing the

"Close" button, the success of these two operations were indicated with the green LEDs (Figure 6.19).
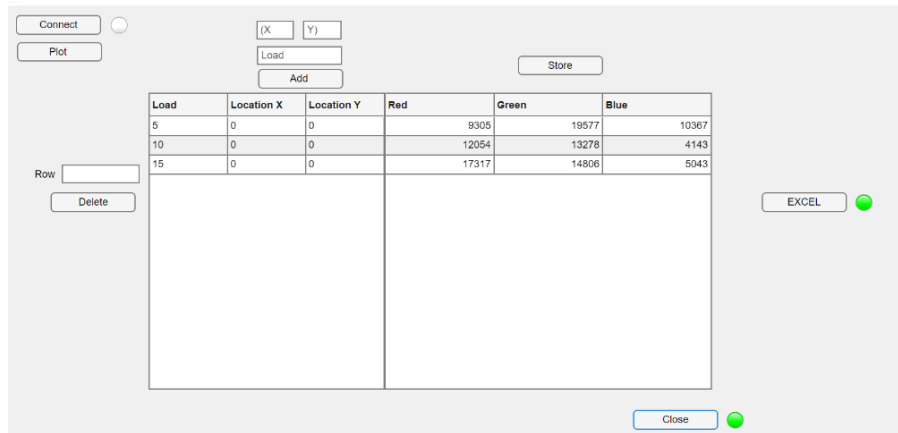
Figure 6.19: Data Exported to Excel and Port Closed

6.2.3 Creating the Training Dataset

To increase the amount, range, and impact of data provided to the network and without having to manually apply the loads, more plots were extrapolated by plotting the behaviour of each point. To have a wide range of load values needed to train the ANN, load values started from 1 kgf (9.81 N) to 51 kgf (500.3 N) in increments of 2 kgf (19.6 N) and were added to the training dataset. Adding the loads in this increment provided the ANN with a lot of training information without greatly increasing the execution time. The change in voltages were taken from the equation of the best fit line of the collected data which can be seen in the example from the medial compartment of the Ring design at point (3,3) (Figure 6.20). Some of the points collected show non-linear behaviour and therefore the best fit line was chosen, mostly a second order polynomial equation. This concluded the process of collecting training data for the device to accommodate for out of boundary load and location predictions.
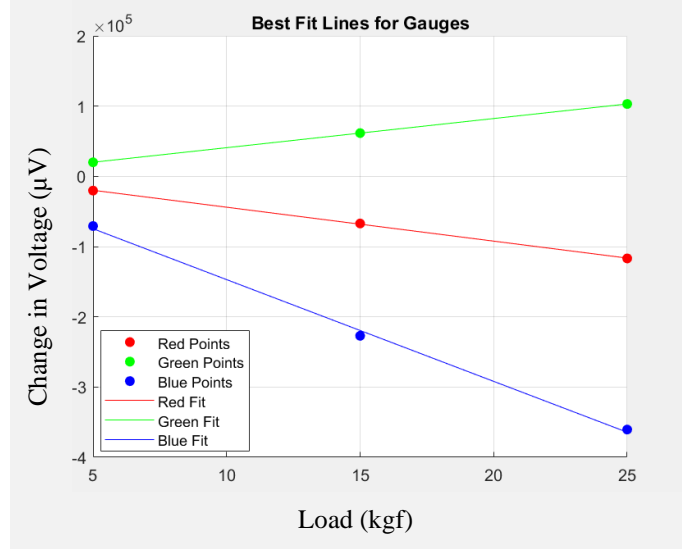
Figure 6.20: Plotted Data at Point (3,3) on Medial Compartment of the Ring Design

Therefore, the training datasets used consisted of the following matrices.

1. Zimmer Specific sensor (Medial Compartment):

Input: $\begin{bmatrix} strain_{1,1} & \cdots & strain_{1,3} \\ \vdots & \ddots & \vdots \\ strain_{364,1} & \cdots & strain_{364,3} \end{bmatrix}$

Output: $\begin{bmatrix} load_{1,1} \\ \vdots \\ load_{364,1} \end{bmatrix} \begin{bmatrix} location_{1,1} & location_{1,2} \\ \vdots & \vdots \\ location_{364,1} & location_{364,2} \end{bmatrix}$

2. Zimmer Specific sensor (Lateral Compartment):

Input: $\begin{bmatrix} strain_{1,1} & \cdots & strain_{1,3} \\ \vdots & \ddots & \vdots \\ strain_{390,1} & \cdots & strain_{390,3} \end{bmatrix}$

Output: $\begin{bmatrix} load_{1,1} \\ \vdots \\ load_{390,1} \end{bmatrix} \begin{bmatrix} location_{1,1} & location_{1,2} \\ \vdots & \vdots \\ location_{390,1} & location_{390,2} \end{bmatrix}$

3. Ring sensor (Medial Compartment):

Input: $\begin{bmatrix} strain_{1,1} & \cdots & strain_{1,3} \\ \vdots & \ddots & \vdots \\ strain_{364,1} & \cdots & strain_{364,3} \end{bmatrix}$

Output: $\begin{bmatrix} load_{1,1} \\ \vdots \\ load_{364,1} \end{bmatrix} \begin{bmatrix} location_{1,1} & location_{1,2} \\ \vdots & \vdots \\ location_{364,1} & location_{364,2} \end{bmatrix}$

4. Ring sensor (Lateral Compartment):

Input: $\begin{bmatrix} strain_{1,1} & \cdots & strain_{1,3} \\ \vdots & \ddots & \vdots \\ strain_{338,1} & \cdots & strain_{338,3} \end{bmatrix}$

Output: $\begin{bmatrix} load_{1,1} \\ \vdots \\ load_{338,1} \end{bmatrix} \begin{bmatrix} location_{1,1} & location_{1,2} \\ \vdots & \vdots \\ location_{338,1} & location_{338,2} \end{bmatrix}$

6.3 Training the ANN

After creating the training dataset, training the ANN involved uncovering the weights and biases to use the trained network with real time data. This process was again repeated for both the medial and lateral compartments of the two sensors: Zimmer Specific and Ring. The process involved preprocessing the data by normalisation and adding noise and then choosing parameters for the network like the transfer function, the number of hidden layers, the training function, and other hyperparameters. This was all done on MATLAB R2022a, using the Deep Learning Toolbox (Beale et al. 2020). Since neural networks are highly dependent on individual training data and the type of problem, the network parameters would need to be individually investigated.

6.3.1 Performance Measurements

The performance of the networks was evaluated by comparing the mean squared error (MSE) and studying the regression plot. The MSE and regression plot were indicators of how the network was performing which was the standard approach and the default method in MATLAB. It is commonly used as the term objective function which should minimised for neural networks (Fiorentini et al. 2022). The MSE is integrated in the backpropagation of neural networks to locate the global minimum and is found using the following formula:

$$MSE = \frac{1}{n}\sum_{i=1}^{n}(e_i)^2 \qquad \text{(Abdul Nasir et al. 2011)}$$

$MSE = mean\ sqaure\ error$

$n = number\ of\ data\ points$

$e_i = vector\ of\ network\ error\ (target\ output - network\ output)$

This is the standard training objective function and used with the following training algorithms: Levenberg-Marquardt backpropagation (LM), and BFGS quasi-Newton backpropagation (BFGS) (Fiorentini et al. 2022).

The Baysian regularization (BR) backpropagation training algorithm uses the MSE as calculated by using the mean square weights (MSW) and the previously calculated MSE creating the following formula:

$$MSW = \frac{1}{n}\sum_{j=1}^{n}(w_j)^2 \qquad \text{(Abdul Nasir et al. 2011)}$$

$n = number\ of\ data\ points$

94

$w_j = vector\ of\ weights$

$$MSE_{br} = \text{MSE}(\beta) + MSW(\alpha)$$

β, α = parameters to be optimsed in the Bayesian framework

This calculation was used in the BR algorithm to optimise the network weights and prevent overfitting as a form of validation instead of partitioning a validation set (Lau et al. 2009; Yue et al. 2011).

Having a low MSE and unacceptable accuracy in real time is an indication that overtraining had occurred. This means the networks learned to respond to the specific data used for training but was unable to predict when new data was introduced indicating the network had poor generalisation.

Visualising the regression plot of the test dataset, which was a built-in function in the Deep Learning Toolbox, provided insight into the accuracy of the network (Figure 6.21). The spread of data along the Y-axis was of interest to indicate the success of the networks since the Y-axis represented the network's prediction where the X-axis represented the actual value. It can be noted that for both the load and location networks, most of these points were concentrated on the dotted line which represents a correct prediction.
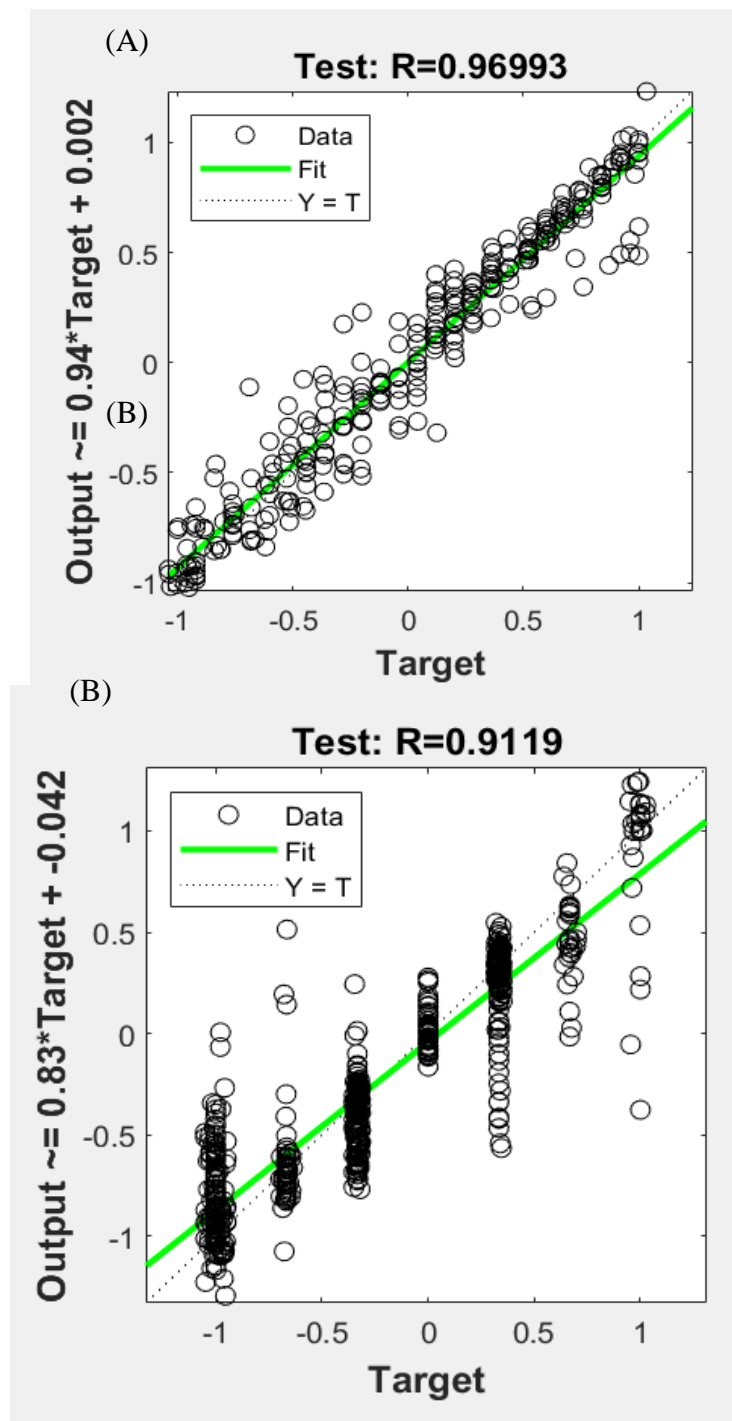
Figure 6.21: Test Dataset Regression Plot a) Load Network b) Location Network

6.3.2 Normalisation

Once the training data was imported as strain, load, and location they were then normalised between the range of [-1,+1] using the MATLAB function "mapminmax".

Normalisation transposes all the variables into the same range, which can improve performance and increase training stability (Godbole et al. 2023). The range of normalisation was chosen to match MATLAB's default activation function which lies in the range of [-1,1] and because the data was normally disturbed with little to no outliers, Figure 6.22 of the Zimmer Specific readings, this range of normalisation was recommended (Godbole et al. 2023).
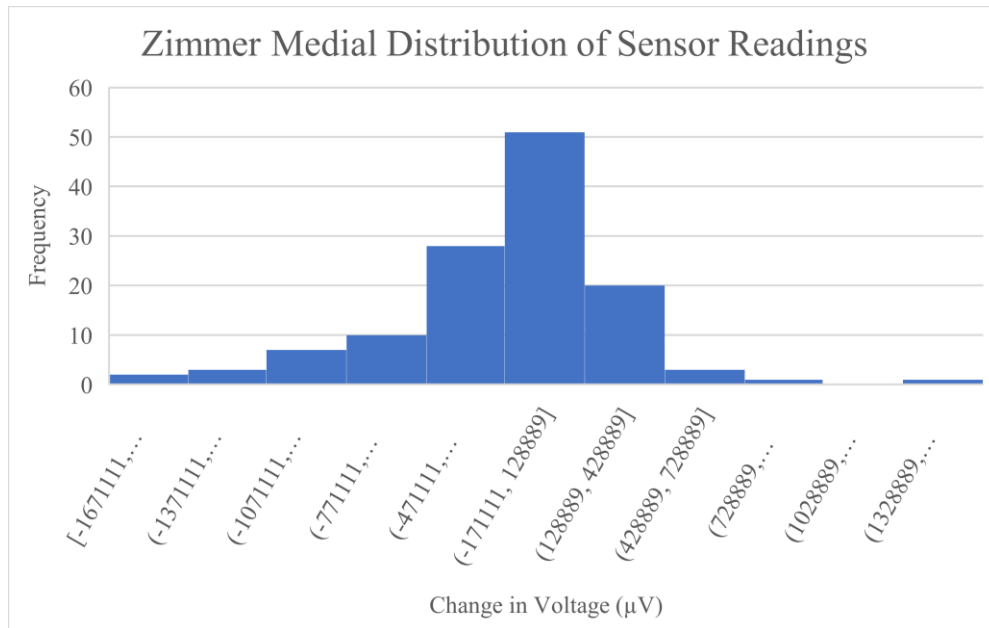
Figure 6.22: Distribution of Data

The original data versus the normalised data can be seen in

Figure 6.23 while

Figure 6.24 combined all the outputs to demonstrate the results on one scale [-1,1].

Original Load vs. Normalised Load

Original Location vs. Normalised Location
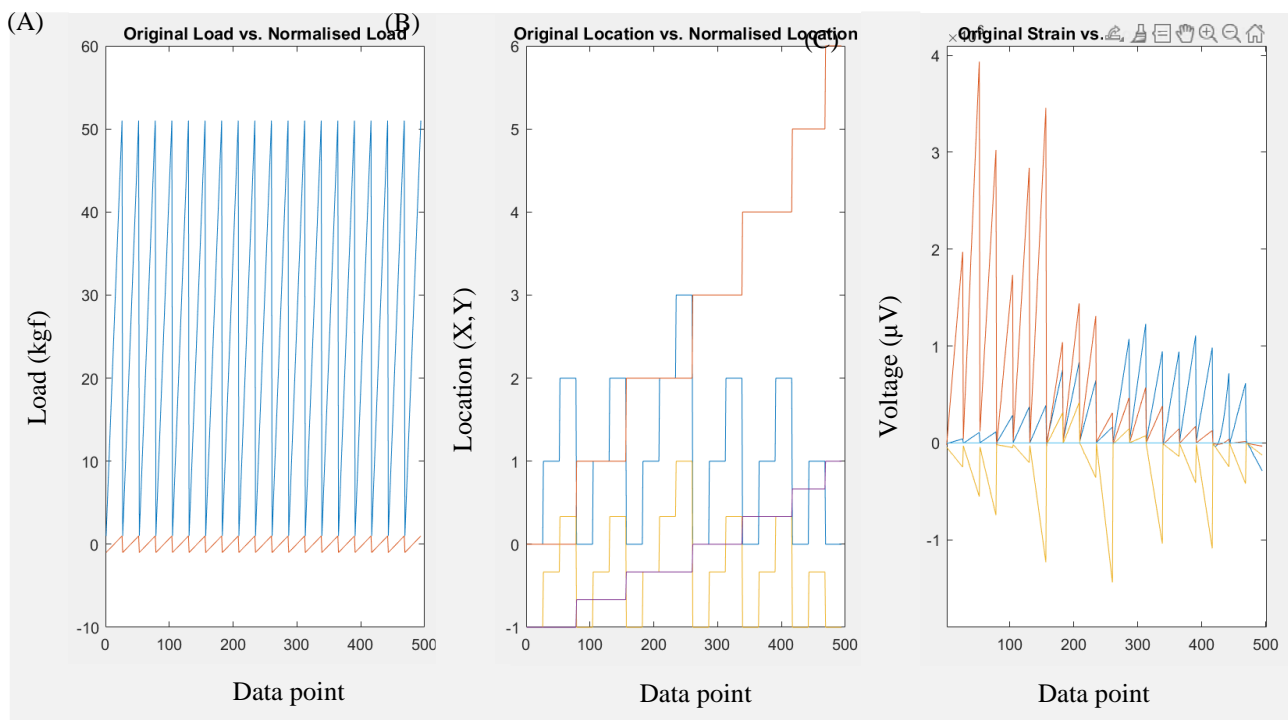
Original Strain vs.

Figure 6.23: Normalised Data versus Original Data a) Load b) Location c) Strain

Normalised Datasets
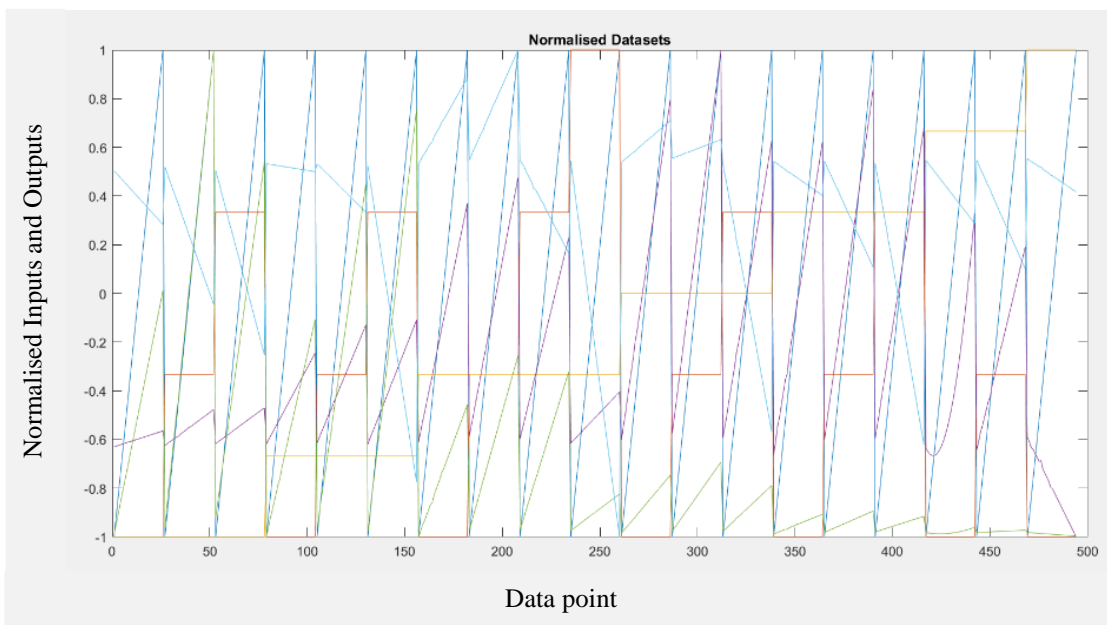
Figure 6.24: All Datasets Normalised

After the variables were normalised, noise was injected into the dataset to help generalise better.

6.3.3 Noise Injection

Noise injection into the training dataset of deep learning algorithms has been a long-standing practice where its importance was demonstrated mathematically by Matsuoka (1992). The success of noise injection includes improved generalisation capabilities and encourages the optimal solution and network convergence with low computational expense (Sietsma and Dow 1988; Matsuoka 1992; Bishop 1995; An 1996).

There were two methods of adding noise which were explored deeper in this section: multiplicative and Gaussian noise, which was a type of additive noise (Figure 6.25 and Table 6.3). Gaussian distributed noise led to a significant increase in accuracy of ANNs in several studies (Xiao et al. 2022; Jiang and Zhang 2023). Wang and Principe (1999) found that adding Gaussian noise moved the convergence of their neural network from the local minimum to the global minimum. Another study used multiplicative and gaussian noise methods at varying levels and found that even small levels of noise significantly reduced the error for both (Isaev and Dolenko 2018). Throughout the literature it was determined that the method of noise injection and the level of noise added was dependent on individual datasets and applications.

Table 6.3: Summary of Noise Types Explored

Categories	Type of Noise	
	Multiplicative	**Additive (Gaussian)**
Common Distribution	Normal or Uniform	Normal
Application	Applied by element-wise multiplication	Added to original data
Frequency	Can change the frequency content, particularly impacting low-amplitude components	Equal distribution of energy across all frequencies
Characterisation of statistical properties	Scaling factor	Mean and standard deviation (SNR)
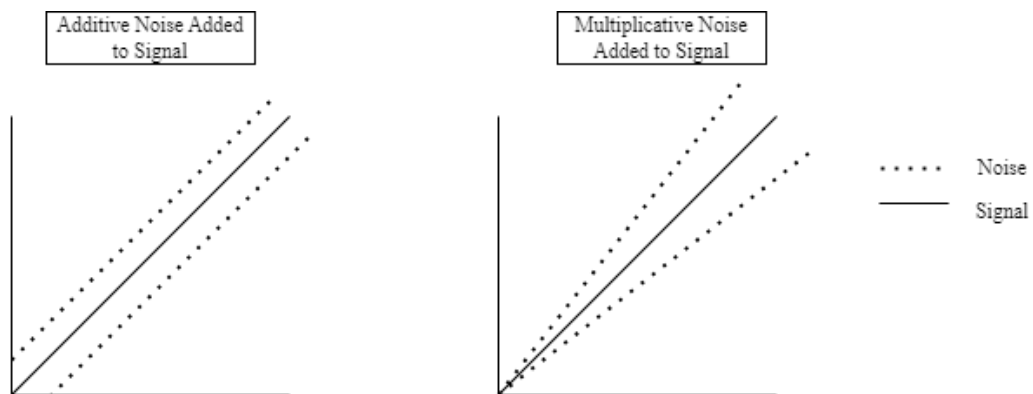
Figure 6.25: Impact of Additive Noise and Multiplicative Noise on Signal

For this application both multiplicative and additive noise methods were chosen since they were most popular methods of adding noise for a variety of deep learning applications over time (Holmstrom and Koistinen 1992; Matsuoka 1992; An 1996; Wang and Principe 1999; Wright et al. 2000; Zur et al. 2009; Isaev and Dolenko 2016, 2018; Xiao et al. 2022; Jiang and Zhang 2023).

Finding the optimal noise for the best generalisation and performance outcomes was dependent on each network and application. Therefore, different methods of generating and applying noise were investigated. The maximum noise range was 20% for the multiplicative noise which was centred around zero (-10% - +10%) of the original data and a range of 10% (-5% - +5%) was also explored. The multiplicative noise was added by randomly generating a number within the selected range to a matrix the size of each dataset and multiplying each element in the dataset by the random noise dataset such that:

```
[rows, columns] = size(dataset);
randomvalues = -0.05 + (0.1*rand(rows, columns));
%rand generates numbers randomly between 0 and 1 (-0.05 centres around 0)
noise=dataset.*randomvalues;
```

For the Gaussian Noise, literature suggests that an optimal signal-to-noise ratio (SNR) was specific to the dataset and different SNRs were compared visually to the multiplicative noise levels to add a similar level. As a result, the two SNRs chosen were 20 decibels (dB) and 30 dB where a higher SNR (dB) indicates less added noise.

The Gaussian noise was added using MATLAB's **"awgn"** (additive white Gaussian noise) function which was described as:

```
 Y = awgn(dataset,SNR)
```

The noise was added to all datasets including strain, load, and location which would then become the inputs and outputs for training the ANN. A histogram of both the multiplicative noise (10%) and Gaussian noise (30 dB) can be seen in in Figure 6.26.
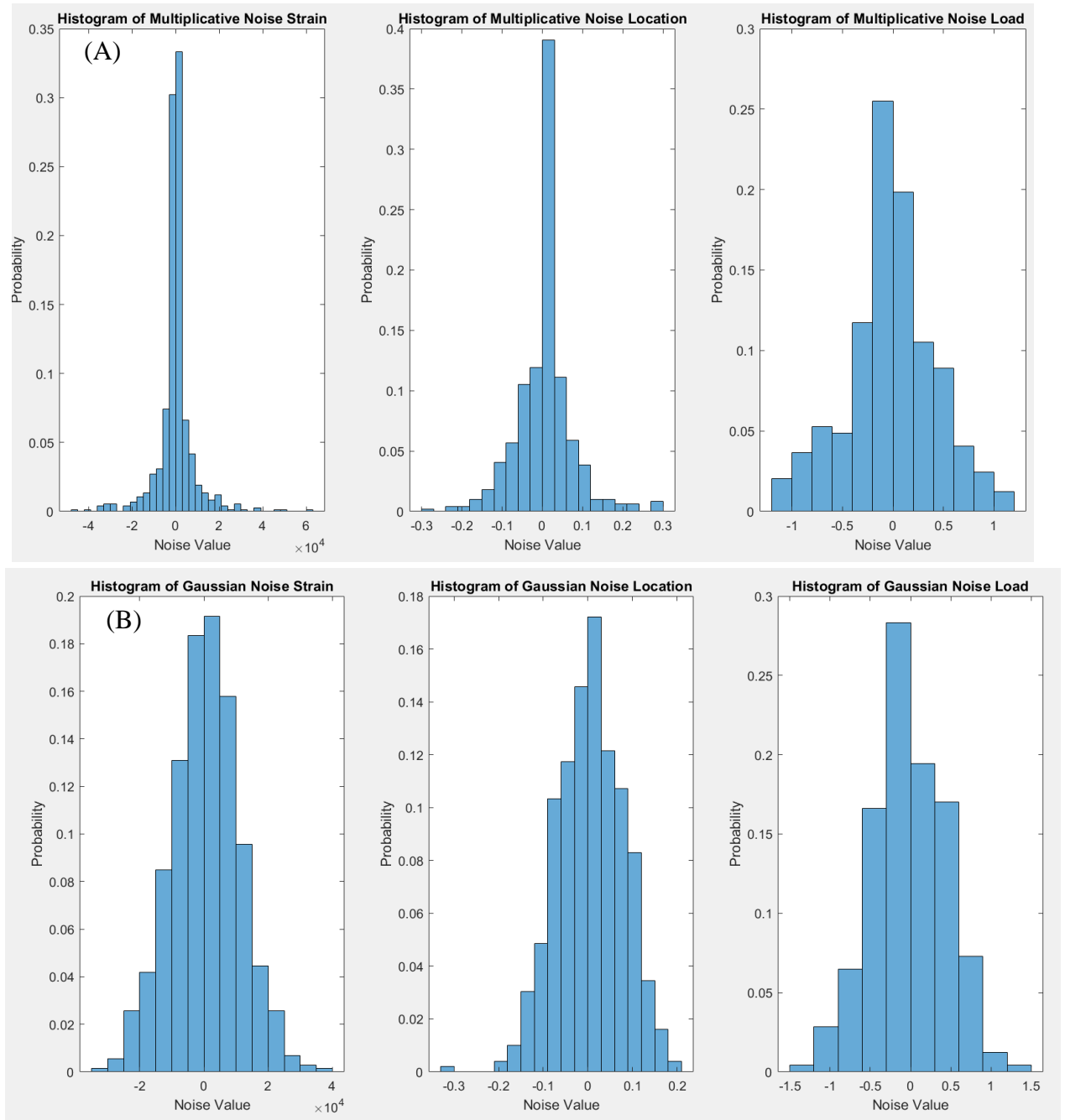
Figure 6.26: Noise Distribution a) Multiplicative Noise (10%) b) Gaussian Noise (30 dB)

The noise was added to the original datasets which doubled the size of the training datasets. To visualize the noise added to the data the noisy data was superimposed to the original which can be seen in Figure 6.27 and Figure 6.28.
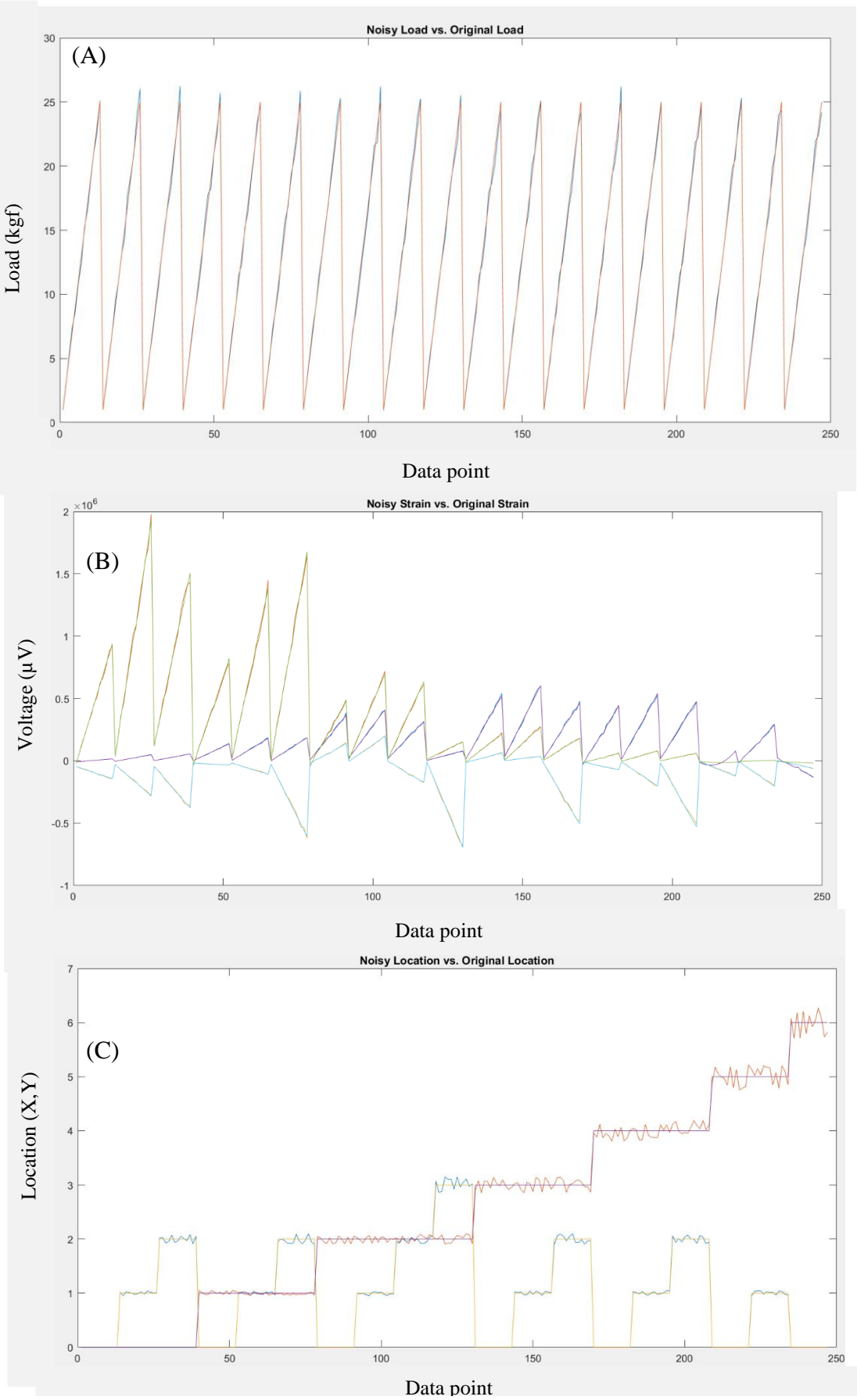
Figure 6.27: Multiplicative (10%) Noisy Data Superimposed onto Original Data a) Load b) Strain c) Location

(A)

(B)

(C)
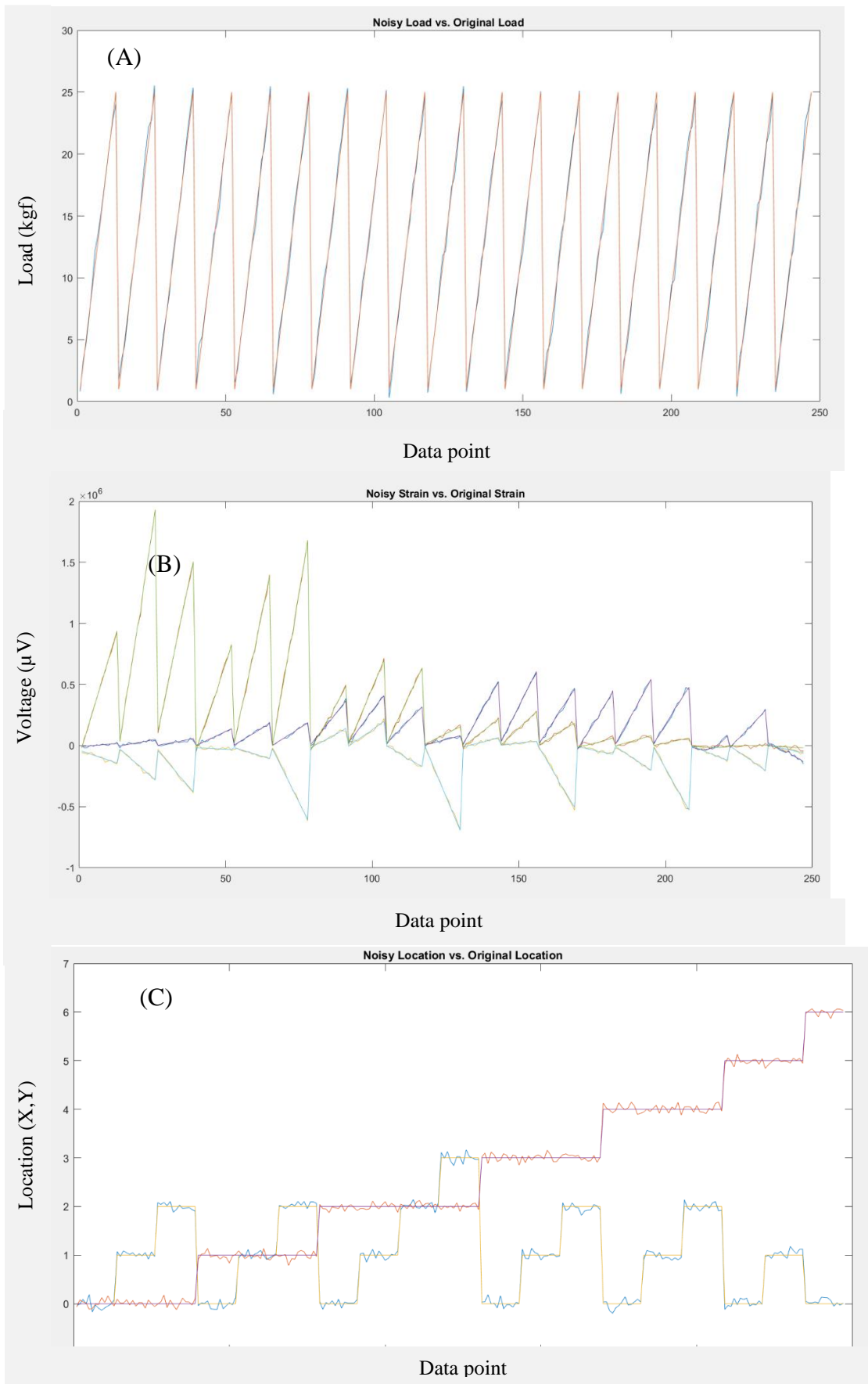
Figure 6.28: Gaussian (30 dB) Noise Superimposed onto Original Data a) Load b) Strain c) Location

To investigate the impact of the noise on the training of the networks the various noises were added to the datasets and two networks were trained: one for the load predictions and another for the location predictions. The ANNs can be seen in Figure 6.29.
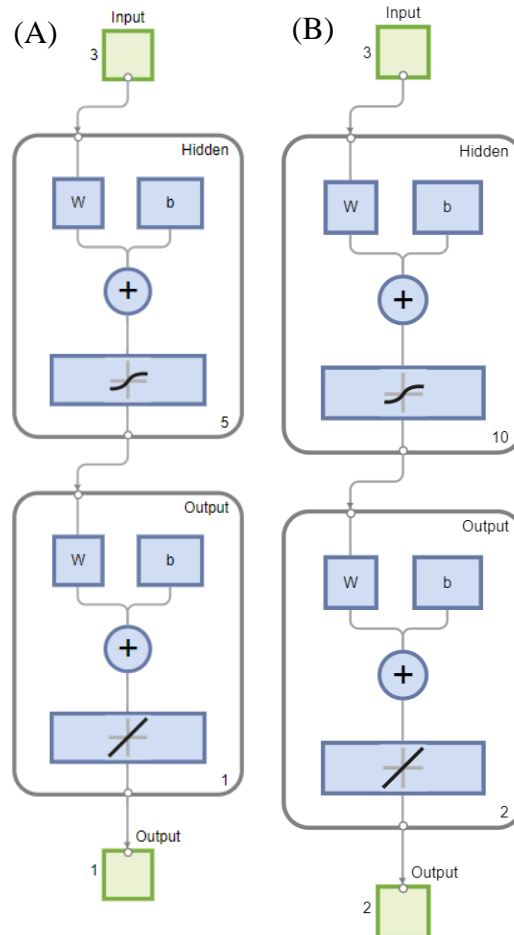
Figure 6.29: ANN Block Diagrams a) Load Network b) Location Network

To assess the impact of the added noises the network parameters were defaulted and left the same for each network. The parameters investigated were the linear regression of the testing dataset and the mean square error (MSE). The dataset was separated randomly each time where 85% of the data was used for training and 15% was used for testing. Each network was trained five times and the MSE and regression of the test dataset was recorded and averaged.

In total, the best performing dataset was recorded when 10% Multiplicative Noise was added, although only significantly better than the 20 dB Gaussian Noise in terms of mean square error (MSE) and linear regression of the test dataset (Figure 6.30) $(p<0.05)$.
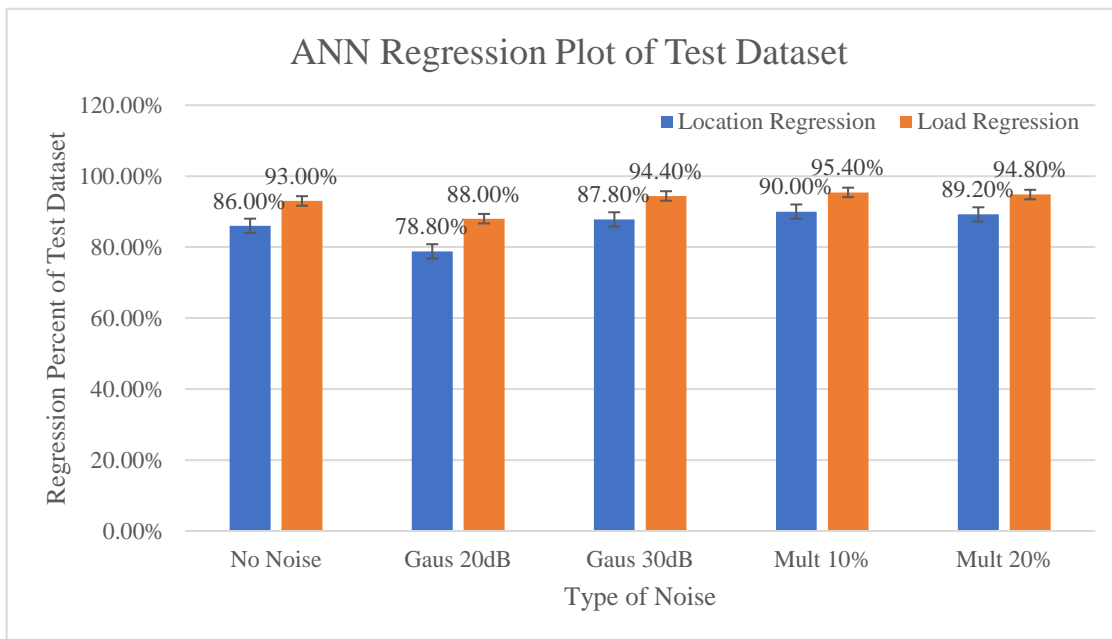
Figure 6.30: Linear Regression Percent for Different Noises Added to the Load and Location Prediction Networks

It was important to note that the linear regression and MSE do not necessarily imply good generalisation abilities and only imply such. However, from this investigation multiplicative noise of 10% was added to all datasets herein.

Next was to design the ANN architecture. The parameters investigated included the number of hidden layers, training functions, division of data, maximum number of epochs, learning rate, performance function, and transfer functions. The proper design should consider the complexity of the problem and the size of the dataset. To determine the best parameters for the network some of these factors were explored here.

6.3.4 Activation and Transfer Functions

In this application, the default hyperbolic tangent sigmoid transfer function was used as activation function with a linear transfer function (Figure 6.31). This allowed the network to learn non-linear relationships between the data by deciding which signals to be passed on to the next layer in the forward propagation stage. The activation function was used between hidden layers while the transfer function was used for the output layer.

106

In hidden layer multilayer networks like this, a tangent sigmoid activation function was typically used (Prasad et al. 2013). Other research using ANNs for contact force predictions found success using this while also using a linear transfer function for the output layer (Choi et al. 2018; Wu and Wang 2021).
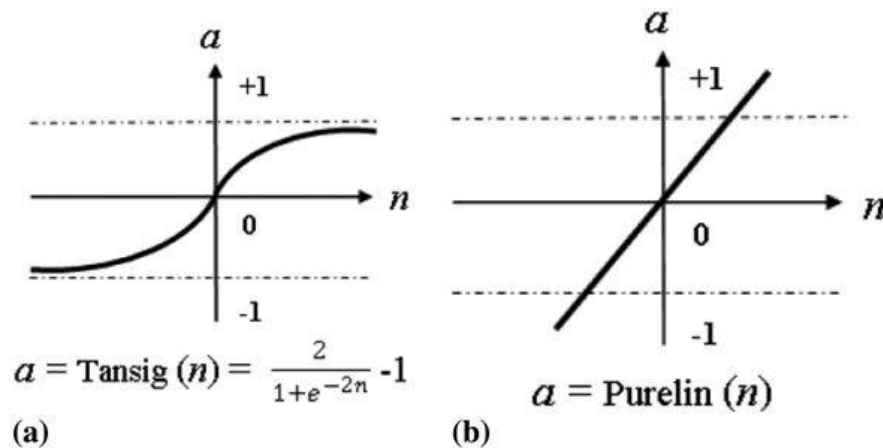
Figure 6.31: a) Activation Function b) Transfer Functions (Hamidian et al. 2019)

6.3.5 Training Algorithm

In general, backpropagation training algorithm in neural networks aim to provide a link between inputs and outputs which are represented by weights and biases. First the training data is propagated through the hidden layers to the output layer. The predicted and actual values are compared, and the error is calculated. Then the error is propagated back through the network and the weight is then adjusted based on this error which is known as backpropagation. This process is repeated until convergence. The method of adjustments made to the weights and biases and calculations of the error function are dependent on the algorithm used.

The three algorithms, built into MATLAB's Deep Learning Toolbox, with the best success in literature were the Levenberg-Marquardt (LM), Bayesian regularisation backpropagation (BR), and Broyden–Fletcher–Goldfarb–Shanno (BFGS) Algorithm.

In a wide variety of applications, including the calibration of a load cell, the LM algorithm was seen to outperform all other algorithms (Nouir et al. 2007; Vasquez 2011; Narayan et al. 2022; Ayaz et al. 2023). The BFGS method was another popular algorithm which outperformed other methods and required fewer iterations to converge (Robitaille et al. 1996).

107

1. Levenberg-Marquardt backpropagation (LM) (`trainlm`)(Beale et al. 2020):

The LM algorithm uses a combination of gradient descent and Newton's methods. In gradient descent the gradient is calculated by finding the loss function/error, or the derivative of the curve, which contains the direction and the magnitude of the steepest increase in the loss function. Therefore, gradient descent updates the weights based on the negative gradient to reduce the loss as quick as possible. This can take a long time to reach a global minimum and for complicated problems, can get stuck local minima. Newton's methods operate by using the second derivative of the loss function, called the Hessian matrix, to find a better training direction.

The LM algorithm avoids computing the Hessian matrix by approximating it using the Jacobian matrix of the first derivates of the network errors with respect to the weights and biases. Then the LM algorithm uses a combination coefficient, μ, to determine whether the approximated Hessian matrix is used or gradient descent. The combination coefficient is decreased after each reduction in performance function and increased when it would result in an increase to the performance function (Gavin 2019). This makes the LM algorithm quick to reach the global minimum. According to research, the LM function was found to be successful when investigating a load prediction problem (Cooper and DiMaio 2018), and the time taken to converge was found to be much quicker when comparing other algorithms (Du and Swamy 2006; Rao and Kumar 2007).

2. Bayesian regularization (BR) backpropagation (`trainbf`) (Beale et al. 2020)

The BR training algorithm occurs within the Levenberg-Marquardt (LM) algorithm but minimises the squared errors and weights simultaneously to control the complexity to prevent overfitting and promote good generalisation qualities (MacKay 1992; Foresee and Hagan 1997). Instead of using the MSE as the performance function, as done in the LM algorithm, the BR algorithm uses the mean square weights (MSW) plus the MSE as a new MSE value as explained in section 6.3.1. Computing the performance in this manner aims to improve generalisation abilities (Doan and Liong 2004; Abu Osman and Wan Abas 2011).

3. BFGS quasi-Newton backpropagation (BFGS) (`trainbfg`) (Beale et al. 2020):

Another algorithm investigated was the BFGS algorithm, where the convergence of this method was generally fast, but it does require more computation in each iteration

and more storage (Rafati and Marica 2020). The basic weight update of this Newton's method was found as a function of the Hessian matrix (second derivatives of the loss function).

Each algorithm was trained and run 10 times from the data collected from the lateral compartment of the Zimmer Specific sensor. The regression of the test dataset was averaged, the results were depicted in Figure 6.32.
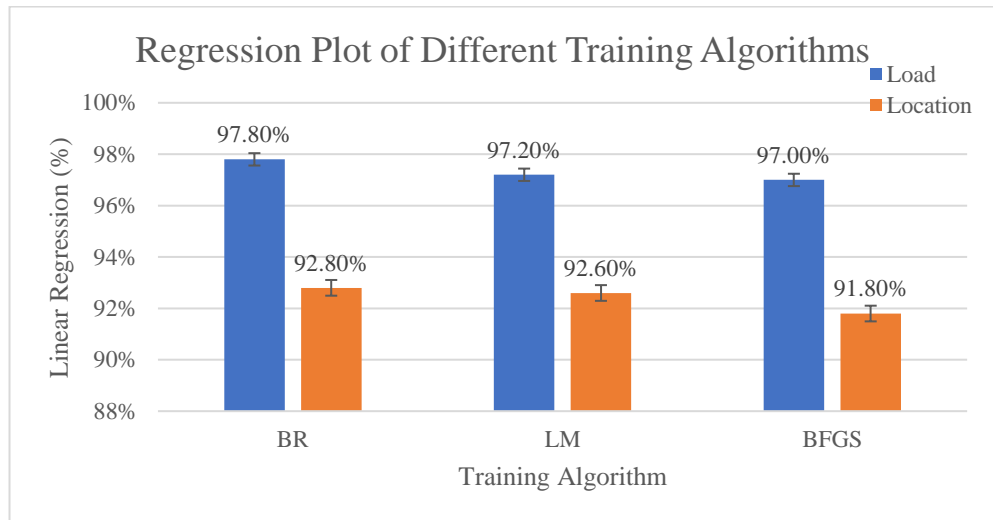
Figure 6.32: Training Algorithm Investigation

There was no significant difference between the three algorithms investigated ($p>0.05$) which could be expected especially since there was little difference in the theory behind the LM and the BR algorithm. However, because of the good generalisation abilities of the BR algorithm, it was ultimately chosen.

6.3.6 Hidden Layers

Choosing the appropriate number of hidden layers was another parameter investigated since too few hidden layers can cause the network to fail to converge to a solution and too many hidden layers increase the training time with the risk of overfitting. Underfitting and overfitting limits a networks ability to perform appropriately with new data.
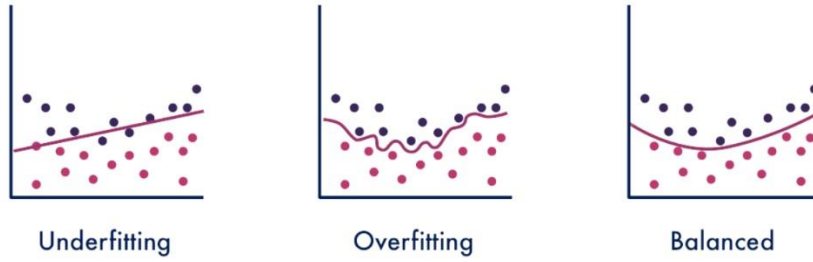
Figure 6.33:Different Classifications of Network Fitting

The number of hidden layers is roughly dependent on the size of the data; however, Mouloodi et al. (2020) found 5 hidden layers to be optimal and Le (2020) used 15. There was no real way to determine the optimal number of hidden layers except through trial and error.

For the datasets in this research, 3,5,10, and 15 hidden layers were investigated for both the location ANN and the load ANN for both sensors. Each hidden layer was run 10 times, and the average was recorded for the Zimmer Specific sensor.
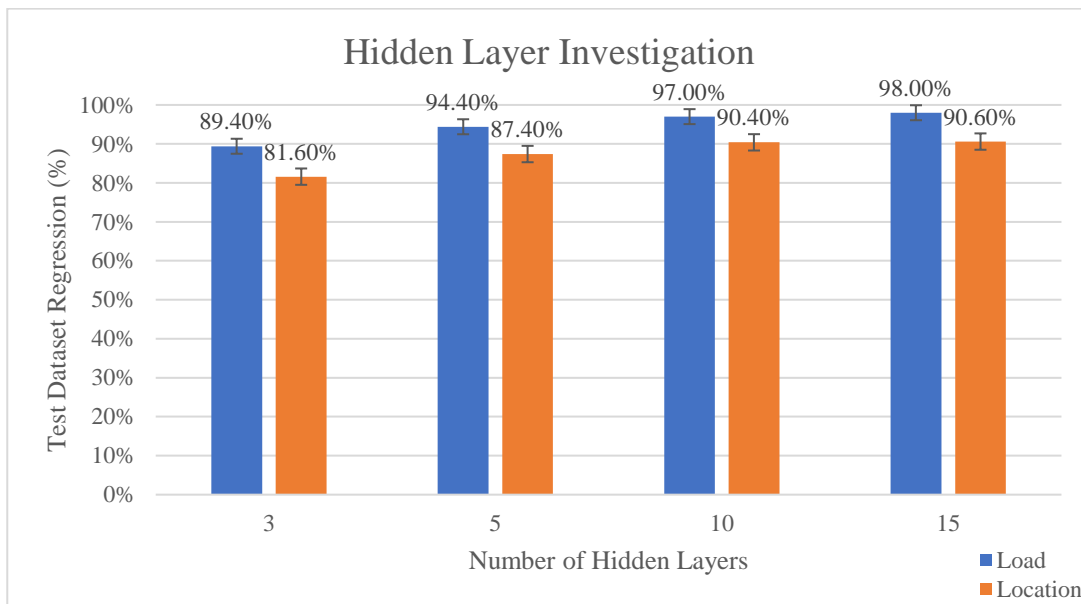
Figure 6.34: Hidden Layers Investigation

The was no significant difference (*p>0.05*) for the MSE and regression plot between any of the hidden layers except 3 and 15 for both the load and location networks. The regression percent for the different hidden layers can be seen in Figure 6.34 and the MSE table can be seen in Table 6.4.

Table 6.4: MSE for Different Hidden Layers (Load and Location Networks)

Hidden Layers	Load (kgf)	Location (mm)
3	0.07	0.12
5	0.04	0.08
10	0.02	0.07
15	0.02	0.07

Since there was little difference in the results from the regression percent and MSE, of the hidden layer investigation, another method of evaluation was introduced. This involved manipulating the training data to create a new testing dataset which had not been introduced to the network during the training of the networks. With the trained networks, 18 different test points were input to the networks, and the bias was calculated as the difference between the actual value and predicted value.

Table 6.5: Bias of Load Predictions (kgf) for Trials 1-18 for a Hidden Layer Investigation

Test No	15 HL	10 HL	5 HL	3 HL
Avg. of 10 trials	-0.01	-0.17	-0.56	-0.44
Sum of 10 trials	-0.12	-3.05	-10.01	-7.92

Table 6.6: Bias of Location Predictions (mm) for Trials 1-18 for a Hidden Layer Investigation

Distance of All Predicted Points from Actual Points (mm)			
Test No	15 HL	10 HL	5 HL	3 HL
Avg. of 10 trials	1.65	1.87	2.98	3.42
Sum of 10 trials	29.75	33.75	53.70	61.63

These results indicated that 15 hidden layers for the load network predicted load values closest to the actual load applied, although not statistically significant ($p>0.05$) when comparing to each of the other 3 hidden layer values. For the location network 15 hidden layers predicted location values closest to the actual points, which was significantly better when comparing the results from 5 and 3 hidden layers ($p<0.05$) but not compared to 10 hidden layers ($p>0.05$). This exercise provided information about the networks ability to generalise with new loads and location, but not with different contact points.

The last method of evaluating the hidden layer involved identifying the ability for the network to generalise with new contact points. Since different implant systems may

be used, even with the same femoral implant, the contact point could be different based on the orientation of the knee and size of the sensor. Therefore, it may be more optimal to have a network that can not only generalise well for new load data, but also with new contact points. As a result, a small ball bearing (7.17 mm diameter), a large ball bearing (19.08 mm diameter), and the inverse, convex shape of the tibial sensor (Figure 6.35) were used to apply a 5 kgf load to the point (2,1) on the lateral compartment of the Zimmer Specific design. This was done to provide an understanding of how the networks would generalise in the clinical setting.

Figure 6.35: Contact Point to Apply Load (Convex Lateral Compartment Shape)

Table 6.7 depicted the average load predictions for 10 trials of each contact point, where 5 hidden layers performed significantly better than any other hidden layer ($p<0.05$). Additionally, the average bias represented the difference between the predicted load value and the actual value in kgf.

Table 6.7: Load Predictions (kgf) for Different Contact Points and Hidden Layer

Contact Point	15HL	10HL	5HL	3HL
Small	5.34	3.53	5.67	8.08
Large	4.01	2.09	5.13	6.66
Whole Surface	2.43	3.90	4.15	4.42
Average Bias	-1.05	-2.10	<u>0.02</u>	1.45

The same process was completed with the location predictions; however, when the load was applied to the whole surface, as with the convex contact point, the exact location was unknown, so it was omitted from the analysis. Table 6.8 described the distance in mm of the predicted point from the actual point. The 5 hidden layers

location network predictions were significantly closer ($p<0.05$) to the actual location of the applied load compared to 10, 5 or 3 hidden layers.

Table 6.8: Distance (mm) of Location Predictions from Actual Location with Different Contact Points

mm	Distance From Actual Point (1,2)			
Contact Points	15HL	10HL	5HL	3HL
Small	2.39	2.97	1.50	4.49
Large	4.09	2.13	1.84	4.77
Average Distance	3.87	2.50	<u>1.77</u>	4.68
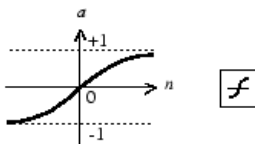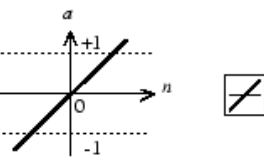
As a result, the number of hidden layers chosen was 5 for both the load and the location networks. This was based on its ability to generalise well for different contact points, which also implied its ability to generalise in various conditions while avoiding overfitting. This process was repeated for each compartment for both the Ring design and the Zimmer Specific design, and similar results were found.

6.3.7 Conclusion

Once the load and location networks were properly trained, they underwent accuracy testing described in the next chapter.

In summation, the training of the Ring design and the Zimmer Specific design used the following parameters and hyperparameters, some of which were the default settings in MATLAB's Deep Learning Toolbox (Table 6.9).

Table 6.9: Summary of Final Network Parameters for Both Sensors

Training Algorithm	Bayesian regularisation backpropagation (BR)
Hidden Layer Activation Function	Hyperbolic Tangent Sigmoid $$Tansig(n) = \frac{2}{1 + e^{-2n}} - 1$$ $a = tansig(n)$ Tan-Sigmoid Transfer Function
Output Layer Transfer Layer	Linear $a = purelin(n)$ Linear Transfer Function

Hidden Layers	5
Learning Rate	0.1
Max no of epoch	1,000
Division of Data:	Training - 85% Testing -15%

The BR algorithm did not use a validation set when it came to the division of data. This was because instead of using a validation set, the BR algorithm stopped based on how many times the dataset improved or not. The LM and BFGS algorithm did use a validation set so when investigating those algorithms, the division was set to 70% training, 15% validation, and 15% testing. The general process of training was summarised in Figure 6.36.
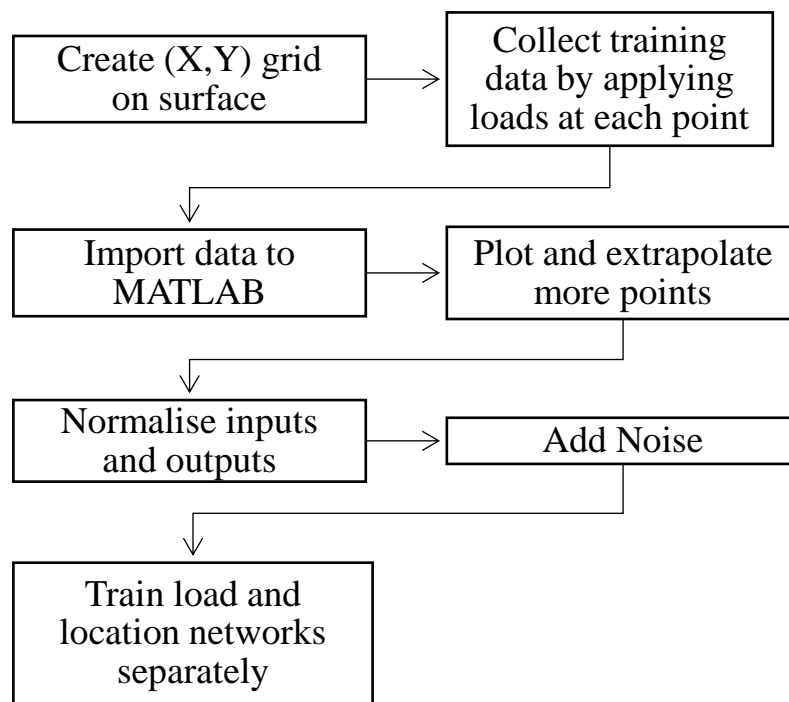
Figure 6.36: Preprocessing and Training

6.4 Graphical User Interface

The next task was designing the graphical user interface (GUI) for the use of the sensor in real time. This involved visualising the load and location predictions in real time in each compartment in a clear and concise manner.

6.4.1 Data acquisition and processing

To start communication between the microcontroller and MATLAB, the serial port was opened. Then five seconds of data was collected and averaged from all 6

gauges (3 medial and 3 lateral). The average was then subtracted from the future real time readings to zero the results.

After this, the zeroed readings were normalised using the parameters from the training dataset before being passed to the networks.

Then, the data was input to the network to make predictions for load and location on each compartment. Since the load and location predictions in the network were normalised, they were then scaled to be understandable to the user. The block diagram depicts what happened to the data collected in real time for one of the sensors.
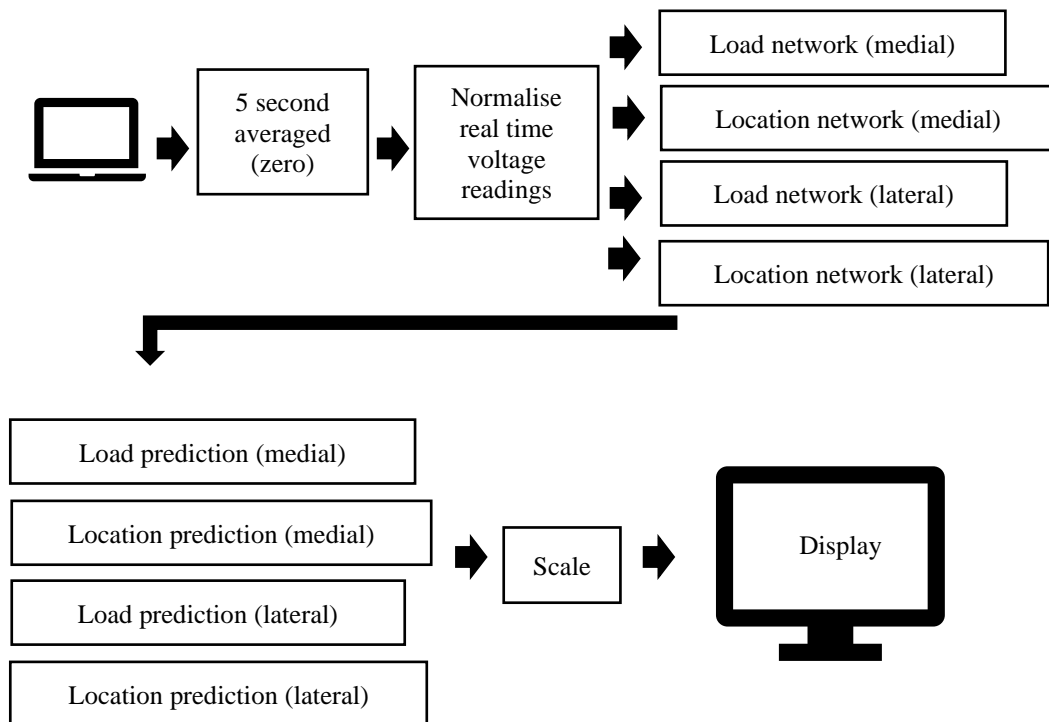
Figure 6.37: Block Diagram of Data Processing

6.4.2 Real time display

Once the data was put through the network and scaled, it was displayed in real time for the surgeon to be able to make informed decisions on the balancing of the knee while in surgery.

The display contained the medial and lateral compartments where the locations were plotted on the coordinate system with the drawing of the tibial insert aligned in the background. The points used for training were plotted on the figure and the actual predicted load was displayed with a larger point on top of the image. The load and

115

location predictions were written in the corners of each compartment to provide the surgeon with the quantifiable data in real time.

Additionally, a button was added to the display to zero the readings whenever needed without having to stop and re-run the code (bottom left). This display can be seen in Figure 6.38.
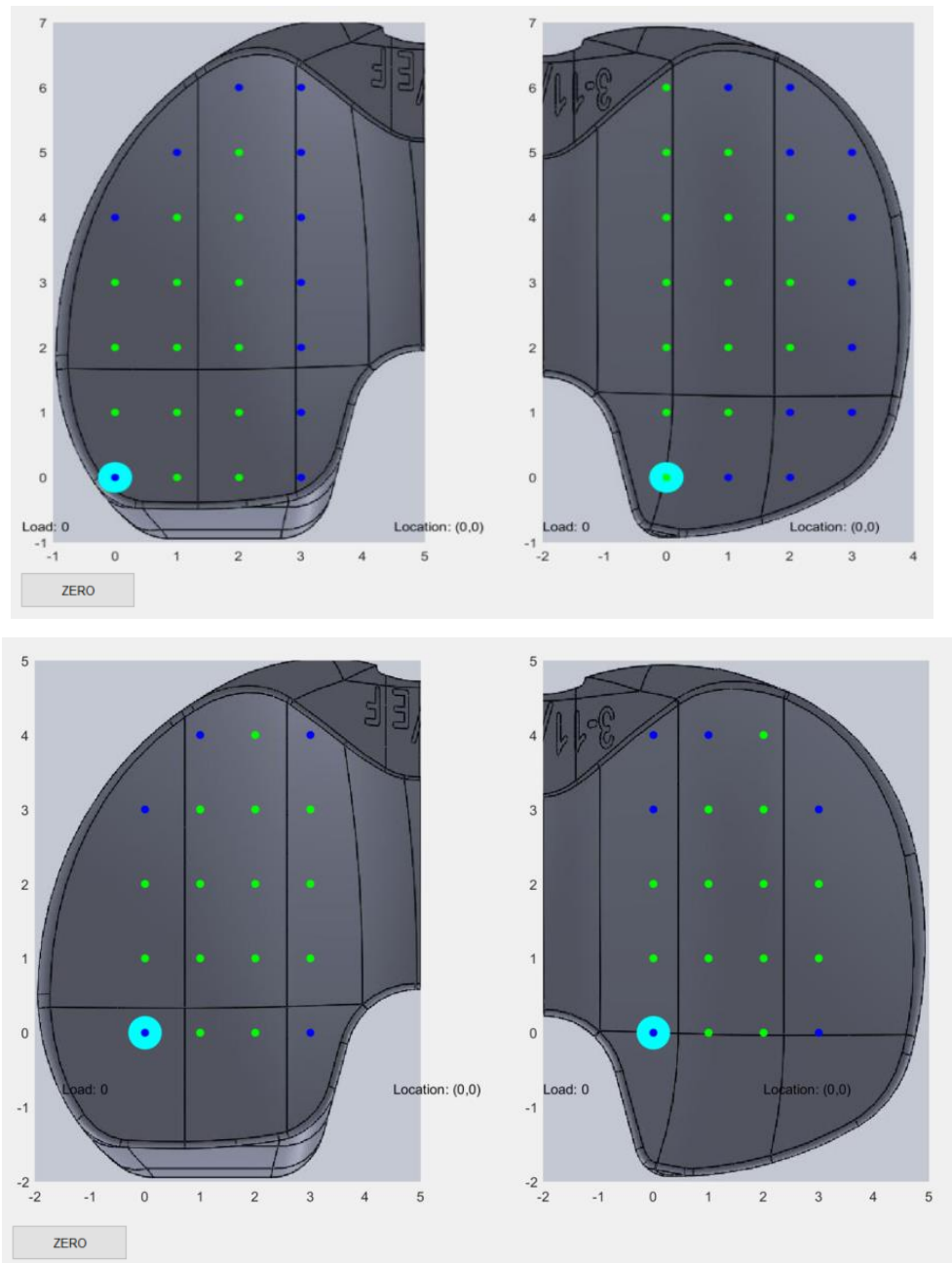
Figure 6.38: Display of Sensor in Real Time a) Zimmer Specific b) Ring Design

Chapter 7: Laboratory Accuracy Testing

7.1   Introduction

The next stage was to test the accuracy and precision of the ANN in predicting the load and location of a variety of new loads at different locations. Across the two sensors and two compartments 15 points were tested.

The aim of this chapter was to investigate the accuracy and precision of the networks in predicting the load and location of the points applied to the sensor. To evaluate the function of the sensor's networks, the testing points aimed to cover the following points:

Location:

1.   Points outside sensing area
2.   Points across the whole surface
3.   Points not included in the training set
4.   Differences in medial/lateral compartments

Load:

1.   Loads outside of the sensing area
2.   Loads not included in the training set
3.   Loads across the whole surface
4.   Difference in medial/lateral compartments

Another aim of this chapter was to investigate the network's ability to generalise with a new contact point and in real time with new data.

7.2   Methodology

For testing, the same UTM was used to apply a known load in newtons (N) to the sensor using a larger (19.08 mm) ball bearing (Figure 7.1). The loads used were 58 N (6 kgf), 117 N (12 kgf) and 235 N (24 kgf) to provide a range of loads not previously introduced to the network as well as a larger ball bearing to increase the contact surface of the applied load. A larger ball bearing was used to more closely replicate the femoral implant which would be used intraoperatively.

Figure 7.1: Contact Points a) Training b) Testing

The medial and lateral compartments of each load sensor were tested individually, where points were chosen to cover the surface of the sensor, including points outside of the triangular sensing area and points which were not included in the training dataset. These points can be seen in Figure 7.2, where a total of 15 points were tested (7- Zimmer Specific and 8-Ring). For both compartments, at each location and for each load applied, 10 trials were performed, and the predicted result values were analysed and displayed in the results section.
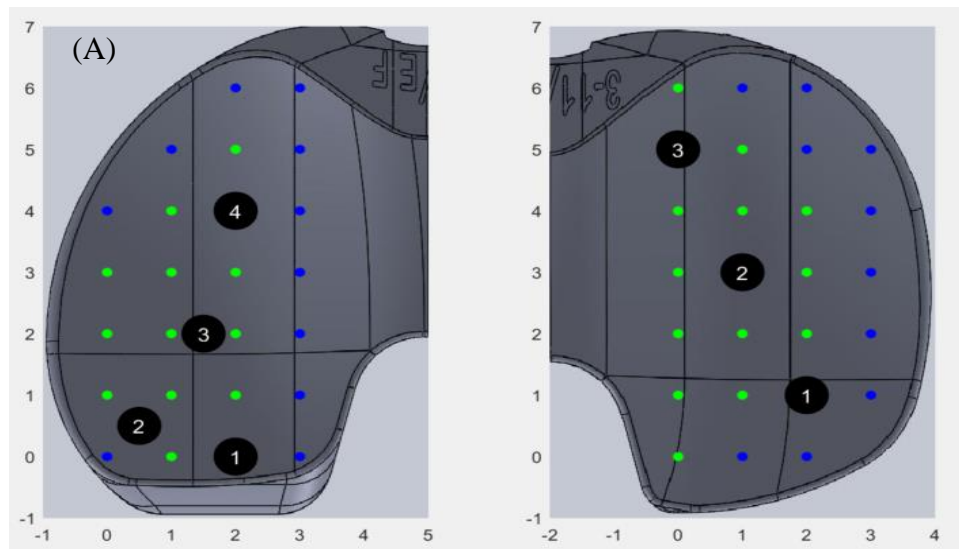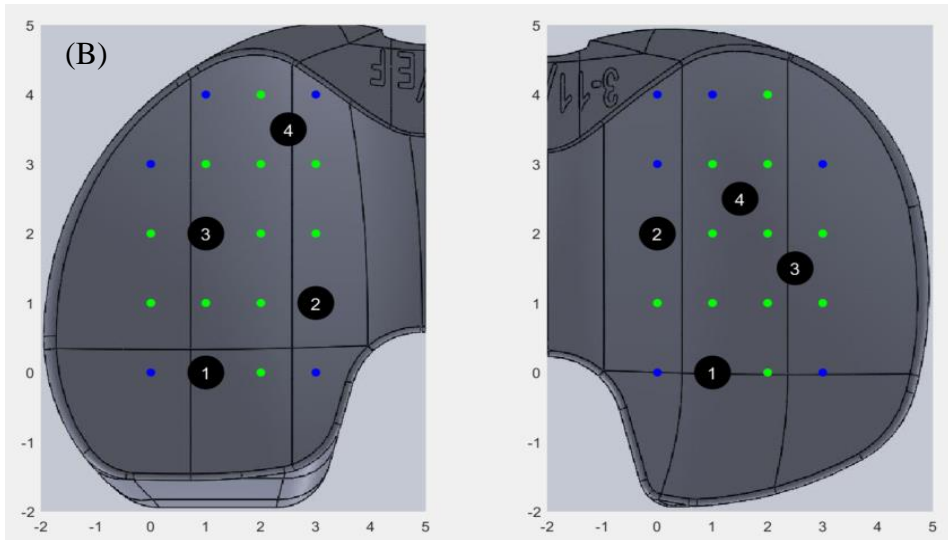
Figure 7.2: Testing Points a) Zimmer Specific b) Ring

7.3 Results

To investigate the aims of this sensor, namely the ability to sense over the whole surface and outside of the sensing area, the testing points were separated based on Figure 7.3. The research questions were compared by finding the biases, the difference between predicted and actual loads (kgf), and the distance (mm) of the predicted points from the actual points to determine the accuracy. Moreover, the precision was represented as the standard deviation to measure random error while the significance level was set to 0.05.
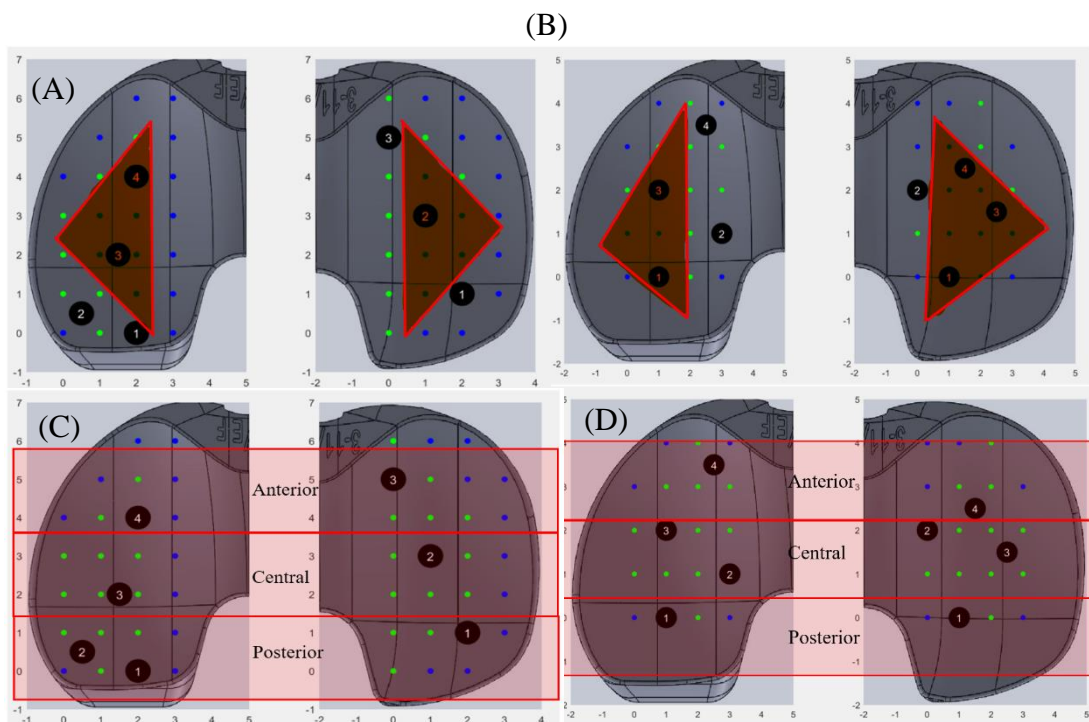
For the Zimmer Specific sensor, the overall average accuracy was about 90% in predicting the applied load and the average distance of the location predictions from the actual location was 5.30 mm ± 1.12 mm for both compartments. For the Ring sensor, the average bias was about 88% in load predictions and the total average error of the location predictions was 4.39 mm ± 1.81 mm (Figure 7.4 and Table 7.1). The measurement of the accuracy aimed to provide insight into systematic errors and included the whole surface of the tibial insert with loads and locations which were not part of the training dataset for the networks.

Table 7.1: Average Accuracy Across All Locations of Each Compartment of Both Sensors

Applied Load	Zimmer Specific		Ring	
	Medial	Lateral	Medial	Lateral
6 kgf	95.17%	95.33%	96.00%	86.67%
12 kgf	93.42%	91.67%	93.50%	99.58%
24 kgf	88.42%	75.67%	80.13%	73.21%
Average	92.33%	87.56%	89.88%	86.49%
Total average	89.94%		88.18%	
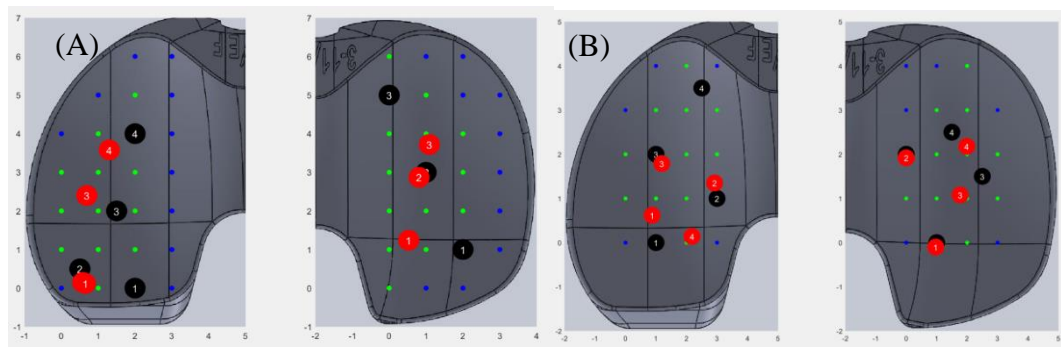
Figure 7.4: Location Predictions vs. Actual Locations a) Zimmer Specific Sensor b) Ring Sensor

The increase in bias of the load predictions at 24 kgf; however, not significant (*p>0.05*), may be a result of difficulty in applying higher loads to the curved geometry as slight slipping might be occurring.

Moreover, when comparing the accuracy of the load and location predictions between both sensors, Zimmer Specific and Ring, there was no significant difference (*p>0.05*).

7.3.1 Sensing Area

Through literature it was found that most of the knee sensors operated using triangulation where the sensing area only occupied a small percentage of the surface of the compartments. Investigating the load and location predictions inside and outside of the sensing area aimed to uncover the impacts of the training methodology for the AI and the use and implementation of the AI in general as compared to the sensors in literature without. To investigate this, the data points were divided based on Figure 7.3 (a and b) and were combined across the two sensors. There was no significant difference between the biases overall for the load predictions (*p>0.05*) in relation to the sensing area; however, there was a significant difference in the location predictions (*p<0.05*). The average accuracy for the load predictions was 94.31% vs. 92.44% for loads inside the sensing area compared to those outside respectively (Figure 7.5). The average distance of the location predictions from the actual location were 3.52 mm vs. 6.91 mm when comparing points inside vs. outside respectively (Figure 7.6).
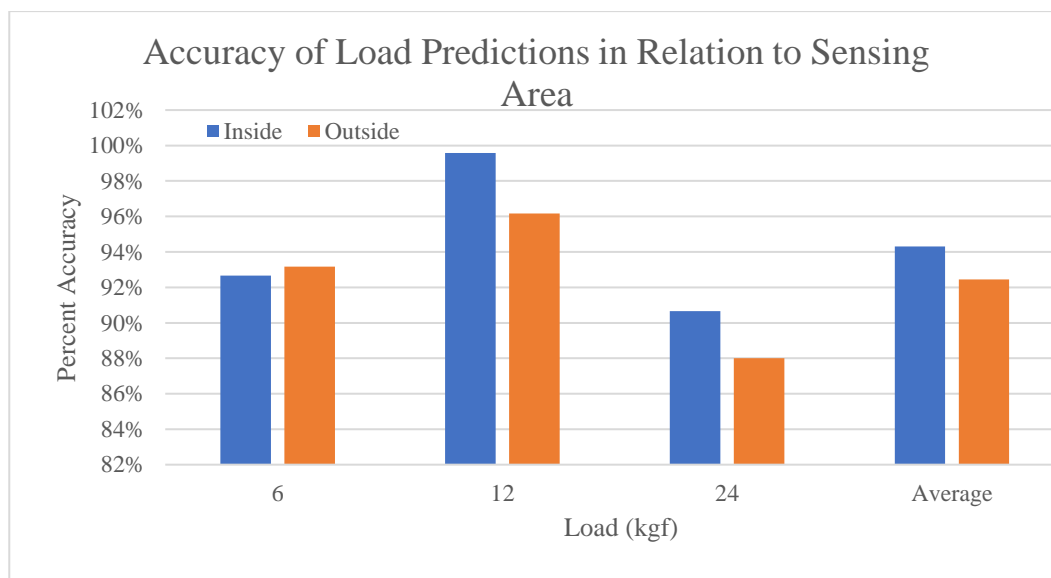
Figure 7.5: Accuracy of Load Predictions Inside versus Outside of Sensing Area for Each Load Applied
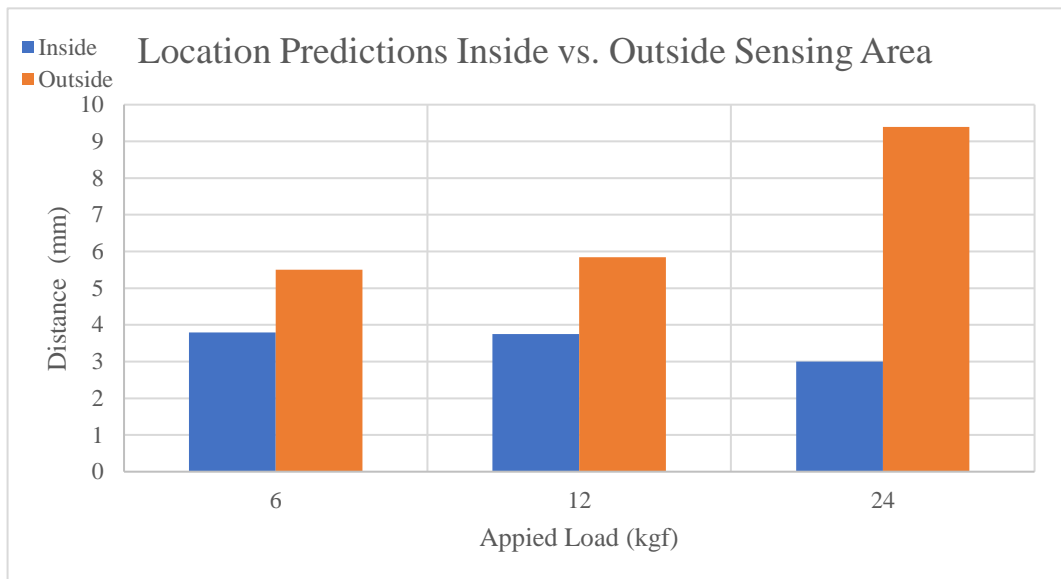
Figure 7.6: Average Distance of Location Predictions Inside versus Outside of Sensing Area for Each Load Applied

Investigating Location Prediction Errors Specifically in Predictions Outside Sensing Area

Understanding the errors of the predictions made outside of the sensing area could help improve training and predictions in future iterations. The errors of the predictions outside of the sensing area could be contributed to a few factors. First, human error could account for loss of accuracy since when applying the loads in both training and testing the points outside the sensor area were also points with higher curvatures. This increased the difficulty of applying these loads without slipping. The use of robotics in the application of these loads for training would increase the accuracy of the networks.

Moreover, further investigation into the loads applied outside of the sensing area uncovered that when loads were applied to points not included in the training dataset, the network predicted the location poorly. For example, on the medial compartment of the Ring sensor, Point 4 (2.5,3.5) and Point 2 (3,1) were both located outside of the sensing area. However, Point 2 was located on a point which was part of the training dataset and Point 4 was not. The results of the location predictions varied greatly where the average distance of the predicted points were 16.37 mm and 2.15 mm (Point 4 and Point 2 respectively) away from the actual points (Figure 7.7).
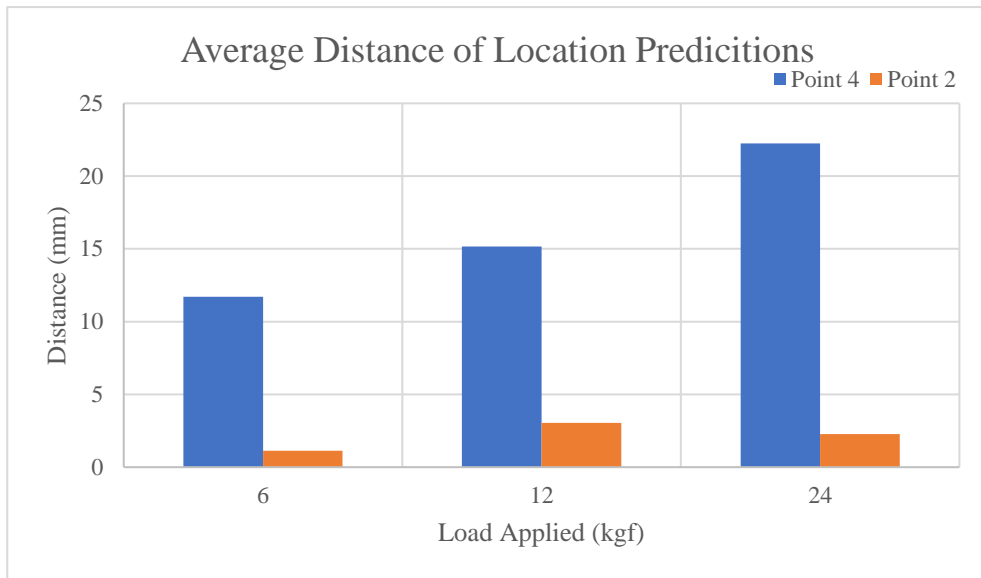
Figure 7.7: Error in Location Predictions of Ring Design Medial of Points Outside Sensing Area

Furthermore, when observing all points outside of the sensing area, although not statistically significant (*p>0.05*), the points which were included in the training dataset (Zimmer Specific: Point 1 (medial) and Point 3 (lateral) and Ring: Points 2 (medial and lateral)) made more accurate location predictions than points not included (Figure 7.8).
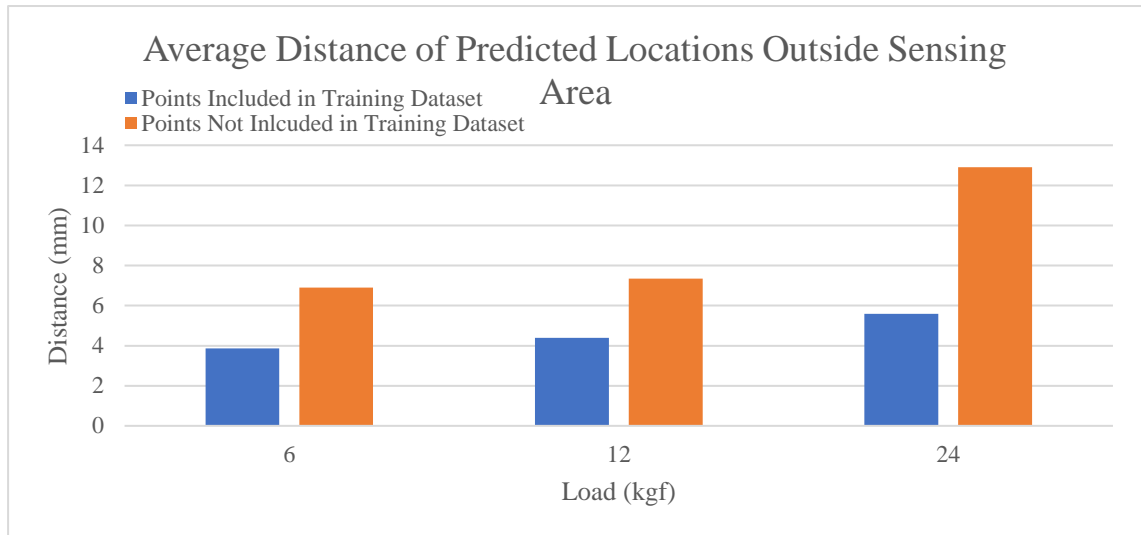
Figure 7.8: Accuracy of Location Predictions Outside the Sensing Area based on Inclusion in Training Dataset

Furthermore, the points outside of the sensing area which were included in the training dataset were further divided based on if they were on top of a strain gauge because of an assumption that this could be impacting the accuracy. Points on the gauges were thought to be problematic since applying the loads directly on top of the gauges introduced randomness to the readings and therefore, the predictions. Points which were on the gauges because of the increased ball bearing size and were included in the training set were Point 1 (2,0) on the medial compartment of the Zimmer Specific sensor and Point 3 (0,5) on the lateral compartment of the same sensor. Comparing these points to the points which were also training points and not on gauges Ring design: (medial) Point 2 and (lateral) Point 2 to the points on gauges showed a significant ($p<0.05$) increase in distance of the location prediction from the actual locations when loads were away from the gauges (Table 7.2).

Table 7.2: Location Predictions Outside Sensing Area (Part of Training Dataset) On Gauge vs. Away from Gauge

Distance from Actual Point (mm)		
Load Applied (kgf)	Not on Gauge	On Gauge
6	1.05	6.68
12	1.78	7.02
24	1.71	9.47
Average	1.51	7.72

This investigation into the predictions outside of the sensing area uncovered possible methods for improving results in future iterations. This includes refining the gride size outside of the sensing area to include more training points to provide sufficient data for the network to learn due to the high nonlinearity in this area. Additionally, training points should not include points which lie on top of the gauges to decrease the introduction of this random error into the learning of the network.

7.3.2 Whole Surface of the Sensor

Another aim of this sensor was to be able to sense over the whole surface. To evaluate these sensor's abilities in doing this, three regions were separated, forming the anterior, central, and posterior regions of the surface of the sensors, seen on Figure 7.3 (c and d). There was no significant difference ($p>0.05$) between the load predictions and the actual loads applied in all three regions (Figure 7.9).
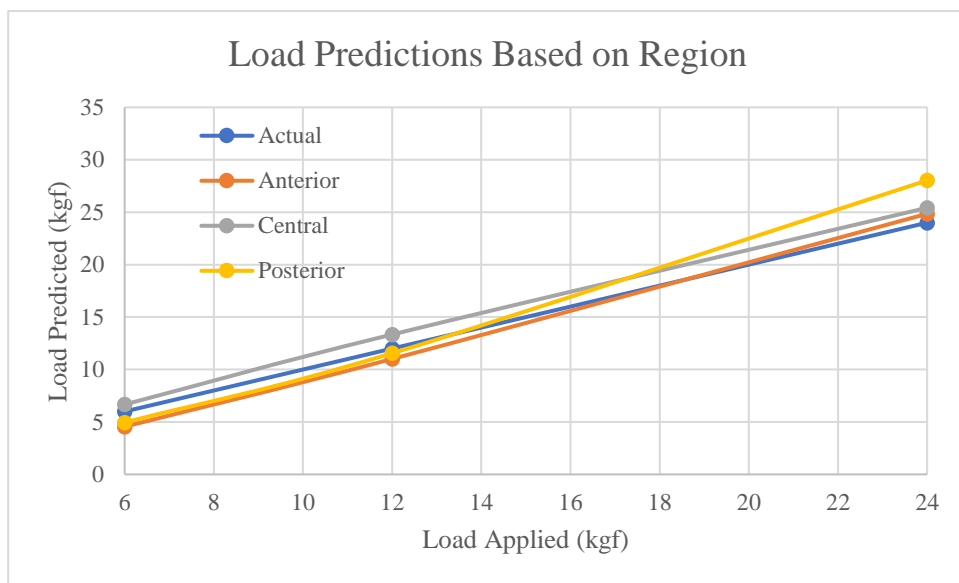
Figure 7.9: Load Predictions Based on Region

The location predictions across the sensor were significantly different ($p<0.05$) based on the region. However, this was thought to be impacted mostly by the proximity of these points to the sensing area, uncovered in the previous section, since the central region provided more accurate location predictions while the anterior region had the least accurate results which, mentioned in the previous section, could be due to the proximity to the gauges, proximity to the sensing region, curvature of the geometry, or the inclusion of these points in the training dataset.

126
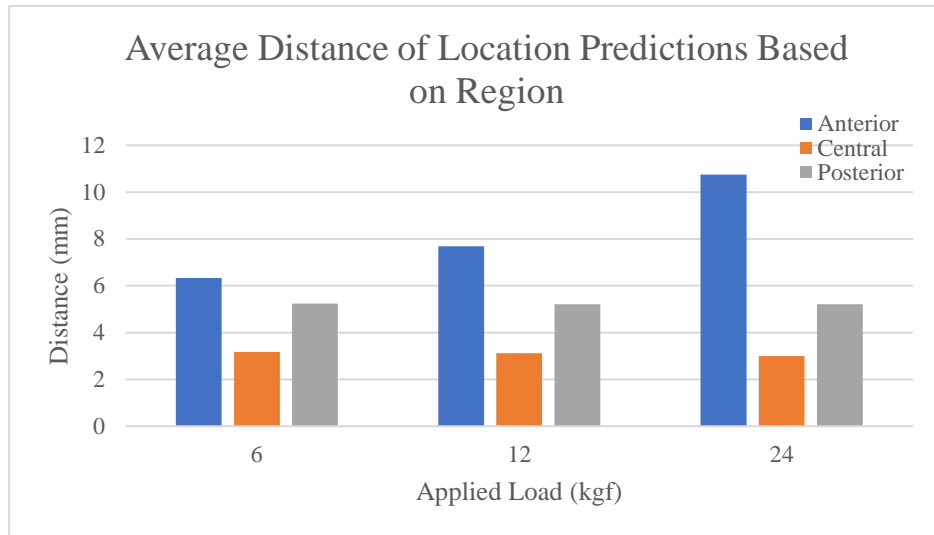
Figure 7.10: Location Predictions Distance from Actual Location Based on Region

7.3.3 Comparison of Each Compartment

Finally, since balancing occurs between the medial and lateral compartments intraoperatively, there should be no significant difference in predictions between the two which would result in balancing to be misrepresented. This was the case between the load predictions ($p>0.05$) in each compartment (Figure 7.11). For the location predictions (Figure 7.12), there was also no significant difference ($p>0.05$) in predictions when 6 kgf and 24 kgf was applied to each compartment and when the outlier of Point 4 on the Ring sensor (medial) was removed there was also no significant difference between the compartments when 12 kgf was applied ($p>0.05$).
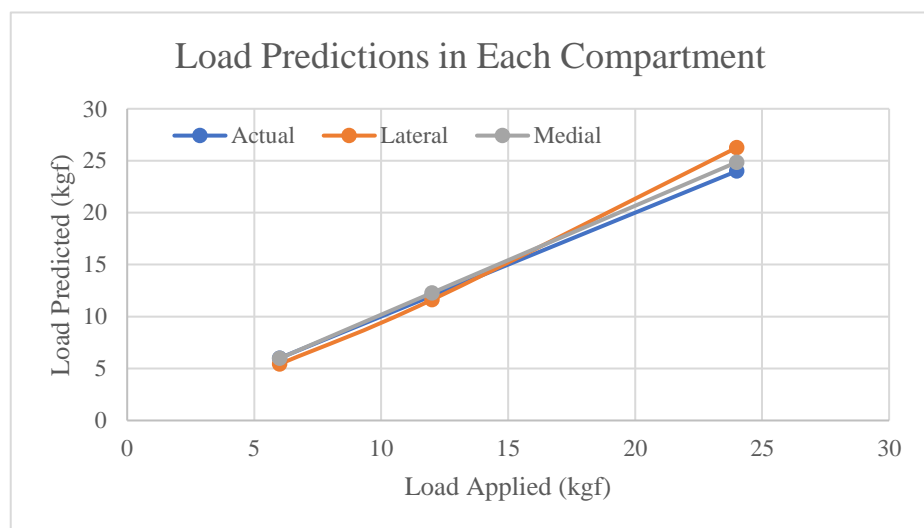
Figure 7.11: Load Predictions in Each Compartment
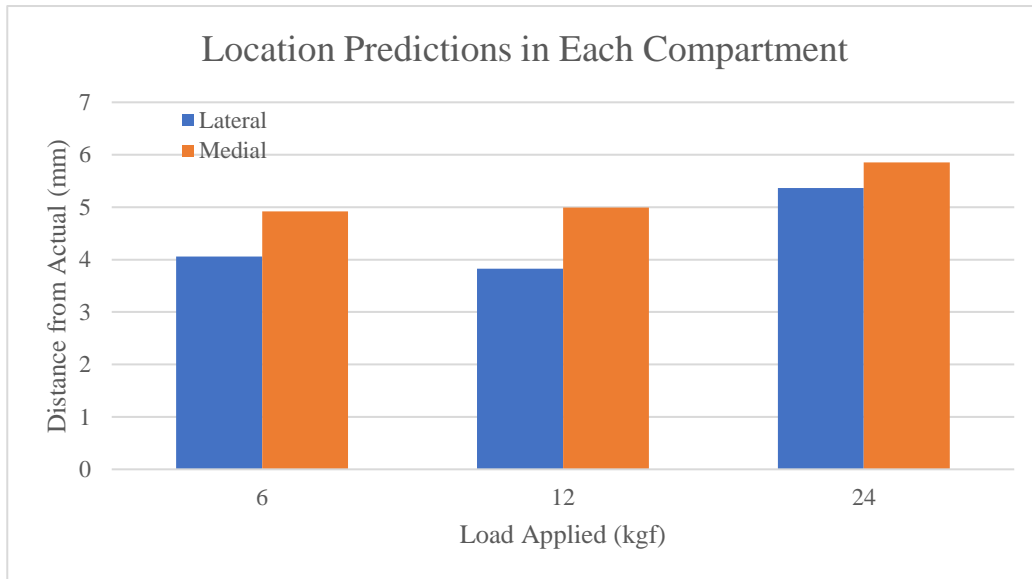
Figure 7.12: Distance of Predicted Location from Actual Location in Each Compartment

7.4 Two-Contact Point Investigation

In this section, using the training data, two contact points were applied simultaneously to the surface of the Zimmer Specific sensor on the lateral compartment. This was done to investigate the predictions based on more than one contact point being applied to the surface. To investigate this, three loading positions, with two different loading conditions, for a total of 6 predications were investigated based on Figure 7.13.
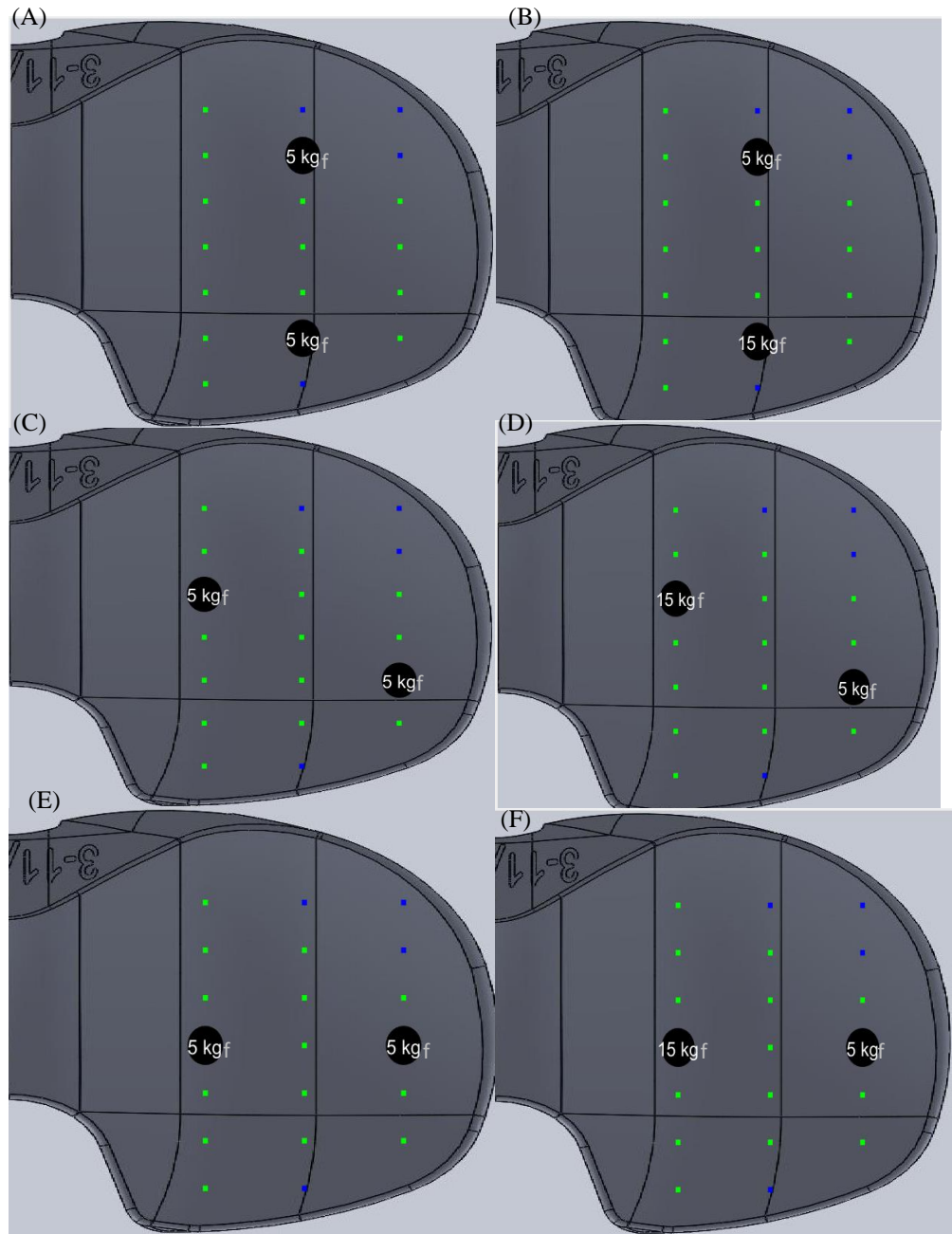
Figure 7.13: Zimmer Specific Lateral Two-Contacts Points Applied

The predicated locations based on the above applied loads can be seen in Figure 7.14.
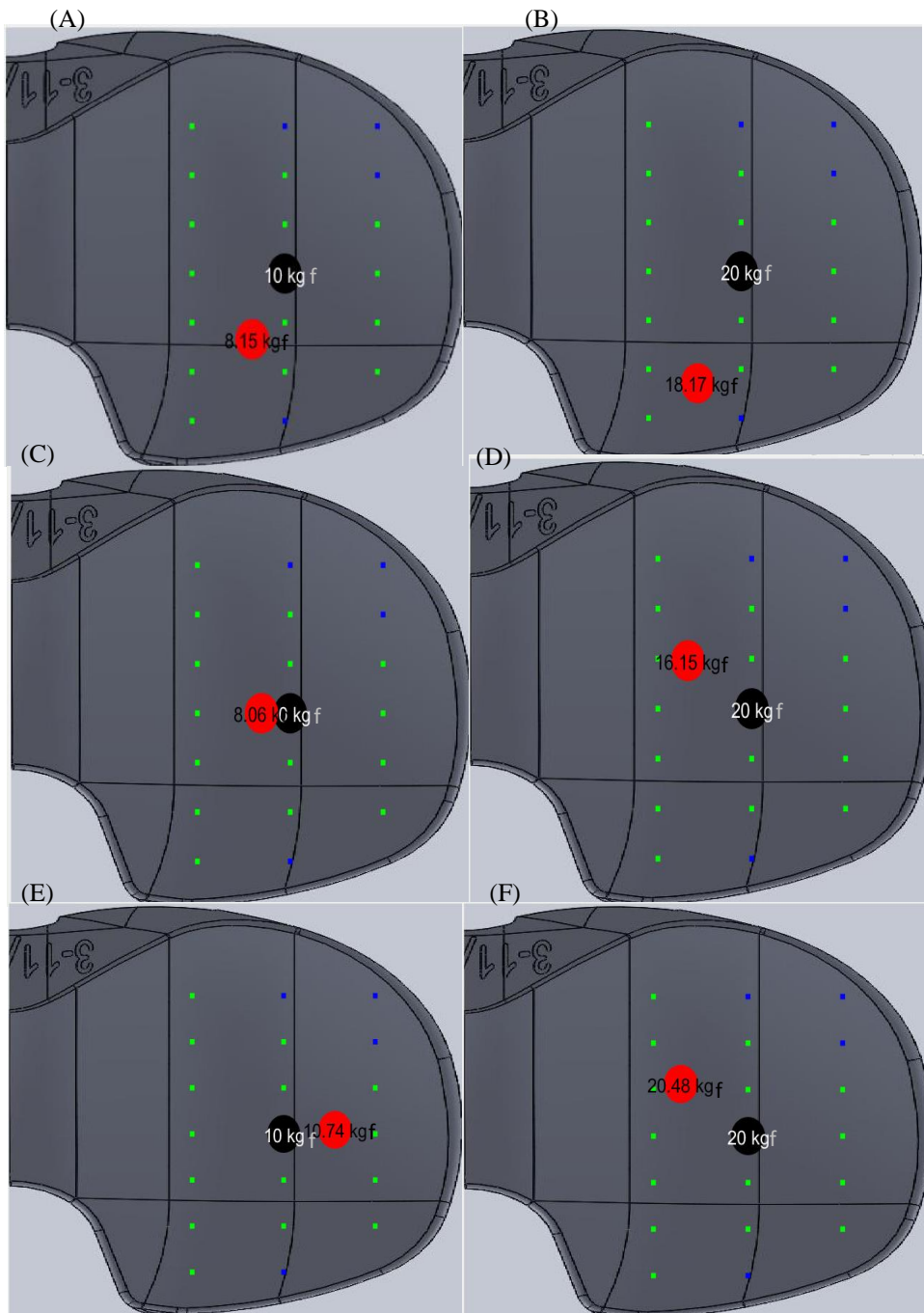
Figure 7.14: Zimmer Specific Two-Contact Points Expected vs. Actual

Overall, the accuracy for load predictions was 87.32% which proves the networks accuracy in handling more than one contact point being applied.

Table 7.3: Zimmer Specific Lateral Two-Contact Points Load Results

Actual Load (kgf)	Predicted Load (kgf)	Accuracy
10	8.15	81.50%
10	8.06	80.60%
10	10.74	92.60%
20	18.17	90.85%
20	16.15	80.75%
20	20.48	97.60%

The average distance of the predicted point from the actual point was 5.92 mm.

Table 7.4: Zimmer Specific Lateral Two-Contact Point Location Results

Actual Location (X,Y)	Precited Location (X,Y)	Distance from actual (mm)
(1,3)	(0.65, 1.66)	6.92
(1,3)	(0.53,0.71)	11.69
(1,3)	(0.69,3.00)	1.55
(1,3)	(0.32,3.96)	5.88
(1,3)	(1.56,3.09)	2.84
(1,3)	(0.29,4.12)	6.63

These results indicted when two points were applied over the surface of the sensor the load and location results can be predicted accurately based on the results displayed in Table 7.3 and Table 7.4.

7.5 Impact of Temperature

The change in temperature from the training environment to the in-situ use of the sensor is not thought to impact the results of the ANN's performance. To simulate this, the voltages from point (1,3) of the lateral compartment of the Zimmer Specific sensor were altered by 5% to represent a change in temperature. Following this, the predictions were analysed and compared to the results of the predictions without any impact from temperature.

The results of this investigated indicated the impact of temperature was negligible. The change in voltage still provided the sensor with an accuracy of 99.73% when temperature changes were simulated compared to a 99.78% accuracy when there was no impact from temperature. Moreover, the average difference in measured centre of pressure was 3.17 mm from the actual applied load in comparison to 3.15 mm when there was no impact from temperature. The results of the temperature effected results

can be seen in Figure 7.15 (a,b, and c) while the impacted results can be seen in Figure 7.15 (d,e and f). There was no significant difference *(p>0.05)* in the results of both the load and location predictions due to change in temperature. Additionally, it is worth nothing that for this application the operating theatre is a highly controlled environment due to the risk infection from changes in temperature.
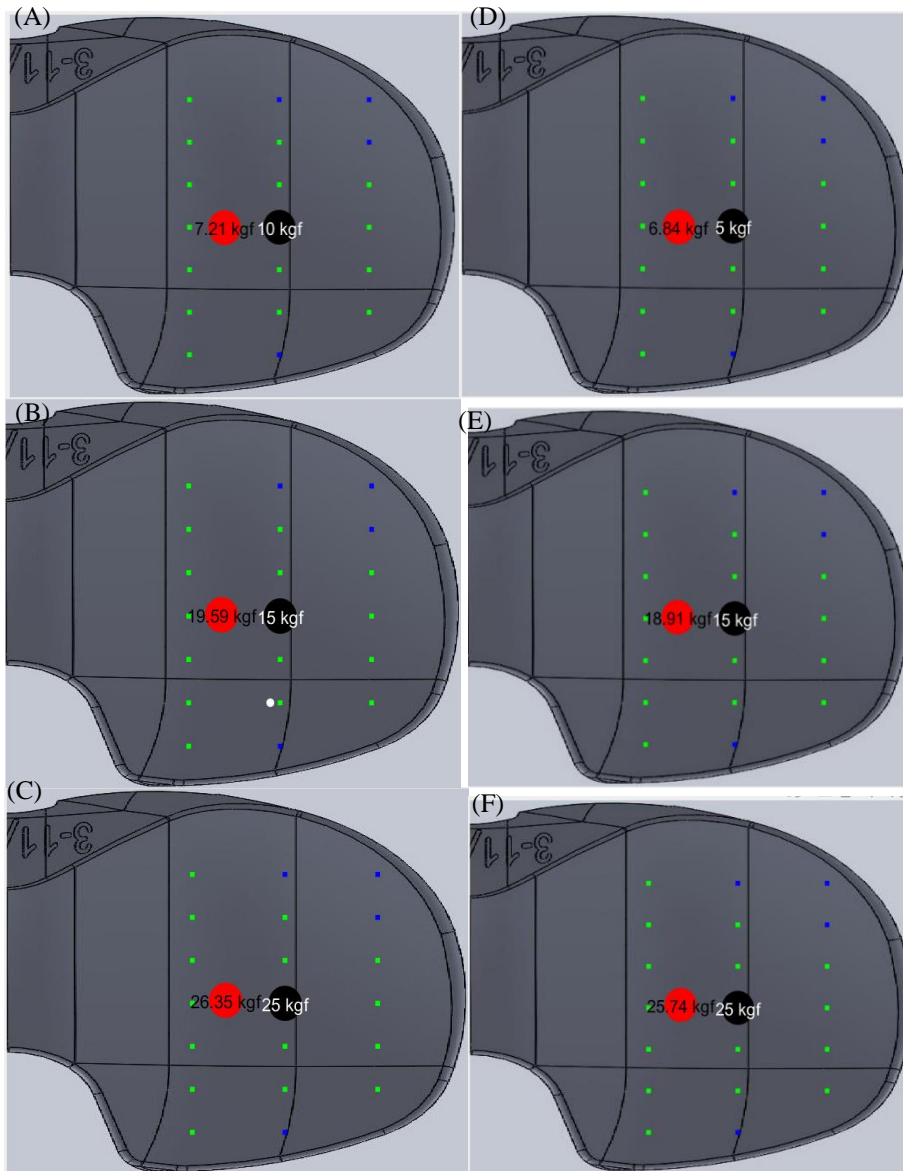
Figure 7.15: Actual Load and Location vs. Predicted Load and Location with Simulated Change in Temperature a) Temperature Impact at 5 kgf b) Temperature Impact at 15 kgf c) Temperature Impact at 25 kgf d) No Temperature Impact at 5 kgf e) No Temperature Impact at 15 kgf f) No Temperature Impact at 25 kgf

7.6 Summary of Results

The results suggest that the accuracy of both sensors was acceptable for both load and location predictions and with minor improvements to the training data collection, more accuracy could be seen.

Temperature of the operating theatre is highly controlled in order to minimise risk of infection. As a result, temperature compensation from the strain gauges in the Wheatstone bridge suffice due to the device being re-zeroed and measurements occurring before the any drift in the system can occur.

7.7 Discussion

The aim of this research was to investigate the accuracy of two sensors: Ring and Zimmer Specific sensors in predicting the location of the contact points and the magnitude of the loads. To investigate the robustness of the sensors, the two sensors and their two compartments, points inside and outside of the sensing area, and points across the whole surface of the sensor were compared.

The main findings were that 1) there was no significant difference ($p>0.05$) in load predictions between sensors, compartments, region on the sensor, or sensing area 2) there was a significant difference ($p<0.05$) in location predictions for all these comparisons 3) the errors of both the load and locations predictions were relatively low where minor improvements to the training process could significantly improve the results of both predictions especially outside of the sensing area.

The first key finding from the testing of these sensors was that load predictions were not significantly different ($p>0.05$) between the two sensor designs, the sensing area, and the region, while also having a low bias. In total, the average accuracy across both sensors was about 89% for load predictions and the average location prediction was 4.85 mm ± 1.47 mm, where the surface areas of the medial and lateral compartments were 1099.72 mm^2 and 1088.46 mm^2 respectively. Compared to other sensors, Wang et al. (2022) had a maximum error of 2% for their load sensor with a testing range below 1kg (10 N). Additionally, some limitations to their sensor included an operation range between 0-5.1 kgf (0-50 N), not sensing over the whole surface, and not displaying the location. Another force sensor using piezoresistive sensors to

133

measure the load in the knee had an error of ±0.51 kgf (±5 N). However, the sensor only had a measurement range between 0-4.59 kgf (0-45 N) and did not measure the location (Jiang et al. 2019). Another paper by Crottet et al. (2005) had an error of 0.5% in location and load predictions in a laboratory setting; however, when using a bone model, the error jumped to 13% which the authors described as a result of cumulative errors in the device and experiment. This is an important finding since in order to set the correct tension in the joint intraoperatively, the surgeon needs to have similar accuracies in the load values between compartments. Moreover, the load values across the whole sensor should not be significantly different since the surgeon will be comparing the values at different orientations which moves the centre of pressure along different regions of the sensor. Moreover, when two contact points were applied to the surface of the sensor, the load was predicted with an average of 87.32% accuracy where there was no significant difference between applied and predicted loads ($p>0.05$).

One of the main advantages of using AI was an increase in the sensing area. Although there was a significant difference ($p<0.05$) in location predictions outside compared to inside the sensing area, the load predictions were not significantly different ($p>0.05$). The testing of this sensor uncovered some proposed improvements to increase the accuracy of the location predictions outside of the sensing area. Location predictions outside of the sensing area were investigated and when the tested locations were between training points the accuracy significantly decreased ($p<0.05$). Furthermore, points which were on top of the strain gauges introduced random data and error in the networks ability to predict the location. Since the data outside the sensing area was highly nonlinear a simple solution to this error would be to create a finer grid outside of the sensor area during training which would provide the network with more information to converge, while avoiding points on top the strain gauges. Despite this, the average distance of the points outside of the sensing error was 6.91 mm ± 2.15 mm with one outlier of Point 4 on the Ring sensor. Once removed, the error was 5.24 mm ± 1.51 mm which compared to the overall size of the sensor was still a relatively small error. The point of this finding is to ensure the location of the centre of pressure is accurate for the surgeon to ensure the femur is articulating of the tibial properly. As a result, the decrease in accuracy compared to the load is acceptable for the surgeon to be able to make an informed decision on setting the joint. Also, the investigations into the results provide a clear methodology for improving these results.

The load predictions of the sensor made in this research had a lower bias compared to VERASENSE both inside and outside of the sensing area. A study of the accuracy of VERASENSE by Nicolet-Petersen et al. (2018) found that when observing points across the sensor through a range of loads, the bias of the load readings was -2.36 kgf ± 1.18 kgf inside the sensing area and -6.12 kgf ± 2.13 kgf outside the sensing area. The sensor created in this research had an average bias of 0.61 kgf ± 1.43 kgf inside the sensing area and 0.98 kgf ± 1.70 kgf outside. This demonstrated the improvement AI made to abilities of the sensors which satisfies the criteria determined by Roth et al. (2017) for creating an accurate and robust measuring device to inform TKRs.

In futures iterations of testing the accuracy of these networks, a bone model can be constructed using the prosthetic implants from the PKS to more closely mimic the intraoperative condition for which the sensor will be used. Moreover, to increase the accuracy, increasing the ceiling of load values to get the whole behaviour should be done in the next iteration.

7.8 Conclusion

Intraoperative load sensors aim to measure the intercompartmental loads and provide surgeons with a quantitative tool to balance the loads. This tool can be beneficial for surgeons, patients, hospitals, the National Health Services (NHS), stakeholders, and biomedical companies. Surgeons and patients can see a reduction in early revision surgeries and better postoperative outcomes. Hospitals, the NHS, and stakeholders can benefit from better patient outcomes, lower costs in revision surgeries, and shorter hospital stay postoperatively. Moreover, biomedical companies and stakeholders can use the data of load distributions intraoperatively to better design implant systems and inform regulatory agencies.

In this research, one sensor was amended to fit Persona's shim system and the other was adjusted to have a more general design to incorporate other implant systems. The benefits of these sensors were that its use of AI allowed it to identify loads and locations over the entire surface of the insert while also upholding high accuracy and precision over a wide range of loads. This research investigated the accuracy of the sensor by investigating the ability of AI to predict both the load and location of a known point load. The sensors both performed with good accuracy and precision in both load and location predictions across the whole of the sensors. The main findings were that

the load predictions were low and had no significant difference across sensor design, sensing area, or region of the surface. The main difference in location predictions arose from the proximity to sensing region, where a deeper investigation uncovered that a finer grid size outside the sensing area should increase the accuracy of the location predictions in this region, while avoiding locations on top of the strain gauges. An added benefit of using an AI was that retraining can be done quickly and simply as more research is done on the performance and training process, making the iterative process of optimisation cheaper and relatively quick.

This accuracy testing of the sensors not only helped to understand the performance of the sensor but also to shed light on where errors may be originating in order to adjust the data collection or training accordingly.

This system, when combined with robotic technology can significantly improve the reliability and repeatability of the quantification of contact forces and locations during the operation. This would more allow for accurate tracking of the ideal loads and contacts points linked to patient specific data like size and gender. Identifying the ideal load intensity is the optimal goal that this device can help identify. Combined with the robot's ability to produce identical cuts, the subjective nature of joint replacement surgeries can be eliminated.

Chapter 8: Cadaveric Testing

8.1   Introduction

The Zimmer Specific sensor was tested in cadavers at the Clinical Anatomy Skills Centre, Glasgow University and the Royal College of Physicians and Surgeons of Glasgow (RCPS Glasgow), Scotland on June 27th, 2023. Zimmer Biomet was the sponsor of the research conducted at RCPS Glasgow and Zimmer Biomet confirmed that all regulatory requirements for the use of donor material in the research described were in place prior to the work being conducted. Under the sponsorship agreement between Zimmer Biomet and RCPS Glasgow, the latter confirmed to BU that permission was in place to use the data and publish the results in this thesis. Since the sensor created in this research was the only sensor compatible with the Persona Knee System (PKS), qualitative results were discussed based on expected outputs from trends in joint loading, and kinematic pivot patterns. The normal and TKR knee kinematic and kinetic patterns were described in Chapters 2 and 3, which provided context to the quantitative cadaveric results. Additionally, surgeon's qualitative comments were discussed based on several factors including the useability of the device, compatibility with Persona's Shim System, and integration with the standard surgical workflow.

8.2   Surgical Procedure

The surgical procedure was performed in conjunction with a surgical training session organised by Zimmer Biomet. This involved surgical trainees performing TKRs on cadavers under the supervision of experienced orthopaedic surgeons. The cadavers used in this research underwent a right knee cruciate retaining (CR) TKR using the PKS. This was compatible with the Zimmer Specific sensor and the Ring sensor created in this research. The Zimmer Specific sensor was used in two full body cadavers. In accordance with Scotland's ethical procedures surrounding human tissue (Human Tissue Act 2004), the identities were concealed, and no photographs of the cadavers were taken. The following research by Cho et al. (2018) depicts a cadaveric knee using VERASENSE which provided an idea of what the knee looked like with the sensor made in this research inserted.
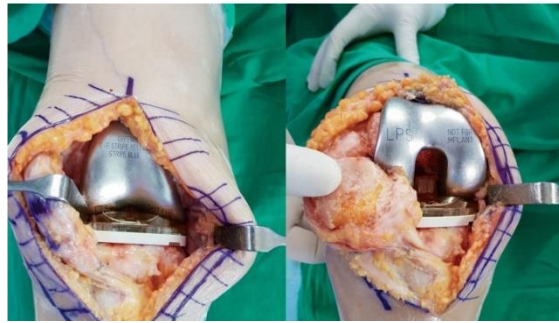
Figure 8.1: Cadaver with sensor (Cho et al. 2018)

To investigate the function of the Zimmer Specific sensor intraoperatively the sensor replaced the tibial spacer as seen in Figure 8.2. The PCB, the temperature compensation gauges, and laptop were placed on a trolly next to the cadaver during the use of this system.
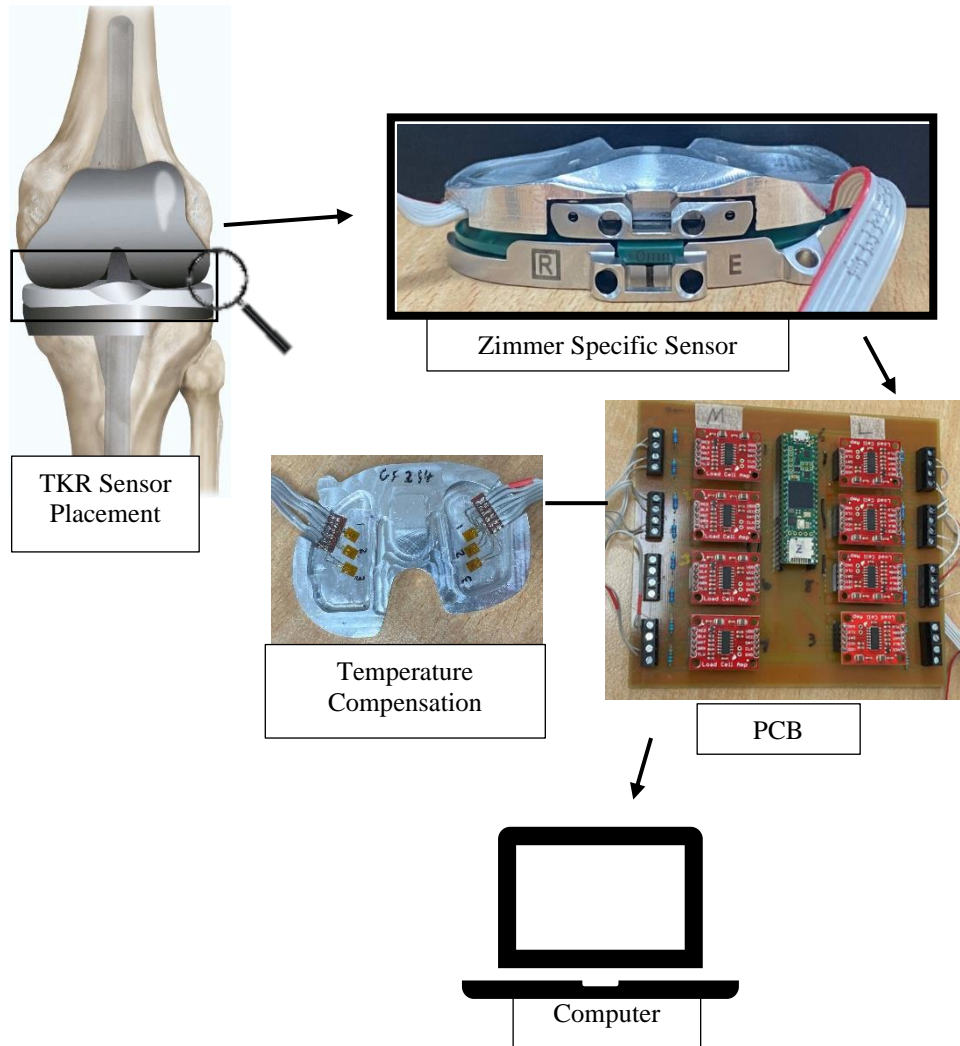
Figure 8.2: Placement of Sensor and Electronics

During the intraoperative use of the Zimmer Specific sensor the thickness of the shims were increased (10 mm-13 mm) to observe the impacts of the tensioned soft tissue on intraoperative load. During a real TKR, surgeon's trial different thicknesses to "feel" if the proper tension is achieved while the knee is moved through a ROM (0°/10°, 45°, and 90°) and with varus and valgus stresses applied. The same process was done with this sensor to ensure that the values reflected what was expected at these orientations in the passive state. The two cadavers were tested with the 10 mm, 11 mm, 12 mm and 13 mm shim inserted twice at different degrees of flexion (0°/10°, 45°, and 90°). The load and location predications were averaged and recorded. When thicker shims were inserted, the knee does not reach full extension of 0° and therefore full extension is reached at 10° instead. Figure 8.3 depicts the Zimmer Specific sensor with the 13 mm thickness shim being inserted which was one of the 4 variable thicknesses used.

Figure 8.3: Zimmer Specific Sensor with 13 mm Shim

8.3   Results and Discussion

Since there is currently no verified system which is compatible with the PKS, characteristics of the general performance were described. Described below are the trends which should be observed, found in literature, and were compared to the load and locations values recorded in this study.

8.3.1 Compartmental Loads

Firstly, as the shim thickness increased the loads observed in both compartments should also increase. Figure 8.4 depicted the changes in load measurements in the medial and lateral compartments at 0°/10°, 45°, and 90° when the shim thickness was increased from 10-13 mm in increments of 1 mm for both cadavers. Increasing the thickness of the shim should increase the load in the compartments since the soft tissue was not released during this process. This finding was substantiated by research which found an increase in tibiofemoral forces when the PE insert thicknesses were increased (Tzanetis et al. 2021).

This was the case for almost all orientations in both compartments and both cadavers. Where the medial compartment of Cadaver 1 at 45° was the only case where the overall load greatly decreased as the thickness increased.

Moreover, the average measurements from the cadavers in full extension with the increasing shim size can be compared to another research by Kuriyama et al. (2023) which used a knee sensor and thicknesses from 10-16 mm in 1 mm increments. The R^2 values for the linear relationship were 0.88 (lateral), 0.97 (medial) in the study by Kuriyama et al. (2023) (Figure 8.5) and 0.85 for both medial and lateral compartments in this study (Figure 8.6). This implied that the sensor was able to register the increase in compartmental loads that would be expected as the thickness of the insert increased.
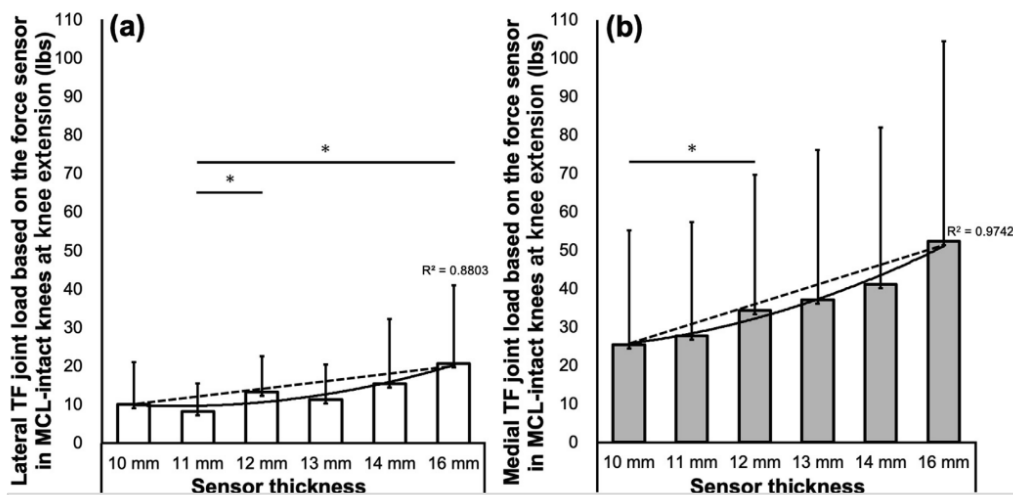
Figure 8.5: Results from Research by Kuriyama et al. (2023) at Full Extension with Increasing Thickness

8.3.2 Loads through the Flexion Arc

Secondly, following a TKR the contact forces should greatly decrease as the flexion angle increases to 45° then slightly increase to 90° (Jeffcote et al. 2007; Schnaser et al. 2015; Verstraete et al. 2017; Kebbach et al. 2019; Manning et al. 2019; Sabatini et al. 2021; Shah et al. 2021). Therefore, observing the total load difference between full extension and 90° should provide a good insight into the function of the sensor. Figure 8.7 depicts the average of each cadaver for all shim inserts, as well as the total average. These results follow the trend described above and depicted in Figure 2.9, Figure 2.10, Figure 2.11, and Figure 2.12.
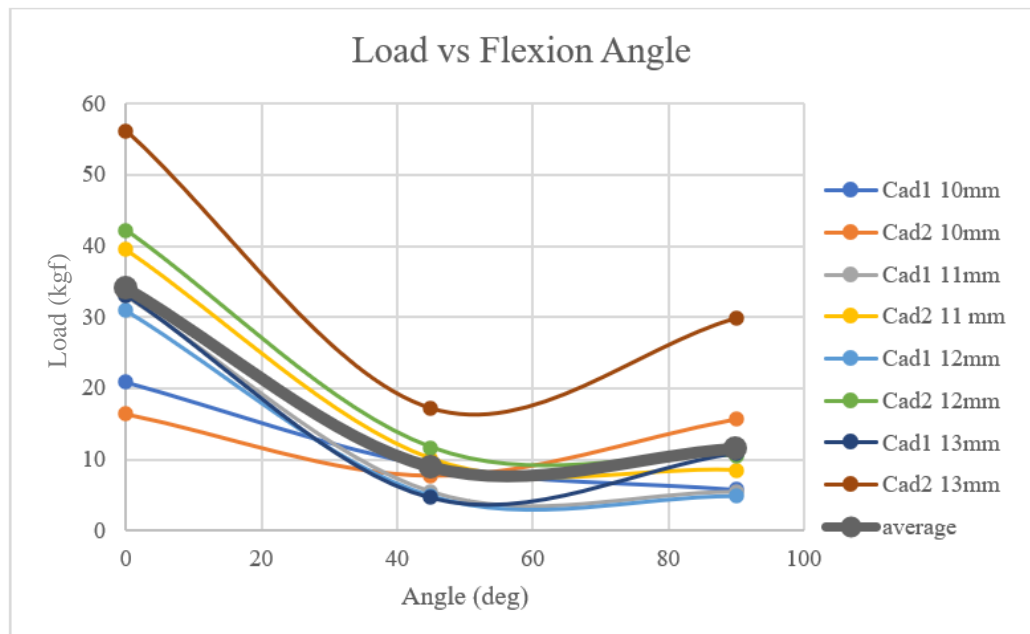
Figure 8.7: Loads through the Flexion Arc

Moreover, since standard measuring tools were used to place the knee in varying degrees of flexion there may be some error, in the clinical use of the system an IMU can be combined with this system to ensure the proper angle is being achieved. Additionally, linking this system with robotic technology would provide a seamless integration of the technology with the surgical workflow.

8.3.3 Intercompartmental Load Balancing

Another kinematic observation was that the loads may be higher medially than laterally throughout the flexion arc, however this was based on the surgeon's ability to

143

balance the knee. When averaging all flexion angles the loads were higher medially than laterally for both cadavers (Figure 8.8), which was observed in studies using both VERASENSE and independent load sensors (Meere et al. 2016; Verstraete et al. 2017; Manning et al. 2020; Song et al. 2020; Sabatini et al. 2021).
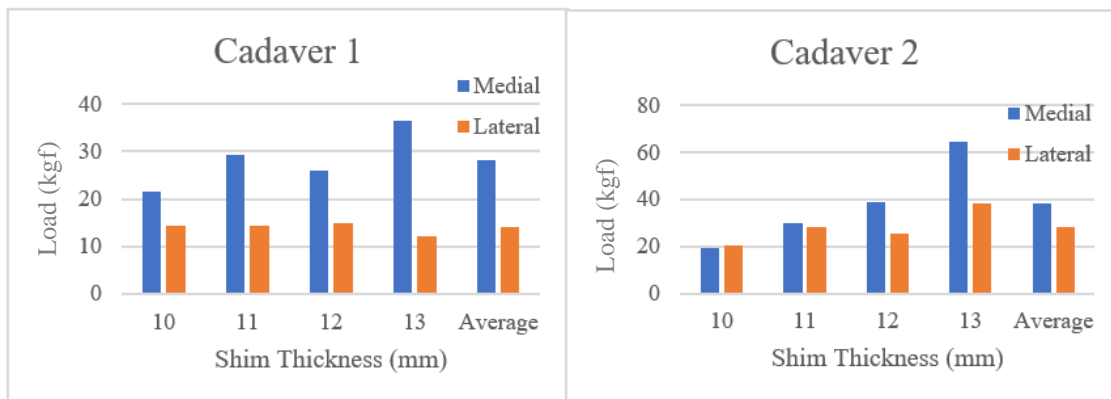
Figure 8.8: Compartmental Load Balancing Using Zimmer Sensor in Both Cadavers

Moreover, the intercompartmental load difference provides insight into the balancing of the knee joint. VERASENSE developers and literature surrounding joint balancing found that the intercompartmental load difference should be ≤ 6.80 kgf (66.70 N or 15 lbf) (Gustke et al. 2017; Risitano et al. 2017; Song et al. 2020). The mediolateral compartmental difference was tabulated in Table 8.1. Since the cadavers underwent a TKR performed by surgical trainees using standard tools it was expected the joint would be unbalanced. The results in Table 8.1 were colour coordinated according to the state of balance labelled in the legend below.

Table 8.1: Intercompartmental Loads

Thickness	Cad1	Cad2
10 mm	9.00 kgf	3.35 kgf
11 mm	23.00 kgf	7.25 kgf
12 mm	20.10 kgf	12.25 kgf
13 mm	26.90 kgf	7.25 kgf

Legend 1

Balanced ≤ 6.80 kgf

6.80 kgf< moderately unbalanced ≤ 13.60kgf

13.60kgf $\leq$ severely unbalanced

8.3.4 Varus-Valgus Stress Tests

Surgeons often perform varus-valgus stress tests to uncover the condition of the surrounding knee stabilisers, which is often performed at 30° (Al-Jabri et al. 2021). With the varus-valgus stress test the loads should be much greater in one compartment when the leg is pulled varus or valgus (to the medial or lateral compartment) respectively. This was observed when testing both cadavers by applying varus and valgus forces to the knee at 30° as seen in Table 8.2. Cadaver 1 was performed with the 12 mm insert and Cadaver 2 with a 10 mm insert.

Table 8.2: Varus-Valgus Testing

	Varus		Valgus	
	Medial	Lateral	Medial	Lateral
Cadaver 1	24.10 kgf	3.00 kgf	0.80 kgf	42.20 kgf
Cadaver 2	34.45 kgf	2.10 kgf	7.85 kgf	46.65 kgf

It can be observed that the medial forces are slightly lower than the lateral when the varus/valgus forces were applied respectively. This can be attributed to the soft tissue (LCL) being tighter laterally, meaning more force was required by the surgeon to move the leg in varus direction, which was dependent on the surgeon's bone cuts and gap balancing (Meloni et al. 2014). However, as expected the forces recorded by the sensor were significantly *(p<0.05)* higher in the direction which the knee was pulled.

8.3.5 Location Predictions

For the location predictions, it was difficult to discern what location predictions were accurate since it was dependent on how the surgeon was holding the leg (varying degrees of varus/valgus and flexion) and the overall laxity in the joint. The average of all location predictions were plotted to Figure 8.9 and compared with research conducted by Deckard et al. (2022) on VERASENSE. The orange dots represent the predictions found in this research where the blue dots were from the research conducted by Deckard et al. (2022) and transposed on to the Zimmer Specific sensor. Since the implants were not the same size the locations were estimated onto the Zimmer Specific sensor as accurately as possible. One similarity was that the lateral location predictions were more anterior compared to the medial compartment. This was consistent to what is known about the kinematic pivot patterns in the knee through the flexion arc (Iwaki et al. 2000; Dennis et al. 2003; Moonot et al. 2009; Meneghini et al. 2017; Pinskerova and Vavrik 2020; Deckard et al. 2022; Hashimoto et al. 2022).
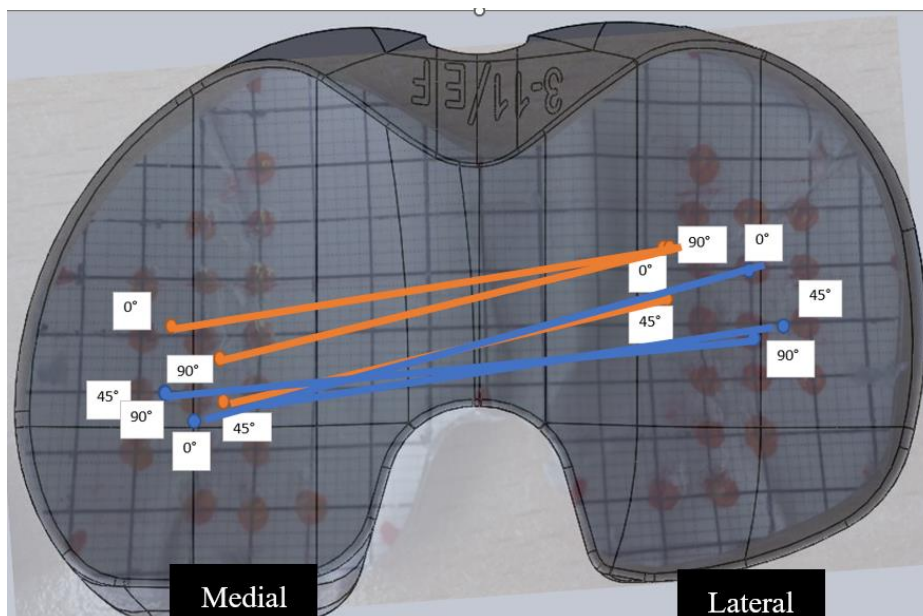
Figure 8.9: Location Predications through the Flexion Arc: VERASENSE vs Zimmer Specific Sensor

8.4   Qualitative Analysis

The cadaveric testing provided valuable insight into the qualitative performance of the sensor with the unique perspective of an experienced orthopaedic surgeon. The graphical user interface (GUI) included CAD drawings of the surface of the tibial insert which was identical to the surface of the sensor. Moreover, the Cartesian-coordinate system was aligned with training points to increase the coherence between the sensor and what was depicted to the surgeon. During training and lab testing, the font size of the load values was acceptable for the user. However, during the surgery the surgeon stood farther away from the screen and as a result the load prediction font size needed to be increased. The other features like zeroing the device were easy to use by a technician during the surgery.

Moreover, since this was a working prototype, the wires emerged from the front of the sensor while the skin and tissue covered the sensor including the wires during intraoperative use. The positioning of the wires from the front of the sensor can be seen in Figure 8.10. However, despite this the wires were durable and from the surgeon's perspective did not interfere with his work. Additionally, the shims were easily exchangeable and there were no problems with the sensor throughout the cadaveric testing including with the electronics, GUI, or physical compatibility with the PKS.

146

Figure 8.10: Wires from Front of Zimmer Specific Sensor

In addition, the sensor was durable and robust demonstrated by being able to withstand the high loads from varus and valgus stresses, more than 391 N (40 kgf). Additionally, the sensor was not handled with extreme care and was able to withstand being pulled and pushed in and out of the knee without being damaged. The knee (femoral implant) was able to glide smoothly over the surface of the sensor throughout the ROM. For the final design, a plastic coating can be applied over the sensor to prevent tissue and liquid from entering the sensor. However, the sensor was water resistant, so it was able to be used for the duration of the cadaveric testing without problems. A coating would make the sensor easier and quicker to clean by removing the need to wipe down the grooves in the sensor when increasing the shim thickness. This would in turn decrease the already short addition of the sensor to the operation time. This system could also be reusable through sterilisation which would contribute to global and UK efforts towards sustainability.

Moreover, in terms of the accuracy of the results it was noted that during the cadaveric testing the surgeon observed that the Cadaver 2 felt more balanced than Cadaver 1, without viewing the load values on the screen. This was reflected by the results in Table 8.2 where the literature suggests an intercompartmental load difference of ≤ 6.80 kgf (66.70 N or 15 lbf) (Gustke et al. 2017; Risitano et al. 2017; Song et al. 2020). Table 8.3 reflects the distance of the load difference from the suggested load differential. Cadaver 2 was significantly more balanced than Cadaver 1 *(p<0.05)* and the total differences were +51.70 kgf and +2.90 kgf greater than the maximum suggested load difference of 6.80 kgf for Cadaver 1 and Cadaver 2 respectively.

Table 8.3: Load Differential

Thickness	Cadaver 1	Cadaver 2
10 mm	+2.20 kgf	-3.45 kgf
11 mm	+16.20 kgf	+0.45 kgf
12 mm	+13.20 kgf	+5.45 kgf
13 mm	+20.10 kgf	+0.45 kgf
Total	+51.70 kgf	+2.90 kgf

8.5 Conclusion

In conclusion, the cadaveric testing provided valuable insight into the performance of the sensor in real time. Despite not having another sensor to compare the results to, the literature surrounding kinematic and kinetic patterns of the knee and TKRs provided an argument for the successful use of the sensor intraoperatively. Moreover, an orthopaedic surgeon who has experience using VERASENSE was able to provide commentary on the useability and performance of the sensor. The cadaveric testing implied the success of the sensor for intraoperative use.

Also, this highlighted the need for repeatability that can be reinforced over time by creating a database storing the patient specific data along with their recorded load and location values used to set the tension in the knee. Over time functional and patient reported outcome can be recorded to link the load intensities to the patient outcomes, thus determining ideal load values based on patient specific data.

Following the integration of the improvements discovered in previous chapters, the Ring sensor can be retested in the next round of cadaveric testing.

Chapter 9: Discussion and Conclusion

9.1   Introduction

An arthritic knee joint limits the quality of life of patients causing them to suffer from pain and limited ROM amongst other ailments. A TKR aims to replace the joint and provide patients with a better quality of life; however, improper tension leaves patients unsatisfied and requiring revision surgeries. Studies have reported pain and poor functional outcomes as the primary reasons for patient reported dissatisfaction (Halawi et al. 2019; Muertizha et al. 2022). The previous chapters described the literature review, prototyping and fabricating of different knee sensor designs, training the sensor for use of AI, implementing tracking and load prediction over the whole surface of the sensor with a GUI, testing the accuracy in a laboratory setting, and cadaveric testing of the sensor.

This knee balancing system proved its robustness and accuracy through lab and cadaveric testing along with improvements for the next iteration. The knee balancing system aims to overcome ambiguity from surgeons in balancing the load between compartments in the knee. The following chapter critically evaluates the previous chapters involved in creating and testing this system.

9.2   Sensor Design and Fabrication

The process of designing and fabricating these sensors was centred around two key design ideas: one design which was compatible with Zimmer's PKS, and one which was a general design. Both sensors required a method to adjust the height to increase or decrease the tension in the joint. Moreover, the design features of the PKS like the curved surface of the sensor and the difference in compartment sizes aimed to maintain anatomical accuracy and increase congruency between components and were maintained when designing both sensors. Finally, features added to the design of the sensors allowed for the stress to be raised to the tabs where the strain gauges were placed, to reduce load sharing between compartments, and reduce the occurrence of mechanical crosstalk.

For the electronics, a half bridge Wheatstone bridge with temperature compensation was used. The strain gauges had no upper limit meaning they are highly accurate within its linear range. The PCB and electronics chosen were acceptable for this prototype; however, for the future, miniaturisation of the electronics would allow it

to be enclosed in the sensor reducing the bulk of the system and reducing the number and length of the wires. Additionally, Bluetooth would allow for wireless communication between the sensor and the computer which would increase the compactness of the system by eliminating the wiring.

The maximum allowable load for training was limited by the physical structural integrity of the sensor and not the strain gauges. As a result, in the future a stronger material like Titanium can be used for training higher point loads for increased accuracy of the AI, ideally a maximum point load of 450 N should be applied according to literature (Roth et al. 2017). Furthermore, 3D printed designs were investigated and ultimately not used for training or testing because of residual stresses decreasing the structural integrity of the design and the concerns regarding steralisation (Xie et al. 2022). As a result, CNC machining was used with an aluminium alloy. Moreover, casting could possibly be used since this process reduces the imperfections that are associated with additive manufacturing.

9.3 Artificial Intelligence

The optimisation of any AI system is based on the collected data and the application. Therefore, determining appropriate parameters and hyperparameters to yield the optimal weights and biases for the network was based on trial and error. Since this problem was a prediction problem, an ANN was used.

9.3.1 Training Data Collection

To train the neural network, a training dataset was created using physically collected data of the changes in voltage from the unbalanced Wheatstone bridge along with the corresponding load and location values of the applied loads. The use of the raw voltage data from the Wheatstone bridge instead of converting to strain, reduced the complexity of the system and the computational effort of the system. Although an iterative development of the training process ensued, there were still unexplored methods, like robotics, which could increase the accuracy and reduce the time and effort required to train this system. This will be especially important for the mass production of the devices.

First, to increase the repeatability a grid should be printed to the surface of the surface. In theory, if it is identical between sensors, then the same network could be used for mass production. Moreover, a material with a higher yield strength should be used to increase the training range inputted to the network. Finally, the grid size, mainly outside of the sensing area, should be finer. From the results of the accuracy testing, it was uncovered that due to the high nonlinearity outside of the sensing area, the network could benefit from more data to be able to converge.

9.4   Accuracy Testing

The accuracy testing of the sensor involved using a larger ball bearing to mimic the contact between the femoral implant and the sensor. However, in the future an additional test could be done by using the actual femoral implant at different orientations to replicate the flexion angle and simulate the real time intraoperative use of the sensor more accurately. Since with a larger uneven surface the centre of pressure is not easy to calculate, the use of AI in this system will allow for precise understanding of the location of the force through the knee. This is especially important since tools like gait analysis use ground reaction forces to approximate the direction of the force through the knee but does not take into account different limb alignments. Additionally, further testing could be split into one compartment loading and two compartment loading to investigate different loading conditions.

9.5   Cadaveric Testing

The quantitative results of the cadaveric testing were compared with literature on the expected kinematic and kinetic patterns of the joint, which mimicked the results from the Zimmer Specific sensor.

Additionally, the cadaveric testing provided valuable insight into the qualitative use of the sensor. Since there was no available sensor for comparison the qualitative feel of a balanced knee was used as a marker to investigate if the sensor agreed with the surgeon. In the future, the PCB should be miniaturised, and the electronics should be packaged better to reduce the bulk of the system. Moreover, the surgeon was able to identify that the font size of the GUI should be increased since surgeons stand farther away from the screen than technicians. Also, initially thought to

be problematic, the wires did not interfere with the surgery. To make the sensor easier to resterilise, the slits and space underneath could be covered and/or filled. A plastic coating for the top surface and a flexible filling for the cavity underneath could prevent damage and allow for reuse via sterilisation and long-term use. This contributes to sustainability efforts.

In the future, the Ring sensor should be improved based on this research and then tested in cadavers to identify any more possible design oversights. One consideration which could be predicted based on the cadaveric testing done in this research, would be to amend how the rings attach to allow for the surgeon to easily change the rings where currently it could be difficult considering the gloves worn during surgery both globally and in the UK, where the author found no other mentions in literature of such device being reuseable.

9.6   Contribution to Knowledge

This research was able to contribute to the pool of knowledge surrounding real time joint force measuring and tracking. This developed sensor along with the AI has provided surgeons with a sensor which covers the criteria established by Roth et al. (2017) to create an accurate and robust knee joint sensor.

The contributions made by this research included:

1. Developed a novel smart-sensor which could track the magnitude and location of the load across the whole surface of the sensor, withstand high forces, and maintain a reasonably low error.
2. Created a GUI to train the AI and to display the real time sensor data for easy visualisation by the surgeon.
3. Developed a training procedure and AI optimisation which can be used for similar sensors in other joints.
4. Provided rationale for the long-term development of joint assessment technology

This research provides a strong justification for the strength of AI in orthopaedic surgeries in order to instil confidence in such technology. Currently, the TKR process is reliant on the skill of the surgeon and the skill of engineers in creating an implant system and a joint that will provide patients with an improved quality of life. As the use of AI is becoming more prevalent in all areas of society, more trust is being given to the

integrity of these systems, including autonomous driving vehicles. Since the surgeon uses this validated device as a tool to make an informed decision during the surgery, the combined surgeon and sensor skill reduces the risk associated with either one alone.

9.7   Future Works

In the future a final prototype should be made with the consideration from this research. This includes a Titanium design with a coating, miniaturised electronics, which would be trained with robotics over a wider range of loads (0-450 N). This new sensor could then be tested in the clinical setting following a more robust lab accuracy testing which would mimic the cadaveric testing procedure and then in cadavers.

For approval of this device for clinical use, Food and Drug Administration (FDA) or Medicines and Healthcare products Regulatory Agency (MHRA) approval should be obtained.

The potential of this device is not limited to intercompartmental balancing, where the optimal load intensity for improved postoperative outcomes can be revealed. Following clinical trials, a database can be created, and patient outcomes can be measured to determine ideal quantification of a balanced knee. The continued use of this validated and accurate device will correlate the load intensity in the knee to the optimal function and patient reported outcomes, reducing the frequency of early revision surgeries.

This technology should not be limited to the knee where the same theory can be applied to other joints in the body including, hip, shoulder, ankle, elbow, vertebrae and many more. This would help set the ideal tension for other joint surgeries.

References

Abdul Nasir, A. S., Mashor, M. and Hassan, R., 2011. Detection of Acute Leukaemia Cells Using Variety of Features and Neural Networks. *In*: *IFMBE Proc*. 40–46.

Abulhasan, J. F. and Grey, M. J., 2017. Anatomy and physiology of knee stability. Journal of Functional Morphology and Kinesiology, 2 (4).

Abu Osman, N. A. and Wan Abas, W. A. B., 2011. IFMBE Proceedings: Foreword. *IFMBE Proceedings*, 35 IFMBE (June).

Achakri, H., Yoav, B.-S., Blom, A., Boulton, C., Bridgens, J., Brittain, R., Clark, E., Dawson-Bowling, S., Deere, K., Esler, C., Espinoza, O., Evans, J., Goldberg, A., Gregson, C., Hamoodi, Z., Howard, P. and J, S., 2023. *The National Joint Registry 20th Annual Report 2023*. The National Joint Registry Annual Report. London.

Alexiadis, A., Reynolds, P., Al-Mouazzen, L., Toms, A., Phillips, J. and Waterson, B., 2024. Revision total knee replacement finances: a detailed cost-analysis of operative practice at a regional tertiary referral centre. *BMC Health Services Research*, 24 (1), 1–7.

Al-Jabri, T., Brivio, A., Maffulli, N. and Barrett, D., 2021. Analysis of intercondylar notch size and shape in patients with cyclops syndrome after anterior cruciate ligament reconstruction. *Journal of Orthopaedic Surgery and Research* [online], 16, 729. Available from: https://doi.org/10.1186/s13018-021-02878-5 [Accessed 11 Sep 2023].

Al-Nasser, S., Noroozi, S. and Harvey, A., 2024. Design of a Novel Intraoperative Sensor for Load Balancing and Tracking during Total Knee Replacements (TKR), 8 (1), 1–9.

Amundsen, S., Lee, Y.-Y. and González Della Valle, A., 2017. Algorithmic pie-crusting of the medial collateral ligament guided by sensing technology affects the use of constrained inserts during total knee arthroplasty. *International orthopaedics*, 41 (6), 1139–1145.

An, G., 1996. The Effects of Adding Noise During Backpropagation Training on a Generalization Performance. *Neural Computation* [online], 8 (3), 643–674. Available from: https://doi.org/10.1162/neco.1996.8.3.643.

Anastasiadis, A., Magnissalis, E. and Tsakonas, A., 2010. A novel intraoperative sensor for soft tissue balancing in total knee arthroplasty. *Journal of Medical Engineering and Technology*, 34 (7–8), 448–454.

Andriacchi, T. P., Stanwyck, T. S. and Galante, J. O., 1986. Knee biomechanics and total knee replacement. *The Journal of arthroplasty*, 1 (3), 211–219.

Andriacchi, T.P.; Mikosz, R. P., 1991. Musculoskeletal dynamics locomotion and clinical applications. [online], New York, New York, Usa Illus 51-92. Available from: https://eurekamag.com/research/032/456/032456802.php.

Anon., 2024a. VeraSense for Triathlon | Stryker [online]. Available from: https://www.stryker.com/hk/en/joint-replacement/products/VeraSense_for_Triathlon.html [Accessed 5 Aug 2024].

Anon., 2024b. eLIBRA Dynamic Knee Balancing System® (DKBS) [online]. Available from: https://www.zimmerbiomet.lat/en/medical-professionals/knee/product/elibra-dynamic-knee-balancing-system.html [Accessed 5 Aug 2024].

Asano, H., Hoshino, A. and Wilton, T. J., 2004. Soft-tissue tension total knee arthroplasty1 1No benefits or funds were received in support of this study. *The*

Journal of Arthroplasty [online], 19 (5), 558–561. Available from: https://www.sciencedirect.com/science/article/pii/S0883540304001445.

Babazadeh, S., Stoney, J. D., Lim, K. and Choong, P. F. M., 2009. The relevance of ligament balancing in total knee arthroplasty: how important is it? A systematic review of the literature. *Orthopedic reviews*, 1 (2), e26.

Bartel, D. L., Bicknell, V. L. and Wright, T. M., 1986. The effect of conformity, thickness, and material on stresses in ultra-high molecular weight components for total joint replacement. *The Journal of bone and joint surgery. American volume*, 68 (7), 1041–1051.

Batailler, C., Swan, J., Marinier, E. S., Servien, E. and Lustig, S., 2021. Current role of intraoperative sensing technology in total knee arthroplasty. *Archives of Orthopaedic and Trauma Surgery*, 141 (12), 2255–2265.

Beale, M. H., Hagan, M. T. and Demuth, H. B., 2020. Deep Learning Toolbox [TM] User's Guide How to Contact MathWorks.

Bishop, C. M., 1995. Training with noise is equivalent to Tikhonov regularization. *Neural computation*, 7 (1), 108–116.

Blankevoort, L., Huiskes, R. and Lange, A. De, 1991. Recruitment of knee joint ligaments. *Journal of Biomechanical Engineering : Transactions of the ASME* [online], 113 (1), 94–103. Available from: https://asmedigitalcollection.asme.org/biomechanical/article-abstract/113/1/94/399269 [Accessed 8 Sep 2023].

Bozic, K. J., Kurtz, S. M., Lau, E., Ong, K., Chiu, V., Vail, T. P., Rubash, H. E. and Berry, D. J., 2010. The epidemiology of revision total knee arthroplasty in the United States. *Clinical orthopaedics and related research*, 468 (1), 45–51.

Bull, A. M. J., Kessler, O., Alam, M. and Amis, A. A., 2008. Changes in knee kinematics reflect the articular geometry after arthroplasty. Clinical Orthopaedics and Related Research, 466 (10), 2491–2499.

Cho, K.-J., Seon, J.-K., Jang, W.-Y., Park, C.-G. and Song, E.-K., 2018. Objective quantification of ligament balancing using VERASENSE in measured resection and modified gap balance total knee arthroplasty. *BMC musculoskeletal disorders* [online], 19 (1), 266. Available from: https://pubmed.ncbi.nlm.nih.gov/30053812.

Choi, H. S., Lee, C. H., Shim, M., Han, J. I. and Baek, Y. S., 2018. Design of an Artificial Neural Network Algorithm for a Low-Cost Insole Sensor to Estimate the Ground Reaction Force (GRF) and Calibrate the Center of Pressure (CoP). *Sensors (Basel, Switzerland)*, 18 (12).

Chow, J. C. and Breslauer, L., 2017. The Use of Intraoperative Sensors Significantly Increases the Patient-Reported Rate of Improvement in Primary Total Knee Arthroplasty. *Orthopedics*, 40 (4), e648–e651.

Cochetti, A., Ghirardelli, S., Iannotti, F., Giardini, P., Risitano, S. and Pier, I., 2020. Sensor-guided technology helps to reproduce medial pivot kinematics in total knee arthroplasty. *Journal of orthopaedic surgery (Hong Kong)*, 28.

Cooper, S. B. and DiMaio, D., 2018. Static load estimation using artificial neural network: Application on a wing rib. *Advances in Engineering Software*, 125 (January), 113–125.

Crottet, D., Maeder, T., Fritschy, D., Bleuler, H., Nolte, L. P. and Pappas, I. P., 2005. Development of a force amplitude- and location-sensing device designed to improve the ligament balancing procedure in TKA. *IEEE transactions on bio-medical engineering*, 52 (9), 1609–1611.

Deckard, E. R., Ziemba-Davis, M. and Meneghini, R. M., 2022. Tibiofemoral Contact Forces Influence Intraoperative Kinematic Pivot Pattern Dependent on Posterior Cruciate Ligament Resection in Primary Total Knee Arthroplasty. *Journal of the American Academy of Orthopaedic Surgeons. Global research & reviews*, 6 (4).

Delanois, R. E., Mistry, J. B., Chughtai, M., Klika, A. K., Khlopas, A., Barsoum, W. K., Higuera, C. A., Bhave, A. and Mont, M. A., 2016. Novel Sensor Tibial Inserts in Total Knee Arthroplasty: A Review. *Surgical technology international*, 29, 255–260.

Dennis, D. A., Komistek, R. D., Mahfouz, M. R., Haas, B. D. and Stiehl, J. B., 2003. Conventry Award Paper: Multicenter Determination of In Vivo Kinematics After Total Knee Arthroplasty. *Clinical Orthopaedics and Related Research®* [online], 416. Available from: https://journals.lww.com/clinorthop/fulltext/2003/11000/conventry_award_paper_ _multicenter_determination.5.aspx.

D'Lima, D. D., Fregly, B. J., Patil, S., Steklov, N. and Colwell, C. W., 2012. Knee joint forces: Prediction, measurement, and significance. *Proceedings of the Institution of Mechanical Engineers, Part H: Journal of Engineering in Medicine*, 226 (2), 95–102.

D'Lima, D. D., Townsend, C. P., Arms, S. W., Morris, B. A. and Colwell Jr, C. W., 2005. An implantable telemetry device to measure intra-articular tibial forces. *Journal of biomechanics*, 38 (2), 299–304.

Doan, C. H. I. D. and Liong, S., 2004. Generalization for Multilayer Neural Network Bayesian Regularization or Early Stopping. *Network*, (119260), 1–8.

Draganich, L., Andersson, G., Andriacchi, T. P. and Galante, J., 1984. The effect of the cruciate ligaments in femoral-tibial contact movement during knee flexion. *Transactions of the 30th Annual Meeting of the Orthopedic Research Society, Atlanta*, 29.

Du, K. L. and Swamy, M. N. S., 2006. Neural networks in a softcomputing framework. *Neural Networks in a Softcomputing Framework*, 1–566.

Dungl , P., 2005. *Ortopedie*. Praha: Grada.

Edwards, E., Miller, J. and Chan, K. H., 1988. The effect of postoperative collateral ligament laxity in total knee arthroplasty. *Clinical orthopaedics and related research*, (236), 44–51.

Ellis, M. I., Seedhom, B. B., Wright, V. and Dowson, D., 1980. An Evaluation of the Ratio between the Tensions along the Quadriceps Tendon and the Patellar Ligament. *Engineering in Medicine* [online], 9 (4), 189–194. Available from: https://doi.org/10.1243/EMED_JOUR_1980_009_049_02.

Ellison, A. E. and Berg, E. E., 1985. Embryology, anatomy, and function of the anterior cruciate ligament. *The Orthopedic clinics of North America*, 16 (1), 3–14.

Elmallah, R. K., Mistry, J. B., Cherian, J. J., Chughtai, M., Bhave, A., Roche, M. W. and Mont, M. A., 2016. Can We Really 'Feel' a Balanced Total Knee Arthroplasty? *The Journal of arthroplasty*, 31 (9 Suppl), 102–105.

Fehring, T. K., 2000. Rotational Malalignment of the Femoral Component in Total Knee Arthroplasty. *Clinical Orthopaedics and Related Research®* [online], 380. Available from: https://journals.lww.com/clinorthop/Fulltext/2000/11000/Rotational_Malalignment _of_the_Femoral_Component.10.aspx.

Felson, D. T., Naimark, A., Anderson, J., Kazis, L., Castelli, W. and Meenan, R. F., 1987. The prevalence of knee osteoarthritis in the elderly. The Framingham Osteoarthritis Study. *Arthritis and rheumatism*, 30 (8), 914–918.

Fiorentini, N., Pellegrini, D. and Losa, M., 2022. Overfitting Prevention in Accident Prediction Models: Bayesian Regularization of Artificial Neural Networks. *Transportation Research Record* [online], 2677 (2), 1455–1470. Available from: https://doi.org/10.1177/03611981221111367.

Forchelet, D., Simoncini, M., Arami, A., Bertsch, A., Meurville, E., Aminian, K., Ryser, P. and Renaud, P., 2014. Enclosed electronic system for force measurements in knee implants. *Sensors (Switzerland)*, 14 (8), 15009–15021.

Foresee, F. D. and Hagan, M. T., 1997. Gauss-Newton approximation to Bayesian learning. *Proceedings of International Conference on Neural Networks (ICNN'97)* [online], 3, 1930–1935 vol.3. Available from: https://api.semanticscholar.org/CorpusID:18793440.

Del Gaizo, D. J. and Della Valle, C. J., 2011. Instability in primary total knee arthroplasty. *Orthopedics*, 34 (9), e519-21.

Gavin, H. P., 2019. The Levenberg-Marquardt Algorithm For Nonlinear Least Squares Curve-Fitting Problems. *Duke University* [online], 1–19. Available from: http://people.duke.edu/~hpgavin/ce281/lm.pdf.

Ge, J., Sun, X., Liu, C., Zhang, Q., Wang, B. and Guo, W., 2023. Intraoperative sensor technology quantifies inter-prosthesis pressure for predicting lower limb alignment after Oxford unicompartmental knee arthroplasty. *Frontiers in Bioengineering and Biotechnology*, 11 (August), 1–9.

Ghirardelli, S., Bala, A., Peretti, G., Antonini, G. and Indelli, P. F., 2019. Intraoperative Sensing Technology to Achieve Balance in Primary Total Knee Arthroplasty: A Review of the Literature. *JBJS Reviews*, 7 (10), 1–6.

Gianotti, S. M., Marshall, S. W., Hume, P. A. and Bunt, L., 2009. Incidence of anterior cruciate ligament injury and other knee ligament injuries: a national population-based study. *Journal of science and medicine in sport*, 12 (6), 622–627.

Godbole, V., Dahl, G. E., Gilmer, J., Shallue, C. J. and Nado, Z., 2023. *Deep Learning Tuning Playbook* [online]. Google for Developers. Available from: http://github.com/google-research/tuning_playbook [Accessed 14 Dec 2023].

Golladay, G. J., Bradbury, T. L., Gordon, A. C., Fernandez-Madrid, I. J., Krebs, V. E., Patel, P. D., Suarez, J. C., Higuera Rueda, C. A. and Barsoum, W. K., 2019. Are Patients More Satisfied With a Balanced Total Knee Arthroplasty? *The Journal of arthroplasty*, 34 (7S), S195–S200.

Graichen, F., Arnold, R., Rohlmann, A. and Bergmann, G., 2007. Implantable 9-channel telemetry system for in vivo load measurements with orthopedic implants. *IEEE Transactions on Biomedical Engineering*, 54 (2), 253–261.

Gustke (a), K., Golladay, G. J., Roche, M. W., Elson, L. C. and Anderson, C. R., 2014. Primary TKA Patients with Quantifiably Balanced Soft-Tissue Achieve Significant Clinical Gains Sooner than Unbalanced Patients. *Advances in orthopedics*, 2014, 628695.

Gustke (b), K., Golladay, G. J., Roche, M. W., Jerry, G. J., Elson, L. C. and Anderson, C. R., 2014. Increased satisfaction after total knee replacement using sensor-guided technology. *The bone & joint journal*, 96-B (10), 1333–1338.

Gustke (c), K., Golladay, G. J., Roche, M. W., Elson, L. C. and Anderson, C. R., 2014. A new method for defining balance: promising short-term clinical outcomes of sensor-guided TKA. *The Journal of arthroplasty*, 29 (5), 955–960.

Gustke (d), K. A., 2014. Soft-tissue and alignment correction. *The Bone & Joint Journal* [online], 96-B (11_Supple_A), 78–83. Available from: https://doi.org/10.1302/0301-620X.96B11.34339.

Gustke, K., 2012. Use of smart trials for soft-tissue balancing in total knee replacement surgery. *The Journal of bone and joint surgery. British volume*, 94 (11 Suppl A), 147–150.

Gustke, K. A., Golladay, G. J., Roche, M. W., Elson, L. C. and Anderson, C. R., 2017. A Targeted Approach to Ligament Balancing Using Kinetic Sensors. *The Journal of arthroplasty* [online], 32 (7), 2127–2132. Available from: https://pubmed.ncbi.nlm.nih.gov/28285037/ [Accessed 26 Jul 2023].

Halawi, M. J., Jongbloed, W., Baron, S., Savoy, L., Williams, V. J. and Cote, M. P., 2019. Patient dissatisfaction after primary total joint arthroplasty: the patient perspective. *The Journal of arthroplasty*, 34 (6), 1093–1096.

Halewood, C. and Amis, A. A., 2015. Clinically relevant biomechanics of the knee capsule and ligaments. *Knee Surgery, Sports Traumatology, Arthroscopy* [online], 23 (10), 2789–2796. Available from: https://link.springer.com/article/10.1007/s00167-015-3594-8 [Accessed 8 Sep 2023].

Han, S.-H., Kim, K. W., Kim, S. and Youn, Y. C., 2018. Artificial Neural Network: Understanding the Basic Concepts without Mathematics. *Dementia and neurocognitive disorders*, 17 (3), 83–89.

Hasenkamp, W., Thevenaz, N., Villard, J., Bertsch, A., Arami, A., Aminian, K., Terrier, A. and Renaud, P., 2013. Design and test of a MEMS strain-sensing device for monitoring artificial knee implants. *Biomedical Microdevices*, 15 (5), 831–839.

Hashemi, J., Breighner, R., Chandrashekar, N., Hardy, D. M., Chaudhari, A. M., Shultz, S. J., Slauterbeck, J. R. and Beynnon, B. D., 2011. Hip extension, knee flexion paradox: A new mechanism for non-contact ACL injury. *Journal of Biomechanics*, 44 (4), 577–585.

Hashimoto, S., Oshima, A., Ohsawa, T., Ueno, A., Omae, H., Takase, R., Kaneko, S. and Chikuda, H., 2022. An Analysis of the Medial Pivot Pattern in Intraoperative Kinematics Using a CT-Free Navigation System Improved Patient-Reported Outcomes of Total Knee Arthroplasty. *SSRN Electronic Journal*, 1–16.

Heinlein, B., Kutzner, I., Graichen, F., Bender, A., Rohlmann, A., Halder, A. M., Beier, A. and Bergmann, G., 2009. ESB Clinical Biomechanics Award 2008: Complete data of total knee replacement loading for level walking and stair climbing measured in vivo with a follow-up of 6-10 months. *Clinical biomechanics (Bristol, Avon)*, 24 (4), 315–326.

Holbert, S. E., Brennan, J., Cattaneo, S., King, P., Turcotte, J. and MacDonald, J., 2023. Trends in the reasons for revision total knee arthroplasty. *Journal of Orthopaedics, Trauma and Rehabilitation* [online], 0 (0), 22104917231176572. Available from: https://doi.org/10.1177/22104917231176573.

Holmstrom, L. and Koistinen, P., 1992. Using additive noise in back-propagation training. *IEEE transactions on neural networks*, 3 (1), 24–38.

Hood, R. W., Wright, T. M. and Burstein, A. H., 1983. Retrieval analysis of total knee prostheses: a method and its application to 48 total condylar prostheses. *Journal of biomedical materials research*, 17 (5), 829–842.

Huberti, H. H., Hayes, W. C., Stone, J. L. and Shybut, G. T., 1984. Force ratios in the quadriceps tendon and ligamentum patellae. *Journal of orthopaedic research : official publication of the Orthopaedic Research Society*, 2 (1), 49–54.

Hungerford, D. S. and Barry, M., 1979. Biomechanics of the patellofemoral joint. *Clinical orthopaedics and related research*, (144), 9–15.

Isaev, I. and Dolenko, S., 2016. Training with noise as a method to increase noise resilience of neural network solution of inverse problems. *Optical Memory and Neural Networks*, 25, 142–148.

Isaev, I. and Dolenko, S., 2018. Training with Noise Addition in Neural Network Solution of Inverse Problems: Procedures for Selection of the Optimal Network∗∗This study has been conducted at the expense of Russian Science Foundation, grant no. 14-11-00579. *Procedia Computer Science* [online], 123, 171–176. Available from: https://www.sciencedirect.com/science/article/pii/S1877050918300292.

Ives, L., Pace, A., Bor, F., Jing, Q., Wade, T., Cama, J., Khanduja, V. and Kar-Narayan, S., 2022. Conformable and robust microfluidic force sensors to enable precision joint replacement surgery. *Materials and Design* [online], 219, 110747. Available from: https://doi.org/10.1016/j.matdes.2022.110747.

Iwaki, H., Pinskerova, V. and Freeman, M. A. R., 2000. Tibiofemoral movement 1: The shape and relative movements of the femur and tibia in the unloaded cadaver knee. *Journal of Bone and Joint Surgery - Series B*, 82 (8), 1189–1195.

Jacobs, C. A., Christensen, C. P. and Karthikeyan, T., 2016. Greater Medial Compartment Forces During Total Knee Arthroplasty Associated With Improved Patient Satisfaction and Ability to Navigate Stairs. *The Journal of arthroplasty*, 31 (9 Suppl), 87–90.

Jain, M., Hossain, N. A., Towfighian, S., Willing, R., Stanacevic, M. and Salman, E., 2021. Self-Powered Load Sensing Circuitry for Total Knee Replacement. *IEEE Sensors Journal*, 21 (20), 22967–22975.

Jeffcote, B., Nicholls, R., Schirm, A. and Kuster, M. S., 2007. The variation in medial and lateral collateral ligament strain and tibiofemoral forces following changes in the flexion and extension gaps in total knee replacement. *The Journal of Bone & Joint Surgery British Volume* [online], 89-B (11), 1528–1533. Available from: https://doi.org/10.1302/0301-620X.89B11.18834.

Jiang, C. and Zhang, Y., 2023. A Noise-Based Novel Strategy for Faster SNN Training. *Neural Computation* [online], 35 (9), 1593–1608. Available from: https://doi.org/10.1162/neco%5C_a%5C_01604.

Jiang, H., Xiang, S., Guo, Y. and Wang, Z., 2019. A wireless visualized sensing system with prosthesis pose reconstruction for total knee arthroplasty. *Sensors (Switzerland)*, 19 (13).

Kallala, R. F., Vanhegan, I. S., Ibrahim, M. S., Sarmah, S. and Haddad, F. S., 2015. Financial analysis of revision knee surgery based on NHS tariffs and hospital costs. *The Bone & Joint Journal* [online], 97-B (2), 197–201. Available from: https://doi.org/10.1302/0301-620X.97B2.33707.

Kappel, A., Laursen, M., Nielsen, P. T. and Odgaard, A., 2018. Relationship between outcome scores and knee laxity following total knee arthroplasty: a systematic review. *Acta Orthopaedica* [online], 90 (1), 46–52. Available from: https://actaorthop.org/actao/article/view/429.

Kaufman, K. R., Kovacevic, N., Irby, S. E. and Colwell, C. W., 1996. Instrumented implant for measuring tibiofemoral forces. *Journal of Biomechanics*, 29 (5), 667–671.

Kebbach, M., Grawe, R., Geier, A., Winter, E., Bergschmidt, P., Kluess, D., D'Lima, D., Woernle, C. and Bader, R., 2019. Effect of surgical parameters on the

biomechanical behaviour of bicondylar total knee endoprostheses – A robot-assisted test method based on a musculoskeletal model. *Scientific Reports*, 9, 1–11.

Kubíček, M. and Florian, Z., 2009. Stress Strain Analysis of Knee Joint. *Engineering Mechanics*, 16 (5), 315–322.

Kuriyama, S., Nishitani, K., Nakamura, S. and Matsuda, S., 2023. An electronic force sensor accurately detects increased but not decreased soft tissue tension in total knee arthroplasty. *Knee* [online], 42, 210–219. Available from: https://doi.org/10.1016/j.knee.2023.03.020.

Kuster, M. S., Bitschnau, B. and Votruba, T., 2004. Influence of collateral ligament laxity on patient satisfaction after total knee arthroplasty: a comparative bilateral study. *Archives of orthopaedic and trauma surgery*, 124 (6), 415–417.

Kuster, M. S., Wood, G. A., Stachowiak, G. W. and Gächter, A., 1997. Joint load considerations in total knee replacement. *The Journal of bone and joint surgery. British volume*, 79 (1), 109–113.

Kutzner, I., Heinlein, B., Graichen, F., Bender, A., Rohlmann, A., Halder, A., Beier, A. and Bergmann, G., 2010. Loading of the knee joint during activities of daily living measured in vivo in five subjects. *Journal of biomechanics*, 43 (11), 2164–2173.

Kwon, S. K., Kwon, H. M., Kong, Y. and Park, K. K., 2017. The impact of generalized joint laxity on clinical outcomes of total knee arthroplasty. *Knee Surgery, Sports Traumatology, Arthroscopy* [online], 25 (11), 3360–3365. Available from: https://doi.org/10.1007/s00167-017-4486-x.

LaPrade, R. F., Heikes, C., Bakker, A. J. and Jakobsen, R. B., 2008. The reproducibility and repeatability of varus stress radiographs in the assessment of isolated fibular collateral ligament and grade-III posterolateral knee injuries. An in vitro biomechanical study. *The Journal of bone and joint surgery. American volume*, 90 (10), 2069–2076.

Lau, K.-T., Guo, W., Kiernan, B., Slater, C. and Diamond, D., 2009. Non-linear carbon dioxide determination using infrared gas sensors and neural networks with Bayesian regularization. *Sensors and Actuators B: Chemical*, 136 (1), 242–247.

Le, T.-T., 2020. Surrogate Neural Network Model for Prediction of Load-Bearing Capacity of CFSS Members Considering Loading Eccentricity. *Applied Sciences* [online], 10 (10). Available from: https://www.mdpi.com/2076-3417/10/10/3452.

Ledet, E. H., Liddle, B., Kradinova, K. and Harper, S., 2018. Smart implants in orthopedic surgery, improving patient outcomes: a review. *Innov Entrep Health*, 41–51.

Lee, T. Q., 2014. Biomechanics of hyperflexion and kneeling before and after total knee arthroplasty. *Clinics in orthopedic surgery*, 6 (2), 117–126.

Lombardi Jr, A. v, Berend, K. R. and Adams, J. B., 2014. Why knee replacements fail in 2013: patient, surgeon, or implant? *The bone & joint journal*, 96 (11_Supple_A), 101–104.

MacKay, D. J. C., 1992. Bayesian Interpolation. *Neural Comput.* [online], 4 (3), 415–447. Available from: https://doi.org/10.1162/neco.1992.4.3.415.

Malekjafarian, A., OBrien, E. J. and Micu, L. A., 2017. Investigation of Buckling Capacity of Metal Materials Manufactured by Laser 3D Printing. *Procedia Manufacturing* [online], 7, 696–700. Available from: https://www.sciencedirect.com/science/article/pii/S2351978916302669.

Manning, W. A., Blain, A., Longstaff, L. and Deehan, D. J., 2019. A load-measuring device can achieve fine-tuning of mediolateral load at knee arthroplasty but may

lead to a more lax knee state. *Knee surgery, sports traumatology, arthroscopy : official journal of the ESSKA*, 27 (7), 2238–2250.

Manning, W., Ghosh, M., Wilson, I., Hide, G., Longstaff, L. and Deehan, D., 2020. Improved mediolateral load distribution without adverse laxity pattern in robot-assisted knee arthroplasty compared to a standard manual measured resection technique. *Knee Surgery, Sports Traumatology, Arthroscopy* [online], 28 (9), 2835–2845. Available from: https://doi.org/10.1007/s00167-019-05631-y.

Matsuda, Y., Ishii, Y., Noguchi, H. and Ishii, R., 2005. Varus-valgus balance and range of movement after total knee arthroplasty. *Journal of Bone and Joint Surgery - Series B*, 87 (6), 804–808.

Matsumoto, T., Muratsu, H., Kubo, S., Matsushita, T., Kurosaka, M. and Kuroda, R., 2011. The influence of preoperative deformity on intraoperative soft tissue balance in posterior-stabilized total knee arthroplasty. *The Journal of arthroplasty*, 26 (8), 1291–1298.

Matsuoka, K., 1992. Noise injection into inputs in back-propagation learning. *IEEE Transactions on Systems, Man, and Cybernetics*, 22 (3), 436–440.

Meere, P. A., Schneider, S. M. and Walker, P. S., 2016. Accuracy of Balancing at Total Knee Surgery Using an Instrumented Tibial Trial. *The Journal of arthroplasty*, 31 (9), 1938–1942.

Meloni, M. C., Hoedemaeker, R. W., Violante, B. and Mazzola, C., 2014. Soft tissue balancing in total knee arthroplasty. *Joints*, 2 (1), 37–40.

Meneghini, R. M., Deckard, E. R., Ishmael, M. K. and Ziemba-Davis, M., 2017. A Dual-Pivot Pattern Simulating Native Knee Kinematics Optimizes Functional Outcomes After Total Knee Arthroplasty. *Journal of Arthroplasty* [online], 32 (10), 3009–3015. Available from: http://dx.doi.org/10.1016/j.arth.2017.04.050.

Meneghini, R. M., Ziemba-Davis, M. M., Lovro, L. R., Ireland, P. H. and Damer, B. M., 2016. Can Intraoperative Sensors Determine the 'Target' Ligament Balance? Early Outcomes in Total Knee Arthroplasty. *The Journal of arthroplasty*, 31 (10), 2181–2187.

Moonot, P., Mu, S., Railton, G. T., Field, R. E. and Banks, S. A., 2009. Tibiofemoral kinematic analysis of knee flexion for a medial pivot knee. *Knee Surgery, Sports Traumatology, Arthroscopy*, 17 (8), 927–934.

Mouloodi, S., Rahmanpanah, H., Burvill, C. and Davies, H. M. S., 2020. Prediction of load in a long bone using an artificial neural network prediction algorithm. *Journal of the Mechanical Behavior of Biomedical Materials* [online], 102, 103527. Available from: https://www.sciencedirect.com/science/article/pii/S1751616119305600.

Moussa, M. E., Lee, Y.-Y., Westrich, G. H., Mehta, N., Lyman, S. and Marx, R. G., 2017. Comparison of Revision Rates of Non-modular Constrained Versus Posterior Stabilized Total Knee Arthroplasty: a Propensity Score Matched Cohort Study. *HSS journal : the musculoskeletal journal of Hospital for Special Surgery*, 13 (1), 61–65.

Muertizha, M., Cai, X., Ji, B., Aimaiti, A. and Cao, L., 2022. Factors contributing to 1-year dissatisfaction after total knee arthroplasty: a nomogram prediction model. *Journal of Orthopaedic Surgery and Research* [online], 17 (1), 367. Available from: https://doi.org/10.1186/s13018-022-03205-2.

Munro, P., 2010. Backpropagation BT - Encyclopedia of Machine Learning. *In*: Sammut, C. and Webb, G. I., eds. [online]. Boston, MA: Springer US, 73. Available from: https://doi.org/10.1007/978-0-387-30164-8_51.

Mutsuzaki, H., Takeuchi, R., Mataki, Y. and Wadano, Y., 2017. Target range of motion for rehabilitation after total knee arthroplasty. *Journal of Rural Medicine*, 12, 33–37.

Nicholls, R. L., Schirm, A. C., Jeffcote, B. O. and Kuster, M. S., 2007. Tibiofemoral force following total knee arthroplasty: Comparison of four prosthesis designs in vitro. *Journal of Orthopaedic Research*, 25 (11), 1506–1512.

Nicolet-Petersen, S. J., Howell, S. M. and Hull, M. L., 2018. Tibial contact force and contact location errors of the VERASENSE. *Journal of Biomechanical Engineering*, 140 (12), 1–6.

Nodzo, S. R., Franceschini, V. and Gonzalez Della Valle, A., 2017. Intraoperative Load-Sensing Variability During Cemented, Posterior-Stabilized Total Knee Arthroplasty. *The Journal of arthroplasty*, 32 (1), 66–70.

Nolten, U., Schmidt, F., Firmbach, F. P., Radermacher, K. and Mokwa, W., 2009. Sensor integrated tibial inlay for soft-tissue balancing. *Procedia Chemistry* [online], 1 (1), 1251–1254. Available from: http://dx.doi.org/10.1016/j.proche.2009.07.312.

Nordin, M., Frankel, V. H. and Yelle, L., 1989. *Basic Biomechanics of the Musculoskeletal System* [online]. Lea \& Febiger. Available from: https://books.google.co.uk/books?id=TNVqAAAAMAAJ.

Okazaki, K., Miura, H., Matsuda, S., Takeuchi, N., Mawatari, T., Hashizume, M. and Iwamoto, Y., 2006. Asymmetry of mediolateral laxity of the normal knee. *Journal of Orthopaedic Science* [online], 11 (3), 264–266. Available from: https://www.sciencedirect.com/science/article/pii/S0949265815325586.

Pande, S. and Dhatrak, P., 2021. Recent developments and advancements in knee implants materials, manufacturing: A review. *Materials Today: Proceedings* [online], 46, 756–762. Available from: https://doi.org/10.1016/j.matpr.2020.12.465.

Parcells, B., 2017. *Hip and Knee Book* [online]. Basics of Arthroplasty Textbok. Available from: https://hipandkneebook.com/ [Accessed 3 Feb 2022].

Park, C. H. and Song, S. J., 2021. Sensor-Assisted Total Knee Arthroplasty: A Narrative Review. *Clinics in orthopedic surgery*, 13 (1), 1–9.

Parratte, S. and Pagnano, M. W., 2008. Instability after total knee arthroplasty. *The Journal of bone and joint surgery. American volume*, 90 (1), 184–194.

Perera, A. T. K., Song, K., Umezu, S. and Sato, H., 2023. Recent progress in functionalized plastic 3D printing in creation of metallized architectures. *Materials & Design* [online], 232, 112044. Available from: https://www.sciencedirect.com/science/article/pii/S0264127523004598.

Perry, J., Antonelli, D. and Ford, W., 1975. Analysis of knee-joint forces during flexed-knee stance. *The Journal of bone and joint surgery. American volume*, 57 (7), 961–967.

Pinskerova, V. and Vavrik, P., 2020. Knee Anatomy and Biomechanics and its Relevance to Knee Replacement. *In*: Rivière, C. and Vendittoli, P.-A., eds. *Personalized Hip and Knee Joint Replacement* [online]. Cham: Springer International Publishing, 159–168. Available from: https://doi.org/10.1007/978-3-030-24243-5_14.

Prasad, N., Singh, R. and Lal, S. P., 2013. Comparison of Back Propagation and Resilient Propagation Algorithm for Spam Classification. *In*: *Proceedings of the 2013 Fifth International Conference on Computational Intelligence, Modelling and*

Simulation [online]. USA: IEEE Computer Society, 29–34. Available from: https://doi.org/10.1109/CIMSim.2013.14.

Rafati, J. and Marica, R. F., 2020. Quasi-Newton Optimization Methods for Deep Learning Applications BT - Deep Learning Applications. *In*: Wani, M. A., Kantardzic, M., and Sayed-Mouchaweh, M., eds. [online]. Singapore: Springer Singapore, 9–38. Available from: https://doi.org/10.1007/978-981-15-1816-4_2.

Rao, A. R. and Kumar, B., 2007. Neural modeling of square surface aerators. *Journal of Environmental Engineering* [online], 133 (4), 411 – 418. Available from: https://www.scopus.com/inward/record.uri?eid=2-s2.0-34547624150&doi=10.1061%2F%28ASCE%290733-9372%282007%29133%3A4%28411%29&partnerID=40&md5=d3568ef52fe6fdce470f86e7dd3caf0f.

Risitano, S., Karamian, B. and Indelli, P. F., 2017. Intraoperative load-sensing drives the level of constraint in primary total knee arthroplasty: Surgical technique and review of the literature. *Journal of clinical orthopaedics and trauma* [online], 8 (3), 265–269. Available from: https://pubmed.ncbi.nlm.nih.gov/28951645.

Robitaille, B., Marcos, B., Veillette, M. and Payre, G., 1996. Modified Quasi-Newton methods for training neural networks. *Computers and Chemical Engineering*, 20 (9), 1133–1140.

Roche, M., Elson, L. and Anderson, C., 2014. Dynamic Soft Tissue Balancing in Total Knee Arthroplasty. *The Orthopedic clinics of North America*, 45, 157–165.

Rodriguez-Merchan, E. C., 2011. Instability following total knee arthroplasty. *HSS journal : the musculoskeletal journal of Hospital for Special Surgery* [online], 7 (3), 273–278. Available from: https://pubmed.ncbi.nlm.nih.gov/23024625.

Rönn, K., Reischl, N., Gautier, E. and Jacobi, M., 2011. Current surgical treatment of knee osteoarthritis. *Arthritis*, 2011, 454873.

Roth, J. D., Howell, S. M. and Hull, M. L., 2017. An Improved Tibial Force Sensor to Compute Contact Forces and Contact Locations In Vitro After Total Knee Arthroplasty. *Journal of biomechanical engineering*, 139 (4).

Roth, J. D., Howell, S. M. and Hull, M. L., 2021. Tibial forces are more useful than varus-valgus laxities for identifying and correcting overstuffing in kinematically aligned total knee arthroplasty. *Journal of Orthopaedic Research* [online], 39 (6), 1271–1280. Available from: https://doi.org/10.1002/jor.24779.

Roussot, M. A. and Haddad, F. S., 2019. The evolution of patellofemoral prosthetic design in total knee arthroplasty: How far have we come? *EFORT Open Reviews*, 4 (8), 503–512.

Rowe, P. J., Myles, C. M., Walker, C. and Nutton, R., 2000. Knee joint kinematics in gait and other functional activities measured using flexible electrogoniometry: how much knee motion is sufficient for normal daily life? *Gait & posture*, 12 (2), 143–155.

Sabatini, L., Bosco, F., Barberis, L., Camazzola, D., Bistolfi, A., Risitano, S., Massè, A. and Indelli, P. F., 2021. Kinetic sensors for ligament balance and kinematic evaluation in anatomic bi-cruciate stabilized total knee arthroplasty. *Sensors*, 21 (16).

Safaei, M., Dupre, S., Hoummadi, E. and Anton, S. R., 2019. Design, analysis, and fabrication of a piezoelectric force tray for total knee replacements. *Journal of Intelligent Material Systems and Structures*, 30 (20), 3163–3176.

Sanz-Pena, I., Zapata, G. E., Verstraete, M. A., Meere, P. A. and Walker, P. S., 2019. Relationship Between Ligament Forces and Contact Forces in Balancing at Total Knee Surgery. *The Journal of arthroplasty*, 34 (6), 1261–1266.

Schnaser, E., Lee, Y. yu, Boettner, F. and Gonzalez Della Valle, A., 2015. The Position of the Patella and Extensor Mechanism Affects Intraoperative Compartmental Loads During Total Knee Arthroplasty: A Pilot Study Using Intraoperative Sensing to Guide Soft Tissue Balance. *Journal of Arthroplasty* [online], 30 (8), 1348-1353.e3. Available from: http://dx.doi.org/10.1016/j.arth.2015.03.004.

Shah, D. S., Taylan, O., Verstraete, M., Berger, P., Vandenneucker, H. and Scheys, L., 2021. Can intraoperative intra-articular loads predict postoperative knee joint laxity following total knee arthroplasty? A cadaver study with smart tibial trays. *Sensors*, 21 (15).

Shalhoub, S., Lawrence, J. M., Keggi, J. M., Randall, A. L., DeClaire, J. H. and Plaskos, C., 2019. Imageless, robotic-assisted total knee arthroplasty combined with a robotic tensioning system can help predict and achieve accurate postoperative ligament balance. *Arthroplasty today*, 5 (3), 334–340.

Sharkey, P. F., Lichstein, P. M., Shen, C., Tokarski, A. T. and Parvizi, J., 2014. Why are total knee arthroplasties failing today—has anything changed after 10 years? *The Journal of arthroplasty*, 29 (9), 1774–1778.

Sietsma, J. and Dow, R. J. F., 1988. Neural net pruning-why and how. *IEEE 1988 International Conference on Neural Networks* [online], 325–333 vol.1. Available from: https://api.semanticscholar.org/CorpusID:15320568.

Skrinskas, T. V, Viskontas, D. G., Ferreira, L., Chess, D. G. and Johnson, J. A., 2003. Application of an Intra-operative Load Measuring, 246–253.

Somireddy, M. and Czekanski, A., 2020. Anisotropic material behavior of 3D printed composite structures – Material extrusion additive manufacturing. *Materials & Design* [online], 195, 108953. Available from: https://www.sciencedirect.com/science/article/pii/S0264127520304871.

Song, S. J., Kang, S. G., Lee, Y. J., Kim, K. Il and Park, C. H., 2019. An intraoperative load sensor did not improve the early postoperative results of posterior-stabilized TKA for osteoarthritis with varus deformities. *Knee surgery, sports traumatology, arthroscopy : official journal of the ESSKA*, 27 (5), 1671–1679.

Song, S. J., Lee, H. W., Kim, K. Il and Park, C. H., 2020. Load imbalances existed as determined by a sensor after conventional gap balancing with a tensiometer in total knee arthroplasty. *Knee Surgery, Sports Traumatology, Arthroscopy*, 28 (9), 2953–2961.

Spoerk, M., Holzer, C. and Gonzalez-Gutierrez, J., 2020. Material extrusion-based additive manufacturing of polypropylene: A review on how to improve dimensional inaccuracy and warpage. *Journal of Applied Polymer Science* [online], 137 (12), 48545. Available from: https://onlinelibrary.wiley.com/doi/abs/10.1002/app.48545.

Steinkamp, L. A., Dillingham, M. F., Markel, M. D., Hill, J. A. and Kaufman, K. R., 1993. Biomechanical considerations in patellofemoral joint rehabilitation. *The American journal of sports medicine*, 21 (3), 438–444.

Szivek, J. A., Anderson, P. L. and Benjamin, J. B., 1996. Average and peak contact stress distribution evaluation of total knee arthroplasties. *The Journal of arthroplasty*, 11 (8), 952–963.

Traina, F., Fine, M. D. and Affatato, S., 2013. Anatomy of the hip and suitable prostheses. *Wear of Orthopaedic Implants and Artificial Joints*, 93–114.

Tzanetis, P., Marra, M. A., Fluit, R., Koopman, B. and Verdonschot, N., 2021. Biomechanical consequences of tibial insert thickness after total knee arthroplasty: A musculoskeletal simulation study. *Applied Sciences (Switzerland)*, 11 (5).

Unitt, L., Sambatakakis, A., Johnstone, D. and Briggs, T. W. R., 2008. Short-term outcome in total knee replacement after soft-tissue release and balancing. *The Journal of bone and joint surgery. British volume*, 90 (2), 159–165.

Verstraete, M. A., Meere, P. A., Salvadore, G., Victor, J. and Walker, P. S., 2017. Contact forces in the tibiofemoral joint from soft tissue tensions: Implications to soft tissue balancing in total knee arthroplasty. *Journal of Biomechanics*, 58, 195–202.

Walker, L. C., Clement, N. D., Ghosh, K. M. and Deehan, D. J., 2018. What is a balanced knee replacement? *EFORT open reviews*, 3 (12), 614–619.

Walker, P. S., Meere, P. A. and Bell, C. P., 2014. Effects of surgical variables in balancing of total knee replacements using an instrumented tibial trial. *The Knee*, 21 (1), 156–161.

Wang, C. and Principe, J. C., 1999. Training neural networks with additive noise in the desired signal. *IEEE Transactions on Neural Networks*, 10 (6), 1511–1517.

Wang, F.-X., Wu, Z.-Y., Lin, Q.-H., Chen, T., Kuang, S.-L., Gan, M.-F., Huang, L.-X. and Sun, L.-N., 2022. Novel Force Measurement System for Soft Tissue Balance in Total Knee Arthroplasty Based on Flexible Pressure Sensor Arrays. *Advanced Intelligent Systems*, 4 (4), 2100156.

Wasielewski, R. C., Galat, D. D. and Komistek, R. D., 2004. An intraoperative pressure-measuring device used in total knee arthroplasties and its kinematics correlations. *Clinical Orthopaedics and Related Research*, 427 (427), 171–178.

Watanabe, T., Koga, H., Katagiri, H., Otabe, K., Nakagawa, Y., Muneta, T., Sekiya, I. and Jinno, T., 2020. Coronal and sagittal laxity affects clinical outcomes in posterior-stabilized total knee arthroplasty: assessment of well-functioning knees. *Knee Surgery, Sports Traumatology, Arthroscopy* [online], 28 (5), 1400–1409. Available from: https://doi.org/10.1007/s00167-019-05500-8.

Watanabe, T., Muneta, T., Sekiya, I. and Banks, S. A., 2013. Intraoperative Joint Gaps Affect Postoperative Range of Motion in TKAs With Posterior-stabilized Prostheses. *Clinical Orthopaedics and Related Research®* [online], 471 (4). Available from: https://journals.lww.com/clinorthop/Fulltext/2013/04000/Intraoperative_Joint_Gaps_Affect_Postoperative.41.aspx.

Winemaker, M. J., 2002. Perfect balance in total knee arthroplasty: The elusive compromise. *The Journal of Arthroplasty* [online], 17 (1), 2–10. Available from: https://www.sciencedirect.com/science/article/pii/S0883540302929840.

Wismans, J., Veldpaus, F., Janssen, J., Huson, A. and Struben, P., 1980. A three-dimensional mathematical model of the knee-joint. Journal of Biomechanics [online], 13 (8), 677–685. Available from: https://www.sciencedirect.com/science/article/pii/0021929080903541.

Wood, T. J., Winemaker, M. J., Williams, D. S., Petruccelli, D. T., Tushinski, D. M. and de Beer, J. de v, 2021. Randomized Controlled Trial of Sensor-Guided Knee Balancing Compared to Standard Balancing Technique in Total Knee Arthroplasty. *The Journal of Arthroplasty* [online], 36 (3), 953–957. Available from: https://doi.org/10.1016/j.arth.2020.09.025.

Wright, W. A., Ramage, G., Cornford, D. and Nabney, I. T., 2000. Neural network modelling with input uncertainty: Theory and application. *Journal of VLSI Signal Processing Systems for Signal, Image, and Video Technology*, 26 (1), 169–188.

Wu, J., Wang, G., Ye, D. and Wang, Y., 2009. A new system for soft-tissue alance easurement in total knee replacement. *IEEE Transactions on Instrumentation and Measurement*, 58 (10), 3627–3632.

Wu, M. and Wang, J., 2021. Estimating Contact Force Chains Using Artificial Neural Network. *Applied Sciences* [online], 11 (14). Available from: https://www.mdpi.com/2076-3417/11/14/6278.

Xiao, L., Zhang, Z., Jiang, J. and Peng, Y., 2022. Noise optimization in artificial neural networks. *In*: *2022 IEEE 18th International Conference on Automation Science and Engineering (CASE)*. IEEE, 1595–1600.

Xie, D., Lv, F., Yang, Y., Shen, L., Tian, Z., Shuai, C., Chen, B. and Zhao, J., 2022. A Review on Distortion and Residual Stress in Additive Manufacturing. *Chinese Journal of Mechanical Engineering: Additive Manufacturing Frontiers* [online], 1 (3), 100039. Available from: https://www.sciencedirect.com/science/article/pii/S2772665722000216.

Yapp, L. Z., Robinson, P. G., Clement, N. D. and Scott, C. E. H., 2021. Total Knee Arthroplasty and Intra-Articular Pressure Sensors: Can They Assist Surgeons with Intra-Operative Decisions? *Current reviews in musculoskeletal medicine*, 14 (6), 361–368.

Yin, M., Liu, T., Li, T., Guan, Z., Zhang, K., Yin, S., Gou, G., Sun, J., Ma, T., Cheng, J., Chen, G., Liu, C. and Xue, N., 2023. Development of the Force Detecting Liner for Total Knee Arthroplasty. *IEEE Sensors Journal*, 23 (10), 10342–10349.

Yin, S., Liu, C., Zhang, Z., Lin, Y., Wang, D., Tejedor, J., Zheng, T. F. and Li, Y., 2015. Noisy training for deep neural networks in speech recognition. *EURASIP Journal on Audio, Speech, and Music Processing* [online], 2015 (1), 2. Available from: https://doi.org/10.1186/s13636-014-0047-0.

Yue, Z., Songzheng, Z. and Tianshi, L., 2011. Bayesian regularization BP Neural Network model for predicting oil-gas drilling cost. *In*: *2011 International Conference on Business Management and Electronic Information*. 483–487.

Zlotnicki, J. P., Naendrup, J.-H., Ferrer, G. A. and Debski, R. E., 2016. Basic biomechanic principles of knee instability. *Current reviews in musculoskeletal medicine*, 9 (2), 114–122.

Zur, R. M., Jiang, Y., Pesce, L. L. and Drukker, K., 2009. Noise injection for training artificial neural networks: a comparison with weight decay and early stopping. *Medical physics*, 36 (10), 4810–4818.

Appendix

A.I: Material Properties for Sensors
1. Aluminium Alloy

Aluminium Alloy 6082   **Material Data Sheet**

Scope

Aluminium alloy 6082 is a medium strength alloy with excellent corrosion resistance. It has the highest strength of 6000 series alloys. Alloy 6082 is known as a structural alloy. In plate form, 6082 is the alloy most commonly used for machining. As a relatively new alloy, the higher strength of 6082 has seen it replace 6061 in many applications. The addition of a large amount of manganese controls the grain structure which in turn results in a stronger alloy. It is difficult to produce to produce thin walled, complicated extrusion shapes in alloy 6082. The extruded surface finish is not as smooth as other similar strength alloys in the 6000 series. In the T6 and T651 temper, 6082 machines well and produces tight coils of swarf when chip breakers are used.

Application

This material is used for milk churns, trusses, cranes, ore skips, beer barrels, bridges, highly stressed applications and transport applications.

Supplied Forms

- Sheet
- Plate
- Extrusions
- Tube
- Bar

Alloy Designations

Aluminium alloy 6082 also corresponds to: AA6082, HE30, DIN 3.2315, EN AW-6082, ISO: Al Si1MgMn and A96082.

Temper Types

The most common tempers for 6082 aluminium are: O - Soft, T4 - Solution heat treated and naturally aged to a substantially stable condition, T6 - Solution heat treated and artificially aged and T651 - Solution heat treated, stress relieved by stretching then artificially aged.

Fabrication

- Solderability: Good
- Weldability – Gas: Good
- Weldability – Arc: Good
- Weldability - Resistance: Good
- Brazability: Good
- Workability – Cold: Good
- Machinability: Good

Chemical Composition

Element	% Present
Manganese (Mn)	0.40 - 1.00
Iron (Fe)	0.0 - 0.50
Magnesium (Mg)	0.60 - 1.20
Silicon (Si)	0.70 - 1.30
Copper (Cu)	0.0 - 0.10
Zinc (Zn)	0.0 - 0.20
Titanium (Ti)	0.0 - 0.10
Chromium (Cr)	0.0 - 0.25
Aluminium (Al)	Balance

Mechanical properties at room temperature

Property	Value
Proof Stress	310 MPa
Tensile Strength	340 MPa
Elongation	11%
Shear Strength	210 MPa
Hardness Vickers	100 HV

Properties above are for material in the T6 / T651 condition.

Reference data for some physical properties (for guidance only)

Property	Value
Density	2.70 Kg/m^3
Melting Point	555 °C
Thermal Expansion	24 x 10^{-6} /K
Modulus of Elasticity	70 GPa
Thermal Conductivity	180 W/m.K
Electrical Resistivity	0.038 x 10^{-6} Ω .m

2. PU Rigid 1000 Resin

MATERIAL PROPERTIES DATA   **PU Rigid 1000 Resin**

	METRIC [1]	IMPERIAL [1]	METHOD
	Post-Cured [2]	Post-Cured [2]	
Tensile Properties			
Ultimate Tensile Strength	35 ± 3.5 MPa	5 ± 0.5 ksi	ASTM D638
Young's Modulus	0.92 ± 0.09 GPa	133 ± 13 ksi	ASTM D638
Elongation at Break	80 ± 8%	80 ± 8%	ASTM D638
Flexural Properties			
Flexural Strength	32 ± 1.6 MPa	4.6 ± 0.2 ksi	ASTM D 790-15
Flexural Modulus	0.75 ± 0.03 GPa	109 ± 4.4 ksi	ASTM D 790-15
Ross Flexing Fatigue (unnotched)	> 50,000 cycles (PASS-no crack propagation)		ASTM D 1052 (23 °C)
Impact Properties			
Notched Izod	170 J/m	3.18 ft-lbs/in	ASTM D 256-10
Charpy Impact Test (Notched)	23 kJ/m^2	11 ft-lbs/in^2	ISO 179-1:2010(E)
Tabor Abrasion	177 mm^3	0.01 in^3	ISO 4649 (40rpm, 10N load)
Physical Properties			
Hardness	74D		ASTM D 2240
Density (solid)	1.16 g/cm^3	72.42 lb/ft^3	ASTM D 792-20
Viscosity (@ 25 °C)	1193 cP		
Viscosity (@ 35 °C)	567 cP		
Thermal Properties			
Heat Deflection Temp. @ 1.8 MPa	64 °C	147 °F	ASTM D 648-16
Heat Deflection Temp. @ 0.45 MPa	79 °C	174 °F	ASTM D 648-16
Thermal Expansion	142 μm/m/°C	78.9 μin/in/°F	ASTM E 813-13
Glass Transition Temperature (Tg1)	-22 °C	-8 °F	DMA*
Glass Transition Temperature (Tg2)	131 °C	268 °F	DMA*
Electrical Properties			
Dielectric Strength	1.8 x 10^7 V/m	460 V/mil	ASTM D149-20
Dielectric Constant	3.9		ASTM D 150, 0.5 MHz
Dielectric Constant	4.3		ASTM D 150, 1.0 MHz
Dissipation Factor	0.077		ASTM D 150, 0.5 MHz
Dissipation Factor	0.081		ASTM D 150, 1.0 MHz
Volume resistivity	6.5 x 10^{11} ohm-cm	2.56 x 10^{11} ohm-in	ASTM D257-14
Flammability Properties			
Flammability rating	HB		UL 94
Smoke Density	(D s 1.5) = 31 (PASS) (D s 4.0) = 244 (FAIL)		ASTM E662-21
Automotive Specific Testing			
Volatile Organic Compounds	199 μg/g	0.03 oz/lb	VOC VDA 278
Fogging	3.2 mg	1.1 x 10^{-4} oz	DIN 75201, Method B

3. Polypropylene Glass Beaded (PP GB)

Wrist guard

Cooling/A/C system part

Material Specification

Material Properties
Flexural strength: 33 MPa
Flexural modulus: 2000 MPa
Elongation at break: 58 %
Color: Light Grey

Advantages

> Cost Effective: Innovative and cost–effective material enabled by BASF Forward AM. It meets and exceeds the requirements of most printed components, which results in cost reduction and value increment significantly.

> High Rigidity: From prototype validation to functional parts, PP–GB exhibits excellent dimensional stability and high rigidity for demanding applications.
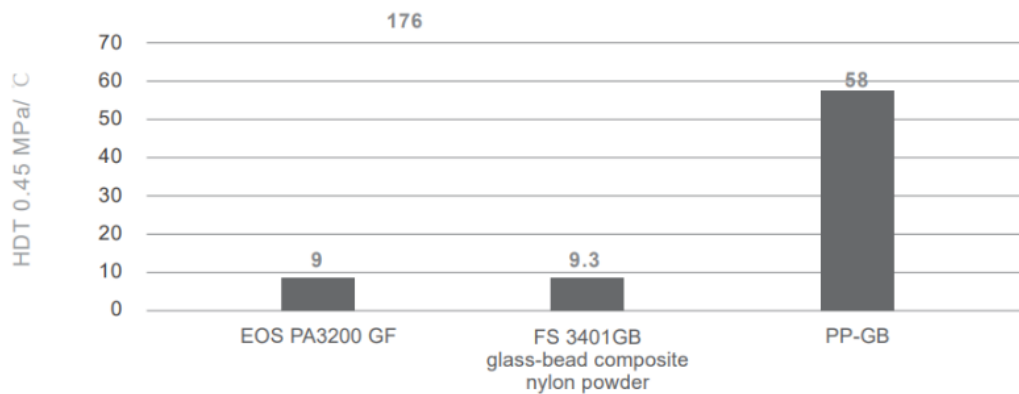
(PP-GB has higher toughness compared with other glass-bead materials.)

A.II: Engineering Drawings of Physical Sensor

1. Ring Design
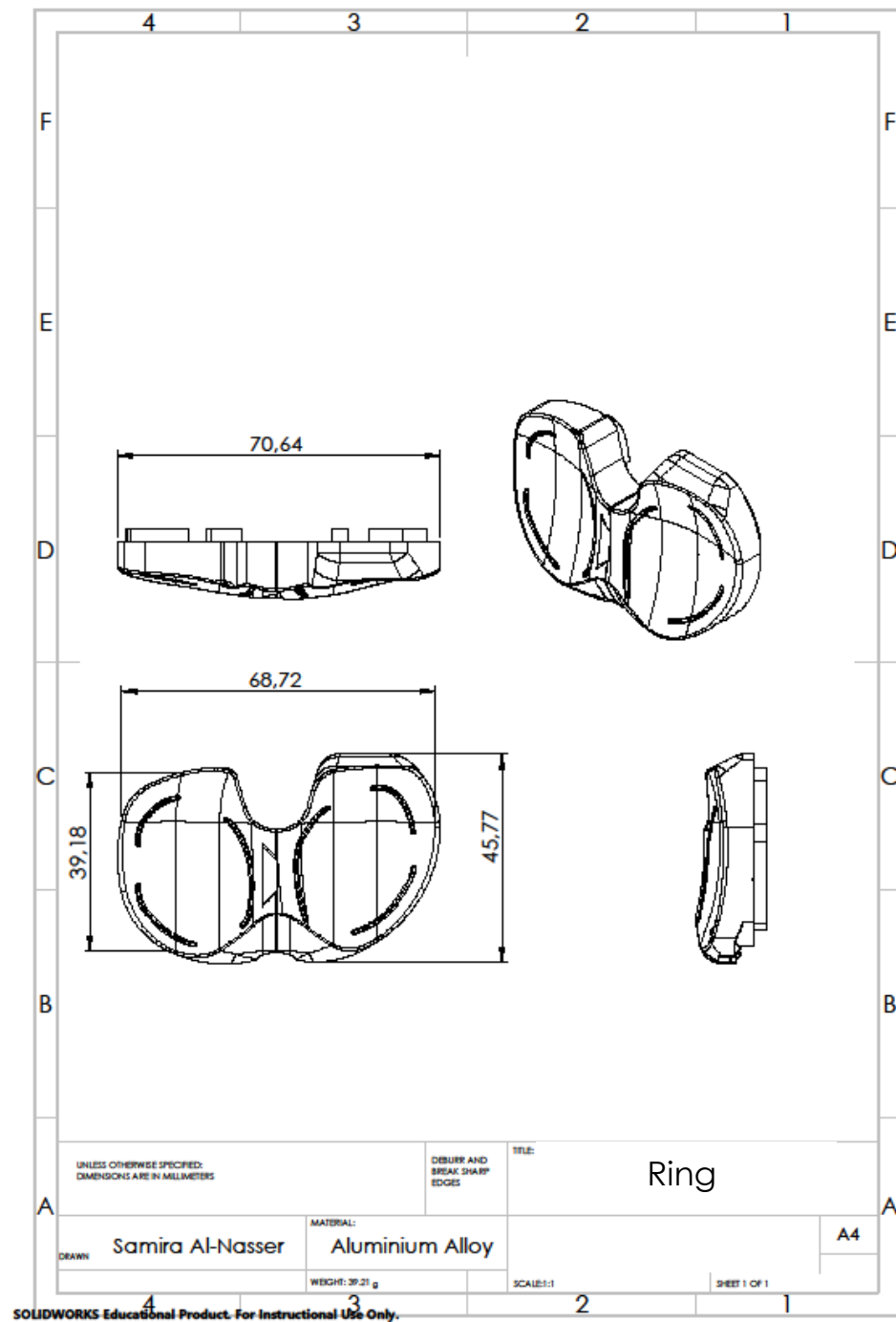
2. Zimmer Specific

70,64

43,07

45,77

1:1/6F

Name: Samira Al-Nasser

TITLE:
Zimmer Specific

MATERIAL:
Aluminium 6063-T83

WEIGHT: 21.82 g

SCALE:1:1

SHEET 1 OF 1

A4
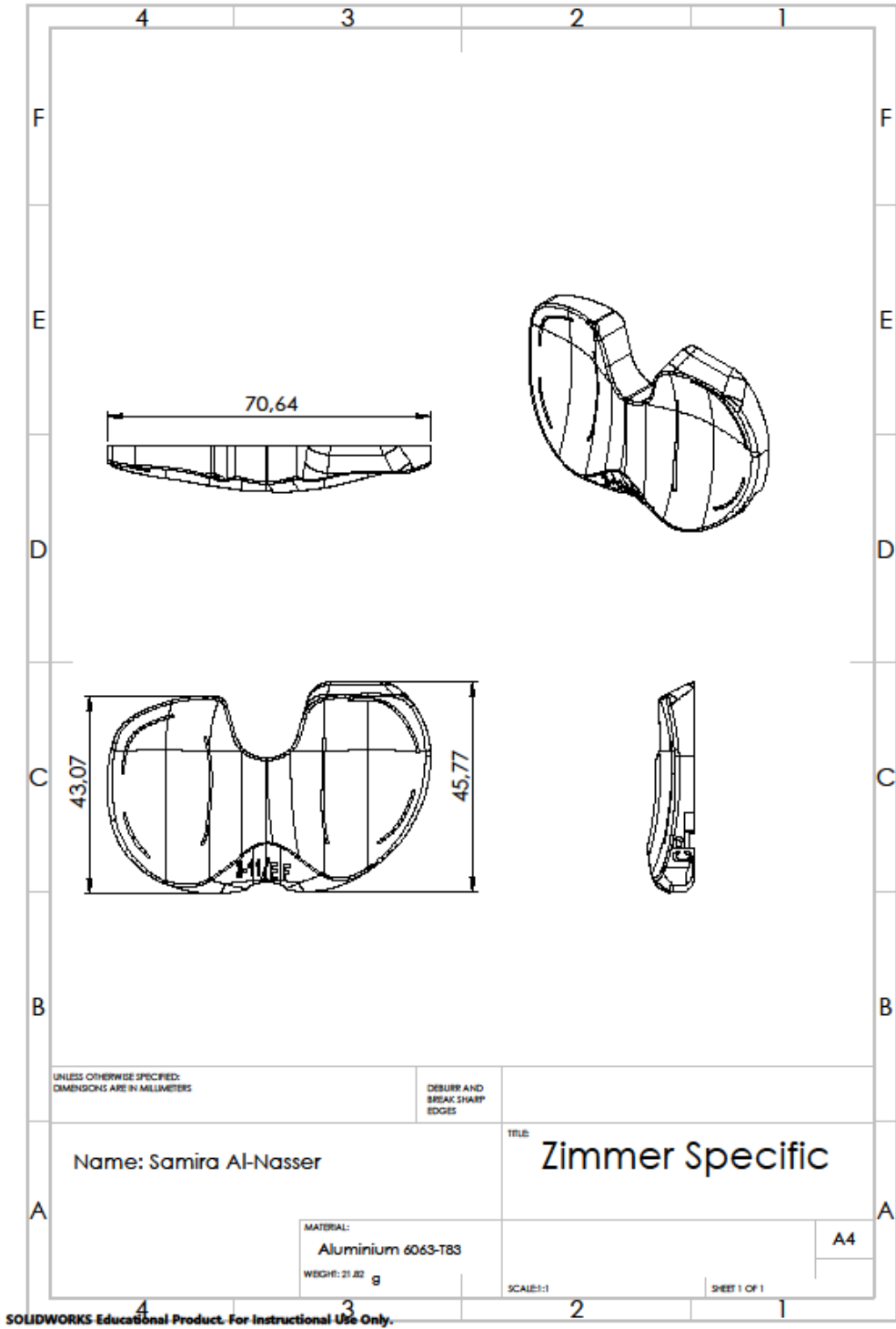
A.III: Electronics Datasheets
1. Strain gauges

TRANSDUCER QUALITY STRAIN GAGE
LINEAR PATTERN STRAIN GAGES

The linear pattern strain gages are used to measure strain in a single direction. They are used for experimental stress analysis, and transducer applications. The strain gage pattern is shown on the left side of the table. The "arrows" indicate the principal stress direction of the gage. OMEGA offers miniature linear patterns for strain measurement of a stress concentration or high gradient areas, and larger sizes. The solder pads/ribbon leads are offered both at one end of the grid, or with one at each end of the grid. Wide or narrow linear grid patterns are available.

Dimensions are listed for pattern gage grid length (A) and width (B), and the matrix or carrier length (C) and width (D). The patterns include alignment triangles.

Note: To determine if the strain gages have temperature characteristics matched to steel or aluminum, see the column labeled "COMP" short for compensation, "ST" indicates steel, "AL" indicates aluminum. See the column labeled "BTP" for accessory bondable terminal pad model numbers.

†Dimensions Key:
GRID
A: Active gage length
B: Active gage width
CARRIER
C: Matrix length
D: Matrix width
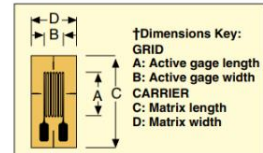
To Order

GAGE PATTERN Leads not shown	MODEL NO. Pkg of 5	NOM. RESIS-TANCE (Ω)	GRID		CARRIER		MAX V* (Vrms)	TERMINATION	TEMP COMP	TERM PAD
			A	B	C	D				
Shown actual size 4 mm	SGT-1/350-TY11	350	1.0 (0.039)	1.8 (0.071)	4.0 (0.157)	3.0 (0.118)	4.5	Ribbon Leads	ST	BPT-1
	SGT-1/350-TY13	350	Miniature linear pattern, measurement of stress concentration 350 Ω				6	Ribbon Leads	AL	
	SGT-1/350-TY41	350					4.5	Solder Pads	ST	
	SGT-1/350-TY43	350					6	Solder Pads	AL	

2. Load Cell Amplifier (HX711)

海芯科技 AVIA Semiconductor

HX711

24-Bit Analog-to-Digital Converter (ADC) for Weigh Scales

DESCRIPTION

Based on Avia Semiconductor's patented technology, HX711 is a precision 24-bit analog-to-digital converter (ADC) designed for weigh scales and industrial control applications to interface directly with a bridge sensor.

The input multiplexer selects either Channel A or B differential input to the low-noise programmable gain amplifier (PGA). Channel A can be programmed with a gain of 128 or 64, corresponding to a full-scale differential input voltage of ±20mV or ±40mV respectively, when a 5V supply is connected to AVDD analog power supply pin. Channel B has a fixed gain of 32. On-chip power supply regulator eliminates the need for an external supply regulator to provide analog power for the ADC and the sensor. Clock input is flexible. It can be from an external clock source, a crystal, or the on-chip oscillator that does not require any external component. On-chip power-on-reset circuitry simplifies digital interface initialization.

There is no programming needed for the internal registers. All controls to the HX711 are through the pins.

FEATURES

- **Two selectable differential input channels**
- **On-chip active low noise PGA with selectable gain of 32, 64 and 128**
- **On-chip power supply regulator for load-cell and ADC analog power supply**
- **On-chip oscillator requiring no external component with optional external crystal**
- **On-chip power-on-reset**
- **Simple digital control and serial interface:** pin-driven controls, no programming needed
- **Selectable 10SPS or 80SPS output data rate**
- **Simultaneous 50 and 60Hz supply rejection**
- **Current consumption including on-chip analog power supply regulator:** normal operation < 1.5mA, power down < 1uA
- **Operation supply voltage range: 2.6 ~ 5.5V**
- **Operation temperature range: -40 ~ +85℃**
- **16 pin SOP-16 package**

APPLICATIONS

- **Weigh Scales**
- **Industrial Process Control**
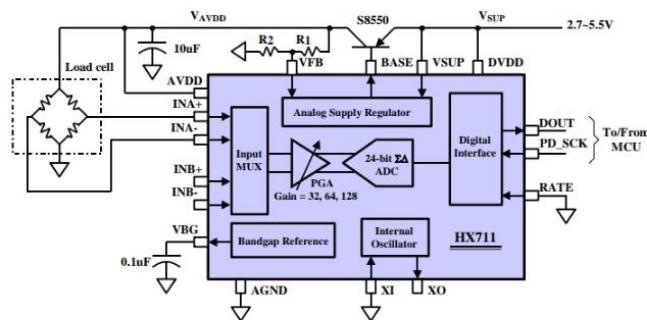
Fig. 1 Typical weigh scale application block diagram

A.IV: Arduino Code

```
#include "HX711.h"
// HX711 circuit wiring
const int LOADCELL_DOUT_PIN1 = 0;
const int LOADCELL_SCK_PIN1 = 1;
HX711 scale1;

const int LOADCELL_DOUT_PIN2 = 7;
const int LOADCELL_SCK_PIN2 = 8;
HX711 scale2;

const int LOADCELL_DOUT_PIN3 = 28;
const int LOADCELL_SCK_PIN3 = 29;
HX711 scale3;

const int LOADCELL_DOUT_PIN4 = 21;
const int LOADCELL_SCK_PIN4 = 20;
HX711 scale4;

const int LOADCELL_DOUT_PIN5 = 16;
const int LOADCELL_SCK_PIN5 = 17;
HX711 scale5;

const int LOADCELL_DOUT_PIN6 = 34;
const int LOADCELL_SCK_PIN6 = 35;
HX711 scale6;

void setup() {
  Serial.begin(38400);
  scale1.begin(LOADCELL_DOUT_PIN1, LOADCELL_SCK_PIN1);
  scale2.begin(LOADCELL_DOUT_PIN2, LOADCELL_SCK_PIN2);
  scale3.begin(LOADCELL_DOUT_PIN3, LOADCELL_SCK_PIN3);
  scale4.begin(LOADCELL_DOUT_PIN4, LOADCELL_SCK_PIN4);
  scale5.begin(LOADCELL_DOUT_PIN5, LOADCELL_SCK_PIN5);
  scale6.begin(LOADCELL_DOUT_PIN6, LOADCELL_SCK_PIN6); }

void loop() {
  long reading1 = scale1.read();
  long reading2 = scale2.read();
  long reading3 = scale3.read();
  long reading4 = scale4.read();
  long reading5 = scale5.read();
  long reading6 = scale6.read();
  Serial.print(reading1);
  Serial.print("\t");
  Serial.print(reading2);
  Serial.print("\t");
  Serial.print(reading3);
  Serial.print("\t");
  Serial.print(reading4);
  Serial.print("\t");
  Serial.print(reading5);
  Serial.print("\t");
  Serial.println(reading6);
  delay(100);
}
```

A.V: Training App MATLAB Code

```matlab
classdef app1 < matlab.apps.AppBase
    % Properties that correspond to app components
    properties (Access = public)
        UIFigure           matlab.ui.Figure
        ConnectButton      matlab.ui.control.Button
        PlotMedialButton   matlab.ui.control.Button
        UITable            matlab.ui.control.Table
        StoreButton        matlab.ui.control.Button
        EditField          matlab.ui.control.EditField
        AddButton          matlab.ui.control.Button
        UITable2           matlab.ui.control.Table
        EditField_2        matlab.ui.control.EditField
        EditField_3        matlab.ui.control.EditField
        RowEditFieldLabel  matlab.ui.control.Label
        RowEditField       matlab.ui.control.EditField
        DeleteButton       matlab.ui.control.Button
        Lamp               matlab.ui.control.Lamp
        CloseButton        matlab.ui.control.Button
        Lamp_2             matlab.ui.control.Lamp
        EXCELButton        matlab.ui.control.Button
        Lamp_3             matlab.ui.control.Lamp
    end
    properties (Access = private)
        T % Table to share between callbacks
        T1
data1
data2
data3
    end
    % Callbacks that handle component events
    methods (Access = private)
        % Button pushed function: ConnectButton
        function ConnectButtonPushed(app, event)
      app.Lamp_2.Color=[1,1,1];
            app.Lamp.Color=[1,0,0];
global arduin
arduin= serialport("COM4",9600);
    app.Lamp.Color=[0,1,0];
        end
        % Button pushed function: PlotMedialButton
        function PlotMedialButtonPushed(app, event)
            global arduin
             app.Lamp.Color=[1,1,1];
time(1)=0;
data_length=400000;
tit=zeros(data_length,1);
data1tit=zeros(data_length,1);
data2tit=zeros(data_length,1);
data3tit=zeros(data_length,1);
t_axis=zeros(data_length,1);
data_input = {}; % To save data
tic
while (toc<=5)
toc
readz3=str2num(readline(arduin));
data10=mean(readz3(1));
data20=mean(readz3(2));
```

```matlab
data30=mean(readz3(3));
end
figure(1)
h1 = plot(nan,nan,'linewidth',1,'color','red');
hold on
h2 = plot(nan,nan,'linewidth',1,'color','green');
hold on
h3 = plot(nan,nan,'linewidth',1,'color','blue');
lg = legend('X','Y','Z');
lg.FontSize = 16;
grid on
i = 1;
tic
while (toc<=40000)
toc;
ti = toc;
readz3=str2num(readline(arduin));
  szz = size(readz3);
  if szz(1,2) > 0
    app.data1 = readz3(1) - data10;
    app.data2 = readz3(2) - data20;
    app.data3 = readz3(3) - data30;
  else
    app.data1 = 0;
    app.data2 = 0;
    app.data3 = 0;
  end
data_input{i,1} = app.data1;
data_input{i,2} = app.data2;
data_input{i,3} = app.data3;
t_axis = [t_axis(2:end) ; i];
data1tit = [data1tit(2:end) ; app.data1];
data2tit = [data2tit(2:end) ; app.data2];
data3tit = [data3tit(2:end) ; app.data3];
h1.XData = t_axis;
h1.YData = data1tit;
h2.XData = t_axis;
h2.YData = data2tit;
h3.XData = t_axis;
h3.YData = data3tit;
i = i +1;
end
    full_table = cell2mat(data_input);
    f_name = append('Number of data points',num2str(i),'.txt');
    writematrix(full_table,f_name,'Delimiter',',','QuoteStrings',true)
        end
        % Button pushed function: StoreButton
        function StoreButtonPushed(app, event)
            % Color= {'Red';'Green';'Blue'};
            strain1 = app.data1;
            strain2= app.data2;
            strain3= app.data3; %data1tit data2tit data3tit
          nr1={strain1 strain2 strain3};
            app.UITable.Data=[app.T;nr1];
            app.T=app.UITable.Data;
        end
        % Button pushed function: AddButton
        function AddButtonPushed(app, event)
```

```matlab
                Load=app.EditField.Value;
                LocationX=app.EditField_2.Value;
                 LocationY=app.EditField_3.Value;
                  nr={Load LocationX LocationY};
                  app.UITable2.Data=[app.T1;nr];
                  app.T1=app.UITable2.Data;
            end
        % Callback function: DeleteButton, RowEditField
        function DeleteButtonPushed(app, event)
                num=round(app.RowEditField.Value);
                app.UITable2.Data(num,:)=[];
app.T1 = app.UITable2.Data;
        end
        % Callback function
        function ButtonPushed(app, event)
        end
        % Button pushed function: CloseButton
        function CloseButtonPushed(app, event)
if ~isempty(instrfindall)
    fclose(instrfindall);
    delete(instrfindall);
end
clearvars -global arduin;
close all
        app.Lamp_2.Color=[0,1,0];
            end
        % Button pushed function: EXCELButton
        function EXCELButtonPushed(app, event)
            ResultsLL=[app.T1 app.T];
 ResultsLL=cell2table(ResultsLL);
                writetable(ResultsLL,'Book2.xlsx', 'WriteVariableNames',true);
   app.Lamp_3.Color=[0,1,0];
            end
        % Callback function
        function PlotButtonPushed(app, event)
          LocationX=app.LocationEditField.Value;
           LocationY=app.LocationEditField_2.Value;
            app.UITable2.Data=[app.T1;nr];
             app.T1=app.UITable2.Data;
        end
        % Callback function: UITable, UITable, UITable, UITable2,
        % UITable2, UITable2
        function UITable2CellEdit(app, event)
        end
        % Callback function
        function UITableKeyPress(app, event)
        end
        % Callback function
        function UITableCellEdit(app, event)
            indices = event.Indices;
            newData = event.NewData;
        end
    end
    % Component initialization
    methods (Access = private)
        % Create UIFigure and components
        function createComponents(app)
            % Create UIFigure and hide until all components are created
```

177

```matlab
            app.UIFigure = uifigure('Visible', 'off');
            app.UIFigure.Position = [100 100 1695 952];
            app.UIFigure.Name = 'MATLAB App';
            % Create ConnectButton
            app.ConnectButton = uibutton(app.UIFigure, 'push');
            app.ConnectButton.ButtonPushedFcn = createCallbackFcn(app,
@ConnectButtonPushed, true);
            app.ConnectButton.Position = [29 907 100 23];
            app.ConnectButton.Text = 'Connect';
            % Create PlotMedialButton
            app.PlotMedialButton = uibutton(app.UIFigure, 'push');
            app.PlotMedialButton.ButtonPushedFcn = createCallbackFcn(app,
@PlotMedialButtonPushed, true);
            app.PlotMedialButton.Position = [30 866 100 23];
            app.PlotMedialButton.Text = 'Plot Medial';
            % Create UITable
            app.UITable = uitable(app.UIFigure);
            app.UITable.ColumnName = {'Red'; 'Green'; 'Blue'};
            app.UITable.RowName = {};
            app.UITable.ColumnEditable = [true true true];
            app.UITable.CellEditCallback = createCallbackFcn(app,
@UITable2CellEdit, true);
            app.UITable.CellSelectionCallback = createCallbackFcn(app,
@UITable2CellEdit, true);
            app.UITable.DisplayDataChangedFcn = createCallbackFcn(app,
@UITable2CellEdit, true);
            app.UITable.Position = [528 425 427 392];
            % Create StoreButton
            app.StoreButton = uibutton(app.UIFigure, 'push');
            app.StoreButton.ButtonPushedFcn = createCallbackFcn(app,
@StoreButtonPushed, true);
            app.StoreButton.Position = [713 844 100 23];
            app.StoreButton.Text = 'Store';
            % Create EditField
            app.EditField = uieditfield(app.UIFigure, 'text');
            app.EditField.Position = [368 856 100 22];
            % Create AddButton
            app.AddButton = uibutton(app.UIFigure, 'push');
            app.AddButton.ButtonPushedFcn = createCallbackFcn(app,
@AddButtonPushed, true);
            app.AddButton.Position = [369 822 100 23];
            app.AddButton.Text = 'Add ';
            % Create UITable2
            app.UITable2 = uitable(app.UIFigure);
            app.UITable2.ColumnName = {'Load'; 'Location X'; 'Location Y'};
            app.UITable2.RowName = {};
            app.UITable2.ColumnEditable = [true true true];
            app.UITable2.CellEditCallback = createCallbackFcn(app,
@UITable2CellEdit, true);
            app.UITable2.CellSelectionCallback = createCallbackFcn(app,
@UITable2CellEdit, true);
            app.UITable2.DisplayDataChangedFcn = createCallbackFcn(app,
@UITable2CellEdit, true);
            app.UITable2.Position = [220 425 308 392];
            % Create EditField_2
            app.EditField_2 = uieditfield(app.UIFigure, 'text');
            app.EditField_2.Position = [367 892 44 22];
```

```matlab
            % Create EditField_3
            app.EditField_3 = uieditfield(app.UIFigure, 'text');
            app.EditField_3.Position = [422 892 45 22];
            % Create RowEditFieldLabel
            app.RowEditFieldLabel = uilabel(app.UIFigure);
            app.RowEditFieldLabel.HorizontalAlignment = 'right';
            app.RowEditFieldLabel.Position = [56 695 30 22];
            app.RowEditFieldLabel.Text = 'Row';
            % Create RowEditField
            app.RowEditField = uieditfield(app.UIFigure, 'text');
            app.RowEditField.ValueChangedFcn = createCallbackFcn(app,
@DeleteButtonPushed, true);
            app.RowEditField.Position = [101 695 100 22];
            % Create DeleteButton
            app.DeleteButton = uibutton(app.UIFigure, 'push');
            app.DeleteButton.ButtonPushedFcn = createCallbackFcn(app,
@DeleteButtonPushed, true);
            app.DeleteButton.Position = [94 659 100 23];
            app.DeleteButton.Text = 'Delete';
            % Create Lamp
            app.Lamp = uilamp(app.UIFigure);
            app.Lamp.Position = [151 908 20 20];
            app.Lamp.Color = [1 1 1];
            % Create CloseButton
            app.CloseButton = uibutton(app.UIFigure, 'push');
            app.CloseButton.ButtonPushedFcn = createCallbackFcn(app,
@CloseButtonPushed, true);
            app.CloseButton.Position = [874 349 100 23];
            app.CloseButton.Text = 'Close';
            % Create Lamp_2
            app.Lamp_2 = uilamp(app.UIFigure);
            app.Lamp_2.Position = [986 350 20 20];
            app.Lamp_2.Color = [1 1 1];
            % Create EXCELButton
            app.EXCELButton = uibutton(app.UIFigure, 'push');
            app.EXCELButton.ButtonPushedFcn = createCallbackFcn(app,
@EXCELButtonPushed, true);
            app.EXCELButton.Position = [1048 659 100 23];
            app.EXCELButton.Text = 'EXCEL';
            % Create Lamp_3
            app.Lamp_3 = uilamp(app.UIFigure);
            app.Lamp_3.Position = [1158 660 20 20];
            app.Lamp_3.Color = [1 1 1];
            % Show the figure after all components are created
            app.UIFigure.Visible = 'on';
        end
    end
    % App creation and deletion
    methods (Access = public)
        % Construct app
        function app = app1
            % Create UIFigure and components
            createComponents(app)
            % Register the app with App Designer
            registerApp(app, app.UIFigure)
            if nargout == 0
                clear app
            end
```

```matlab
        end
        % Code that executes before app deletion
        function delete(app)
            % Delete UIFigure when app is deleted
            delete(app.UIFigure)
        end
    end
end
```

A.VI Pre-processing and Training Code

```matlab
%% ALL PREPROCESSING
clear all;
load('FEA2.mat');
%Normalization (-1,1)
a = load';
[load_normalized,PS] = mapminmax(a,-1,1);
w = Strain(:,1)';
x =Strain(:,2)';
y =Strain(:,3)';
[Strain1_normalized,PS1] = mapminmax(w,-1,1);
[Strain2_normalized,PS2] = mapminmax(x,-1,1);
[Strain3_normalized,PS3] = mapminmax(y,-1,1);
Strain_normalized(1,:)= Strain1_normalized;
Strain_normalized(2,:)= Strain2_normalized;
Strain_normalized(3,:)= Strain3_normalized;

b = location(:,1)';
c = location(:,2)';
[xlocation_normalized,PS4] = mapminmax(b,-1,1);
[ylocation_normalized,PS5] = mapminmax(c,-1,1);
location_normalized(1,:)= xlocation_normalized;
location_normalized(2,:)=ylocation_normalized;

%%%%%%  Multiplicative Noise 10% %%%%%%%%%%%%%%%%%%%%%%%%%%%
dataset=Strain_normalized;
ogStrain_normalized=Strain_normalized;
datasetload_normalized=load_normalized;
ogload_normalized=load_normalized;
datasetlocation_normalized=location_normalized;
oglocation_normalized=location_normalized;

[rows, columns] = size(dataset);
randomvalues = -0.1 + (0.2*rand(rows, columns));
noise=dataset.*randomvalues;
noisyStrain_normalized1 = dataset + noise;
noisyStrain_normalized2= [noisyStrain_normalized1 ogStrain_normalized];

[rows, columns] = size(datasetlocation_normalized);
randomvalues2 =  -0.1+(0.2*rand(rows, columns)); %10
noise1=datasetlocation_normalized.*randomvalues2;
noisylocation_normalized1 = datasetlocation_normalized + noise1;
noisylocation_normalized2= [noisylocation_normalized1 oglocation_normalized];

[rows, columns] = size(datasetload_normalized);
randomvalues3 = -0.1+ (0.2*rand(rows, columns)); %10
noise2=datasetload_normalized.*randomvalues3;
noisyload_normalized1 = datasetload_normalized + noise2;
noisyload_normalized2= [noisyload_normalized1 ogload_normalized];

Strain_normalized= [noisyStrain_normalized2];
location_normalized=[noisylocation_normalized2];
load_normalized=[noisyload_normalized2];

%%%%%%%%%%%%%%%%%%%%% TRAINING LOCATION  %%%%%%%%%%%%%%%%%%%%%

x = Strain_normalized;
 t =location_normalized;
```

```matlab
trainFcn = 'trainbr';

hiddenLayerSize = 10;
netLocation = fitnet(hiddenLayerSize,trainFcn);

% Choose Input and Output Pre/Post-Processing Functions
% For a list of all processing functions type: help nnprocess

% Setup Division of Data for Training, Validation, Testing
% For a list of all data division functions type: help nndivision
netLocation.trainParam.lr = 0.1;
netLocation.divideFcn = 'dividerand';  % Divide data randomly
netLocation.divideMode = 'sample';  % Divide up every sample
netLocation.divideParam.trainRatio = 85/100;
netLocation.divideParam.valRatio = 0/100;
netLocation.divideParam.testRatio = 15/100;

netLocation.trainParam.epochs=1000;
% nettainParam.goal=0.01;
% Choose a Performance Function
% For a list of all performance functions type: help nnperformance
netLocation.performFcn = 'mse';  % Mean Squared Error
% Choose Plot Functions
% For a list of all plot functions type: help nnplot
netLocation.plotFcns = {'plotperform','plottrainstate','ploterrhist', ...
    'plotregression','plotconfusion'};
% Train the Network
[netLocation,tr] = train(netLocation,x,t);
% Test the Network
y = netLocation(x);
e = gsubtract(t,y);
performance = perform(netLocation,t,y)
% Recalculate Training, Validation and Test Performance
trainTargets = t .* tr.trainMask{1};
valTargets = t .* tr.valMask{1};
testTargets = t .* tr.testMask{1};
trainPerformance = perform(netLocation,trainTargets,y)
valPerformance = perform(netLocation,valTargets,y)
testPerformance = perform(netLocation,testTargets,y)

%%%%%%%%%%%%%%%%%%%%%%% Train Load %%%%%%%%%%%%%%%

x = Strain_normalized;
 t =load_normalized;
trainFcn = 'trainbr';

hiddenLayerSize = 5;
netLoad = fitnet(hiddenLayerSize,trainFcn);

% Choose Input and Output Pre/Post-Processing Functions
% For a list of all processing functions type: help nnprocess

% Setup Division of Data for Training, Validation, Testing
% For a list of all data division functions type: help nndivision
netLoad.trainParam.lr = 0.1;
netLoad.divideFcn = 'dividerand';  % Divide data randomly
netLoad.divideMode = 'sample';  % Divide up every sample
netLoad.divideParam.trainRatio = 85/100;
```

```
netLoad.divideParam.valRatio = 0/100;
netLoad.divideParam.testRatio = 15/100;

netLoad.trainParam.epochs=1000;
netLoad.performFcn = 'mse';  % Mean Squared Error
% Choose Plot Functions
% For a list of all plot functions type: help nnplot
netLoad.plotFcns = {'plotperform','plottrainstate','ploterrhist', ...
    'plotregression','plotconfusion'};
% Train the Network
[netLoad,tr] = train(netLoad,x,t);
% Test the Network
y = netLoad(x);
e = gsubtract(t,y);
performance = perform(netLoad,t,y)
% Recalculate Training, Validation and Test Performance
trainTargets = t .* tr.trainMask{1};
valTargets = t .* tr.valMask{1};
testTargets = t .* tr.testMask{1};
trainPerformance = perform(netLoad,trainTargets,y)
valPerformance = perform(netLoad,valTargets,y)
testPerformance = perform(netLoad,testTargets,y)
```

A.VI: Real time GUI

```matlab
%%ZIMMER
global arduin
  global data10
  global data20
  global data30
   global data40
  global data50
  global data60
%  ZIMMER
 load('ZimmerALL_NEW')
zeroing=@myGUI;
time(1)=0;
data_length=500;
%lateral
tit=zeros(data_length,1);
data1tit=zeros(data_length,1);
data2tit=zeros(data_length,1);
data3tit=zeros(data_length,1);
%medial
data4tit=zeros(data_length,1);
data5tit=zeros(data_length,1);
data6tit=zeros(data_length,1);
t_axis=zeros(data_length,1);
data_input = {}; % To save data
tic
while (toc<=5)
toc
readz3=str2num(readline(arduin));
%lateral
data10=mean(readz3(1));
data20=mean(readz3(2));
data30=mean(readz3(3));
%medial
data40=mean(readz3(4));
data50=mean(readz3(5));
data60=mean(readz3(6));
end
zeroing();
figure(1) %medial
subplot(1,2,1)
hold on;
xlim([-1, 5]);
ylim([-1, 7]);
im = imread('medial.png');
flipim=flipud(im);
im_handle = imagesc('XData', [min(xlim), max(xlim)], 'YData', [min(ylim),
max(ylim)], 'CData', flipim);
set(gca, 'YDir', 'normal');  % Make sure the y-axis is oriented correctly
h1 = plot(nan,nan, 'co', 'MarkerSize', 24, 'MarkerFaceColor', 'cyan',
'MarkerEdgeColor', 'cyan');
plot(0,0,'b.','MarkerSize', 20, 'MarkerFaceColor','b');
plot(1,0,'g.','MarkerSize', 20, 'MarkerFaceColor','g');
plot(2,0,'g.','MarkerSize', 20, 'MarkerFaceColor','g');
plot(3,0,'b.','MarkerSize', 20, 'MarkerFaceColor','b');
plot(0,1,'g.','MarkerSize', 20, 'MarkerFaceColor','g');
plot(1,1,'g.','MarkerSize', 20, 'MarkerFaceColor','g');
plot(2,1,'g.','MarkerSize', 20, 'MarkerFaceColor','g');
```

```matlab
plot(3,1,'b.','MarkerSize', 20, 'MarkerFaceColor','b');
plot(0,2,'g.','MarkerSize', 20, 'MarkerFaceColor','g');
plot(1,2,'g.','MarkerSize', 20, 'MarkerFaceColor','g');
plot(2,2,'g.','MarkerSize', 20, 'MarkerFaceColor','g');
plot(3,2,'b.','MarkerSize', 20, 'MarkerFaceColor','b');
plot(0,3,'g.','MarkerSize', 20, 'MarkerFaceColor','g');
plot(1,3,'g.','MarkerSize', 20, 'MarkerFaceColor','g');
plot(2,3,'g.','MarkerSize', 20, 'MarkerFaceColor','g');
plot(3,3,'b.','MarkerSize', 20, 'MarkerFaceColor','b');
plot(0,4,'b.','MarkerSize', 20, 'MarkerFaceColor','b');
plot(1,4,'g.','MarkerSize', 20, 'MarkerFaceColor','g');
plot(2,4,'g.','MarkerSize', 20, 'MarkerFaceColor','g');
plot(3,4,'b.','MarkerSize', 20, 'MarkerFaceColor','b');
plot(1,5,'b.','MarkerSize', 20, 'MarkerFaceColor','b');
plot(2,5,'g.','MarkerSize', 20, 'MarkerFaceColor','g');
plot(3,5,'b.','MarkerSize', 20, 'MarkerFaceColor','b');
plot(2,6,'b.','MarkerSize', 20, 'MarkerFaceColor','b');
plot(3,6,'b.','MarkerSize', 20, 'MarkerFaceColor','b');
text_load = text(-1.5, -0.75, 'Load Value: 0');
text_location=text(4.5,-0.75,'Location: (X,Y)');
% figure(2) lateral
subplot(1,2,2)
hold on;
xlim([-2, 4]);
ylim([-1, 7]);
im2 = imread('lateral.png');
flipim2=flipud(im2);
im_handle2 = imagesc('XData', [min(xlim), max(xlim)], 'YData', [min(ylim),
max(ylim)], 'CData', flipim2);
set(gca, 'YDir', 'normal');  % Make sure the y-axis is oriented correctly
 h12 = plot(nan,nan, 'o', 'MarkerSize', 24, 'MarkerFaceColor', 'cyan',
'MarkerEdgeColor', 'cyan');
plot(0,0,'g.','MarkerSize', 20, 'MarkerFaceColor','g');
plot(1,0,'b.','MarkerSize', 20, 'MarkerFaceColor','b');
plot(2,0,'b.','MarkerSize', 20, 'MarkerFaceColor','b');
plot(0,1,'g.','MarkerSize', 20, 'MarkerFaceColor','g');
plot(1,1,'g.','MarkerSize', 20, 'MarkerFaceColor','g');
plot(2,1,'b.','MarkerSize', 20, 'MarkerFaceColor','b');
plot(3,1,'b.','MarkerSize', 20, 'MarkerFaceColor','b');
plot(0,2,'g.','MarkerSize', 20, 'MarkerFaceColor','g');
plot(1,2,'g.','MarkerSize', 20, 'MarkerFaceColor','g');
plot(2,2,'g.','MarkerSize', 20, 'MarkerFaceColor','g');
plot(3,2,'b.','MarkerSize', 20, 'MarkerFaceColor','b');
plot(0,3,'g.','MarkerSize', 20, 'MarkerFaceColor','g');
plot(1,3,'g.','MarkerSize', 20, 'MarkerFaceColor','g');
plot(2,3,'g.','MarkerSize', 20, 'MarkerFaceColor','g');
plot(3,3,'b.','MarkerSize', 20, 'MarkerFaceColor','b');
plot(0,4,'g.','MarkerSize', 20, 'MarkerFaceColor','g');
plot(1,4,'g.','MarkerSize', 20, 'MarkerFaceColor','g');
plot(2,4,'g.','MarkerSize', 20, 'MarkerFaceColor','g');
plot(3,4,'b.','MarkerSize', 20, 'MarkerFaceColor','b');
plot(0,5,'g.','MarkerSize', 20, 'MarkerFaceColor','g');
plot(1,5,'g.','MarkerSize', 20, 'MarkerFaceColor','g');
plot(2,5,'b.','MarkerSize', 20, 'MarkerFaceColor','b');
plot(3,5,'b.','MarkerSize', 20, 'MarkerFaceColor','b');
plot(0,6,'g.','MarkerSize', 20, 'MarkerFaceColor','g');
plot(1,6,'b.','MarkerSize', 20, 'MarkerFaceColor','b');
plot(2,6,'b.','MarkerSize', 20, 'MarkerFaceColor','b')
```

185

```matlab
text_load2 = text(-1.5, -0.75, 'Load Value: 0');
text_location2=text(4.5,-0.75,'Location: (X,Y)');
i = 1;
tic
while (toc<=500000)
toc;
ti = toc;
readz3=str2num(readline(arduin));
  szz = size(readz3);
  if szz(1,2) > 0
%lateral
    data1 = readz3(1) - data10;
    data2 = readz3(2) - data20;
    data3 = readz3(3) - data30;
%medial
    data4 = readz3(4) - data40;
    data5 = readz3(5) - data50;
    data6 = readz3(6) - data60;
  else
    data1 = 0;
    data2 = 0;
    data3 = 0;
    data4 = 0;
    data5 = 0;
    data6 = 0;
  end
%medial
  Strain1_normalized = mapminmax('apply',data4,PS1);
Strain2_normalized =  mapminmax('apply',data5,PS2);
Strain3_normalized = mapminmax('apply',data6,PS3);
data_input1 = [Strain1_normalized Strain2_normalized Strain3_normalized];
y1=sim(netLocationZM,data_input1');
y2=sim(netLoadZM,data_input1');
 y1=y1';
 y2=y2';
data_input1= [0 0 0];
 %lateral
  ZL_Strain1_normalized = mapminmax('apply',data1,PS7);
  ZL_Strain2_normalized = mapminmax('apply',data2,PS8);
   ZL_Strain3_normalized = mapminmax('apply',data3,PS9);
data_input2 = [ZL_Strain1_normalized ZL_Strain2_normalized
ZL_Strain3_normalized];
y3=sim(netLocationZL,data_input2');
y4=sim(netLoadZL,data_input2');
 y3=y3';
 y4=y4';
data_input2= [0 0 0];
 % MEDIAL
% Receiving new load value
load = y2(1); % Exam replace with actual value
 load_scaled{i,1} = mapminmax('reverse',y2,PS);
load_scaled1=cell2mat(load_scaled);
location_scaled{i,1}= mapminmax('reverse',y1(1),PS4);
location_scaled{i,2}= mapminmax('reverse',y1(2),PS5);
location_scaled1(i,1)=cell2mat(location_scaled(i,1));
location_scaled1(i,2)=cell2mat(location_scaled(i,2));
h1.XData = location_scaled1(i,1);
h1.YData = location_scaled1(i,2);
```

```matlab
    set(text_load, 'String', ['Load:   '
num2str(abs(round(load_scaled1(i,1),1))) ' kg']);
  set(text_location, 'String', ['Location: ('
num2str(round(location_scaled1(i,1),1)) ','
num2str(round(location_scaled1(i,2),1)) ')']);
 %LATERAL
  % Receiving new load value
 load_scaled2{i,1} = mapminmax('reverse',y4,PS6);
load_scaled2b=cell2mat(load_scaled2);
location_scaled2{i,1}= mapminmax('reverse',y3(1),PS10);
location_scaled2{i,2}= mapminmax('reverse',y3(2),PS11);
location_scaled2b(i,1)=cell2mat(location_scaled2(i,1));
location_scaled2b(i,2)=cell2mat(location_scaled2(i,2));
h12.XData = location_scaled2b(i,1);
h12.YData = location_scaled2b(i,2);
    set(text_load2, 'String', ['Load:   '
num2str(abs(round(load_scaled2b(i,1),2))) ' kg']);
  set(text_location2, 'String', ['Location: ('
num2str(round(location_scaled2b(i,1),2)) ','
num2str(round(location_scaled2b(i,2),2)) ')']);
  i = i +1;
end
disp('Done!!!')
function myGUI()
    % create the GUI figure
    fig = figure(1);
  global arduin
  global data10
  global data20
  global data30
    global data40
  global data50
  global data60
    % create the button
    btn = uicontrol('Style', 'pushbutton', 'String', 'ZERO', ...
        'Position', [20 20 100 30], 'Callback', @executeCode);
    % define the function to execute when the button is pressed
    function executeCode(~, ~)
     tic
while (toc<=5)
toc
readz3=str2num(readline(arduin));
dataA=mean(readz3(1));
dataB=mean(readz3(2));
dataC=mean(readz3(3));
dataD=mean(readz3(4));
dataE=mean(readz3(5));
dataF=mean(readz3(6));
end
disp('Code executed!');
data10=dataA;
data20=dataB;
data30=dataC;
data40=dataD;
data50=dataE;
data60=dataF;
    end
```

```matlab
end
global arduin
  global data10
  global data20
  global data30
   global data40
  global data50
  global data60
%  Ring
  load('RINGALL_NEW.mat');
%medial
zeroing=@myGUI;
time(1)=0;
data_length=500;
%lateral
tit=zeros(data_length,1);
data1tit=zeros(data_length,1);
data2tit=zeros(data_length,1);
data3tit=zeros(data_length,1);
%medial
data4tit=zeros(data_length,1);
data5tit=zeros(data_length,1);
data6tit=zeros(data_length,1);
t_axis=zeros(data_length,1);
data_input = {}; % To save data
tic
while (toc<=5)
toc
readz3=str2num(readline(arduin));
%lateral
data10=mean(readz3(1));
data20=mean(readz3(2));
data30=mean(readz3(3));
%medial
data40=mean(readz3(4));
data50=mean(readz3(5));
data60=mean(readz3(6));
end
zeroing();
figure(1) %medial
subplot(1,2,1)
hold on;
xlim([-2, 5]);
ylim([-2, 5]);
im = imread('medial.png');
flipim=flipud(im);
im_handle = imagesc('XData', [min(xlim), max(xlim)], 'YData', [min(ylim),
max(ylim)], 'CData', flipim);
set(gca, 'YDir', 'normal');  % Make sure the y-axis is oriented correctly
text_load = text(-1.5, -0.75, 'Load: 0');
text_location=text(4.5,-0.75,'Location: (0,0)');
h1 = plot(nan,nan, 'o', 'MarkerSize', 24, 'MarkerFaceColor', 'cyan',
'MarkerEdgeColor', 'cyan');
%Training Points
plot(0,0,'b.','MarkerSize', 20, 'MarkerFaceColor','b');
plot(1,0,'g.','MarkerSize', 20, 'MarkerFaceColor','g');
plot(2,0,'g.','MarkerSize', 20, 'MarkerFaceColor','g');
plot(3,0,'b.','MarkerSize', 20, 'MarkerFaceColor','b');
```

188

```matlab
plot(0,1,'g.','MarkerSize', 20, 'MarkerFaceColor','g');
plot(1,1,'g.','MarkerSize', 20, 'MarkerFaceColor','g');
plot(2,1,'g.','MarkerSize', 20, 'MarkerFaceColor','g');
plot(3,1,'g.','MarkerSize', 20, 'MarkerFaceColor','g');
plot(0,2,'g.','MarkerSize', 20, 'MarkerFaceColor','g');
plot(1,2,'g.','MarkerSize', 20, 'MarkerFaceColor','g');
plot(2,2,'g.','MarkerSize', 20, 'MarkerFaceColor','g');
plot(3,2,'g.','MarkerSize', 20, 'MarkerFaceColor','g');
plot(0,3,'b.','MarkerSize', 20, 'MarkerFaceColor','b');
plot(1,3,'g.','MarkerSize', 20, 'MarkerFaceColor','g');
plot(2,3,'g.','MarkerSize', 20, 'MarkerFaceColor','g');
plot(3,3,'g.','MarkerSize', 20, 'MarkerFaceColor','g');
plot(1,4,'b.','MarkerSize', 20, 'MarkerFaceColor','b');
plot(2,4,'g.','MarkerSize', 20, 'MarkerFaceColor','g');
plot(3,4,'b.','MarkerSize', 20, 'MarkerFaceColor','b');
% lateral
subplot(1,2,2)
 %lateral
hold on;
xlim([-2, 5]);
ylim([-2, 5]);
im2 = imread('lateral.png');
flipim2=flipud(im2);
im_handle2 = imagesc('XData', [min(xlim), max(xlim)], 'YData', [min(ylim),
max(ylim)], 'CData', flipim2);
set(gca, 'YDir', 'normal');  % Make sure the y-axis is oriented correctly
text_load2 = text(-2, -0.75, 'Load: nan');
text_location2=text(2,-0.75,'Location: (nan,nan)');
h12 = plot(nan,nan, 'o', 'MarkerSize', 24, 'MarkerFaceColor', 'cyan',
'MarkerEdgeColor', 'cyan');
%Ring LATERAL NEW
plot(0,0,'b.','MarkerSize', 20, 'MarkerFaceColor','b');
plot(1,0,'g.','MarkerSize', 20, 'MarkerFaceColor','g');
plot(2,0,'g.','MarkerSize', 20, 'MarkerFaceColor','g');
plot(3,0,'b.','MarkerSize', 20, 'MarkerFaceColor','b');
plot(0,1,'g.','MarkerSize', 20, 'MarkerFaceColor','g');
plot(1,1,'g.','MarkerSize', 20, 'MarkerFaceColor','g');
plot(2,1,'g.','MarkerSize', 20, 'MarkerFaceColor','g');
plot(3,1,'g.','MarkerSize', 20, 'MarkerFaceColor','g');
plot(0,2,'g.','MarkerSize', 20, 'MarkerFaceColor','g');
plot(1,2,'g.','MarkerSize', 20, 'MarkerFaceColor','g');
plot(2,2,'g.','MarkerSize', 20, 'MarkerFaceColor','g');
plot(3,2,'g.','MarkerSize', 20, 'MarkerFaceColor','g');
plot(0,3,'b.','MarkerSize', 20, 'MarkerFaceColor','b');
plot(1,3,'g.','MarkerSize', 20, 'MarkerFaceColor','g');
plot(2,3,'g.','MarkerSize', 20, 'MarkerFaceColor','g');
plot(3,3,'b.','MarkerSize', 20, 'MarkerFaceColor','b');
plot(0,4,'b.','MarkerSize', 20, 'MarkerFaceColor','b');
plot(1,4,'b.','MarkerSize', 20, 'MarkerFaceColor','b');
plot(2,4,'g.','MarkerSize', 20, 'MarkerFaceColor','g');
i = 1;
tic
while (toc<=500000)
toc;
ti = toc;
readz3=str2num(readline(arduin));
  szz = size(readz3);
```

189

```matlab
    if szz(1,2) > 0
%lateral
    data1 = readz3(1) - data10;
    data2 = readz3(2) - data20;
    data3 = readz3(3) - data30;
%medial
    data4 = readz3(4) - data40;
    data5 = readz3(5) - data50;
    data6 = readz3(6) - data60;
  else
    data1 = 0;
    data2 = 0;
    data3 = 0;
    data4 = 0;
    data5 = 0;
    data6 = 0;
  end
%medial
    Strain1_normalized = mapminmax('apply',data4,PS1);
Strain2_normalized =  mapminmax('apply',data5,PS2);
Strain3_normalized = mapminmax('apply',data6,PS3);
data_input1 = [Strain1_normalized Strain2_normalized Strain3_normalized];
y1=sim(netLocation,data_input1');
y2=sim(netLoad,data_input1');
 y1=y1';
 y2=y2';
data_input1= [0 0 0];
 %lateral
  RL_Strain1_normalized = mapminmax('apply',data1,PS7);
RL_Strain2_normalized = mapminmax('apply',data2,PS8);
RL_Strain3_normalized = mapminmax('apply',data3,PS9);
data_input2 = [RL_Strain1_normalized RL_Strain2_normalized
RL_Strain3_normalized];
y3=sim(netLocation_RL,data_input2');
y4=sim(netLoad_RL,data_input2');
 y3=y3';
 y4=y4';
data_input2= [0 0 0];
 % MEDIAL
% Receiving new load value
load = y2(1); % Exam replace with actual value
 load_scaled{i,1} = mapminmax('reverse',y2,PS);
load_scaled1=cell2mat(load_scaled);
location_scaled{i,1}= mapminmax('reverse',y1(1),PS4);
location_scaled{i,2}= mapminmax('reverse',y1(2),PS5);
location_scaled1(i,1)=cell2mat(location_scaled(i,1));
location_scaled1(i,2)=cell2mat(location_scaled(i,2));
h1.XData = location_scaled1(i,1);
h1.YData = location_scaled1(i,2);
  set(text_load, 'String', ['Load:  '
num2str(abs(round(load_scaled1(i,1),1))) ' kg']);
  set(text_location, 'String', ['Location: ('
num2str(round(location_scaled1(i,1),1)) ','
num2str(round(location_scaled1(i,2),1)) ')']);
 %LATERAL
  % Receiving new load value
 load_scaled2{i,1} = mapminmax('reverse',y4,PS6);
```

```matlab
load_scaled2b=cell2mat(load_scaled2);
location_scaled2{i,1}= mapminmax('reverse',y3(1),PS10);
location_scaled2{i,2}= mapminmax('reverse',y3(2),PS11);
location_scaled2b(i,1)=cell2mat(location_scaled2(i,1));
location_scaled2b(i,2)=cell2mat(location_scaled2(i,2));
h12.XData = location_scaled2b(i,1);
h12.YData = location_scaled2b(i,2);
    set(text_load2, 'String', ['Load:  '
num2str(abs(round(load_scaled2b(i,1),2))) ' kg']);
  set(text_location2, 'String', ['Location: ('
num2str(round(location_scaled2b(i,1),2)) ','
num2str(round(location_scaled2b(i,2),2)) ')']);
  i = i +1;
end
disp('Done!!!')
function myGUI()
    % create the GUI figure
    fig = figure(1);
  global arduin
  global data10
  global data20
  global data30
    global data40
  global data50
  global data60
    % create the button
    btn = uicontrol('Style', 'pushbutton', 'String', 'ZERO', ...
        'Position', [20 20 100 30], 'Callback', @executeCode);
    % define the function to execute when the button is pressed
    function executeCode(~, ~)
     tic
while (toc<=5)
toc
readz3=str2num(readline(arduin));
dataA=mean(readz3(1));
dataB=mean(readz3(2));
dataC=mean(readz3(3));
dataD=mean(readz3(4));
dataE=mean(readz3(5));
dataF=mean(readz3(6));
end
disp('Code executed!');
data10=dataA;
data20=dataB;
data30=dataC;
data40=dataD;
data50=dataE;
data60=dataF;
    end
end
```

A.VII Average Results of Accuracy Testing

Ring Lateral Average					
Actual			Predicted		
Load (kgf)	X Coordinate	Y Coordinate	Load (kgf)	X Coordinate	Y Coordinate
6	1	0	1.80	1.65	0.37
12	1	0	10.40	0.57	-0.64
24	1	0	31.26	0.70	-0.04
6	0	2	6.06	0.00	1.81
12	0	2	12.05	0.00	1.95
24	0	2	24.13	0.01	2.00
6	2.5	1.5	6.99	1.35	0.92
12	2.5	1.5	11.46	1.90	0.92
24	2.5	1.5	22.96	2.07	1.39
6	1.5	2.5	5.96	1.99	2.54
12	1.5	2.5	10.76	1.99	2.06
24	1.5	2.5	24.29	1.99	1.94

Ring Medial Average					
Actual			Predicted		
Load (kgf)	X Coordinate	Y Coordinate	Load (kgf)	X Coordinate	Y Coordinate
6	1	0	5.57	1.01	1.34
12	1	0	12.15	0.77	0.44
24	1	0	26.30	0.84	0.08
6	3	1	7.39	2.77	0.99
12	3	1	14.86	2.97	1.61
24	3	1	30.93	3.00	1.45
6	1	2	5.62	1.35	2.02
12	1	2	13.69	1.23	1.74
24	1	2	24.61	1.00	1.60
6	2.5	3.5	4.24	2.13	1.19
12	2.5	3.5	10.45	2.23	0.48
24	2.5	3.5	25.28	2.19	-1.26

Zimmer Lateral Average					
Actual			Predicted		
Load (kgf)	X Coordinate	Y Coordinate	Load (kgf)	X Coordinate	Y Coordinate
6	2	1	5.05	0.77	0.43
12	2	1	9.90	1.26	0.58
24	2	1	32.58	-0.44	2.70
6	1	3	8.22	0.68	2.78
12	1	3	14.29	0.45	3.14
24	1	3	25.30	1.30	2.64
6	0	5	3.88	0.50	3.89
12	0	5	12.43	0.94	3.75
24	0	5	23.30	1.82	3.51

Zimmer Medial Average					
Actual			Predicted		
Load (kgf)	X Coordinate	Y Coordinate	Load (kgf)	X Coordinate	Y Coordinate
6	2	0	5.53	0.63	0.50
12	2	0	11.54	0.75	0.03
24	2	0	24.88	0.59	-0.12

6	0.5	0.5	9.28	0.67	0.19
12	0.5	0.5	14.11	0.68	0.03
24	0.5	0.5	29.32	0.39	0.20
6	1.5	2	8.14	0.73	2.09
12	1.5	2	12.92	0.73	2.37
24	1.5	2	23.48	0.59	2.53
6	2	4	6.30	1.27	3.17
12	2	4	9.83	1.23	3.54
24	2	4	23.76	1.27	3.88

A.VIII: Ethics for Cadaveric Testing

Permission as given by Zimmer Biomet to join their surgical training session in order to test the system in this research. Zimmer Biomet with the Clinical Anatomy Skills Centre, Glasgow University and the Royal College of Physicians and Surgeons of Glasgow (RCPS Glasgow) arranged for the procurement and disposal of cadavers and adhered to local and international regulations regarding the Human Tissues Act (2004). Zimmer Biomet was the sponsor of the research conducted at RCPS Glasgow and Zimmer Biomet confirmed that all regulatory requirements for the use of donor material in the research described were in place prior to the work being conducted. Under the sponsorship agreement between Zimmer Biomet and RCPS Glasgow, the latter confirmed to BU that permission was in place to use the data and publish the results in this thesis

A.IX: Average Cadaveric Data

Cadaver 1				
10 mm	Medial		Lateral	
Orientation	Load (kgf)	Location (X,Y)	Load (kgf)	Location (X,Y)
0°/10°	14.95	(1.20,2.50)	5.95	(-0.20,4.50)
45°	5.05	(1.95,2.50)	4.05	(0.30,3.95)
90°	1.40	(2.20,1.50)	4.40	(2.25,4.40)

Cadaver 1				
11 mm	Medial		Lateral	
Orientation	Load (kgf)	Location (X,Y)	Load (kgf)	Location (X,Y)
0°/10°	28.00	(1.00,2.90)	5.00	(-0.30,4.60)
45°	0.40	(2.10,1.80)	5.00	(0.10,4.50)
90°	1.00	(1.60,1.90)	4.40	(0.20,3.90)

Cadaver 1				
12 mm	Medial		Lateral	
Orientation	Load (kgf)	Location (X,Y)	Load (kgf)	Location (X,Y)
0°/10°	25.50	(1.60,2.80)	5.40	(-0.2,4.5)
45°	0.20	(1.60,1.90)	4.70	(0.60,3.80)
90°	0.20	(1.60,1.90)	4.70	(0.60,3.80)

Cadaver 1				
13 mm	Medial		Lateral	
Orientation	Load (kgf)	Location (X,Y)	Load (kgf)	Location (X,Y)
0°/10°	30.00	(0.30,3.40)	3.10	(-0.2,4.5)
45°	0.40	(1.80,1.50)	4.20	(0.30,3.40)
90°	6.00	(2.80,0.60)	4.90	(0.60,3.70)

Cadaver 2				
10 mm	Medial		Lateral	
Orientation	Load (kgf)	Location (X,Y)	Load (kgf)	Location (X,Y)
0°/10°	6.50	(1.80,3.05)	9.85	(1.00,3.55)
45°	3.40	(1.65,2.05)	4.35	(0.15,3.65)
90°	9.40	(1.30,2.35)	6.25	(0.35,3.40)

Cadaver 2				
11 mm	Medial		Lateral	
Orientation	Load (kgf)	Location (X,Y)	Load (kgf)	Location (X,Y)
0°/10°	23.35	(-0.40,4.15)	16.10	(1.05,4.95)
45°	3.65	(0.95,2.80)	6.40	(0.15,4.45)
90°	2.80	(1.00,3.25)	5.65	(0.20,4.45)

Cadaver 2				
12 mm	Medial		Lateral	
Orientation	Load (kgf)	Location (X,Y)	Load (kgf)	Location (X,Y)
0°/10°	27.20	(-0.05,2.55)	14.95	(0.2,3.55)
45°	7.30	(1.30,2.50)	4.35	(0.45,3.45)
90°	4.30	(0.50,2.50)	6.20	(0.20,3.85)

Cadaver 2				
13 mm	Medial		Lateral	
Orientation	Load (kgf)	Location (X,Y)	Load (kgf)	Location (X,Y)
0°/10°	31.70	(-0.65,3.50)	24.45	(0.2,4.8)
45°	13.40	(0.30,0.35)	3.80	(0.45,3.30)
90°	19.60	(0.40,4.85)	10.25	(0.35,6.95)

sensors

MDPI

Article

Exploring the Performance of an Artificial Intelligence-Based Load Sensor for Total Knee Replacements

Samira Al-Nasser [1], Siamak Noroozi [1,*], Adrian Harvey [2], Navid Aslani [3] and Roya Haratian [1]

[1] Bournemouth University, Fern Barrow, Poole BH12 3BB, UK; salnasser@bournemouth.ac.uk (S.A.-N.); rharatian@bournemouth.ac.uk (R.H.)
[2] Royal Bournemouth Hospital, Castle Ln E, Bournemouth BH7 7DW, UK; arharvey@doctors.net.uk
[3] Innovid Tech Ltd., 107b Athenlay Road, London SE15 3EJ, UK; navid.aslani3600@gmail.com
* Correspondence: snoroozi@bournemouth.ac.uk

Abstract: Using tibial sensors in total knee replacements (TKRs) can enhance patient outcomes and reduce early revision surgeries, benefitting hospitals, the National Health Services (NHS), stakeholders, biomedical companies, surgeons, and patients. Having a sensor that is accurate, precise (over the whole surface), and includes a wide range of loads is important to the success of joint force tracking. This research aims to investigate the accuracy of a novel intraoperative load sensor for use in TKRs. This research used a self-developed load sensor and artificial intelligence (AI). The sensor is compatible with Zimmer's Persona Knee System and adaptable to other knee systems. Accuracy and precision were assessed, comparing medial/lateral compartments inside/outside the sensing area and below/within the training load range. Five points were tested on both sides (medial and lateral), inside and outside of the sensing region, and with a range of loads. The average accuracy of the sensor was 83.41% and 84.63% for the load and location predictions, respectively. The highest accuracy, 99.20%, was recorded from inside the sensing area within the training load values, suggesting that expanding the training load range could enhance overall accuracy. The main outcomes were that (1) the load and location predictions were similar in accuracy and precision ($p > 0.05$) in both compartments, (2) the accuracy and precision of both predictions inside versus outside of the triangular sensing area were comparable ($p > 0.05$), and (3) there was a significant difference in the accuracy of load and location predictions ($p < 0.05$) when the load applied was below the training loading range. The intraoperative load sensor demonstrated good accuracy and precision over the whole surface and over a wide range of load values. Minor improvements to the software could greatly improve the results of the sensor. Having a reliable and robust sensor could greatly improve advancements in all joint surgeries.

Keywords: joint force sensor; intraoperative load measuring; artificial intelligence; total knee replacement

1. Introduction

The device made and used in this paper was an intraoperative load sensor that used artificial intelligence (AI) to predict the load and location of force in the knee during surgery. This device temporarily replaced the tibial insert to predict the load in both the medial (inside) and lateral (outside) compartments of the knee to allow surgeons to balance the soft tissue in real time with the use of an objective measuring tool. The introduction described the need for such a device by explaining the total knee replacement (TKR) procedure and failure and current devices and their limitations.

1.1. Total Knee Replacements

A total knee replacement (TKR) is the best option for pain relief and restoring function to the knee joint in patients with arthritis. The only treatment for end-stage osteoarthritis

2.

Cadaveric Testing of a Novel Smart Sensor for Total Knee Replacements

Samira Al-N[1]*, Siamak N[1] and Adrian H[2]

[1]Bournemouth University, Fern Barrow, UK

[2]Royal Bournemouth Hospital, UK

Abstract

The aim of this research was to prove the functionality of a smart tibial sensor for use during total knee replacements. The accuracy of such device provides surgeons with an objective tool for load balancing in the knee, where currently the joint is balanced based on the surgeon's 'feel' of a balanced knee. Literature surrounding the kinematics and tibiofemoral joint forces through the flexion arc coupled with qualitative feedback from an orthopedic surgeon provided a basis for proving the functionality of the smart-sensor.

Two full body cadavers underwent a cruciate-retaining total knee replacement using Zimmer's Persona Knee System. Varying thicknesses adjusted the height of the tibial smart-sensor between 10 mm to 13 mm in increments of 1 mm. The contact points and loads were observed through the flexion arc (0°, 45°, and 90°). The results found similar results between the literature surrounding both the compartmental forces and contact points throughout the range of motion. Moreover, qualitative feedback determined that the smart-sensor was robust and durable throughout its use in both cadavers demonstrating its potential as a reusable device. Minor adjustments to the graphical user interface would improve the ease of use for the surgical team. This sensor demonstrated the functionality of the smart-sensor through cadaveric testing in predicating both the load and location throughout a range of motion. Continued development of this sensor would provide surgeons with an accurate and robust tool for intraoperative joint balancing which could extend to all joints in the body.

Abbreviations

mm: Millimeter; N: Newtons; kg: Kilograms; TKR: Total Knee Replacement; lbf: Pounds of force; ROM: Range of Motion; GUI: Graphical User Interface

Introduction

Total Knee Replacement (TKR) surgeries are required in patients with debilitating pain, most commonly from osteoarthritis. The aim of this surgery is to provide patients with a better functioning knee joint to improve quality of life. However, the TKR surgery can be deemed unsuccessful for several reasons, which may require an early revision surgery [1]. Completed a review on 212 revision knee replacements where the top three reasons for revisions were polyethylene wear (25%), aseptic loosening (24.1%), and instability (21.2%). These complications can be attributed to improper tension in the joint. An intraoperative joint load sensor could aid in reducing these complications by balancing the load between the medial and lateral compartments.

To understand results from an intraoperative joint force sensor, it is important to gain a comprehensive background of the joint contact forces and contact points in the knee which were described in the subsequent sections.

Joint contact forces

Joint contact forces from the tibiofemoral joints are responsible for the primary internal forces affecting the knee joint. The tibiofemoral joint contact force is the force on the articulating surface between the tibia and femur. Loads at this joint are a result of external forces such as ground reaction forces, where studies have found that forces in the tibiofemoral joint can reach up to 8.5 times the Body Weight (BW) when walking downhill [2] and can reach 5 to 8 BW during running and side-stepping [3]. Furthermore, the distribution of the force onto the tibia through the medial and lateral compartments are typically not shared evenly. Where it was found that the medial

197

3.

Review Article

Design of a Novel Intraoperative Sensor for Load Balancing and Tracking during Total Knee Replacements (TKR)

Samira Al-Nasser[1]*; Siamak Noroozi[1]; Adrian Harvey[2]
[1]Bournemouth University, Design and Engineering, Poole, England
[2]Royal Bournemouth Hospital, Bournemouth, England

*Corresponding author: Samira Al-Nasser
Bournemouth University, Design and Engineering, Poole, England.
Email: salnasser@bournemouth.ac.uk

Abstract

Intraoperative load sensors have been developed with the aim of balancing the soft tissue in the knee during Total Knee Replacements (TKRs). Literature has shown success in soft tissue balancing however, concerns regarding the accuracy of these sensors remain. For this reason, previous research has attempted to create robust sensors for intraoperative use. The design of the sensor in this research has aimed to address the concerns outlined in the literature to create a new and novel smart-sensor for soft-tissue balancing. This new intraoperative load sensor included design features to increase accuracy while artificial intelligence allowed for comprehensive sensing across the entirety of the sensor, providing unparalleled insight during the operation. Notably, the sensor was designed to withstand loads of at least 450 N, ensuring robust performance of the sensor. To optimize the design process while minimizing cost, Finite Element Analysis was employed. This approach ensured the design features fulfilled their function while maintaining structural integrity to withstand loads. Moreover, the novelty of using training data from simulated data will reduce the iterative process of the labor-intensive collection of training data for the artificial intelligence while reducing human error associated with it. Results from the evaluation demonstrated the ability of this design to successfully bridge the current gap in the market by fulfilling all essential design criteria established within the literature. This innovative smart-sensing tool will in turn enhance patient outcomes and alleviate financial burdens to patients and the healthcare systems by reducing the need for early revision surgeries associated with improper joint tension.

Keywords: Joint force measuring; Soft tissue balancing; Intraoperative sensors; Artificial intelligence; Total knee replacement

Introduction

The soft tissue, namely ligaments, surrounding the knee are responsible for the passive stability of the joint [1,2]. The stability or lack thereof in the knee is a principal factor for success during a Total Knee Replacement (TKR) operation which is required when the cartilage in the joint is worn causing pain, discomfort, or functional problems. The tension created by the soft tissue surrounding the knee is responsible for the passive forces creating stability in the knee [3]. Intraoperative sensors aim to accurately measure tibiofemoral contact forces in real time throughout a Range of Motion (ROM) [4]. The need for such devices was apparent in a study by Batailler et al. where at least 60% of TKRs needed additional balancing procedures, where having a quantitively balanced knee provided higher patient satisfaction scores [5].

Functional improvements, like postoperative ROM and gait analysis, to the knee have also been observed when the surrounding soft tissue was balanced. For example, a 6-minute walking distance showed significant improvements when the knee was balanced intraoperatively with a sensor [6]. Ample research supported this idea where postoperative instability was reported as a major cause for early TKR revisions [7-9].